e-ISSN: 3061-9939

JOURNAL OF NAVAL ARCHITECTURE AND MARINE TECHNOLOGY

ISSUE 228, 2026

www.jnamt.org

RESEARCH ARTICLE

DOI: 10.54926/jnamt.2025.2526

J Nav Architect Mar Technol 2026;228:1-10

Microplastic Pollution in Ship-Sourced Wastewater: Assessment of Pollution Load Risk for Ballast and Bilge Water

Emrah Şık

İstanbul Technical University Faculty of Maritime, Department of Basic Sciences, İstanbul, Türkiye

To cite this article: E. Şık. Microplastic pollution in ship-sourced wastewater: assessment of pollution load risk for ballast and bilge water. *J Nav Architect Mar Technol*. 2026;228:1-10

Received: 08.09.2025 - **Revision Requested:** 02.11.2025 - **Last Revision Received:** 07.11.2025 - **Accepted:** 01.12.2025 - **Publication Date:** 07.01.2026

Abstract

The rapid development of maritime transport also causes a number of negative environmental impacts. One of these problems is marine pollution caused by the operation of ships. Pollution from ship sewage includes ballast water (BAL-W) and bilge water (BIL-W), which are regulated under International Convention for the Prevention of Pollution from Ships Annex IV. Both BAL-W and BIL-W samples were analysed in the study. Many of the microplastic (MP) particles detected in the BAL-W samples were micro sized, while the majority of MPs found in the BIL-W samples were macro (>0.5 mm) and micro (1 µm-<5 mm) in size. The findings show that MPs constitute the majority (53%) of the plastics analysed, followed by 25% mesoplastics and 11% nanoplastics (NPs). Plastics with a size class of 50-300 µm were most abundant in both BAL-W and BIL-W. For BAL-W and BIL-W sources, the average MP sizes were calculated to be 0.025-4.99±0.050 mm and 0.05-0.1±0.050 mm, respectively. Rubber/commercial (PNEU), polyethylene (PET) terephthalate, polystyrene (PS), and polyoxymethylene (POM) were the most abundant polymer types found in the BIL-W samples, accounting for 47.82%, 10.86%, 9.78%, and 6.55%, respectively, while PNEU and PE were the most abundant polymer types found in the BAL-W samples, accounting for 22.91% and 7.98%, respectively. The pollution load index was calculated 7.75 (Hazard Category IV) and 12.17 (Hazard Category V) for BAL-W and BIL-W waters. It is now clear that the BAL-W management system needs to be evaluated to eliminate MP pollution due to the presence of polymers in BIL-W and BAL-W.

Keywords: Marine environmental protection, MARPOL 73/78 Annex IV, sewage from ships, microplastic pollution, pollution load index (PLI)

1. Introduction

The massive amounts of plastic in the world's seas and oceans create a serious hazards to their natural ecological live. It is anticipated that 0.8 to 23.0 million tons of plastic wastes are floating in the seas and oceans [1]. Micro and macroplastics (MPs) contribute significantly to marine plastic pollution. With the increase in global maritime trade, the number of merchant ships is growing every year. As more ships transport, in addition to environmental degradation on land, pollution from ships is growing. The pieces of plastic are categorized based on their size: mesoplastics (5-25 mm), MPs (1-5 mm; MPs), and nanoplastics (<1 µm; NPs) [2-4]. MPs, particularly NPs, are tiny particles that may cause a variety of impacts on marine and coastal organisms. Ingestion of these plastics may threaten marine organisms' growth, survival, and reproduction [5]. They may also be hazardous to human health since they accumulate in seafood [6].

Address for Correspondence: Asst. Prof. Emrah Şık, İstanbul Technical University Faculty of Maritime, Department of Basic Sciences, İstanbul, Türkiye
E-mail: emrahs@itu.edu.tr
ORCID ID: orcid.org/0009-0000-1202-0314

Copyright© 2026 The Author. Published by Galenos Publishing House on behalf of UCTEA Turkish Chamber of Naval Architects and Marine Engineers.
Licensed under a Creative Commons Attribution-NonCommercial-NoDerivatives 4.0 (CC BY-NC-ND) International License

Sources of pollution reaching the seas and oceans include terrestrial origin (44%), atmospheric pollution (33%), pollution from maritime activities (12%), waste and sewage dumping (10%), and offshore drilling and mining (1%) [7,8]. While terrestrial or anthropogenic pollutants are the main sources, pollutants from ships also contribute signific antly to marine pollution. The International Convention for the Prevention of Pollution from Ships (MARPOL 1973/78) is the core international maritime convention adopted by the International Maritime Organization (IMO) to prevent both operational and accidental pollution [9]. The Convention consists of six technical Annexes covering various aspects of marine pollution prevention, e.g., oil, toxic liquids, garbage, and emissions. Two of these annexes are "Annex I. Regulations for the Prevention of Pollution by Oil" and "Annex IV: Prevention of Pollution from Ship Sewage." In addition, The ballast water (BAL-W) Management Convention or BWM Convention (2004) is a treaty adopted by the IMO in order to help prevent the spread of potentially harmful aquatic organisms and pathogens in ships' BAL-W. According to all, the discharge of ship sewage also contributes to marine pollution. Sewage, greywater, debris, oil/water separator effluent, cooling water, boiler and steam generator blow-down, and bilge water (BIL-W) are examples of waste streams on ships [10]. Among these, BAL-W is important for its water-capacity, BIL-W is another waste source with high pollutant potential due to ship operational processes (the engine room and leaks or maintenance operations etc.). Therefore, these two wastewater types were chosen for this study.

Marine pollution is widely described as the hazardous migration of substances or energy that alters physical, chemical, or biological characteristics due to human activity (MARPOL Convention, 1973/78) [11]. However, in this context, organisms carried in BAL-W are regarded as biological agents rather than "substances". BAL-W and BIL-W are regarded as critical vectors for the spread of various pollutants, including MPs, across the world's seas [12,13]. MPs are synthetic plastic particles less than 5 mm in diameter that are persistent and non-biodegradable in the environment [14,15]. These particles not only represent physical pollution, but also threaten the health of ecosystems as they act as carriers for toxic chemicals, heavy metals, and pathogenic microorganisms. BAL-W and BIL-W, in particular, are thought to be key sources of conveyance for the spread of biological pollution and pollutants in the marine environment. However, barely anything has been revealed about the plastics included in BAL-W and BIL-W.

BAL-W: Maritime traffic continues to increase, with around 51,400 merchant ships in operation worldwide and around 3 to 5 billion tons of BAL-W carried by ships every year [7]. Today, BAL-W is one of the most important maritime pollutants and is associated with about one third of documented infestations worldwide. One of the biggest challenges for maritime transport is to find safe solutions for BAL-W management that minimize the environmental impact. To address this issue, following its regular meetings, the IMO has revised Annex IV of MARPOL 73/78 and made it mandatory for large ships to be equipped with a BAL-W management system (BWMS) from September 2025 [11]. This reduces the potential of invasive species spreading as a result of ships discharging untreated BAL-W. However, these waste waters, which are discharged and distributed in vast amounts across the world, are only disinfected for microbiological causes (Table 1) [16,17]. It still allows for the transfer of other pollutant factors, such as MPs. During ballasting, large amounts of seawater are pumped into the ballast tanks of ships. As a result, various creatures and particles prevalent in the maritime environment, including plastics, enter the ballast tanks with the brine and accumulate. Consequently, the collection of BAL-W from polluted territories could lead in MPs entering the port of destination when water treatment does not occur out [18]. In this way, MPs might contribute to marine pollution by BAL-W or BIL-W during marine transportation and act as a reservoir of pollutants.

To meet discharge standards, almost all ships are expected to be equipped with BWMS. Although various technologies such as filtration, chlorination, ozonation, pasteurization,

Table 1. IMO D-2 ballast water discharge standard.

Parameter	The limits for the indicators in the ballast discharge	
	USCG standards [10]	**IMO D2 standards [4]**
Zooplankton, organisms ≥50 µm	<1 viable organisms/100 m^3	<10 viable organisms/m^3
Phytoplankton, organisms 10-50 µm	<1 viable organisms/100 mL	<10 viable organisms/mL
Vibrio cholerae	<1 CFU/100 mL	<1 CFU/100 mL
Escherichia coli	<126 CFU/10 mL	<250 CFU/100 mL
Enterococci	<33 CFU/100 mL	<100 CFU/100 mL

CFU: Colony-forming unit, IMO: International Maritime Organization, USCG: United States Coast Guard

and ultraviolet radiation (alone or in combination) are used for water purification [19,20], these are not effective methods for combating MP pollution. Studies have found that the average content of MPs in ship BAL-W and seawater samples were 12.53 and 11.80 units/L, respectively, with a high concentration of MPs in the 50-300 µm size class. The findings identified the main sources of MPs (such as BAL-W), their transport pathways and the associated ecological risks to marine ecosystems [12].

BIL-W: Various harmful substances, consisting of MPs and heavy metals, might enter the sea from ships through a variety of sources, including grey water, wastewater, ship cooling water, and treated sewage. Wastewater from regular ship operations persists and poses a significant risk to coastal aquatic ecosystems [21,22]. The wastewater has a pH range of 6.8 to 9.0, a salinity of 25 to 35 g/L, an oil concentration of 36 to 2953 mg/L, and a high chemical oxygen demand> 3-15 g/L [23]. In addition, studies have found MPs in wastewater [12]. For these reasons, strict environmental regulations on wastewater discharges and the tendency to reuse treated water make wastewater treatment a critical factor. MARPOL 73/78 regulates BIL-W management, limiting oil content to ≤15 mg/L when discharged into the sea. The literature reports on various types of BIL-W treatment methods, including coagulation, flocculation, membrane filtration, electrocoagulation, flotation, and combinations of these processes [24,25].

In addition, investigations have demonstrated that MPs accumulate in a variety of marine animals [26-28], and because of their small size, these particles can be ingested by a wide range of marine organisms [12]. Also, MPs have the ability to adhere to a variety of marine contaminants, including heavy metals, and accelerate their build up in the marine environment [29,30]. Human exposure to MPs and other contaminants that build up in marine food webs may have negative consequences [14]. All of this emphasizes how our seas are affected by MP contamination. Although there is few research on the migration of MPs through BAL-W, there aren't many on the migration of MPs through BIL-W. BAL-W and BIL-W pollutants, which have been studied in small quantities for MPs [12].

The aims of this study were to investigate MPs abundance and their characteristics, including size, polymer type, and chemical composition, in the BAL-W and BIL-W of ships, and to determine the pollution load index (PLI) of MPs in the BAL-W and BIL-W.

2. Materials and Methods

2.1. The Sampling Stations

The sampling work was conducted from April to September, 2024. There were seven sampling stations (Table 1) set up, 4 BAL-W and 3 BIL-W in the different type of ships, and seven waste water samples from ship-originated were obtained by collecting sample at each station. The vessels from which water samples were selected at random from three seas: the Black Sea, the Mediterranean Sea, and the Marmara Sea, regardless of type or tonnage. Table 2 shows information about each of the ships that were sampled for ship sewage, and Table 3 shows the physical and chemical measurement results of the samples. The BAL-W volume of the ships ranged from 500 m^3 to 10,000 m^3.

2.2. Sample Collection

Samples were collected from 7 sampling station (Table 3) as vertically water column. BAL-W sampling depth varied from 2 m to 6 m, while the BIL-W samples were taken from a depth of around 1 m below the surface. For this purpuse, 7 samples the volumes are given in Table 2, were collected with containers to include MPs. Then all the samples were transferred into the glass bottle and treated with hydrogen peroxide (30% v/v, Merck, Germany) to in order to remove organic material [31-33]. The bottles were rinsed several times with ethanol before use. Checked for any potential contamination occurring in the sample in the field and laboratory. Water samples were stored in dark and cold conditions until MP analysis.

Table 2. Information on the sampled ships.

Station	Matrix	Date	Type of vessel	GRT	BWMS	Sampling location	Sample volume (L)
1	BAL	31.09.2024	Oil tanker	3225	D2 UV/filter	Mediterranean/Italy/Ravina	5
2	BIL	31.09.2024	Oil tanker	3225	-	Mediterranean/Italy/Ravina	5
3	BAL	18.05.2024	Chemical tanker	3776	D2 UV/filter	Novorossysk/Russia	5
4	BAL	18.05.2024	Chemical tanker	3776	D2 UV/filter	Novorossysk/Russia	5
5	BIL	04.04.2024	Cargo	1554	-	Tuzla/İstanbul/Türkiye	3
6	BIL	25.04.2024	Tugboat	939	-	Tuzla/İstanbul/Türkiye	3
7	BAL	01.09.2024	Cargo	1243	-	Mersin/Türkiye	5

2-BAL: Dry cargo ship pre-BWMS sample, 3-BAL: Dry cargo ship post-BWMS sample, BIL: Bilge, BAL: Ballast

Table 3. Physical and chemical analysis results of ship sewage samples.

Station	Matrix	pH (-)	Conductivity (mS)	Salinity (g/kg)	Method
1	BAL	7.80	41.3	30.8	Vertical water column
2	BIL	8.20	1.33	0.78	
3	BAL	8.26	34.0	26.7	
4	BAL	8.22	34.6	26.6	
5	BIL	8.24	7.25	0.28	
6	BIL	7.80	2.64	0.25	
7	BAL	8.65	54.9	41.6	

2.3. Analysis

The polymer type of each presumed MP particle was determined by attenuated total reflection Fourier-transform infrared spectroscopy (micro-ATR-FTIR) at the laboratory. The samples were passed through a cellulose pre-filter and then filtered through 13 mm diameter aluminium oxide membrane filters with a 0.1 µm pore size (Whatman Cytiva Anodisc, Germany) into glass petri dishes. The collected samples were left under a fume hood for 2 hours and prepared for measurement with the micro-FTIR device. This technique produces high-quality spectral images of sample areas, with a pixel resolution of 6, 25, 25, or 50 micro meters. The dried filters were stored in a dust-free environment until the time of analysis. The filters were scanned in the imaging mode of the Perkin Elmer FTIR Spotlight 400 device using the Spectrum Image application (optical imaging), and transmittance measurements (chemical imaging) were taken across the entire filter surface. The chemical imaging was performed within a 10 mm x 10 mm area, scanning a 200 µm x 200 µm surface in the IR spectrum range of 690-4000 cm^{-1} using the Spectrum 3 application. Spectra were compiled after applying atmospheric correction, and data processing (MP mapping) was carried out using the siMPle application (Aalborg University-Denmark, Alfred-Wegener Institute-Germany). The results compiled from the siMPle application were used to create a MP distribution table.

2.4. PLI

This method has been commonly employed in earlier investigations of heavy metal pollution in sediment [34,35], and researchers are currently applying it for assessing the risk of MPs [36-38]. The PLI is a standard method for observing and evaluating pollution levels at various locations.

Tomlinson et al. [39] (1980) developed the pollutant load index. The PLI calculates pollution load by taking into account various contaminants (e.g., all metals) at various location. It is a basic geometric mean for the pollution factor (*CF*). The *CF* is calculated according to Equation 1 [40].

$$CF = CF_i / C_o \quad (1)$$

In Equation 1, *CF*; CF_i and C_o are the observed concentration of MPs at sampling location and the lowest concentration/background value of MP detected in the sample, respectively.

The PLI was derived with Equation (2):

$$\text{PLI} = \prod_i^n \left(CF_i \right)^{0.5} \quad (2)$$

Where *i* represents a sample, *n* represents the number of samples, C_i represents the abundance of plastic in sample *i*, and C_o represents the lowest element concentration found in the accessible literature [41]. However, in the lack of background data from similar environments, the lowest baseline limit for MP abundance identified in this study was set at 0.05 units/m^3 based on data from the study conducted by Mutuku et al. [42] (2024) in five major oceans.

3. Results and Discussion

3.1. MPs Size Distribution from Ship-Sewage

MPs were detected in all BAL-W and BIL-W samples. The BAL-W and BIL-W samples presented in Figure 1 and Figure 2 included 96 and 92 plastic particles, respectively. Figure 2 shows the mean number of MPs in BAL-W and seawater. MPs amounts in the BAL-W and BIL-W samples were 5.28 (±3.57) and 6.20 (±3.20) items/L, respectively. There was no significant difference (p-value> 0.05) in the number of MPs between BAL-W and BIL-W. The abundance of MPs in the bilge tanks of the ships was moderately higher (36±4.99 items/L) than in the ballast tanks (5.0±1.39 items/L) (Figures 1 and 2).

The Persian Gulf (Bushehr port and Assaluyeh port) found concentrations ranging from 5.53 to 21.6 items/m^3 [12], whereas our concentrations in the BAL-W samples were similarly level with a range between 4.8 to 27 items/m^3. Furthermore, research by Matiddi et al. [43] investigated levels of MP in the BAL-W of nine commercial ships and found values ranging from 100 to 1410 items/m^3, with a mean of 651 items/m^3.

The BAL-W samples contained 55.6.0% particles between 25 and 50 µm, 38.8% with particles larger than 50 µm, and 5.6% with particles smaller than 25 µm. But, 48.0% of the

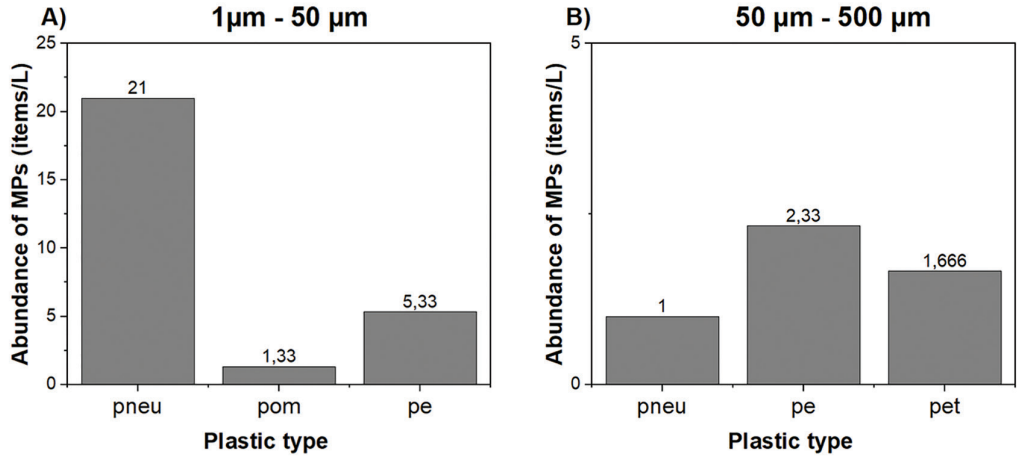


Figure 1. Types of plastic in BAL-W according to size classes 1-50 µm, and 50 -500 µm.

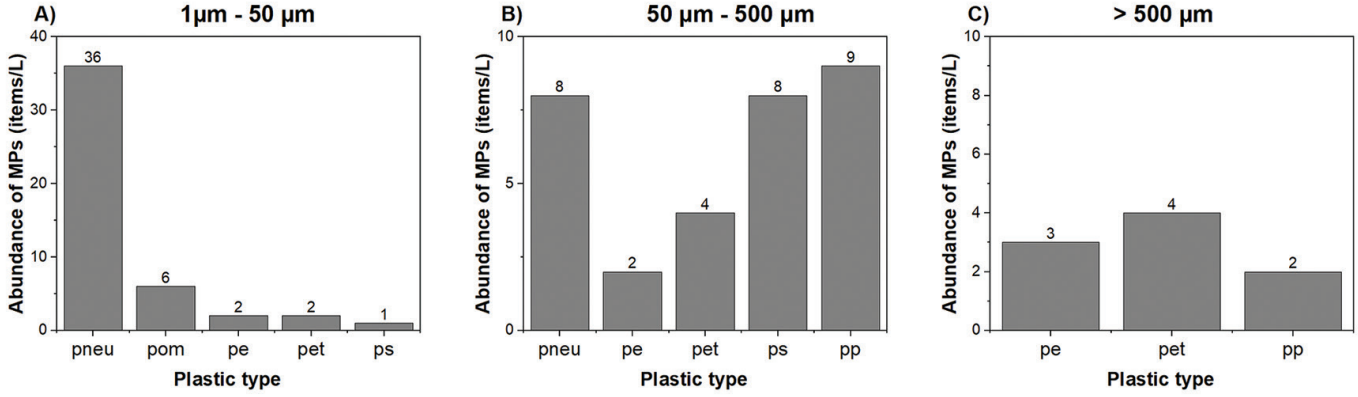


Figure 2. Types of plastic in BIL-W according to size classes 1-50 µm, 50 -500 µm, and >500 µm.

plastics in the SS samples were 0.05-0.1 mm particles, 24.0% were 0.1-0.25 mm particles, and the remaining 28% were plastics larger than 0.25 mm. Previous research found that MPs were most prevalent in seawater in the Persian Gulf, Iran [44], Caspian Sea, Iran [45], and Marmara Sea, Türkiye [46] with sizes of 1000-3000, 1000-5000, and 1-100 µm, respectively.

In BAL-W operations, the point of intake is critical. The plastic particle count per unit volume in the ballast sample is predicted to be high when the ballast intake occurs in a hub or busier port. Conversely, the plastic count density will be low in port locations with limited capacity. Terrestrial pollution is also influenced by the port area's population density and residential layout.

Remarkably high abundances of mezo and macro particles were found in two bilge samples (5 and 6), up to 4.69 and 15.33 items/L. However, 1.55 to 4.8 µm/L particles were quantified in the ballast tank, which is also located in the 7th sample. In samples 5 and 7, which show the highest plastic abundance, it is noticeable that these two sampling sites are commercial port areas with heavy shipping traffic. It is assumed that the intensive commercial activities, population density, and terrestrial contaminants in these areas have contributed to the increase in plastic density.

Particularly in aquatic bodies, MPs gradually degrade into smaller MP and even NP fragments due to regular abrasion [47]. An enormous major threat in the proliferation of these small plastic particles is their potential hazard to organisms that continuously ingest them and their bioaccumulation in living organisms [48,49]. Based on this objective, it is anticipated that the elements of ship sewage tanks might add to the MP pollution that is already there and spread the related chemical and biological pollutants. It is crucial to note that MPs are effective vectors for the transport of heavy metals

and chemical pollutants across many miles. The presence of MPs in the marine environment, may migrate to enter of MPs and connected contaminants into food chains and eventually ingested by human [50]. Therefore, it is stressed to adopt strict regulations to minimize MP levels in ship sewage tanks before discharge through effective treatment systems [51].

3.2. Chemical Characterization of Microplastics

This study investigated the presence of MPs in the BAL-W and BIL-W of ships sailing in various seas and ports. The 188 plastic particles in the BS and SS samples belong to six polymer types: polyethylene (PE), polyethylene terephthalate (PET), polyoxymethylene (POM), polypropylene (PP), polystyrene (PS), and Rubber/commercial (PNEU). The chemical composition of the plastics has been confirmed using micro-FTIR spectroscopy. Figure 3 displays the color codes for the different polymer types observed in the BAL-W and BIL-W samples. However, particles containing protein, cellulose, crustaceans and etc. have been excluded from the particle count. Our study of the MP samples from the ship sewage indicates that the main constituent is PNEU (rubber/commercial), with POM and PET being the other two typically identified polymers. PNEU and POM are engineering thermoplastics used for manufacturing specific components with high stiffness, low friction, and superior dimensional stability. Seals and rubbers are commonly utilized in marine machinery and auxiliary operations for both static and dynamic applications. PNEU pneumatic systems provide several advantages. Furthermore, POM polymer is employed in high-performance technical components such as tiny gears, ball bearings, skid plates, fasteners, clamps, and locking mechanisms. As therefore, long-lasting polymers like POM and PNEU are chosen in corrosive and abrasive conditions like seawater. In contrast, PET is generally used in areas such as the food industry, beverage packaging, packaging film, plastic boxes, kitchenware, mechanical engineering and packaging. It is also a preferred material in the manufacture of moving parts that operate under high pressure. Unlike PNEU and POM, emissions in ship-sourced wastewater are assumed to be caused by human or essential activity. Although the maritime environment contains a wide range of plastics, MPs such as polyvinyl chloride, PP, PE, PS, PET, and polyamide are prevalent [32,54]. According to published studies, the most popular polymer types in the Persian Gulf of Iran are PE, PET, and nylon [53], PP and PE are the most prevalent polymer types in the surface waters of China's Yellow Sea region [53], and nylon is the most prevalent polymer type in Antarctica's Ross Sea [46]. For example, pneumatic rubber fenders are used in ports and on ships to minimize structural damage in the event of collisions [54]. However, the rubber broken from these collisions can enter the marine ecosystem and be carried into the tanks during ballast transportation. The findings of this study are coherent with previous studies, but also provide new details about BIL-W that have been little discussion thus far. The differences in the abundance of MPs and the types of polymers may be due to various factors such as traffic, fishing and marine tourism on various coasts of the world.

While most MP particles were observed in BAL-W samples 7 and 1 in Figure 4a, the particles in BIL-W samples 1 and 4 were mostly micro- and mesoplastic (Figure 4b). While sample 2 contained more plastic fragments (Figure 5b), sample 5 contained predominantly mesoplastic particles (Figure 5a). The BIL-W samples contained fewer particles in the 1-5 mm size range, while the BAL-W samples had the most particles in the <50 mm range.

The findings of this investigation indicated that MPs were not eliminated by the BAL-W disinfection system, and that both wastewaters included polymers of various types and sizes.

3.3. Risk Assessment of MP PLI

Pollution indexes are widely used to assess plastic pollution in aquatic and terrestrial environments [38,55]. These indexes provide a quantitative framework for assessing pollution levels and potential ecological risks [37]. As macro-, micro- and NPs mostly originate from anthropogenic sources, the determination of a reference background level (C_o) for the assessment of plastic pollution remains a crucial challenge [56]. As there are no defined standards for assessing for

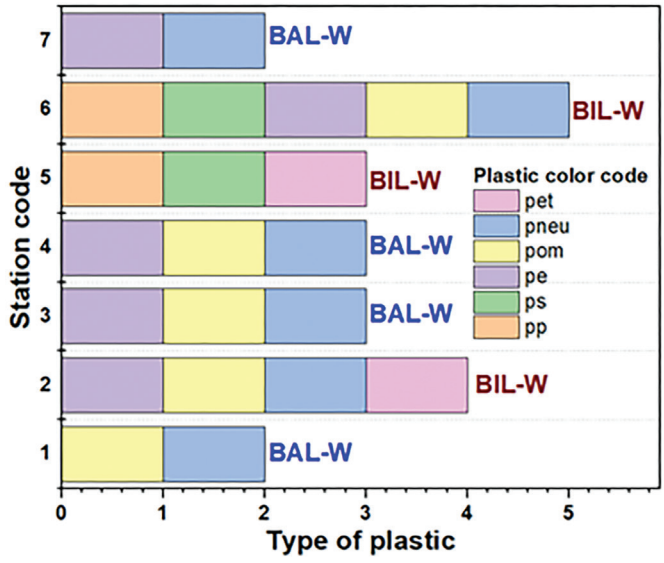


Figure 3. Distribution of MPs detected in ship-sewage sample.

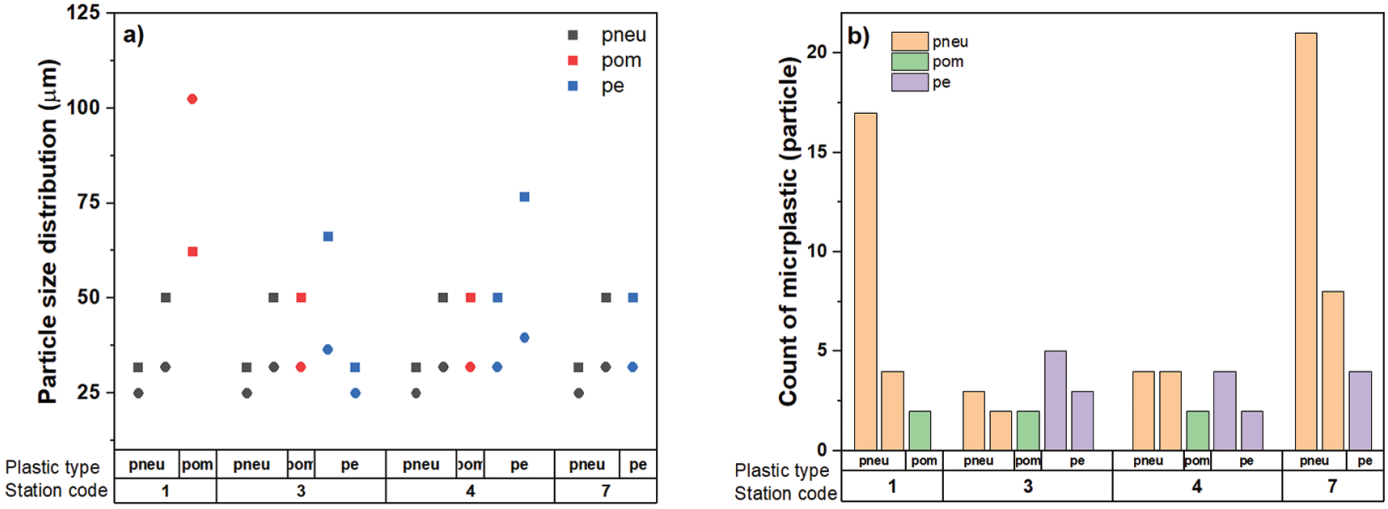


Figure 4. MP analysis in ballast water samples a) size distribution by species, b) Count of MPs.

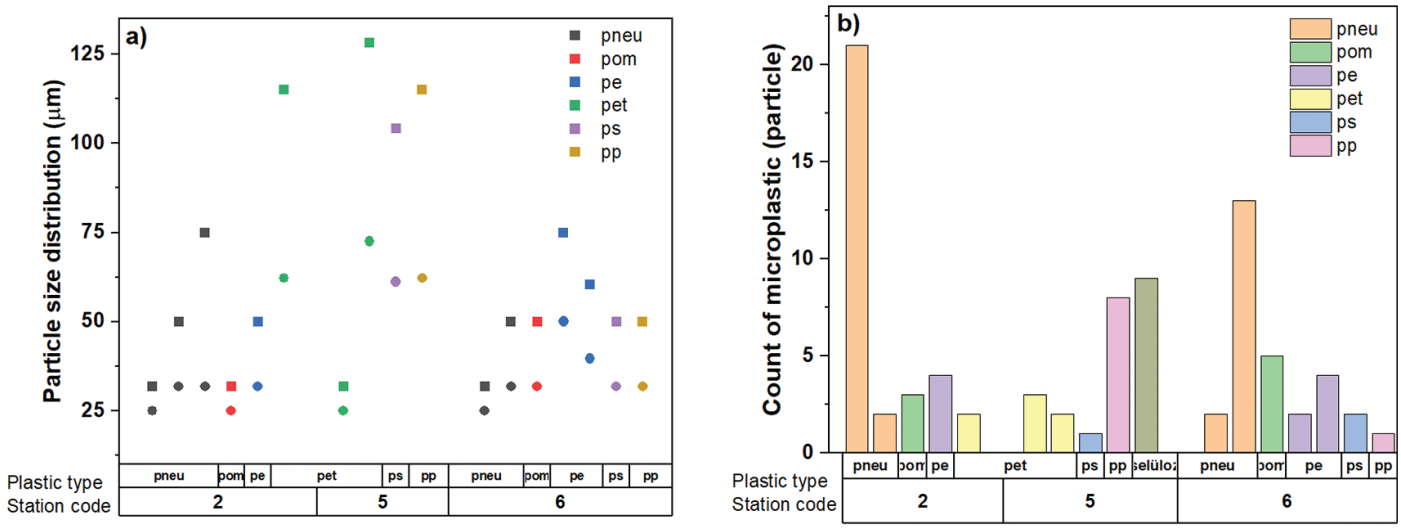


Figure 5. MP analysis in bilge water samples a) size distribution by species, b) Count of MPs.

the risk assessment of plastics, the results of the PLI largely depend on the chosen reference background value of plastic abundance [57]. However, these reference values may vary considerably from study to study. Some research employs probabilistic analytical values based on species sensitivity distributions [58], whereas others utilize the minimal abundance values at the sampling site as baseline concentrations [59]. These methodological inadequacies contribute to large variations in PLI-based risk evaluations for MPs [55]. The concentration of MPs in the seas varies from 0.002 to 22 pc/m^3, revealing a skewed distribution. The average concentration was highest in the Atlantic Ocean (2.58 pc/m^3) and lowest in the Southern Ocean (0.04 pc/m^3) [42].

Table 4 represents the PLI calculated for the BAL-W and BIL-W samples. The estimated pollutant load index indicated significant pollution risks in two BAL-W samples and a very high pollution risk in five samples. A high PLI score indicate the region is contaminated with MPs.

The calculated PLI values for all BIL-W samples were $10.2 \leq PLI < 12.17$, indicating a very high level of very high pollution (Hazard Category V). The calculated PLI values for BAL-W ranged from Hazard Category IV to Hazard Category V. This type of risk assessment for ship sewage

Table 4. Pollution load index (PLI) calculated for BAL-W and BIL-W samples.

Station	Matrix	CF	PLI	Hazard Level
1	BAL	92	9.6	V, very high pollution
2	BIL	148	12.17	V, very high pollution
3	BAL	60	7.75	IV, significant pollution
4	BAL	64	8.0	IV, significant pollution
5	BIL	104	10.2	V, very high pollution
6	BIL	128	11,3	V, very high pollution
7	BAL	132	11.5	V, very high pollution

C_o: The lowest value found in the literature was set at 0.05 units/m^3. BIL-W: Bilge water, BAL-W: Ballast water, *CF*: Pollution factor.

is unique to this study; similar results have been reported for Categories IV and V in urban sewage [60] and seawater [61,62]. Previous research by Dar and Gani [55] (2025) has found that the PLI ranged from 3.9 (Hazard Category I) to 40 (Hazard Category IV), indicating that glaciers are moderately to severely polluted. The findings of the PLI of MPs reveal that the environmental impact of MP pollution in the oceans, as well as the contribution of ship sewage (BAL-W and BIL-W), represent a significant risk to marine ecosystems. BAL-W and BIL-W wastewater may transport MP particles and pollutants in these plastics between ports.

In addition, MP fragments have the potential to be significant carriers of pollutants [63,64]. These transports can retain pollutants on their surfaces through physical adsorption, depending on potential pollutants such as heavy metals, pharmaceuticals, etc., in the regional marine and ocean ecosystem, and even transfer them to marine organisms or humans that feed on them.

Based on the findings of this study, BIL is an important source of MPs, as it is exposed to intense pollution from ship auxiliary operational processes. BAL is also a potential source of MPs, which can act as a carrier of these particles and related pollutants between different ports and could potentially have harmful effects on the marine environment, aquatic organisms, and, consequently, human health. As a result, macro-, micro-, and NPs are capable of acting as vectors for pollutant transmission, hence their inclusion as an environmental impact element in ship sewage regulations (e.g., MARPOL Annex I or Annex IV) is beneficial and raising awareness is necessary in the maritime sector.

4. Conclusion

The micro-FTIR analysis of BAL-W and BIL-W samples conducted in this work revealed that ship sewage poses a serious environmental risk in terms of MP pollutants. The most prevalent polymers identified in BAL-Ws were POM, PNEU, and PET, whereas POM, PET, PS, and PNEU were found in BIL-Ws. The abundance of MPs in the bilge tanks of the ships was moderately higher (37±0.7 particles/L) than in the ballast tanks (24.0±1.0 particles/L). We concluded that the MP content in BIL-W is often higher than in BAL-W, making BIL-Ws popular places to find MP pollution due to the impacts of various operational and natural factors, such as tank position, personnel activities, environmental conditions, waves, and wind, causing bilge tanks more prone to the accumulation of large amounts of MP. The findings reveal that the BWMS implemented by the IMO as part of the MARPOL Convention for the Protection of the Marine Environment are insufficient for eliminating MPs contamination.

According to the pollutant load index, ship-sewage from BAL-W and BIL-W is rated as Hazard Category IV (significant pollution) and Hazard Category V (extreme pollution), causing serious environmental risk. All of the study's findings highlight the importance of ships in sea ecosystem, as well as their far-reaching influence as a result of their many interactions with the environment. The findings of this study, which focus on the kind and concentration of MPs that collect in ship sewage, can be utilized as primary data to inform future research on the impact of MPs on ships. Based on the findings of the study, it is recommended to implement effective waste management systems, introduce stricter regulations, and raise marine sector awareness.

Footnotes

Financial Disclosure: The author declared that this study received no financial support.

References

[1] M. Strokal, P. Vriend, M. P. P. Bak, C. Kroeze, J. van Wijnen, and T. van Emmerik, "River export of macro- and microplastics to seas by sources worldwide", *Nature Communications,* vol. 10, no. 14, pp. 4842, Aug 2023.

[2] P. Madala, A. Waikar, and H. Parate, "Detection to remediation: strategies for managing microplastic pollution in freshwater systems", *International Journal of Computational and Experimental Science and Engineering*, vol. 11, no. 3, pp. 5301-5316, 2025.

[3] GESAMP, "Sources, fate and effects of microplastics in the marine environment: a global assessment", (Kershaw, P.J., ed.). Rep. Stud. GESAMP, 90-96, 2015.

[4] A.L. Andrady "The plastic in microplastics: a review", *Marine Pollution Bulletin,* vol. 119, no. 1, pp. 12-22, Jun 2017.

[5] M. Cole, C. Lindeque Halsband, and T. S. Galloway, "Microplastics as contaminants in the marine environment: A review", *Marine Pollution Bulletin*, vol. 62, no. 12, 2588-2597, Dec 2011.

[6] M. R. M. Zaki, and A. Z. Aris, "An overview of the effects of nanoplastics on marine organisms", *Science Total Environmental*, vol. 20, no. 831, pp. 154757, 2022.

[7] M. Čović, B. Bacalja, M. Krčum, and G. J. Mrčelić, "From ballast water to harmful air emissions: how to reduce the impact of shipping on the pollution of the marine environment -a review", *WIT Transactions on The Built Environment,* vol. 204, pp. 105-116, Sep 2021.

[8] G. Potters, Marine Pollution. Bookboon, 1st edition. ISBN 978-87-403-0540-1, 2013.

[9] IMO (International Maritime Organization), "International convention for the control and management of ships' ballast water and sediments", London, BWM/CONF/36, London, U.K. 2004.

[10] WHO, Guide to ship sanitation. 3rd edition. World Health Organization; 2011.

[11] M. Convention, "International convention for the prevention of pollution from ships", *MARPOL Conventional Outlet.* 1973. http://www.imo.org

[12] A. Zendehboudi, et al. "Analysis of microplastics in ships ballast water and its ecological risk assessment studies from the Persian Gulf", *Marine Pollution Bulletin*, vol. 198, pp. 115825, Jan 2024.

[13] M. Arienzo, L. Ferrara and Marco Trifuoggi, "The dual role of microplastics in marine environment: sink and vectors of pollutants", *Journal of Marine Science Engineering*, vol 9, pp. 642, Jun 2021.

[14] A. Anthony, "Microplastics in the marine environment", *Marine Pollution Bulletin*, vol. 62, no. 8, pp. 1596-1605, Aug 2011.

[15] L. Peng, D. Fu, H. Qi, C.Q. Lan, H. Yu, & C.bGe, "Micro-and nano-plastics in marine environment: source, distribution and threats — a review", *Science of the Total Environment,* vol. 698, 134254, Jan 2020.

[16] U.S. Environmental Protection Agency (EPA), "*Generic protocol for the verification of ballast water treatment technology*", version 5.1. In: Report Number EPA/600/R-10/146. United States Environmental Protection Agency, Washington, DC. 2010.

[17] Global TestNet, "Ballast Water Management system", 2021. https://globaltestnet.org/our-work.html

[18] U.S. Coast Guard, "In: standards for living organisms in ships' ballast water discharged in U.S. waters", Final Rule. FR, 77, 17254-17304, 2012.

[19] E. Tsolaki, and E. Diamadopoulos, "Technologies for ballast water treatment: a review", *Journal of Chemical Technology & Biotechnology,* vol. 85, no. 1, pp. 19-32, Jan 2010.

[20] W. A. Gerhard, K. Lundgreen, G. Drillet, R. Baumler, H. Holbech, and C.K. Gunsch, "Installation and use of ballast water treatment systems – implications for compliance and enforcement", *Ocean & Coastal Management*, vol. 181, no. 1, 104907, Nov 2019.

[21] J. Lloret, N. Zaragoza, D. Caballero, and V. Riera, "Impacts of recreational boating on the marine environment of Cap de Creus (Mediterranean Sea)", *Ocean & Coastal Management,* vol. 51, no. 11, pp. 749-754, 2008.

[22] O. V. Malakhov, O. M. Palagin, A. I. Naydyonov, K. A. Lytkhoglyad, and A. V. Bondarenko, "Bilge and oily water treatment during operation of vessel", *TransNav,* vol. 18, no. 2, pp. 433-445, 2024.

[23] J. Church, et al. "Identification and characterization of bilgewater emulsions", *Science of the Total Environment*, vol. 691, pp. 981-995, Nov 2019.

[24] M. Han, J. Zhang, W. Chu, J. Chen, and G. Zhou, "Research progress and prospects of marine oily wastewater treatment: a review", *Water,* vol. 11, no. 12, pp. 2517, Nov 2019.

[25] S. Soeprijanto, D. F. Nury, and L. Pudjiastuti, "Treatment of oily wastewaters from Tanjung Perak Port by electrocoagulation using aluminium electrodes", *IOP Conference Series: Materials Science and Engineering*, vol. 543, 012098, Jun 2019.

[26] X. Li, et al. "From marine to freshwater environment: a review of the ecotoxicological effects of microplastics Ecotoxicology*", Journal of Environment and Safety*, vol. 251, pp. 114564, Feb 2023.

[27] M. Cole, P. Lindeque, E. Fileman, C. Halsband, and T. S. Galloway, "The impact of polystyrene microplastics on feeding, function and fecundity in the marine copepod Calanus helgolandicus", *Environmental Science and Technology,* vol. 49, no. 2, pp. 1130-1137, Jan 2015.

[28] D. Neves, P. Sobral, J.L. Ferreira, T. Pereira, "Ingestion of microplastics by commercial fish off the Portuguese coast", *Marine Pollution Bulletin,* vol. 101, no. 1, pp. 119-126, Dec 2015.

[29] F. Haque, and C. Fan, "*Microplastics in the marine environment: a review of their sources, formation, fate, and ecotoxicological impact*", Chapters, in: Monique Mancuso & Teresa Bottari & Ahmed A. Abdelhafez & Mohamed Abbas (ed.), Marine Pollution - Recent Developments, IntechOpen. pp. 1-33, 2022.

[30] J. Kang, L. Zhou, X. Duan, H. Sun, Z,Ao, S. Wang, "Degradation of cosmetic microplastics via functionalized carbon nanosprings", *Matter,* vol. 1, no. 3, pp. 745-758, Sep 2019.

[31] C. B. Crawford, and B. Quinn, "*Microplastic collection techniques",* In: Crawford CB, Quinn B (eds) Microplastic pollutants. Elsevier, pp. 179-202, 2019.

[32] V. Hidalgo-Ruz, L.G. Richard, C. Thompson, M. Thiel, "Microplastics in the marine environment: a review of the methods used for identification and quantification", *Environmental Science & Technology,* vol. 46, pp. 3060-3075, Mar 2012.

[33] T. Rocha-Santos, M.F. Costa, "Catherine Mouneyrac, Handbook of Microplastics in the Environment", pp. 6-16, *Springer Nature Switzerland AG*, ISBN 978-3-030-39041-9 (eBook), 2022.

[34] H. Effendi, M. Kawaroe, D.F. Lestari, "Ecological risk assessment of heavy metal pollution in surface sediment of Mahakam Delta East Kalimantan", *Procedia Environmental Science*, vol. 33, pp. 574-582, 2016.

[35] K. Rezaee Ebrahim Saraee, M. R. Abdi, K. Naghavi, E. Saion, M. A. Shafaei, and N. Soltani, "Distribution of heavy metals in surface sediments from the South China Sea Ecosystem, Malaysia", *Environmental Monitoring Assessment*, vol. 183, no. 1-4, pp. 545-554, Dec 2011.

[36] X. Li, et al. "From marine to freshwater environment: a review of the ecotoxicological effects of microplastics, *Ecotoxicology Environmental Saf*ety, vol. 251, 114564, Feb 2023.

[37] Z. Pan, Q. Liu, R. Jiang, W. Li, X. Sun, and H. Lin, "Microplastic pollution and ecological risk assessment in an estuarine environment: the Dongshan Bay of China", *Chemosphere,* vol. 262, pp. 127876, Jan 2021.

[38] P. Xu, G. Peng, L. Su, Y. Gao, L. Gao, and D. Li, "Microplastic risk assessment in surface waters: a case study in the Changjiang Estuary, China", *Marine Pollution Bulletin,* vol. 133, pp. 647-654, Aug 2018.

[39] D.L. Tomlinson, J.G. Wilson, C.R. Harris, and D.W. Jeffrey, "Problems in the assessment of heavy-metal levels in estuaries and the formation of a pollution index", *Helgoländer Meeresuntersuchungen*, vol. 33, no. 1, pp. 566-575, Mar 1980.

[40] L. Hakanson, "An ecological risk index for aquatic pollution control.a sedimentological approach", *Water Research,* vol. 14, no.8, pp. 975-1001, 1980.

[41] A. H. M. E. Kabir, M. Sekine, T. Imai, K. Yamamoto, A. Kanno, and T. Higuchi, "Assessing small-scale freshwater microplastics pollution, land-use, source-to-sink conduits, and pollution risks: perspectives from Japanese rivers polluted with microplastics", *Science of the Total Environment,* vol. 768, pp. 144655, May 2021.

[42] J. Mutuku, M. Yanotti, M. Tocock, and D. H. MacDonald, "The abundance of microplastics in the world's oceans: a systematic review", *Oceans,* vol. 5, pp. 398-428, Jun 2024.

[43] M. T. A. Matiddi, C. Silvestri, A. M. Cicero, and E. Magaletti, "First evidence of microplastics in the ballast water of commercial ships", *Fate and Impact of Microplastics in Marine Ecosystems From the Coastline to the Open Sea,* pp. 136-137, Jan 2017.

[44] K. Kor, and A. Mehdinia, "Neustonic microplastic pollution in the Persian Gulf", *Marine Pollution Bulletin,* vol. 150, pp. 110665, Jan 2020.

[45] A. Manbohi, A. Mehdinia, R. Rahnama, and R. Dehbandi, "Microplastic pollution in inshore and offshore surface waters of the southern Caspian Sea", *Chemosphere,* vol. 281, 130896, Oct 2021.

[46] V.Z. Sönmez, C. Akarsu, and N. Sivri, "Impact of coastal wastewater treatment plants on microplastic pollution in surface seawater and ecological risk assessment", *Environmental Pollution,* vol. 318, 120922, Feb 2023.

[47] M. Cole, H. Webb, P. K. Lindeque, E. S. Fileman, C. Halsband, and T. S. Galloway, "Isolation of microplastics in biota-rich seawater samples and marine organisms", *Scientific Reports,* vol. 4, no. 4528, pp. 1-8, Mar 2014.

[48] L. G. A. Barboza, A. D. Vethaak, B. R. Lavorante, A. K. Lundebye, and L. Guilhermino, "Marine microplastic debris: an emerging issue for food security, food safety and human health", *Marine Pollution Bulletin,* vol. 133, pp. 336-348, Aug 2018.

[49] N. Von Moos, P. Burkhardt-Holm, A. Köhler, "Uptake and effects of microplastics on cells and tissue of the blue mussel Mytilus edulis L. after an experimental exposure", *Environmental Science and Technology,* vol. 46, pp. 11327-11335, Oct 2012.

[50] R. K. Naik, P. Chakraborty, P. M. D'Costa, N. Anilkumar, R. Mishra, and V. Fernandes, "A simple technique to mitigate microplastic pollution and its mobility (via ballast water) in the global ocean", *Environmental Pollution,* vol. 283, pp. 117070, Aug 2021.

[51] S. Dobaradaran, F. Soleimani, I. Nabipour, R. Saeedi, and M. J. Mohammadi, "Heavy metal levels of ballast waters in commercial ships entering Bushehr port along the Persian Gulf", *Marine Pollution Bulletin,* vol. 126, pp. 74-76, Jan 2018.

[52] A. Naji, M.A. Nuri, "Microplastics contamination in molluscs from the northern part of the Persian Gulf", *Environmental Pollution,* vol. 235, pp. 113-120, Apr 2018.

[53] X. Sun, J. Liang, M. Zhu, Y. Zhao, and B. Zhang, "Microplastics in seawater and zooplankton from the Yellow Sea", *Environmental Pollution,* vol. 242, pp. 585-595, Nov 2018.

[54] S. M. Park, H. Jin Kim, H. Rim Cho, K. Hwan Kong, D. Kyeom Park, and J. K .Paik, "Effect of pneumatic rubber fenders on the prevention of structural damage during collisions between a ship-shaped offshore installation and a shuttle tanker working side-by-side", *Ships and Offshore Structures*, vol 18, no. 4, pp. 596-608, 2023.

[55] S. A. Dar, and K. M. Gani, "Deciphering the source contribution of microplastics in the glaciers of the North-Western Himalayas", *Journal of Hazardous Materials*, vol. 491, 137975, Jul 2025.

[56] M. Ranjani, et al. "Assessment of potential ecological risk of microplastics in the coastal sediments of India: a meta-analysis", *Marine Pollution Bulletin*, vol. 163, 111969, Feb 2021.

[57] Z. Yin, "The pollution of microplastics in sediments: the ecological risk assessment and pollution source analysis", *Science of the Total Environment*, vol. 859, 160323, Feb 2023.

[58] H. Yang, F. Sun, H. Liao, Y. Guo, T. Pan, and F. Wu, "The pollution of microplastics in sediments of the Yangtze River Basin: occurrence, distribution characteristics, and basin-scale multilevel ecological risk assessment", *Water Research,* vol. 243, 120322, Sep 2023.

[59] K. K. Riya, et al. "Characteristics, contamination levels, and ecosystem risk assessment of microplastics in surface water of a highly urbanized river from a developing country", *ACS Omega*, vol. 9, no. 52, pp. 50922-50932, Dec 2024.

[60] S. Hajiouni, et al. "Occurrence of microplastics and phthalate esters in urban runoff: a focus on the Persian Gulf coastline", *Science of Total Environmental,* vol. 806, no. 1, 150559, Feb 2022.

[61] P. Prarat, and P. Hongsawat, "Microplastic pollution in surface seawater and beach sand from the shore of Rayong province, Thailand: distribution, characterization, and ecological risk assessment", *Marine Pollution Bulletin,* vol. 174, 113200, Jan 2022.

[62] D. Lithner, A. Larsson, and G. Dave, "Environmental and health hazard ranking and assessment of plastic polymers based on chemical composition", *Science of the Total Environment,* vol. 409, pp. 3309-3324, Aug 2011.

[63] G. Liu, Z. Zhu, Y. Yang, Y. Sun, F. Yu, and J. Ma, "Sorption behavior and mechanism of hydrophilic organic chemicals to virgin and aged microplastics in freshwater and seawater", *Environmental Pollution,* vol. 246, pp. 26-33, Mar 2019.

[64] M. J. Stapleton, A. J. Ansari, and F. I. Hai, "Antibiotic sorption onto microplastics in water: a critical review of the factors, mechanisms and implications", *Water Research,* vol. 15, no. 233, 119790, Apr 2023.

RESEARCH ARTICLE

DOI: 10.54926/jnamt.2025.2528

J Nav Architect Mar Technol 2026;228:11-23

Analysis of Operational Drivers of Unscheduled Downtime in a Container Fleet

Araks Ekmekçioğlu

Yıldız Technical University Faculty of Naval Architecture and Maritime, Department of Marine Engineering, İstanbul, Türkiye

To cite this article: A. Ekmekçioğlu. Analysis of operational drivers of unscheduled downtime in a container fleet. *J Nav Architect Mar Technol*. 2026;228:11-23.

Received: 19.09.2025 - **Revision Requested:** 10.10.2025 - **Last Revision Received:** 17.12.2025 - **Accepted:** 24.12.2025 - **Publication Date:** 19.01.2026

Abstract

Unplanned downtime in liner shipping undermines voyage reliability and increases costs. This study systematically compiles 397 unplanned downtime events in a container ship fleet between 2017 and 2021, standardizing them according to system/subsystem and time/location attributes. A risk score consisting of frequency × duration × impact components was defined to quantify the severity of downtime on the operation. Pareto analysis was applied to identify a small number of critical causes. Variables driving downtime were extracted using a Classification and Regression Tree (CART) model and supported by Ward's linked hierarchical clustering. The findings show that 89% (352/397) of downtimes were propulsion/propulsion system-related, representing approximately 1,460 hours of the total 1,767 hours; main engine events predominated in this group with 256 incidents and ~730 hours. Despite their rarity, shaft/propeller/stern-tube failures lead to very long delays per event (≈96 hours on average). CART outputs reveal that the longest downtimes are associated with fuel pump and injection failures (median ≈153.6 hours), while exhaust and lubrication-related failures are also high-impact. Pareto analysis showed that oil mist detector (OMD) related events accounted for 63.1% of the total risk, fuel injection 14.8%, and exhaust 7.9%; these three factors accounted for 85.8% of the risk. The findings suggest prioritizing fleet wide condition-based maintenance packages, targeted spare parts management, exhaust gas trend monitoring, rigorous OMD calibration/validation flows, and role-based training programs across the fuel, exhaust, and lubrication triad. Key indicators should be defined to track annual downtime reductions of ≥10-15% in critical clusters and improvements in diagnostic speed.

Keywords: Unscheduled downtime, Marine propulsion failures, CART decision tree, Pareto analysis

1. Introduction

Maritime transport, which constitutes a large part of global trade, is a strategic sector in a race against time. Ships engaged in container transport in the maritime industry are operated with the goals of on-time delivery, high operational efficiency, and low downtime. However, due to the nature of maritime operations, unplanned downtime is sometimes unavoidable. These stoppages can occur for a wide variety of reasons, such as technical failures, environmental conditions, operational errors, or maintenance negligence, and consequently lead to significant time losses and damage costs.

While there is a significant body of literature on ship malfunctions across diverse areas, such as predictive maintenance, statistical analysis of accident data, and human and organizational factors, these studies often focus on single systems or the single-ship scale, and limited fleet-scale downtime assessment based on event records remains limited. While recent studies have demonstrated the technical potential of data-driven/hybrid approaches for main engine

Address for Correspondence: Asst. Prof. Dr. Araks Ekmekçioğlu, Yıldız Technical University Faculty of Naval Architecture and Maritime, Department of Marine Engineering, İstanbul, Türkiye
E-mail: araks@yildiz.edu.tr
ORCID ID: orcid.org/0000-0002-4821-0272

Copyright© 2025 The Author. Published by Galenos Publishing House on behalf of UCTEA Turkish Chamber of Naval Architects and Marine Engineers. Licensed under a Creative Commons Attribution-NonCommercial-NoDerivatives 4.0 (CC BY-NC-ND) International License

and auxiliary systems (e.g., risk prioritization, maintenance scheduling, contextual effects), the integration of these methods with real-world field incidents in container ship fleets and the direct translation of findings into maintenance prioritization and role-based training planning have not yet been sufficiently demonstrated. In the Turkish context, empirical evidence that quantitatively maps downtime causes at the fleet scale and translates the results into fleet management decisions is lacking. This study aims to fill this gap with a workable framework that organizes field-sourced incident data at the fleet level, introduces risk concentration (Pareto) and waiting time determinants [Classification and Regression Tree (CART)], and links the resulting patterns to condition-based maintenance and role-based training priorities.

The existing literature covers a wide range of topics, focusing on technical system failures and maintenance strategies that cause unplanned downtime. In academic studies on similar topics, predictive maintenance models for ship systems play a critical role in anticipating potential field failures and ensuring uninterrupted ship operations. Kalafatelis et al. [1] noted that artificial intelligence (AI)-supported predictive maintenance systems in the maritime sector have great potential, particularly in terms of preventing failures in main engines and auxiliary equipment. Budimir et al. [2] developed models for optimizing maintenance scheduling using Weibull and Markov-based analyses. A comparative study by Tinga et al. [3] demonstrates how data-driven and physics-based prognostic models can be used in fleet management. Shen et al. [4] aimed to automatically extract information from written text in maintenance/failure records for the rapid identification of malfunction causes and symptoms on ships. They used the graph transformer networks to capture important fragments of the text (e.g., “failure cause”, “symptom”, “equipment name”).

Operationally, Karmelić et al. [5] examine disruptions that reduce voyage reliability in container liner shipping, using both literature and internal operational reports, classifying delay causes into four tiers: land transport, anchorage, port, and cruise. Nguyen [6] has demonstrated with mathematical models that optimal maintenance planning under limited resources and time can directly reduce unplanned downtime. In studies focusing on the human factor, Islam et al. [7] emphasized the triggering effect of environmental influences and organizational deficiencies on human error in maintenance processes. Specifically for Türkiye, Ünlügençoğlu [8] analyzed maritime accidents and statistically evaluated the relationship between human error and equipment failure.

Unplanned stoppages can occur not only during navigation but also during port operations and under the influence of environmental factors. Romano-Moreno et al. [9] linked stoppages at ports to meteorological data, demonstrating that operational planning must include these factors. Millefiori et al. [10] analyzed the effects of coronavirus disease-2019 on global maritime transport, illustrating the pressure of extraordinary conditions on operational continuity.

The system-level literature offers greater technical depth. Simion et al. [11] argued that AI-based predictive maintenance solutions for ship machinery provide efficiency in terms of reliability. Soltani Motlagh et al. [12] and Jimenez et al. [13] reported that the integration of physics-based models with machine learning in propulsion systems provides high accuracy in fault detection. BahooToroody et al. [14] used Gaussian Process Latent Variable Model and Bayesian inference to non-parametrically model the prediction of ship machinery failure risk. The model provides strong evidence for Pareto-based diagnosis and adaptive maintenance planning under uncertainty. Onwuegbuchunam et al. [15] developed models related to the temporal distribution of shaft and gearbox failures. Crankcase explosion risk and oil mist detectors (OMD). Numerical/computational studies of crankcase explosions and experimental research examining the morphological characteristics of oil mist particles provide direct evidence for determining OMD thresholds and reducing false alarms [16,17]. These findings provide a framework for why unplanned downtime originating from the main engine are critical in terms of both safety and operational time. At the critical subsystem level, thermal behavior and wear in stern tube bearings, risk prioritization in boiler systems [18,19], and duty cycle effects in deck equipment [20] have been identified as factors directly contributing to unplanned downtime.

In studies related to hull damage and structural reliability, reliability studies on critical load conditions such as strength comparisons between damaged/intact states and asymmetric bending in container ships confirm from a structural perspective that a limited number of events can produce very high downtime durations [21]. Network and dynamic impact analyses link to maintenance and operational planning by showing how reliability limits change in operational scenarios [22]. Modeling accident data using Bayesian approaches also enables learning cause-effect relationships and prioritizing “high impact–low frequency” risks [23,24].

Taken together, these strands offer robust methods and mechanisms, yet there is limited empirical, fleet-scale synthesis of forced stoppages grounded in incident records—particularly for Turkish container-ship fleets. Our study addresses this gap by organizing field data at fleet level, quantifying risk concentration (Pareto) and waiting-time drivers (CART), and mapping the results to actionable levers for maintenance planning and role-specific training.

This study aims to reveal which systems and subsystems experience the highest concentration of unscheduled downtime events based on five years of records from 50 container ships, and which factors explain the duration of these stops. The research question can be summarized as follows: "Which technical clusters drive the most unplanned stoppages at the fleet level, and which variables are more influential in determining the level of downtime?" To this end, recorded technical stoppages were examined. The 397 incidents identified over the five-year period were coded in a standardized manner according to systems and subsystems. Subsequently, a Pareto analysis was performed using risk scores derived from the frequency-duration-impact components of the events to identify the critical minority, and CART regression was used to extract the variables and threshold distinctions explaining the waiting time. The findings were interpreted through the decision tree structure and importance scores. The objective is to reveal frequently recurring failure patterns, evaluate the impact of these outages on operational performance, and develop recommendations that will contribute to maintenance, training, and fleet management processes based on the results.

This study examines in detail the forced downtime events that occurred on the ships of a shipping company with a container ship fleet between 2017 and 2021. Unplanned downtime during navigation and port operations over a five-year period involving a fleet of 50 ships was analyzed in terms of both technical causes and operational and training impacts. The aim is to identify recurring failure patterns, assess the impact of these stoppages on operational performance, and develop recommendations to contribute to maintenance, training, and fleet management processes based on the findings.

2. Materials and Methods

2.1. Study Area and Data Set

Unplanned downtime events of a private maritime company with a large container ship fleet based in Türkiye were examined over a 5-year period. The company operates 50 vessels and manages Türkiye's largest fleet in this field. The vessels are actively engaged in various trade routes worldwide.

The dataset was created by compiling and digitizing unplanned downtime reports prepared by ship personnel by the company's technical department. The dataset records variables such as ship name, date, duration and location of the stoppage, system/component name, and reason for the stoppage for each event. A total of 397 unplanned downtime events were recorded.

The data was compiled from technical maintenance and incident report forms obtained from the company's operational reporting system. The incidents were digitally entered into the system by engineers on board and ship technical superintendents, who are marine engineers and fleet managers. Standardized analysis tables were created from this raw data. Each incident was classified according to technical category. Within the three main operational categories (propulsion system, cargo operations, and mooring operations), the propulsion system-related issues with the highest number of incidents were divided into subcategories and analyzed in detail.

This study uses incident records from a single Turkish container-ship fleet operating predominantly on liner trades. While this yields high internal consistency (common procedures, documentation standards, and engine families), it constrains external validity in several ways. First, risk concentrations and waiting-time drivers may differ in fleets with distinct operating profiles, vessel types (tanker, bulk carrier, ro-ro), class/age distributions, or propulsion configurations. Second, the dataset intentionally excludes non-technical delays (e.g., weather, port/terminal operations); this design choice isolates technical stoppages but can inflate their relative share of total downtime and limits comparisons with studies using all-cause delays. Third, organization-specific maintenance practices (spares policies, OMD calibration routines, training cadence) may alter shipboard crew competency skills.

Only recorded technical downtimes were included in the analysis. Unreported minor interruptions were excluded from the study; unexpected technical failures that caused operational disruptions were considered. Planned maintenance, adverse weather conditions, port operational delays, or externally caused downtimes were excluded from the analysis; the focus was on technical downtimes. Data processing included data cleaning and categorization. Incomplete, inaccurate, or duplicate records were eliminated.

2.2. Analysis Method

The analytical framework adopted in this study is designed to balance methodological rigor with operational interpretability. Rather than maximizing predictive accuracy through black-box models, the focus is placed on transparent, rule-based methods that allow failure mechanisms and downtime drivers to be directly interpreted by fleet managers and marine engineers. Pareto analysis is employed to identify risk concentration and critical subsystems at the fleet level, while the CART algorithm is used to uncover threshold-based relationships and nonlinear patterns governing downtime duration. This combined approach enables both prioritization of dominant failure modes and actionable insights for maintenance planning and role-based training, grounded in real operational data.

2.2.1. Risk assessment and pareto analysis

Risk scores were calculated for each type of failure to determine the impact of failures on the operational efficiency of ships. Risk scores were determined using a weighted scoring method based on the frequency of occurrence, duration of the failure, and its operational impact. The Pareto chart created using these scores visually demonstrated the dominant effect of main engine failures on waiting time. Pareto analysis was applied to confirm the finding that approximately 80% of the total downtime is concentrated in approximately 20% of the failures.

2.2.2. CART algorithm

The CART algorithm was used to analyze the effects of ship main engine failures on ship waiting times. CART is a powerful and flexible machine learning approach widely used in classification and regression problems [25]. In the regression context, CART creates a binary decision tree structure that iteratively partitions the dataset into two subsets to identify the relationship between variables.

The modeling process begins by treating the entire dataset as a single node (root node). The algorithm then partitions the dataset into two subsets by determining the most appropriate independent variable and threshold value that minimizes the variance or mean square error (MSE) of the target variable. This process continues iteratively until one of the predefined stopping criteria is met (e.g., maximum tree depth, minimum terminal node size). In the final stage, the mean value of the target variable at each terminal node (leaf node) is assigned as the predicted value for all observations belonging to that node.

The CART model, being a nonparametric method, is highly effective in capturing nonlinear relationships between variables. Furthermore, the model's visualizability and interpretability facilitates easy understanding for both technical and operational stakeholders in decision-making processes. In this study, model performance was evaluated using R^2 (coefficient of determination), root MSE (RMSE), MSE, mean absolute deviation (MAD), and mean absolute percentage error (MAPE) statistics.

In addition, a dendrogram analysis was performed using Ward's linkage method and the Euclidean distance metric to support the findings obtained from the CART model. This approach measures the similarity between failure types to form hierarchical clusters, thereby enabling a visual classification of the relationships among different categories of engine failures.

3. Findings

3.1. General Situation: Summary of the Number of Downtime

During the five-year evaluation period, a total of 397 unscheduled downtime events were recorded in the container ship fleet under review. These stoppages were grouped under three main operational categories: Propulsion System, Cargo Operation, and Mooring Operation activities.

When examining the distribution of stoppages by system, as shown in Figure 1, 89% of downtimes (352 incidents) were due to propulsion systems. Stoppages during cargo operations accounted for 10% of unplanned stoppages, with 39 incidents. The remaining 1% (6 incidents) occurred during mooring operations.

Table 1 shows the total number of stoppages and durations by category. The total unplanned stoppage duration was calculated to be approximately 1,767 hours over the five-year period. The duration distribution is also parallel to the number of incidents.

Based on these data, the average duration of a downtime is calculated to be approximately 4.5 hours. Across the fleet, the annual average number of unplanned downtimes per vessel is approximately 1.6. When the average main engine

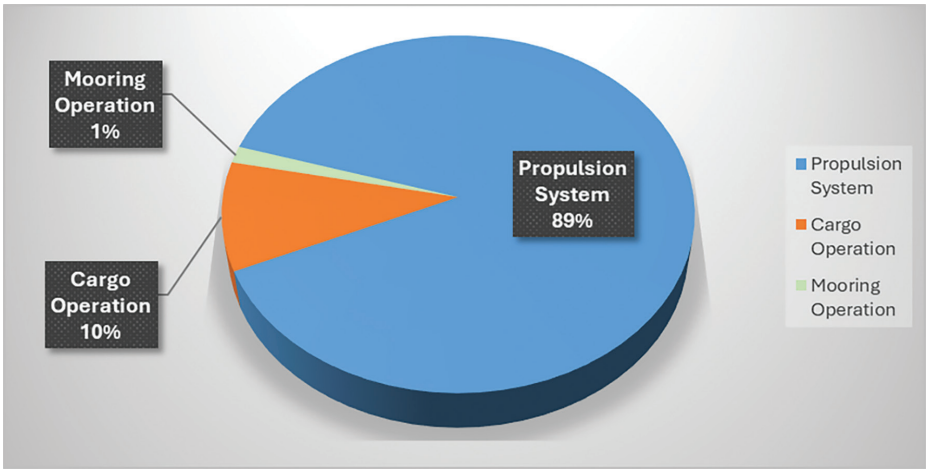


Figure 1. Distribution of stoppages by system.

operating time is assumed to be 4,200 hours per year, the ratio of time spent on downtime to total sailing time is approximately 0.15%. While this low ratio indicates that fleet operations are generally planned and controlled, it also points to the need for priority intervention in terms of propulsion system failure density, maintenance planning, and technical training.

3.2. Distribution by Cause of Downtime

Of the 397 unplanned downtimes that occurred during the five-year period under review, 89% (352 incidents) were directly attributable to propulsion systems. This high percentage highlights how critical main propulsion systems are to operational continuity on container ships.

Based on this criticality, stoppages related to propulsion systems were detailed in terms of their technical components. The propulsion system data, shown in Table 2 with a total of 352 incidents and 1,460 hours of downtime, was broken down into subsystems and analyzed.

Due to the combined reporting of some incidents, mandatory downtime caused by main propulsion systems has been divided into nine main technical categories. This analysis aims to contribute to fleet management, maintenance planning, and technical training content by identifying the subsystems where downtime is concentrated.

In this distribution, main engine failures are clearly ahead not only in terms of the number of incidents but also in total downtime duration. The entire propulsion system alone accounted for approximately 50% of the downtime, with a total of 730 hours of downtime across 256 incidents. The most frequently recurring issues include fuel injection problems, fuel pump (FP) failures, and problems caused by the exhaust system.

In contrast, although only 4 incidents occurred in the propeller, drive shaft, stern tube, and bow thruster group, the total downtime was quite high at 384 hours. This group, with an average downtime of 96 hours per incident, shows that these system failures are rare but cause very long operational interruptions. In such cases, the complete operational downtime of the ship brings with it commercial losses as well as safety risks. These types of failures usually require the ship to wait in port for weeks for repairs. Emergency intervention is not possible; dry docking is usually required. Therefore, these components are considered critical priority. Preventive vibration analysis, oil analysis programs, and proactive maintenance scheduling are vital for this type of system failure.

Some systems with relatively few incidents stand out due to their singular impact. Specifically, in the "Hull/Fire/Maneuvering" category, despite only 8 incidents, the total downtime was 116 hours, with an average interruption of 14.5 hours per incident. This finding demonstrates that some infrequent failures have a high operational impact.

Boiler systems stand out with a total of 151 hours of downtime across 33 incidents. The average downtime of 4.6 hours highlights the need for continuous maintenance and monitoring of this system. Especially, boiler tube perforations lead to prolonged port delays and deviations from estimated arrival times.

Twelve incidents occurred in the Piping, Valves, Pumps, Coolers, and Heaters group, resulting in a total of 36 hours

Table 1. Number of downtimes and durations by category.

	Propulsion system	Cargo operation	Mooring operation	Total
Total downtime (number)	352	39	6	397
Total downtime duration (hours)	1460	272	35	1767

Table 2. Summary of downtime in propulsion systems by subcategory.

Propulsion system	Number of incidents	Duration (hour)	Average duration
Automation & Alarm systems	7	4	0.6
Boiler system	33	151	4.6
Generator load sharing & Black out	25	19	0.8
Hull & Fire & Maneuvering	8	116	14.5
Main engine	256	730	2.9
Piping, valves, P/P, cooler/heater	12	36	3.0
Propeller & Shaft & Stern tube & Thruster	4	384	96.0
Others	7	20	2.9
Total	352	**1460**	**4.1**

of downtime. With an average downtime of 3 hours, these components are classified as medium priority. Diesel generator load sharing, automation and alarm systems, and other groups have a limited impact on propulsion system downtime, with both low frequency and low duration. Most failures in these systems were resolved in less than 1 hour per incident. Incidents under the "Other" category include delays due to GPS display errors, pitch control failures, rudder & pitch-controlled propeller system failures, and items recorded during flag state inspections in port.

As a result, not only the frequency of propulsion system stoppages but also their individual impacts and system-based temporal intensity should be considered in fleet management. In addition to the main engine, boiler systems, maneuvering control systems, and propeller structures are also highlighted as priority areas in terms of preventive maintenance, spare parts inventory management, and training.

3.3. Critical System Analysis: An in-Depth Look

Detailed analysis of fleet data shows that some technical systems fail more frequently than others and have a much greater operational impact. In this section, critical subsystems causing the most downtime or leading to long durations in individual incidents are analyzed separately. The aim is to provide targeted insights for optimizing fleet management and technical maintenance strategies. Table 3 presents the number of main engine failure incidents and their downtimes by subcategory.

In the critical system analysis, main engine-related failures were divided into subcategories and examined. CART regression analysis and hierarchical clustering (Ward-Linkage, Euclidean Distance) methods were evaluated together to determine the impact of main engine failures on ship downtime. The overall goal was to reveal the distribution of downtime events by main engine subcategories and to identify which systems most significantly impact operational continuity.

In the CART regression analysis, waiting time (in hours) was considered the dependent variable and failure types were considered the independent (explanatory) variables. The entire data set consisted of 11 different failure types, and the total number of events and average durations for each failure type were evaluated. The model was evaluated using the median and median absolute deviation (MAD) metrics, taking into account the distribution structure of the data and the sample size. This approach mitigated the impact of outliers in the data set, providing a more robust statistical representation.

Statistical performance metrics for the model generated using the CART method demonstrate that the analysis results have a strong predictive capacity. A total of four predictor variables were used in the resulting model, all of which were found to be statistically significant. The model's coefficient of determination (R^2=99.78%) indicates that almost all of the variance in the dependent variable can be explained. Furthermore, the error measures (RMSE=1.6601, MSE=2.7561, MAD=0.7304, MAPE=0.0377) were quite low. These results demonstrate that the model successfully predicts ship waiting times with high accuracy and low error (Table 4).

Figure 2 demonstrates the variation in model error, measured by Relative MAD, with respect to the number of terminal nodes. While increasing the number of nodes typically lowers the error rate, an excessive number of nodes can

Table 3. Number and duration of main engine incidents by subcategory.

Main engine failures	Number of incidents	Duration (hour)	Duration (day)
Oil mist detector	27	53.8	2.2
Fuel pump & Inj VV/Inj pipe	52	153.6	6.4
Fuel line & Fuel filter	24	60.3	2.5
Exhaust	44	96.1	4.0
Automation & Sensor failure	17	23.6	1.0
Lubrication system & Water in oil & LO filter	16	76.0	3.2
Cooling system & Cover	14	54.0	2.2
Piston & Rings	7	49.5	2.1
Start & Maneuvering & Governor system	24	76.1	3.2
Alpha lubricator	10	15.9	0.7
Other	21	71.3	2.9
Total	**256**	**730.2**	**30.4**

lead to model complexity and overfitting, thereby reducing the model's ability to generalize. Therefore, identifying the optimal trade-off is crucial. The analysis determined the optimal structure to be 8 terminal nodes, where the Relative MAD was minimized to 0.0291. At this optimal configuration, the correlation coefficient of the training set was calculated as 87.33%.

The regression tree generated as a result of the analysis is shown in Figure 3. At the root node of the tree (Node 1), the median waiting time for all faults was determined to be 60.25 hours. This value serves as a general indicator of performance across all fault types examined. The high median absolute deviation (MAD=25.13) indicates significant differences in waiting times across fault types.

The model categorizes failure types into two main groups. The main difference between these two groups is the median values in the waiting time distributions. The first group (Node 2) consists of failures with shorter waiting times on average, while the second group (Node 5) includes failure types characterized by longer waiting times. The first separation of the model was based on the "main engine event type" variable, which revealed two main groups. The first group represents events in the categories of alpha lubricator, automation & sensor, cooling system, fuel line & filter, OMD, piston & rings (Alp_Lub, Au_Sen, Cool, FL, OMD, Pist), while the second group includes events in the categories of exhaust, FP & injection valve (inj vv), lubrication system, other, and start & manuevring (Exh, FP, Lub, Other, Star). The median value for the first group on the left branch was calculated as 51.63, and for the second group on the right branch as 76.05. This shows that waiting times due to engine failures in the second group have a higher impact.

In particular, the median value for FP and valve failures was determined to be 153.64, standing out as the factor with the highest impact on the system. This clearly demonstrates that fuel injection system malfunctions are a key parameter significantly affecting downtime. Fuel injection line malfunctions (pump barrel and plunger wear, control rack/governor lockup, fuel valve nozzle clogging, common-rail pressure leaks, timing deviations) directly reduce cylinder combustion pressure and ignition quality. The resulting effects include power loss, unsteady combustion, exhaust temperature deviations, vibration, and the necessity of slowdowns/stoppages for safety reasons. Many interventions on the fuel injection system at sea can extend downtime due to the need for equipment cooling, fine-tolerance component replacement, calibration, testing procedures, or limited equipment and spare parts availability.

Similarly, faults related to the "Exhaust (Exh)" and "Lubrication (Lub)" systems were observed to have high median values. Because these are critical parameters that directly affect engine performance, they stand out as the most

Table 4. Performance metrics for the CART regression model.

Total predictors	4
Important predictors	4
Number of terminal nodes	8
Minimum terminal node size	1
R-squared	99.78%
Root mean squared error (RMSE)	1.6601
Mean squared error (MSE)	2.7561
Mean absolute deviation (MAD)	0.7304
Mean absolute percent error (MAPE)	0.0377

CART: Classification and Regression Tree

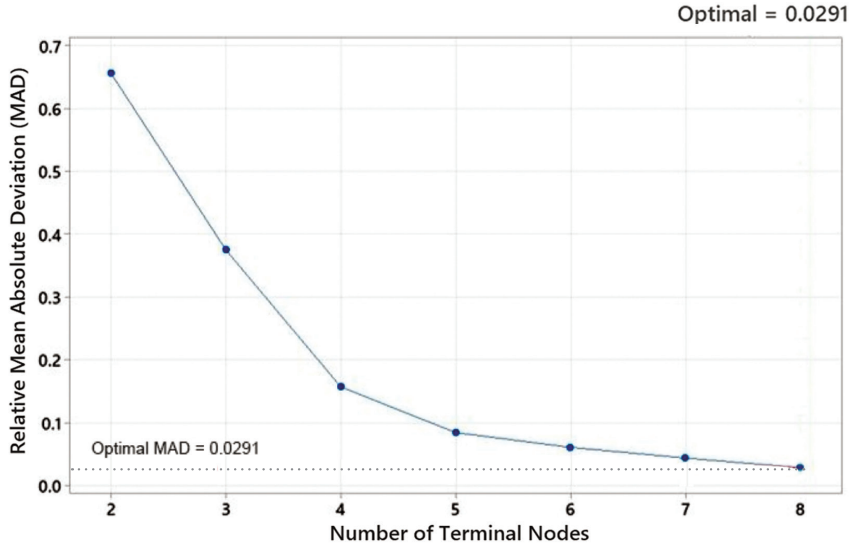


Figure 2. Optimization of the node.

significant contributors to downtime and require careful attention. It is technically expected that exhaust (Exh) and lubrication (Lub) faults produce high median downtime. Soot/oil carryover in the exhaust line, turbocharger fouling, or manifold and seal leaks increase back pressure, disrupting combustion. Safety measures such as power reduction/stop, cooling, cleaning, and rebalancing (turbo, sensor, insulation) prolong downtime. On the lubrication side, pressure drop/pump failure, filter blockage, viscosity and temperature deviations, or increased metal particles lead to critical scenarios such as bearing damage and the risk of crankcase explosion. This necessitates time-consuming interventions such as oil sample analysis, circuit checks, filter and cooler maintenance, and bearing inspections. In conclusion, Exh and Lub faults are critical parameters that directly affect engine performance.

In contrast, failures occurring in the "sub-components (Alp_Lub)", "cooling (Cool)", and "sensor (Au_Sen)" systems have lower median values. This result can lead to shorter downtimes due to the early detection of these failures and rapid intervention during maintenance processes. Failures in these three groups are generally localized and are quickly managed onboard using redundant/twin equipment (stand-by pumps, parallel heat exchangers), isolation valves, and modular component replacement. In cooling circuits, flow is maintained with a pump/heat exchanger switch-over; system safety is maintained by calibration/restart or rapid replacement on the sensor side; and in lubrication sub-components, filter replacement, leak repair, and bypass options shorten downtimes. Furthermore, since these failures are often detected with early warning (alarm), they can be deferred until port under power-limited operation rather than

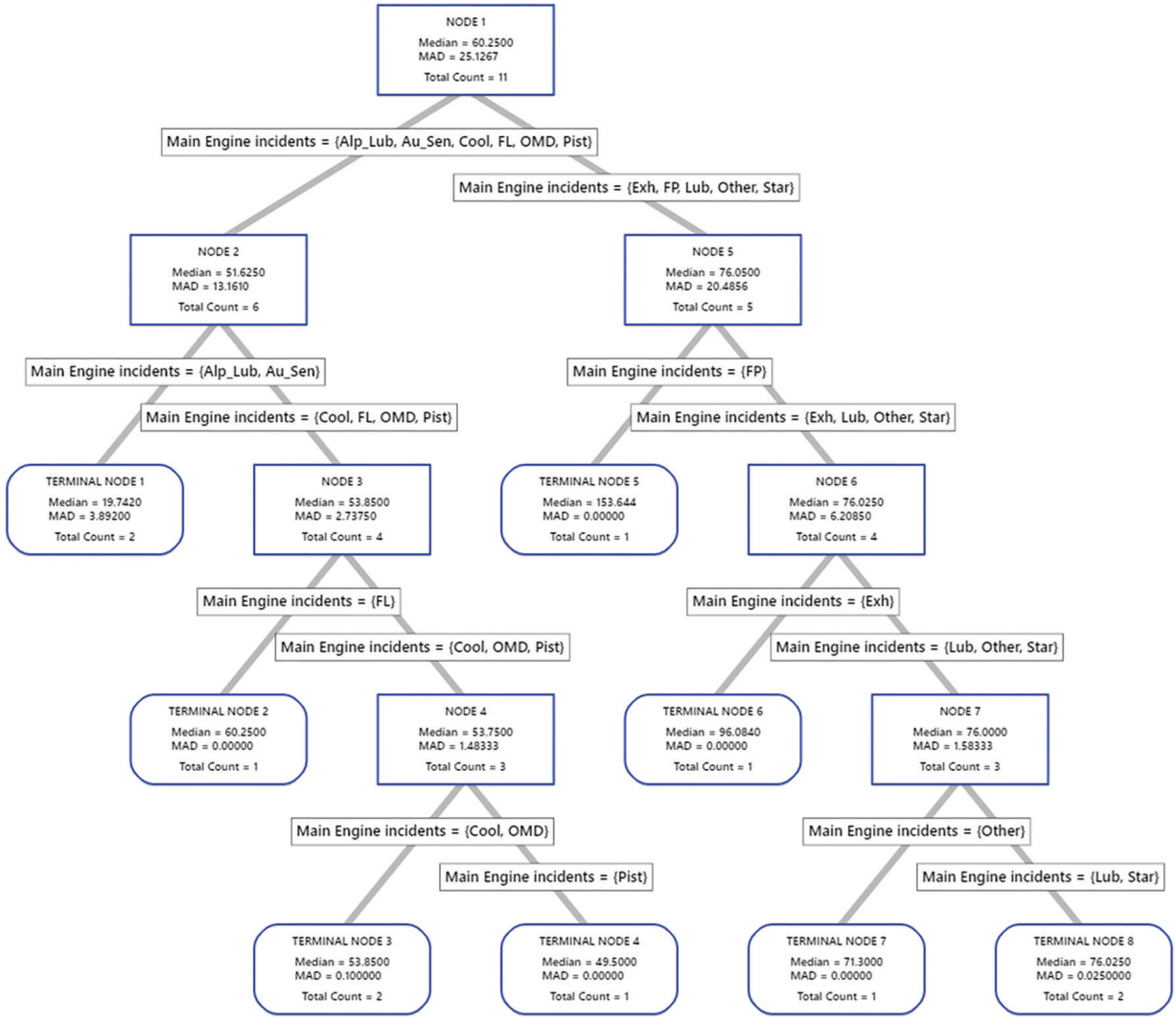


Figure 3. CART regression analysis results showing the effect of main engine failures on downtime.

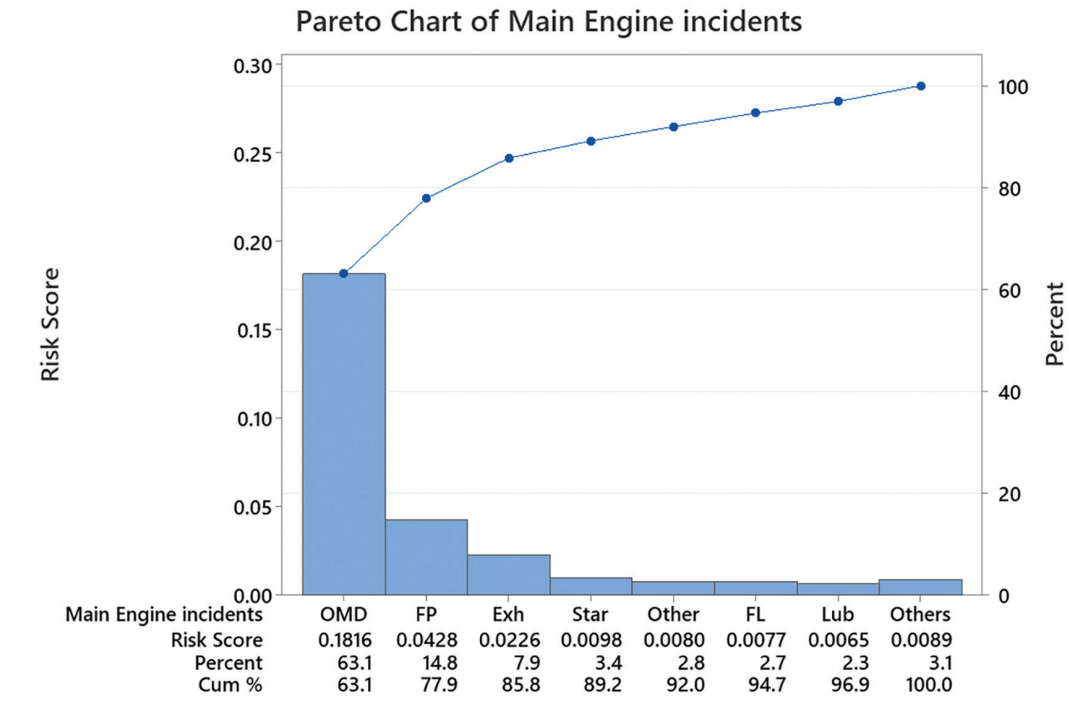


Figure 4. Pareto chart showing the severity of main engine failures according to risk scores.

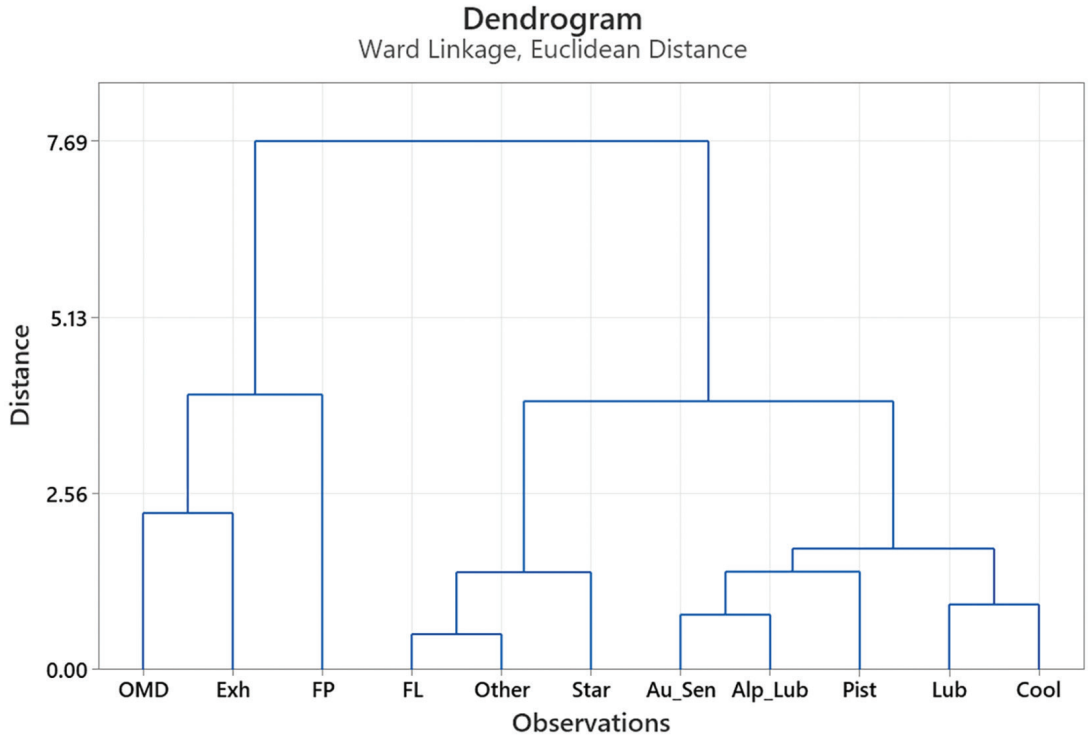


Figure 5. Dendrogram showing the similarity levels of fault types.

a full shutdown for safety reasons; consequently, downtimes are typically short.

Figure 4 shows a Pareto analysis of main engine failures. The graph shows the severity of failure types based on the risk score in ship operations. According to the analysis results, failures caused by OMD were identified as the most critical failure type, accounting for 63.1% of the total risk. This result demonstrates the crucial importance of regular maintenance

and monitoring of OMD systems for main engine safety and operational continuity. OMD alarms are generally based on two factors: actual oil mist detection (crankcase fire risk, high density) or false alarms due to sensor sensitivity and air pressure adjustment. In these events, the operational impact is significant because the engine automatically shuts down or reduces speed. Often, the ship must be shut down until the alarm is verified. While some failures in these systems do not pose a real risk, each one triggers a maximum operational response due to safety protocols. Even if there is a sensor error, the engine must be shut down and the necessary checks performed seriously, just like the actual oil mist risk. A high-priority, critical alarm is due to the potential for major damage to the engine or a crankcase explosion. This demonstrates that factors such as calibration frequency of OMD systems, sensor quality, and crew diagnostic ability are critical for operational continuity.

OMD failures are followed by FP and valve failures (14.8%) and exhaust system (Exh) failures (7.9%). When these three failure types are considered together, they account for 85.8% of the total risk, indicating that operational disruptions in the majority of the system are caused by these components. Other failures (starting system, fuel leakage, lubrication system, etc.) constitute only less than 15% of the total risk.

This finding is consistent with the "80/20 Pareto principle" and demonstrates that preventive maintenance of critical components, particularly OMD, fuel, and exhaust systems, should be prioritized to improve system performance and reduce ship downtime.

Comparing the findings with those obtained through hierarchical cluster analysis (Figure 5), significant parallelism was observed between the two methods. The clustering of "OMD", "Exh", and "FP" failures within the same cluster in the dendrogram is consistent with the high median values of these parameters in the CART analysis. Similarly, the close clustering of "Cool", "Lub", and "Run" failures confirms the high correlation between these components due to common operating conditions (e.g., heat transfer and lubrication processes). Another cluster includes the auxiliary sensor (Au_Sen), alpha lubricator (Alp), and starting system (Star) failures, indicating that these failures are related to electronic control and monitoring systems.

4. Discussion

In this section, the findings obtained in the study are compared with similar studies in the literature and their operational implications are evaluated. The fact that 89% of the unplanned stoppages identified in the study were caused by propulsion systems reveals that ship operations are largely dependent on these systems. This finding coincides with the assessment in Vizentin et al.'s [26] study. Vizentin et al. [26] states that propulsion systems are the main source of failures in container ships, particularly concentrated in the main engine and shaft lines. The high failure rate poses a risk not only technically but also in terms of operational reliability. Numerical and experimental studies on the risk of crankcase explosions and the reliability of OMD provide concrete scientific evidence for optimizing detector threshold values and reducing false alarms by analyzing the morphological characteristics of oil mist particles in the crankcase [16,17].

Failures occurring in systems such as stern tube and propellers cause quite long downtimes despite being observed at low frequencies. This creates a special risk profile in terms of fleet management. A technical report prepared by Kuroiwa et al. [27] states that stern tube bearing failures are mostly caused by deterioration in lubrication systems, leaks in gaskets, and inadequate temperature control. Similarly, an experimental study by Chang et al. [28] showed that water-lubricated shaft sleeve bearings are sensitive to parameters such as temperature, load, and speed, and even a small tolerance deviation can cause long-term operational downtime. In this context, shaft sleeve and propeller systems should be considered strategic critical systems due to their high downtime, despite the low number of incidents.

The source of some unplanned stoppages of ships is not technical failure but rather faulty or overly sensitive alarm notifications from automation systems. In particular, "false positive" alarm events originating from OMD systems create uncertainty in the crew's decision-making mechanism and sometimes lead to unnecessary stoppages. Thorpe and Pabby's [29] comprehensive analysis indicates that the high sensitivity of OMD systems does not always provide a safety advantage; on the contrary, false alarms lead to a loss of confidence and psychological stress among the ship's crew. In this context, it is evident that topics such as alarm management and crew decision-making competence should be an integral part of technical training.

5. Evaluation and Results

This study systematically evaluated 397 unplanned downtimes recorded on container ships during the 2017-2021 period. The center of gravity of downtimes was the propulsion system (352 incidents; 89%), while cargo operations (39 incidents; 10%) and mooring downtimes (6 incidents; 1%) were among the remaining downtimes. Total unplanned downtime was calculated as 1,767 hours, with an average duration per incident across the fleet of approximately 4.5 hours. Downtimes related to the main engine alone, within the propulsion system, accounted for approximately half of the total duration, with 256 incidents and 730 hours.

A detailed examination of the main engine subtypes revealed that FP-injector, exhaust (Exh), and lubrication (Lub)

failures were characterized by high median wait times, while cooling (Cool), sensor (Au_Sen), and subcomponent (Alp_Lub) failures were managed in relatively short times. In the CART regression tree, the root node began with a median wait time of 60.25 hours; after the decomposition, one branch corresponded to a median wait time of 51.63 hours, and the other to 76.05 hours. In this structure, the median for FP failures reached the highest value of ~153.64 hours, indicating that fuel injection failures significantly prolonged wait times. Hierarchical clustering results supported this picture; the close clustering of OMD-Exh-FP indicated a tendency toward long waits, while the association of Cool-Lub-Pist indicated a common behavior related to heat transfer and lubrication conditions. Pareto analysis showed that OMD-related events accounted for 63.1% of the total risk, FP for 14.8%, and Exh for 7.9%; these three items together reached 85.8%. This overall picture indicates that a small number of critical items at the fleet level drive a large portion of the total waiting time.

A condition-based maintenance package is recommended for the fuel-exhaust-lubrication triad, where risks are most pronounced. As a technical maintenance strategy, cyclical component replacement programs should be established fleet-wide for injectors, FPs, and exhaust components. To reduce both fuel and exhaust system problems, main engine performance values, especially maximum combustion pressure values, should be checked more frequently, and maintenance should be planned to anticipate potential problems.

On the fuel side, test bench calibration records for injection pumps/injectors should be regularly maintained. To save time in the event of malfunctions in these systems, especially based on competency, third- or fourth-level engineers should be trained and made aware of maintaining spare parts for replaceable fuel system components.

Exhaust gas temperature trend monitoring should be implemented in the exhaust; deviations above ±30 °C between cylinders can be detected before they reach alarm levels, enabling early intervention. To achieve this, implementing a checklist for systems under the control and monitoring of watchkeeping engineers can prevent forced shutdowns related to the exhaust system, particularly through regular monitoring of exhaust temperatures.

Monthly oil analysis (particulate matter/viscosity/BN) results in the lubrication system should be visualized using a "traffic light" approach. Laboratory results should be closely monitored by the office and the ship. Onboard oil analyses should be increased in frequency, and all engineers should be trained on this subject.

To support these systems, which frequently cause shutdowns, the minimum critical onboard inventory (fuel valve nozzles, plunger/barrel, exhaust valve spares, pressure/temperature sensors, filters) should be recalculated according to route and lead time; low-threshold warnings should be entered into the planned maintenance system. The goal is to reduce the number of stoppages caused by these three by ≥15% per year and to shorten the wait per event by ≥30 min.

Delays in OMD-related shutdowns often arise from the inability to quickly distinguish between true and false alarms. A three-tiered approach is recommended for every ship: (i) Hardware: Sensor calibration intervals should be shortened; a 2-minute quick checklist for aspiration lines, filters, and sampling should be standardized. (ii) Workflow: A one-page "procedure/verification protocol" (reserve sensor, local heat/vibration, oil mist monitoring) to be followed when an alarm occurs should be visible in the engine control room. (iii) Recording: The "alarm time-verification steps-result" fields should be mandatory in the engine room logbook. The goal is to reduce unnecessary OMD-related delays by 30% and reduce verification time in real-world situations to <5 minutes.

The utility of the CART decision tree depends on up-to-date and consistent data. Mandatory, coded fields (system/subsystem, start and end, steps implemented, verification period, result) should be added to incident forms; free text should be kept to a minimum. The model should be retrained at least annually with new data; tree depth, number of terminal nodes, R^2, and RMSE should be reported. The risk thresholds used in Pareto should be updated with annual reviews based on fleet age, fuel quality, or line changes. A "top three root causes - top three actions" table should be communicated to the fleet through ship-to-office feedback meetings. Average waiting per stop, incident frequency, and duration in critical clusters should be monitored as indicators of success.

To translate technical measures into lasting results, a structured fleet-wide competency development program is recommended. A role-based competency matrix (3rd, 2nd, chief engineer, electrician, etc.) should be established. OMD alarm management, critical subsystem diagnostics derived from CART, fuel-exhaust-lubrication package procedures, and shaft line early warning signals should be core modules within this matrix.

Two channels for training delivery: (i) Microlearning (10-12-minute videos/notes), (ii) scenario-based exercises (monthly online + quarterly live demonstration). Standardized checklists and time objectives should be used for each scenario. An onboarding package, familiarization

training (first 30 days) should be mandatory for newly appointed personnel, and competency should be verified with an annual refresher exam (≥80% success). To track the impact of training, KPIs (Key Performance Indicators) (training participation rate, drill success score, and fault response time after training) should be monitored, and ships with low performance should be inspected and trained. The goal is to reduce downtime in critical clusters by 10-15% and diagnosis times by 20% in the first 12 months after training.

6. Conclusion

This study presents a fleet-scale analysis of unscheduled downtime in container ship operations based on five years of operational records from 50 vessels. By combining risk-based Pareto analysis with an interpretable CART regression framework, the research identifies a limited number of technical subsystems that dominate both downtime frequency and duration. The results demonstrate that propulsion-related failures particularly those associated with the main engine fuel, exhaust, lubrication, and oil mist detection systems account for a disproportionate share of operational disruption, despite the presence of numerous lower-impact failure modes.

Beyond identifying critical failure clusters, the study contributes a practical, data-driven framework that links empirical downtime patterns to maintenance prioritization and role-based training strategies. The emphasis on interpretability enables direct translation of analytical outcomes into actionable decisions for fleet managers and marine engineers. While the findings are specific to container ship operations within a homogeneous fleet, the proposed analytical approach is transferable to other vessel types and operational contexts. Future studies may extend this framework by incorporating additional fleets, integrating exposure-normalized indicators, and evaluating long-term performance improvements resulting from targeted maintenance and training interventions.

Footnote

Financial Disclosure: The author declared that this study received no financial support.

References

[1] A. S. Kalafatelis, N. Nomikos, A. Giannopoulos, G. Alexandridis, A. Karditsa, and P. Trakadas, "Towards predictive maintenance in the maritime ındustry: a component-based overview," *Journal of Marine Science and Engineering,* vol. 13, no. 3, 425, Feb 2025,

[2] D. Budimir, D. Medić, V. Ružić, and M. Kulej, "Integrated approach to marine engine maintenance optimization: Weibull Analysis, Markov Chains, and DEA model," *Journal of Marine Science and Engineering,* vol. 13, no. 4, 798, Apr 2025.

[3] T. Tinga, W. Tiddens, F. Amoiralis, and M. Politis, "Predictive maintenance of maritime systems: models and challenges," in *Safety and Reliability – Theory and Applications*, High Tatras Mountains, Tatranské Matliare, Slovak Republic: CRC Press, June 2017, pp. 68.

[4] H. Shen, H. Cao, L. Wang, Z. Ai, and S. Dai, "Multi-granularity graph reasoning for semantic entity recognition in maritime fault knowledge extraction," *Knowledge-Based Systems,* vol. 328, 114170, Oct 2025.

[5] J. Karmelić, M. Jović Mihanović, A. Perić Hadžić, and D. Brčić, "Liner schedule reliability problem: an empirical analysis of disruptions and recovery measures in container shipping," *Logistics*, vol. 9, no. 4, 149, Oct 2025.

[6] V. H. Nguyen, "Optimal ship maintenance scheduling under restricted conditions and constrained resources," *Old Dominion University Libraries,* 2017.

[7] R. Islam, F. Khan, R. Abbassi, and V. Garaniya, "Human error assessment during maintenance operations of marine systems – What are the effective environmental factors?," *Safety Science*, vol. 107, pp. 85-98, Aug 2018.

[8] K. Ünlügençoğlu, "An investigation of maritime accidents in Turkish territorial waters," *Journal of Naval Architecture and Marine Technology,* vol. 2024, no. 226, pp. 65-79, Jan 2025.

[9] E. Romano-Moreno, G. Diaz-Hernandez, A. Tomás, and J. L. Lara, "Multivariate assessment of port operability and downtime based on the wave-induced response of moored ships at berths," *Ocean Engineering*, vol. 283, 115053, Sept 2023.

[10] L. M. Millefiori et al., "COVID-19 impact on global maritime mobility," *Scientific Reports,* vol. 11, no. 1, 18039, Sep 2021.

[11] D. Simion, F. Postolache, B. Fleacă, and E. Fleacă, "AI-driven predictive maintenance in modern maritime transport—enhancing operational efficiency and reliability," *Applied Sciences,* vol. 14, no. 20, 9439, Oct 2024.

[12] H. R. Soltani Motlagh, S. B. Issa-Zadeh, M. R. Zoolfakar, and C. L. Garay-Rondero, "Enhancing ship propulsion efficiency predictions with integrated physics and machine learning," *Journal of Marine Science and Engineering,* vol. 13, no. 8, 1487, Jul 2025.

[13] V. J. Jimenez, N. Bouhmala, and A. H. Gausdal, "Developing a predictive maintenance model for vessel machinery," *Journal of Ocean Engineering and Science*, vol. 5, no. 4, pp. 358-386, Dec 2020.

[14] A. BahooToroody, M. M. Abaei, E. Zio, F. Goerlandt, and M. Chaal, "Gaussian process latent variable model and Bayesian inference for non-parametric failure modeling applied to ship engine," *Reliability Engineering and System Safety,* vol. 265, 111611, Jan 2026.

[15] D. E. Onwuegbuchunam, I. C. Ogwude, C. C. Igboanusi, K. O. Okeke, and N. N. Azian, "Propulsion shaft and gearbox failure in marine vessels: a duration model analysis," *Journal of Transportation Technologies,* vol. 10, no. 04, pp. 291-305, Jan 2020.

[16] L. Chybowski, M. Szczepanek, K. Gawdzińska, and O. Klyus, "Particles morphology of mechanically generated oil mist mixtures of SAE 40 grade lubricating oil with diesel oil in the context of explosion risk in the crankcase of a marine engine," *Energies*, vol. 16, no. 9, 3915, May 2023.

[17] V. S. Ivanov, S. M. Frolov, I. V. Semenov, and M. S. Belotserkovskaya, "Crankcase explosions in marine diesel engines: a computational study of unvented and vented explosions of lubricating oil mist," *Journal of Marine Science and Engineering,* vol. 12, no. 1, p. 82, Dec 2023.

[18] B. O. Ceylan, and M. S. Celik, "Operational risk assessment of marine boiler plant for on-board systems safety," *Applied Ocean Research,* vol. 144, 103914, Mar 2024.

[19] S. Ahmed and X.-C. Gu, "Accident-based FMECA study of marine boiler for risk prioritization using fuzzy expert system," *Results in Engineering*, vol. 6, 100123, Jun 2020,

[20] X. Xu, X. Yan, K. Yang, J. Zhao, C. Sheng, and C. Yuan, "Review of condition monitoring and fault diagnosis for marine power systems," *Transportation Safety and Environment,* vol. 3, no. 2, pp. 85-102, Jun 2021.

[21] M. Tekgoz, Y. Garbatov, and C. Guedes Soares, "Strength assessment of an intact and damaged container ship subjected to asymmetrical bending loadings," *Marine Structures,* vol. 58, pp. 172-198, Mar 2018.

[22] O. Gaidai, F. Wang, Y. Cao, and Z. Liu, "4400 TEU cargo ship dynamic analysis by Gaidai reliability method," *Journal of Shipping and Trade,* vol. 9, no. 1, p. 1, Jan 2024.

[23] X. Zhang, and S. Mahadevan, "Bayesian network modeling of accident investigation reports for aviation safety assessment," *Reliability Engineering & System Safety,* vol. 209, 107371, May 2021.

[24] J. Yu, J. Zhao, X. Wang, and Y. Cao, "Maritime occupational accidents analysis: a data-driven Bayesian network approach," *Ocean Ocean & Coastal Management,* vol. 269, 107785, Oct 2025.

[25] L. Breiman, J. Friedman, C. J. Stone, and R. A. Olshen, *Classification and regression trees (CART)*. Taylor & Francis, 1984. [Online]. Available: https://books.google.com.tr/books?id=JwQx-WOmSyQC

[26] G. Vizentin, G. Vukelic, L. Murawski, N. Recho, and J. Orovic, "Marine propulsion system failures—a review," *Journal of Marine Science and Engineering*, vol. 8, no. 9, p. 662, Aug 2020.

[27] R. Kuroiwa, T. Nishioka, A. Oshima, K. Ohyama, T. Tateishi, and T. Ishijima, "*Reliability ımprovement of stern tube bearing considering propeller shaft forces during ship turning* (Mitsubishi Heavy Industries, Ltd. Technical Review, vol. 44, no. 3)," Mitsubishi Heavy Industries, Ltd. Technical Review, 2007.

[28] X. Chang, J. Liu, X. Yan, F. Sun, H. Zhu, and C. Wang, "Experimental study on the effects of controllable parameters on the healthy operation of SF-2A material water-lubricated stern bearing in multi-point ultra-long shaft systems of ships," *Journal of Marine Science and Engineering*, vol. 13, no. 1, p. 14, Dec 2024.

[29] A. Thorpe and S. Pabby, "Effectiveness of oil mist detectors in relation to oil mist droplet size and concentration," Symposium Series no. 162, 2017.

RESEARCH ARTICLE

DOI: 10.4274/jems.2025.27167

J Nav Architect Mar Technol 2026;228:24-31

An Investigation on the Effects of Different Solvents on the Characteristics of a Carbon Capture System in a Tanker

Furkan Böbür[1], Engin Güler[1,2], Selma Ergin[1]

[1]İstanbul Technical University Faculty of Naval Architecture and Ocean Engineering, Department of Naval Architecture and Marine Engineering, İstanbul, Türkiye

[2]Piri Reis University Faculty of Engineering, Department of Naval Architecture and Marine Engineering, İstanbul, Türkiye

To cite this article: F. Böbür, E. Güler, and S. Ergin. An investigation on the effects of different solvents on the characteristics of a carbon capture system in a tanker. *J Nav Architect Mar Technol*. 2026;228:24-31.

Received: 28.09.2025 - **Revision Requested:** 21.11.2025 - **Last Revision Received:** 22.12.2025 - **Accepted:** 21.01.2026 - **Publication Date:** 04.02.2026

Abstract

Harmful emissions into the atmosphere, such as carbon dioxide (CO_2), are increasing due to the extremely use of fossil fuels in the world. The shipping also increases global CO_2 emissions. This results in critical ecological issues like global warming, climate change and air pollution. Therefore, applications to reduce CO_2 emissions are needed, and carbon capture is one of these. In this study, the effects of mono-ethanolamine (MEA), piperazine (PZ) and ammonia (NH_3) solvents on the carbon capture costs and CO_2 capture rates (%) of the carbon capture system aboard a tanker were investigated for 30 wt% solvents. Capturing performance and economic analyses of the carbon capture system aboard the 49.990 DWT tanker were performed using Aspen HYSYS software. For different solvents, annual captured CO_2 emission amounts and CO_2 capture rates (%) were obtained at 85% engine load-cruise mode. For the same geometries of carbon capture columns, the carbon capture costs of the system per ton of CO_2 are $82.6, $69.6, and $47.3 for MEA, PZ and NH_3 solvents, respectively and the CO_2 capture rates are 30.9%, 36.7%, and 54% for MEA, PZ and NH_3 solvents, respectively. Cost-effective capture of CO_2 emissions released from ships into the atmosphere is important for the widespread use of carbon capture and storage systems.

Keywords: Carbon capture and storage, decarbonization, CO_2 emission, tanker, solvent

1. Introduction

Harmful emissions emitted into the atmosphere by usage of fossil fuels are increasing because of increasing energy need for various industries and home usage. Approximately 87% of carbon dioxide (CO_2) production resulting from human activities is the result of burning fossil fuels [1]. Thus, this causes adverse consequences like global warming, climate change, and air pollution. The shipping sector has a share of over 80% of the goods transported by volume on global trade. Also, its proportion of greenhouse gas (GHG) emission to global GHG emission is approximately 3% [2]. GHG emissions from ships are going up due to the increasing dimensions of ships and fleets even though GHG emissions by maritime industry have small share among other transportation modes and industries. Some regulations, such as the Ship Energy Efficiency Management Plan (SEEMP) and the Energy Efficiency Design Index (EEDI) were launched in amendments to *International Convention for the Prevention of Pollution from Ships*-MARPOL Annex VI by the International Maritime Organization (IMO) [3]. The target of the EEDI is to make ships energy-efficient in the

Address for Correspondence: Prof. Selma Ergin, İstanbul Technical University Faculty of Naval Architecture and Ocean Engineering, Department of Naval Architecture and Marine Engineering, İstanbul, Türkiye

E-mail: ergin@itu.edu.tr

ORCID ID: orcid.org/0000-0001-8343-2455

Copyright© 2026 The Author(s). Published by Galenos Publishing House on behalf of UCTEA Turkish Chamber of Naval Architects and Marine Engineers.
Licensed under a Creative Commons Attribution-NonCommercial-NoDerivatives 4.0 (CC BY-NC-ND) International License

design phase by optimizing their hull form and decreasing electric consumption by operational measures. The SEEMP aims to improve ships' energy efficiency and optimize the operational performance of ships by operational adjustments, such as installing waste heat recovery (WHR) equipment, optimizing the speed of ships, and weather routing. Also, the SEEMP is obligatory for ships above 400 gross tonnages [3]. The Energy Efficiency Existing Ship Index (EEXI) is another regulation by the IMO about enhancement of ships' energy efficiency. The target of the EEXI is to enhance the energy efficiency of ships already in operation and decrease GHG emissions from shipping [4]. The Carbon Intensity Indicator (CII) is another regulation by the IMO regarding the evaluation of GHG emissions on the volume of loads and miles transported. Also, the required annual reduction factor to be met by a ship on her operations is determined by the CII and the efficiency categories are A, B, C, D, and E for a ship [5]. The Monitoring, Reporting and Verification system is a regulation by the European Union (EU) to assess CO_2 emissions from ships by monitoring and reporting fuel consumption and CO_2 emissions of ships per voyage and on yearly basis, based on ships above 5000 gross tonnes at European Economic Area (EEA) ports. Companies from shipping industry must submit a monitoring plan for each ship and the data collected must be verified by accredited third parties [6]. This regulation is significant to increase the transparency and awareness of GHG emissions from shipping for decreasing fuel consumption and emissions. The IMO aims to reach a 20% reduction by 2030 and a 70% reduction by 2040 in GHG emissions, compared to 2008 level. Also, IMO aims to have net zero emissions by 2050 [7]. Moreover, the EU has target to decrease GHG emissions by 55%, based on the 1990 level, by 2030. This is evaluated economically feasible and beneficial by the EU [8]. Therefore, decarbonization of ships and carbon capture and storage (CCS) have become significant working fields to be considered [9].

There are many studies regarding CCS in the literature. Van Duc Long et al. [10] conducted a marine CO_2 capture study on a 3000-kW diesel engine with different configurations to evaluate CO_2 removal performance of the systems. Mono-ethanolamine (MEA), MEA/piperazine, (MEA/PZ) and n-methyl-diethanolamine/PZ are considered as solvents in this study. The results revealed that the CO_2 removal performance of proposed configuration was obtained as 94.7% and there is an increase of 8.4% in comparison with the base case. Tavakoli et al. [11] studied about the feasibility of carbon capture onboard ships. Retrofit and newbuild ships are considered for assessment the technical feasibility using the solvent-based post-combustion capture in this study. The results indicated that limited space and additional power required are challenges for the retrofit case. Also, it is challenging to find adequate space for CO_2 storage in terms of cargo capacity. Brandl et al. [12] conducted a study to obtain the hypothetical solvent to achieve the cost reduction by comparing the performances of various solvents. The results showed that a 65% of cost reduction was achieved and a cost limit of \$26/ton CO_2 (\$: US Dollars, weight unit: ton) was obtained. Zhou et al. [13] conducted a study on the carbon capture specifications of the exhaust gas of a marine engine. In this study, a K_2CO_3 solution was used in the simulation of CO_2 capture from the exhaust gas using ASPEN Plus. Various activators used in the experiment were selected using simulation results. The results showed that the absorption rate of CO_2 from the exhaust gas of the marine engine can be improved by a small amount of activator. Mao et al. [14] conducted a study on a mixed absorbent on the marine carbon capture. The characteristics of absorption and desorption were evaluated for different mole ratios. The results indicated that the average CO_2 absorption rate increased by 48% in comparison with MEA. Güler and Ergin [15] conducted a study on a solvent-based CCS system. Various types of ships are considered to investigate the performance of a system and to analyze its cost for different ships in this study. The results showed that the CCS system is more economic than other CO_2 control methods for ships with high speed. Bayramoğlu [16] conducted a study about post-combustion carbon capture on a marine engine. WHR and carbon capture system are considered to examine the rate of carbon reduction and the EEDI for ships. In this system, there is a 14% reduction of EEDI by WHR, and by 90% with the carbon capture. The results indicated that the carbon capture can be a promising method to meet the regulations.

There is no such study has investigated the effects of various solvents on capturing and economic performance of a solvent-based CCS system aboard a tanker by considering the actual general arrangement of a ship in the literature. Available space of the general arrangement of the ship is evaluated for the system because there is limited space for the columns of the system onboard the ship. The aim of this study is to investigate the effects of various solvents on the annual amount of the CO_2 emission captured and CO_2 capture rate (%) at the engine load of 85%, cruising mode. The other objective is to compute the carbon capture cost of the system per ton of CO_2 captured for different solvents. A 49,990-DWT tanker was examined in this study. MEA, PZ and, ammonia (NH_3) were considered as solvents.

2. Mathematical Model of CCS System

2.1. Carbon Capturing Model

Capturing performance analysis of the solvent-based CCS system aboard a tanker is conducted by using ASPEN software. The CCS system is modeled. MEA, PZ and, NH_3 are considered as solvents in this study. MEA is a common solvent and its some advantages are low volatility and relatively fast kinetics. However, its some disadvantages are high oxidative degradation and relatively high energy demand [17]. PZ has fast kinetics and low degradation rate [10]. Also, it has high thermal stability and less volatility in comparison with conventional amine-based alkanolamine [18]. NH_3 has a lower heat of reaction for absorption of CO_2 compared to MEA and the disadvantage of NH_3 is its volatility [19]. Furthermore, NH_3 is highly corrosive, and metal materials should be protected from contact with it. NH_3 is a toxic substance, and prolonged exposure to it should be avoided for health reasons. Additionally, fast kinetics, less tendency to degradation, less corrosive and less toxicity are some of the criterion on solvent selection for solvent-based CCS system [20]. In the process of absorption of CO_2 by the MEA solution, following chemical reactions take place, as shown in Equations (1-5) [15]:

$$MEACOO^- + H_2O \leftrightarrow MEA + HCO_3^- \quad (1)$$

$$CO_2 + 2H_2O \leftrightarrow HCO_3^- + H_3O^+ \quad (2)$$

$$HCO_3^- + H_2O \leftrightarrow CO_3^{-2} + H_3O^+ \quad (3)$$

$$MEAH^+ + H_2O \leftrightarrow MEA + H_3O^+ \quad (4)$$

$$2H_2O \leftrightarrow H_3O^+ + OH^- \quad (5)$$

MEA solution is a benchmark to compare capturing performance due to its reaction rate [10]. In absorption of CO_2 by the PZ solution, following reactions occur, as shown in Equations (6-10) [18]:

$$H_2O \leftrightarrow H^+ + OH^- \quad (6)$$

$$PZH^+ \leftrightarrow PZ + H^+ \quad (7)$$

$$PZ + CO_2 \leftrightarrow PZCOO^- + H^+ \quad (8)$$

$$PZCOO^- + CO_2 \leftrightarrow PZ(COO^-)_2 + H^+ \quad (9)$$

$$H^+PZCOO^- \leftrightarrow PZCOO^- + H^+ \quad (10)$$

Chemical equilibrium constants for the PZ solution reactions are calculated [18]. For NH_3, following reactions occur, as shown in Equations (11, 12) [19]:

$$CO_2 + OH^- \leftrightarrow HCO_3^- \quad (11)$$

$$NH_3 + CO_2 + H_2O \leftrightarrow NH_2COO^- + H_3O^+ \quad (12)$$

Chemical equilibrium constants for the NH_3 solution reactions are calculated [19]. The annual amount of the CO_2 emissions emitted from the ship into the atmosphere and CO_2 capture rate (%) are required to compute the annual amount of the CO_2 captured by the system. The annual amount of the CO_2 emission emitted from the ship [t] is computed by using specific fuel oil consumption (SFOC) [g/kWh], power [kW], emission factor (EF), and annual operational time [h] of the main engine, as shown in Equation (13).

$$\text{Annual } CO_2 \text{ emission} = \text{SFOC} * \text{Power} * \text{Annual operational time} * \text{EF} \quad (13)$$

CO_2 capture rate (%) is the ratio of the CO_2 transferred from the stripper to CO_2 storage onboard to captured CO_2 by the absorber. The annual amount of the CO_2 captured by the system is calculated by using the annual amount of the CO_2 emission emitted from the ship into the atmosphere and CO_2 capture rate (%), as shown in Equation (14).

$$\text{Annual } CO_2 \text{ captured} = \text{Annual } CO_2 \text{ emission} * CO_2 \text{ capture rate} \quad (14)$$

2.2. Economic Model

The carbon capture cost of the system per ton of CO_2 captured (C_{PCC}) was obtained for different solvents in economic analysis. The equipment and its installation cost (C_{EI}) and the other capital cost (C_O), such as engineering services and commissioning, are calculated using ASPEN software. The total capital cost (C_T) is calculated by the sum of the equipment and its installation cost (C_{EI}) and the other capital cost (C_O), as shown in Equation (15).

$$C_T = C_{EI} + C_O \quad (15)$$

The annualized total capital cost (C_{AT}) is computed by using C_T and the capital recovery factor (CRF), as shown in Equations (16, 17). The life of a ship is assumed as 25 years (n) and interest rate (i) is assumed as 10% without inflation [21].

$$CRF = \frac{i(1+i)^n}{(1+i)^n - 1} \quad (16)$$

$$C_{AT} = C_T CRF \quad (17)$$

The annual operational cost (C_{AO}) is calculated by using the freight loss cost (C_{FL}) due to the weight of the CCS system and additional fuel consumption cost (C_{AFC}) due to the additional power need for the system, as shown in Equation (18).

$$C_{AO} = C_{FL} + C_{AFC} \quad (18)$$

The annual life cycle cost (C_{ALC}) is calculated by using the annualized total capital cost (C_{AT}) and the annual operational cost (C_{AO}), as shown in Equation (19).

$$C_{ALC} = C_{AT} + C_{AO} \quad (19)$$

C_{PCC} is the ratio of the annual life cycle cost (C_{ALC}) to the CO_2 captured annually (T_{CCA}), as shown in Equation (20).

$$C_{PCC} = \frac{C_{ALC}}{T_{CCA}} \quad (20)$$

3. Specification of The Tanker, Selected Solvents and The CCS System

3.1. Specification of the Tanker

In this study, the ship considered and her properties of the diesel main engine at various engine loads are given in Tables 1 and 2.

EFs for a slow-speed marine diesel engine are used in this study. EFs are 3170 kg/ton of fuel for CO_2, 7.4 kg/ton of fuel for CO, 87 kg/ton of fuel for NO_X and 54 kg/ton of fuel for SO_2 [22].

3.2. Properties of Selected Solvents

In this study, MEA, PZ and, NH_3 are considered as solvents. MEA's chemical formula is C_2H_7NO and its molecular weight is 61.1 g. Its density at 20 °C is 1016 kg/m^3, and its melting and boiling points are 4 and 167 °C, respectively [23]. PZ's chemical formula is $C_4H_{10}N_2$ and its molecular weight is 86.1 g. Its density at 50 °C is 1020 kg/m^3, and its melting and boiling points are 35-45 and 110 °C, respectively [23]. NH_3's chemical formula is NH_3 and its molecular weight is 17 g. Its density at 15 °C is 0.73 kg/m^3, and its melting and boiling points are -77.7 and -33.3 °C, respectively.

Table 1. The particulars of the ship [22].

Features	Value
Length overall	183 m
Beam	32.2 m
Draft	16.5 m
Deadweight	49,990 t
Installed power (main engine)	10,320 kW

3.3. Properties of the CCS System

In the CCS system, the CO_2 emissions from the exhaust gas of the main engine is captured in the absorber. The CO_2-rich solvent is directed to pump to transfer to heat exchanger, whereas the clean gas from the residual exhaust gas is released. CO_2-solvent mixture is directed to stripper after heating by the heat exchanger. CO_2 is separated from the mixture in the form of gas in the stripper by heating and transferred to the CO_2 storage tank on-board and liquefied. CO_2-solvent mixture without CO_2 is cooled by the heat exchanger to re-use and directed to absorber, as shown in Figure 1.

Additional power is required for CCS due to processes such as, heating, cooling, pumping, and liquefaction. Also, extra space is needed for CO_2 storage in ships. The dimensions of the absorber and the stripper, and the power of the heat exchanger, and the pump are significant on carbon capture rate, the cost per ton of CO_2 captured, and occupied area on a ship. CCS system has also effects on the stability of ships because of its extra weight, area and location at a ship and freight revenue because of decreasing the amount of goods transported. The main aim of the carbon capture systems is contributing to cleaner and more sustainable environment based on regulations regarding reduction in GHG emissions. The optimization of the cost and dimensions of these systems are important to use widely on ships. In this study, MEA, PZ and, NH_3 are considered as solvents. The carbon capture system is located at the near of the funnel of the ship [24].

Table 2. The properties of the main engine at various engine loads [22].

Load (% Maximum continuous rating)	Power (kW)	SFOC (g/kWh)	Exhaust gas mass flow rate (kg/s)	Exhaust gas temperature (°C)
100	10,320	176.4	23.4	255
95	9,804	175.1	22.4	248
90	9,288	174.1	21.7	243
85	8,772	173.3	20.9	239
80	8,256	172.7	20.1	236
75	7,740	172.3	19.1	235
70	7,224	172.2	18.2	235
65	6,708	172.5	17.1	237
60	6,192	173.0	16.1	240
55	5,676	173.9	14.9	244
50	5,160	174.8	13.8	250

SFOC: Specific fuel oil consumption

4. Results and Discussion

4.1. Capturing Performance Analysis

Capturing performance analysis is carried out by using ASPEN HYSYS package program in this study. Firstly, solvents and fluids considered in this study are selected in the component list. Then, the solution method is selected. Acid gas-chemical solvents package is used in this study. Additionally, acid gas-chemical solvents package is a method, which is developed with the Peng-Robinson equation of state for vapor phase. Afterwards, the components in this system are selected and the system is formed. Conditions, such as temperature, pressure, and mass flow rate, are determined in this system. Lastly, CO_2 capture rates are obtained for MEA, PZ, and NH_3 at the engine load of 85%, cruising mode. The temperature of 30 °C and the pressure of 102 kPa are used for all solvents in this study. The volumetric flow rates of these solvents are 150, 168 and 248 m^3/h for MEA, PZ, and NH_3 solvents, respectively. The diameter and height of the absorber and stripper columns, space available on the ship for the CCS system, annual operational time of the main engine of the ship, and CO_2 EF (g-CO_2/kWh) of the marine main engine are some key parameters in capturing performance analysis. In this study, the absorber and stripper columns' diameters are equal and 1.5 m according to the general arrangement of the tanker. Both absorber and stripper have 10 stages. Also, they are tray columns and tray spaces are 0.6 m. Mass transfer in these columns are computed using the mass, equilibrium, summation of vapor and liquid compositions and heat (MESH) equations by Aspen HYSYS software based on the equilibrium-based model [18]. Additionally, the composition of exhaust gas is modelled as nitrogen of 67%, CO_2 of 12%, water of 11%, and oxygen of 10% by weight, respectively [25]. The annual amount of the CO_2 emission emitted from the ship into the atmosphere at the engine load of 85%, cruising mode, for a duration of 6400 hours of operational time is calculated as 30,842 tons of CO_2. CO_2 capture rates are calculated as 30.9%, 36.7% and 54% for MEA, PZ and NH_3 solvents, respectively. Also, the annual amounts of CO_2 captured are obtained as 9,530 tons, 11,319 tons and 16,655 tons for MEA, PZ and NH_3 solvents, respectively. Annual CO_2 captured is maximum for NH_3 solvent because of higher CO_2 capture rate of NH_3 solvent compared to other solvents in this study, as shown in Figure 2.

4.2. Economic Analysis

Economic analysis is conducted for MEA, PZ and, NH_3 30 wt% (wt: percentage by weight) at the engine load of 85%, cruising mode. In the scope of this analysis, the carbon capture cost of the system per ton of CO_2 (C_{PCC}) is calculated using the system annual life cycle cost and the annual amount of the CO_2 captured by the system. The cost of the system consists of equipment, construction, buildings, engineering and supervision costs [26]. In this analysis, the share of this types of costs are 50.5%, 29%, 4.7% and 15.8%, respectively. The equipment and its installation cost (C_{EI}) is calculated as $2,001,330 and the other capital cost (C_O) is $516,067. The total capital cost (C_T) is $2,517,397 and the CRF is calculated as 0.11 for the life of a ship of 25 years (n) and interest rate (i) of 10% without inflation. The annualized total capital cost (C_{AT}) is $277,342. Also, the annual operational cost (C_{AO})

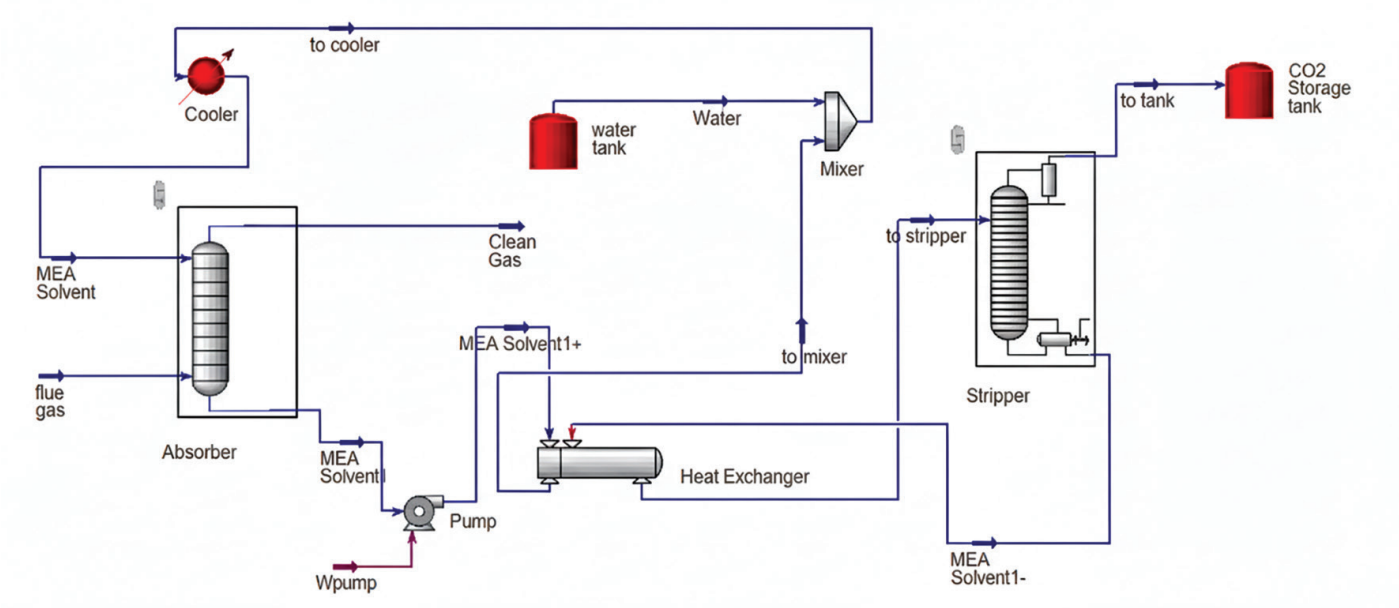


Figure 1. Schematic of CCS system considered in this study.

CCS: Carbon capture and storage, CO_2: Carbon dioxide, MEA: Mono-ethanolamine

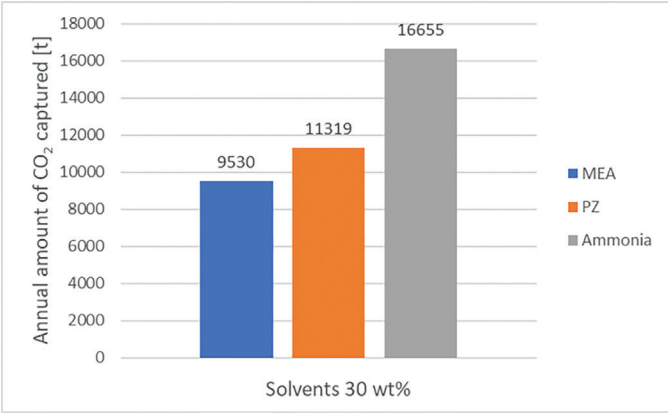


Figure 2. Relation between solvents and annual CO_2 captured by the CCS system.

CCS: Carbon capture and storage, MEA: Mono-ethanolamine, CO_2: Carbon dioxide, PZ: Piperazine

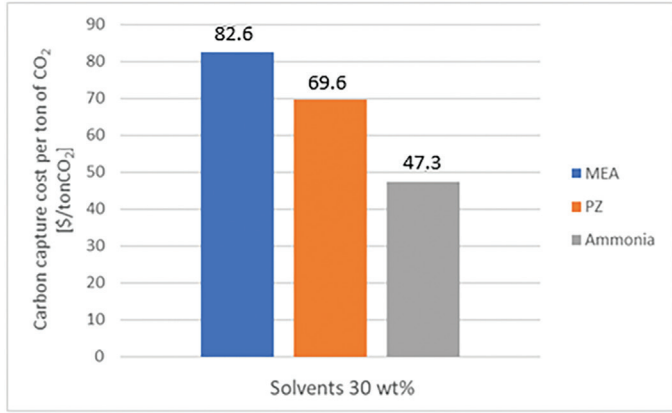


Figure 3. Relation between solvents and C_{PCC} of the CCS system.

CCS: Carbon capture and storage, MEA: Mono-ethanolamine, PZ: Piperazine

is calculated as $510,159 with the assumption of additional fuel consumption cost of the system for capturing the CO_2 emissions as 5% of the fuel consumption of the ship and freight loss cost as 10% of the sum of the equipment and its installation cost (C_{EI}) and the buildings cost [18]. Also, the annual life cycle cost (C_{ALC}) is calculated as $787,501, as shown in Table 3.

C_{PCC} is $82.6 for MEA solvent for the CO_2 capture rate of 30.9%, $69.6 for PZ solvent for the CO_2 capture rate of 36.7% and $47.3 for NH_3 solvent for the CO_2 capture rate of 54%, as shown in Figure 3.

C_{PCC} is minimum for NH_3 solvent because of higher annual CO_2 captured for NH_3 solvent compared to other solvents in this study. Moreover, the EU Emission Trading System (ETS) is a regulation set by the EU. With the ETS, ships pay for their emissions emitted into the atmosphere and the price is determined by the EU using the value of the amount of annual emission from ships and the EU ETS prices are shown in Figure 4.

Table 3. Cost components of the CCS system.

Features	Values
C_{EI}	$2,001,330
C_O	$516,067
C_T	$2,517,397
C_{AT}	$277,342
C_{AO}	$510,159
C_{ALC}	$787,501
CRF	0.11
n	25 years
i	10%

CCS: Carbon capture and storage, CRF: Capital recovery factor

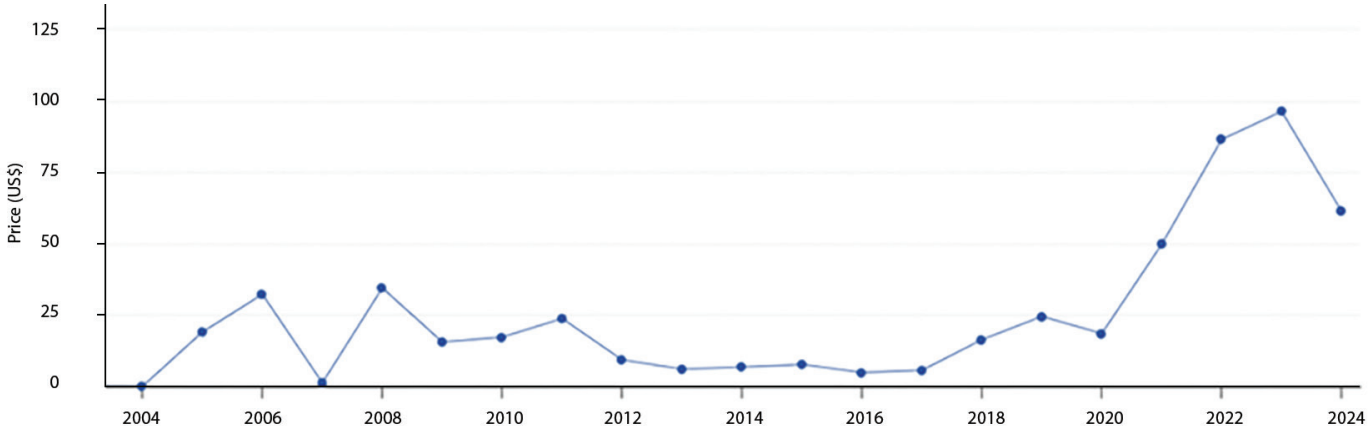


Figure 4. Trends in EU ETS between 2004 and 2024 [$/ton$CO_2$] [27].

EU: European Union, ETS: Emission Trading System

C_{PCC} for MEA and PZ in this study is higher than the EU ETS price in 2024. However, the cost for NH_3 is less than the EU ETS price in 2024. According to the new EU ETS II, carbon prices (in European Currency Unit) can go up €122/tCO_2 ($144/t$CO_2$) in 2030 and a mean of €99/tCO_2 at the period of 2027 and 2030 [28]. In the near future, this technology can be considered economically feasible with increasing ETS prices and decreased C_{PCC} for ships. When C_{PCC} is higher than ETS and/or carbon tax, this is a barrier for these systems to be feasible for ship owners. Therefore, studies for the reduction of C_{PCC} are important for cleaner and sustainable shipping. Economic results from this study and the literature are given in Table 4.

Table 4. Economic results from this study and the literature.

Carbon capture cost ($/ton$CO_2$)	References
149 (capture rate of 60%) 117 (capture rate of 90%)	[17]
70.34 (capture rate of 91%)	[29]
65.35 (capture rate of 34.5%)	[15]
77.50 (capture rate of 73%)	[21]
389 (capture rate of 60%) 296 (capture rate of 80%)	[30]
82.6 (capture rate of 30.9%) 69.6 (capture rate of 36.7%) 47.3 (capture rate of 54%)	From this study

According to Table 4, most of C_{PCC} from different studies are higher than the EU ETS prices. Therefore, the results in this study are consistent with various studies in the literature. Cost-effective reduction of CO_2 emissions released from ships into the atmosphere is important for the widespread use of carbon capture systems. Also, CCS on ships are important to reduce the adverse effects of the emissions of ships to the environment and human health.

5. Conclusion

The effects of MEA, PZ and NH_3 solvents on the carbon capture costs and CO_2 capture rates of the carbon capture system aboard a tanker were investigated for 30 wt% solvents in this study. Capturing performance and economic analyses of the CCS system aboard the 49.990 DWT tanker were performed using ASPEN HYSYS software. For different solvents, annual CO_2 emission amounts and CO_2 capture rates (%) were obtained at 85% engine load-cruise mode. The annual amount of the CO_2 emission emitted from the ship into the atmosphere at the engine load of 85%, cruising mode, for a duration of 6400 hours of operational time is calculated as 30,842 tons of CO_2. For MEA solvent 30 wt%, CO_2 capture rate is calculated 30.9% and the annual amount of CO_2 captured is 9,530 tons. Also, C_{PCC} is $82.6 for MEA solvent 30 wt%. C_{PCC} is $69.6 for PZ solvent 30 wt% for the CO_2 capture rate of 36.7% and the annual amount of CO_2 captured is 11,319 tons. Also, C_{PCC} is $47.3 for NH_3 solvent 30 wt% for the CO_2 capture rate of 54% and the annual amount of CO_2 captured is 16,655 tons. C_{PCC} in this study for MEA and PZ is higher than the EU ETS price in 2024. Whereas, the cost for NH_3 is less than the EU ETS price in 2024. This technology can be considered economically feasible with increasing ETS prices and decreased carbon capture cost per ton of CO_2 captured for ships. CCS on ships are important to reduce the adverse effects of the emissions of ships to the environment and human health in order to have cleaner and sustainable shipping industry based on the IMO's net zero emissions target by 2050.

Acknowledgements

The authors thank the Turkish Scientific and Technological Research Council of Türkiye, TÜBİTAK (2224-A-1919B022507858) and Istanbul Technical University, BAP (FHD-2025-47373 and Project ID: 47929) for the financial support they received during their research.

Footnotes

Authorship Contributions

Concept: E. Güler, and S. Ergin, Design: F. Böbür, and E. Güler, Data Collection or Processing: F. Böbür, E. Güler, and S. Ergin, Analysis or Interpretation: F. Böbür, E. Güler, and S. Ergin, Literature Review: F. Böbür, E. Güler, and S. Ergin, Writing: F. Böbür, E. Güler, and S. Ergin.

Conflict of Interest: No conflict of interest was declared by the authors.

Financial Disclosure: The authors would like to thank İstanbul Technical University Scientific Research Projects Coordination Unit (BAP) for providing financial support to the project numbered 44432.

References

[1] T. Wilberforce, A. G. Olabi, E. T. Sayed, K. Elsaid, and M. A. Abdelkareem, "Progress in carbon capture technologies," *Science of the Total Environment*, vol. 761, 143203, Mar 2021.

[2] UNCTAD, "Review of maritime transport 2023." Accessed: Dec 12, 2024. [Online]. Available: https://unctad.org/system/files/official-document/rmt2023_en.pdf

[3] E. K. Hansen, H. B. Rasmussen, and M. Lützen, "Making shipping more carbon-friendly? Exploring ship energy efficiency management plans in legislation and practice," *Energy Research & Social Science*, vol. 65, 101459, Jul 2020.

[4] S. Lee, "Analysis of the effects of EEDI and EEXI implementation on CO_2 emissions reduction in ships," *Ocean Engineering*, vol. 295, 116877, Mar 2024.

[5] IMO, "IMO regulations to introduce carbon intensity measures enter into force on 1 November 2022." Accessed: Dec 14, 2024. [Online]. Available: https://www.imo.org/en/MediaCentre/PressBriefings/pages/CII-and-EEXI-entry-into-force.aspx

[6] European Parliament, "Monitoring, reporting and verification of CO2 emissions from maritime transport.", Accessed: Dec 14, 2024. [Online]. Available: https://www.europarl.europa.eu/thinktank/en/document/EPRS_BRI(2019)642224

[7] IMO, "2023 IMO Strategy on Reduction of GHG Emissions from Ships." Accessed: Dec 14, 2024. [Online]. Available: https://www.imo.org/en/OurWork/Environment/Pages/2023-IMO-Strategy-on-Reduction-of-GHG-Emissions-from-Ships.aspx

[8] European Commission, "Stepping up Europe's 2030 climate ambition." Accessed: Dec 14, 2024. [Online]. Available: https://eur-lex.europa.eu/legal-content/EN/TXT/?uri=celex:52020DC0562

[9] G. Mallouppas, and E. A. Yfantis, "Decarbonization in shipping industry: a review of research, technology development, and innovation proposals," *Journal of Marine Science and Engineering*, vol. 9, pp. 415, Apr 2021.

[10] N. Van Duc Long, et al. "Improvement of marine carbon capture onboard diesel fueled ships," *Chemical Engineering and Processing-Process Intensification*, vol. 168, 108535, Nov 2021.

[11] S. Tavakoli, et al. "Exploring the technical feasibility of carbon capture onboard ships," *Journal of Cleaner Production*, vol. 452, 142032, May 2024.

[12] P. Brandl, M. Bui, J. P. Hallett, and N. Mac Dowell, "A century of re-exploring CO_2 capture solvents," *International Journal of Greenhouse Gas Control*, vol. 120, 103771, Oct 2022.

[13] S. Zhou, et al. "Experimental study on carbon capture characteristics of marine engine exhaust gas by activated potassium carbonate absorbent," *Environmental Science and Pollution Research*, vol. 30, pp. 80416-80431, Jun 2023.

[14] X. Mao, H. Chen, Y. Wang, X. Zhu, and G. Yang, "Study on benzylamine (BZA) and aminoethylpiperazine (AEP) mixed absorbent on ship-based carbon capture," *Molecules*, vol. 28, 2661, Mar 2023.

[15] E. Güler, and S. Ergin, "An investigation on the solvent based carbon capture and storage system by process modeling and comparisons with another carbon control methods for different ships," *International Journal of Greenhouse Gas Control*, vol. 110, 103438, Sep 2021.

[16] K. Bayramoğlu, "Application of post-combustion carbon capture process in marine diesel engine," *Energy Sources Part a Recovery Utilization and Environmental Effects*, vol. 45, pp. 10909-10925, Aug 2023.

[17] J. A. Ros, et al. "Advancements in ship-based carbon capture technology on board of LNG-fuelled ships," *International Journal of Greenhouse Gas Control*, vol. 114, 103575, Feb 2022.

[18] E. Güler, and S. Ergin, "An investigation of the cooling, heating and power systems integration with carbon capture and storage for LNG carriers," *Ships and Offshore Structures*, vol. 19, pp. 610-624, Mar 2023.

[19] A. Awoyomi, K. Patchigolla, and E. J. Anthony, "CO_2/SO_2 emission reduction in CO_2 shipping infrastructure," *International Journal of Greenhouse Gas Control*, vol. 88, pp. 57-70, Sep 2019.

[20] C. Ji, S. Yuan, M. Huffman, M. M. El-Halwagi, and Q. Wang, "Post-combustion carbon capture for tank to propeller via process modeling and simulation," *Journal of CO2 Utilization*, vol. 51, 101655, Sep 2021.

[21] X. Luo, and M. Wang, "Study of solvent-based carbon capture for cargo ships through process modelling and simulation," *Applied Energy*, vol. 195, pp. 402-413, Jun 2017.

[22] M. Akman, and S. Ergin, "An investigation of marine waste heat recovery system based on organic Rankine cycle under various engine operating conditions," *Proceedings of the Institution of Mechanical Engineers Part M Journal of Engineering for the Maritime Environment*, vol. 233, pp. 586-601, May 2018.

[23] Nouryon, "Product data sheet." Accessed: Jan 2, 2025. [Online]. Available: https://www.nouryon.com/products/

[24] DNV, "The potential of onboard carbon capture in shipping." Accessed: Dec. 15, 2024. [Online]. Available: https://www.dnv.com/maritime/publications/the-potential-of-onboard-carbon-capture-in-shipping-download/

[25] İ. A. Reşitoğlu, K. Altinişik, and A. Keskin, "The pollutant emissions from diesel-engine vehicles and exhaust aftertreatment systems," *Clean Technologies and Environmental Policy*, vol. 17, pp. 15-27, Jun 2014.

[26] Chemical Engineering, "The chemical engineering plant cost index." Accessed: Jan 14, 2025. [Online]. Available: https://www.chemengonline.com/pci-home

[27] World Bank Group, "State and trends of carbon pricing dashboard." Accessed: Jan 3, 2025. [Online]. Available: https://carbonpricingdashboard.worldbank.org/compliance/price

[28] BloombergNEF, Bloomberg Philanthropies, and European Climate Foundation, "EU ETS II pricing scenarios: balancing cuts and costs." Accessed: Sep 22, 2025. [Online]. Available: https://assets.bbhub.io/promo/sites/16/EU_ETS_II_Pricing_Scenarios_Balancing_Cuts_and_Costs.pdf

[29] F. Zea, D. Tinoco, and C. Varela, "A techno-economic evaluation of post-combustion carbon capture using renewable ammonia with different process configurations," *Case Studies in Chemical and Environmental Engineering*, vol. 8, 100502, Dec 2023.

[30] M. Feenstra, J. Monteiro, J. T. Van Den Akker, M. R. Abu-Zahra, E. Gilling, and E. Goetheer, "Ship-based carbon capture onboard of diesel or LNG-fuelled ships," *International Journal of Greenhouse Gas Control*, vol. 85, pp. 1-10, Jun 2019.

RESEARCH ARTICLE

DOI: 10.54926/jnamt.2026.2641

J Nav Architect Mar Technol 2026;228:32-42

Effect of Hull Form Variations on Slamming and Dynamic Response in a Naval Vessel

Marcelo de Oliveira Predes

Brazilian Navy, Rio de Janeiro, Brazil

To cite this article: M. O. Predes. Effect of hull form variations on slamming and dynamic response in a naval vessel. *J Nav Architect Mar Technol*. 2026;228:32-42.

Received: 13.01.2026 - **Revision Requested:** 14.02.2026 - **Last Revision Received:** 23.02.2026 - **Accepted:** 02.03.2026 - **Publication Date:** 17.03.2026

Abstract

This study evaluates the influence of specific hull-form parameters on slamming behavior. The hull of a military frigate was adopted as the baseline geometry, and systematic variations were generated by modifying one form parameter at a time. Ship motions were evaluated using a strip-theory-based seakeeping program, from which radiation damping and hydrostatic restoring coefficients were obtained, together with relative displacements and velocities at the critical hull location. Slamming occurrence frequency was then estimated by combining the motion responses with long-term wave statistics, allowing a probabilistic assessment under realistic sea conditions. The results indicate that variations in hull geometry, particularly near the waterplane area, significantly influence the probability of slamming. The main contribution of this work lies in the direct and isolated evaluation of hull-form parameters and their quantitative relationship with slamming behavior and global dynamic response, providing practical insights for hull-form optimization during the preliminary design stage.

Keywords: Slamming probability, Hull form variation, Ship seakeeping, Dynamic response analysis

1. Introduction

Within seakeeping dynamics, slamming is typically defined as the violent impact of a ship's hull against the water surface. These events can cause damage to onboard equipment and compromise the vessel's structural integrity. Their occurrence and severity are closely linked to both environmental conditions and specific hull design features, potentially limiting a ship's operational effectiveness. Consequently, reducing the likelihood of slamming and its associated impact forces has become a key objective in naval architecture, especially for vessels operating at high speeds or in rough seas. To optimize hull form regarding seakeeping, it is essential to recognize that a ship's dynamic behavior is largely governed by global variations in geometry [1]. Thus, refining hull parameters during the early design stages is crucial to improving overall performance. A practical approach involves characterizing the hull using a set of geometric parameters that allow for systematic performance evaluation.

Several studies have adopted this strategy. Bales [2] applied regression analysis to correlate destroyer-type hull responses with specific form parameters. Lloyd [3] analyzed the influence of hull size and shape on the vertical motions of a frigate, assessing absolute vertical acceleration and relative bow displacement-linked respectively to crew comfort and slamming occurrence. The study concluded that larger hulls (with unchanged form) exhibited attenuated vertical motions. It also found that a lower draft-to-length ratio generally reduced motions but increased the likelihood of keel emergence. Additionally, increasing the forward waterplane area coefficient (C_{WP}) was shown to reduce both absolute

Address for Correspondence: Marcelo de Oliveira Predes, Brazilian Navy, Rio de Janeiro, Brazil
E-mail: marcelo.o.predes@gmail.com
ORCID ID: orcid.org/0009-0001-2189-4088

Copyright© 2026 The Author(s). Published by Galenos Publishing House on behalf of UCTEA Turkish Chamber of Naval Architects and Marine Engineers.
Licensed under a Creative Commons Attribution-NonCommercial-NoDerivatives 4.0 (CC BY-NC-ND) International License

and relative vertical motions and decrease keel emergence probability. In a more recent contribution, [4] investigated seakeeping improvements in a catamaran-type vessel using parametric transformations via the Lackenby method. The study varied block coefficient (C_B) and longitudinal center of buoyancy (*LCB*) by ±10% relative to a baseline model. Analyses were conducted under both regular and irregular wave conditions, incorporating regional sea characteristics. All generated hulls were verified for stability and resistance. Results indicated that variations in *LCB* and C_{WP} significantly influenced seakeeping, while changes in C_B had relatively minor effects. Hakim et al. [5] performed a comparative analysis of slamming probability between U- and V-shaped hull sections using strip theory. Their findings showed that U-shaped hulls had a 20-35% higher likelihood of slamming, emphasizing the role of hull section geometry in impact vulnerability.

More recently, computational fluid dynamics (CFD) methods have been employed to provide deeper insights into slamming and seakeeping behavior. Liao et al. [6] used a Reynolds-averaged Navier–Stokes-based CFD solver with overset grids to analyze trimaran seakeeping and slamming in oblique waves, highlighting distinct behaviors from monohulls and revealing severe bow slamming and green water events under varying speeds and headings. Kapsenberg [1], in earlier work on hull optimization, proposed a methodology combining polynomial functions and Lewis transformations to generate new hull forms. While his method yielded notable performance improvements, the resulting geometries were deemed unrealistic for practical application.

Building upon these foundations, the present study investigates how variations in selected hull form parameters affect a ship's dynamic behavior, with particular emphasis on slamming prediction. The proposed methodology involves independent variation of each parameter, enabling isolated assessment of its influence on ship motions and slamming probability. The analysis incorporates seakeeping simulations based on linear potential theory, including excitation forces, damping coefficients, and relative motions and velocities at a critical point near the bow keel, where slamming is most likely to occur.

2. Parametric Hull Form Variations

This study uses the hull of the Dutch frigate Friesland as the reference geometry for analysis. Figure 1 presents the body plan of the reference geometry, reconstructed from the original offsets data, which serves as the basis for the implemented Bézier and Lewis sectional modifications. The main characteristics of the baseline hull are summarized in Table 1.

Table 1. Main characteristics.

L_{PP}	112.4 m
B	11.74 m
T	4.01 m
C_B	0.562
Pitch radius of gyration	0.233 L_{PP}
Displacement	3046 tons

Due to their relatively smaller size compared to large commercial vessels and their high-speed operational profile, frigates are particularly susceptible to slamming events. Such impacts can damage not only the ship's structure but also critical onboard systems such as sensors, weapons, and ammunition. Hull geometry and seakeeping data for this vessel type are available in [7], which provided the foundation for model generation.

To investigate the influence of specific geometric features on ship response, four hull form parameters were selected for variation:

1. Longitudinal Center of Buoyancy (LCB/L_{PP}),
2. Block Coefficient (C_B),

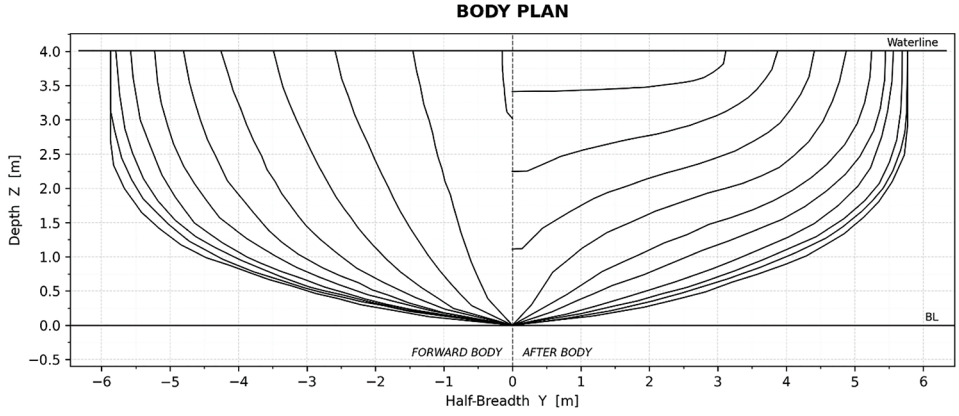


Figure 1. Body plan of the frigate Friesland.

3. Longitudinal Center of Flotation (LCF/L_{PP}),

4. Waterplane Area Coefficient (C_{WP}).

A custom algorithm was developed to generate a large number of hull geometries derived from the baseline model. A filtering process was then applied to retain only those variants in which a single parameter deviated meaningfully from the original configuration, while the remaining three parameters remained close to their baseline values. This ensures that each selected variation isolates the influence of one geometric factor, enabling valid comparative analysis. From this filtered set, the most extreme values observed for each parameter—maximum and minimum—were chosen to define the eight final configurations used in the study:

- *LCB* (+): center of buoyancy shifted forward,
- *LCB* (-): center of buoyancy shifted aft,
- C_B (+): higher block coefficient (fuller hull),
- C_B (-): lower block coefficient (finer hull),
- *LCF* (+): center of flotation shifted forward,
- *LCF* (-): center of flotation shifted aft,
- C_{WP} (+): higher waterplane area coefficient,
- C_{WP} (-): lower waterplane area coefficient.

The complete methodology used to generate, filter, and select the hull variants is detailed in previous work [8], which outlines the geometric framework adopted. A later publication [9] complements this discussion by offering further analysis and interpretations of the parametric variation approach. Based on that process, eight extreme configurations were identified, each designed to isolate the effect of a single hull form parameter while keeping the remaining parameters approximately constant. Notably, more pronounced variations were achieved for the LCF/L_{PP} and C_{WP} parameters, whereas the LCB/L_{PP} and C_B variations were more constrained due to the geometric interdependencies. In order to verify the basic feasibility of the selected variants, all eight hulls were subjected to preliminary stability analyses. Intact stability was assessed according to the criteria defined by the International Maritime Organization (IMO) in Resolution A749(18) (IMO, 1993), and all configurations were found to be compliant. The final values associated with each extreme case are summarized in Table 2.

In addition to the geometric constraints previously described, the normal draft, maximum beam, length between perpendiculars, and the longitudinal profile were kept constant for all hull variants. Furthermore, the sectional beam distribution along the hull was interpolated using a second-degree polynomial function in order to avoid abrupt contour variations at the waterplane. These measures ensured geometric smoothness and consistency across all configurations. Although the selected cases represent extreme values within the investigated parameter ranges, the resulting hull forms remain within the family of conventional displacement ships, preserving sectional characteristics compatible with the assumptions underlying linear strip theory.

3. Mathematical Formulation

3.1. Governing Theory and Hydrodynamic Model

The hydrodynamic modeling adopted in this study is based on linear potential flow theory within the strip theory framework. The fluid domain is assumed to be incompressible, inviscid and irrotational, which permits the use of a velocity potential ϕ that satisfies the Laplace equation (Equation 1):

$$\nabla^2 \phi = 0 \tag{1}$$

This potential must also satisfy boundary conditions at the free surface, hull surface, sea bottom (if applicable), and at infinity. The ship is modeled as a rigid body advancing at constant forward speed in calm water, disturbed by regular or irregular waves. For ships with longitudinal symmetry and slender hull forms, the hydrodynamic forces in surge (longitudinal translation) are significantly smaller than those in heave and pitch and can be neglected without compromising accuracy. Therefore, the system of equations is simplified by considering only vertical (heave) and angular (pitch) motions in the vertical plane. Figure 2 illustrates the coordinate system adopted in this study, with the origin located at the center of gravity (CG). The x-axis is aligned with the ship's longitudinal direction, the z-axis is positive upwards, and the y-axis completes the right-handed coordinate system.

The equations of motion in the frequency domain for heave and pitch are given by Equation (2):

$$\left[-\omega^2(M + A(\omega)) + i\omega B(\omega) + C\right] \eta(\omega) = F(\omega) \tag{2}$$

Table 2. Extreme values.

Parameter	Base	*LCB* (-)	*LCB* (+)	C_B (-)	C_B (+)	*LCF* (-)	*LCF* (+)	C_{WP} (-)	C_{WP} (+)
LCB/L_{PP}	0.489	0.447	0.510	0.358	0.590	0.435	0.515	0.777	0.867
C_B	0.562	0.563	0.561	0.490	0.489	0.793	0.793	0.463	0.460
LCF/L_{PP}	0.461	0.462	0.461	0.462	0.462	0.489	0.491	0.492	0.492
C_{WP}	0.794	0.796	0.792	0.796	0.796	0.560	0.559	0.561	0.561

LCB: Longitudinal center of buoyancy, *LCF*: Longitudinal center of flotation

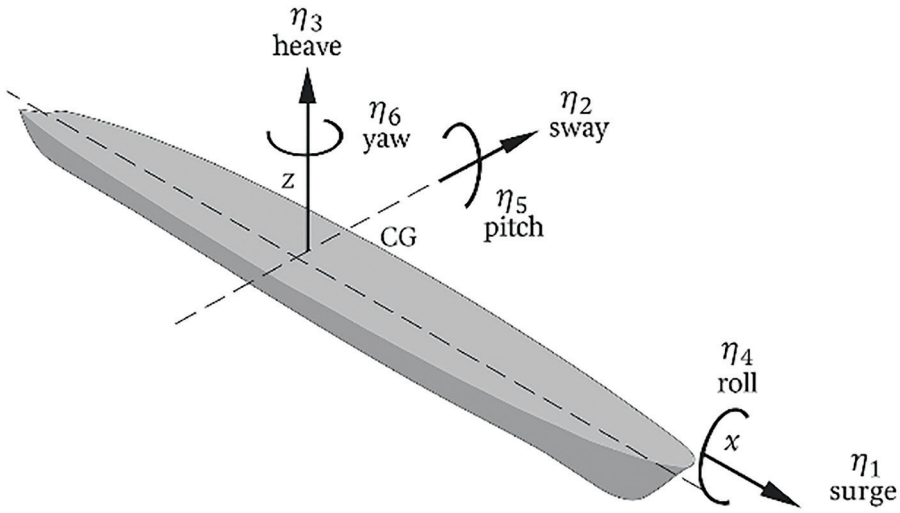


Figure 2. Coordinate system and six degrees of freedom used in the hydrodynamic analysis (adapted from [8]).

Where ω is the encounter frequency, M is the mass matrix, $A(\omega)$ is the added mass, $B(\omega)$ is the radiation damping, C is the hydrostatic restoring stiffness, $\eta(\omega)$ is the motion response vector (heave and pitch), and $F(\omega)$ is the wave excitation force vector. For the parametric hull variants analyzed in this study, the rigid-body mass matrix M was updated to account for the corresponding displacement variations. However, the pitch radius of gyration about the transverse axis was assumed constant and equal to that of the baseline hull. This simplifying assumption was adopted due to the complexity associated with reliably estimating structural mass redistribution for each geometric modification. Therefore, variations in pitch response are primarily attributed to hydrodynamic and hydrostatic changes rather than modifications in mass distribution.

To obtain the hydrodynamic coefficients and wave loads, strip theory is applied as formulated by [10]. The hull is divided into transverse sections, and the two-dimensional potential problem is solved at each section. The global response is then determined by integrating along the ship's length. This approach provides a practical compromise between computational efficiency and accuracy, especially for seakeeping evaluations of slender hulls in moderate sea states. The simulations in this work were conducted using the Seaway Octopus software, which implements this methodology.

3.2. Ship Response in Waves

The ship's dynamic behavior under wave excitation was evaluated through simulations in both regular and irregular seas, using linear frequency-domain potential theory. In the regular wave approach, the vessel is subjected to monochromatic waves across a range of encounter frequencies to determine its fundamental response characteristics. This results in the response amplitude operators (RAOs), which quantify the motion response as a function of frequency and serve as the foundation for spectral analysis in irregular seas. To compute the motion response $\eta(\omega)$ at each frequency, the linear equations of motion described in Section 3.1 are solved in the frequency domain (Equation 3):

$$\eta(\omega) = -\left[-\omega^2(M + A(\omega)) + i\omega B(\omega) + C\right]^{-1} * F(\omega) \quad (3)$$

The RAO for each motion component is given by Equation (4):

$$\mathrm{RAO}_{\eta}(\omega) = \left|\frac{|\eta(\omega)|}{|\zeta_a|}\right| \quad (4)$$

Where ζ_a is the wave amplitude and $\eta(\omega)$ is the complex motion amplitude. In this study, the analysis focused on heave (η_3) and pitch (η_5), while surge, roll, and yaw were neglected due to the longitudinal symmetry of the hull and the head-sea wave condition. Local kinematic responses were also evaluated at a specific analysis point P, located 10% of the ship length from the forward perpendicular, at the keel level. This location lies within the forward impact region commonly adopted in preliminary slamming assessments and is representative of the bow flare area under head-sea conditions. At this point, both absolute and relative motions were computed for vertical displacement and pitch-induced rotation. For heave, the absolute vertical displacement is denoted by $s_3(t)$, and the wave elevation at the same location is $\zeta_P(t)$. The relative vertical displacement between the hull and the wave at point P is therefore expressed according to Equation (5):

$$r_3(t) = s_3(t) - \zeta_P(t) \quad (5)$$

Pitch-induced contributions to the vertical motion at this location were also taken into account, based on the pitch angle $\eta_5(t)$ and the longitudinal offset of point P from the CG. The resulting combined vertical response, which includes both heave and pitch effects, is given by Equation (6):

$$r(t) = \eta_3(t) - \zeta_P(t) + x_P\,\eta_5(t) \tag{6}$$

Where x_P is the longitudinal distance from the CG to point P, taken positive in the forward direction. The relative vertical velocity at this point is then obtained by differentiating Equation (6) with respect to time, as shown in Equation (7):

$$v(t) = r(t)\,\eta_3(t) - \zeta_P(t) + x_P\,\eta_5(t) \tag{7}$$

These quantities were computed in the frequency domain and stored in amplitude-phase format, such as r_A, ε_R for displacement and v_A, ε_V for velocity, to support later analyses of slamming occurrence and hydrodynamic performance comparison. To represent realistic sea conditions, irregular wave responses were evaluated using spectral analysis. The Bretschneider spectrum, defined by Equation (8), was adopted to describe the wave energy distribution:

$$S_\zeta = \frac{173 H_{1/3}^2}{T_1^4}\,\omega^{-5}\exp\left\{\frac{-692}{T_1^4}\,\omega^{-4}\right\} \tag{8}$$

Where $H_{1/3}$ is the significant wave height and T_1 is the mean wave period. The corresponding motion response spectrum for each motion component $\eta(\omega)$ was calculated using Equation (9):

$$S_\eta(\omega) = |\mathrm{RAO}_\omega|^2 * S_\zeta(\omega) \tag{9}$$

Finally, the zeroth-order spectral moment, used later in the slamming probability formulation, was obtained by numerical integration of the motion spectrum, as shown in Equation (10):

$$m_0 = \int_0^\infty S_\eta(\omega)d\omega \tag{10}$$

These spectral moments were evaluated for both relative displacement and velocity at point P. In combination with long-term sea statistics, they form the basis for the probabilistic assessment of slamming events. To ensure that the computed responses reflect realistic and demanding operational conditions, wave data were extracted from the Octopus statistical database for a region near the southern tip of South America, where adverse sea states are frequent. The joint probability distribution of significant wave height and mean wave period used in this study is shown in Figure 3. These values were applied to compute weighted slamming probabilities across multiple sea states, incorporating real-world operational variability into the evaluation.

3.3. Slamming Predictions

The probabilistic estimation of slamming occurrence in this study is based on the method originally proposed by

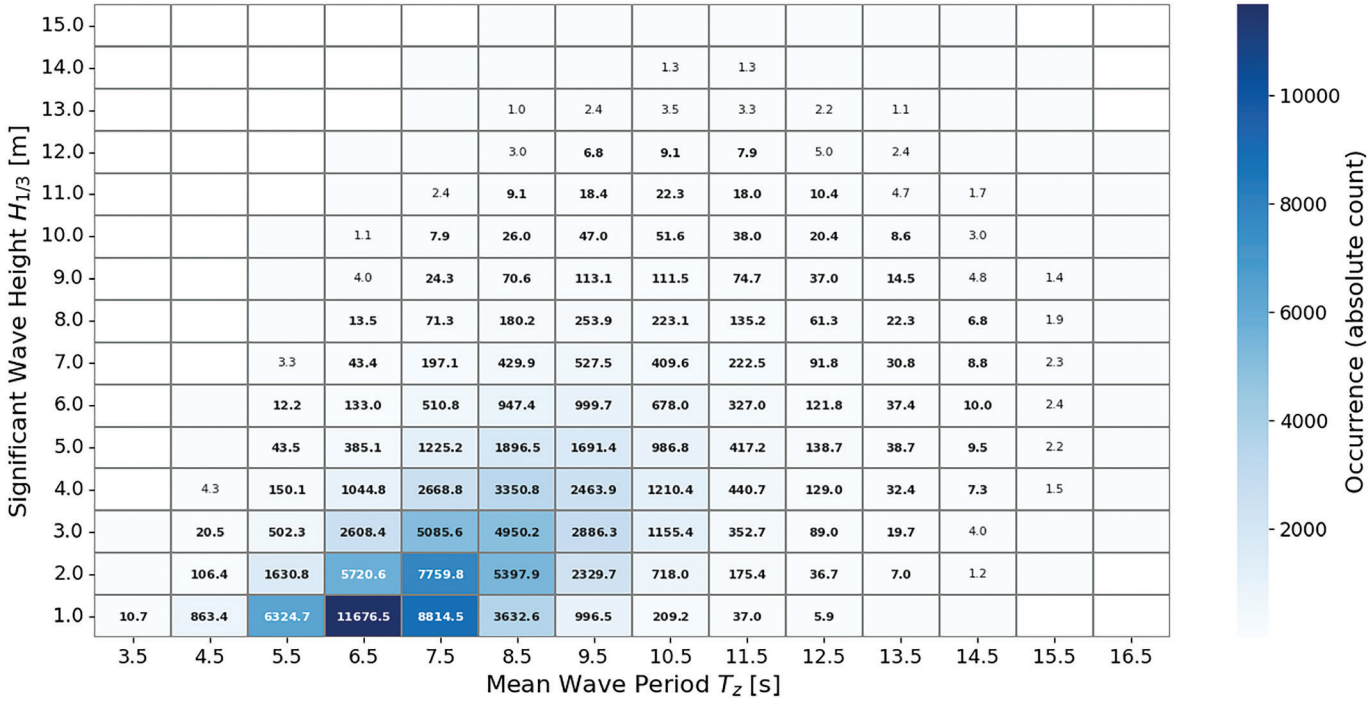


Figure 3. Joint probability distribution-South Atlantic Region.

Ochi [11], which defines the event as resulting from the simultaneous occurrence of two statistically independent conditions at a critical point on the hull: 1) emergence of the point above the free surface, and 2) its reentry with a vertical velocity exceeding a critical threshold. This dual-condition approach provides a simplified yet robust framework for evaluating slamming frequency in irregular seas. In this study, the critical point P is located at 10% of the ship's length from the bow along the keel, where slamming is most likely to occur. To model sea conditions, the Bretschneider spectrum was employed to represent irregular waves. For each sea state in the long-term database, the zeroth-order spectral moments of displacement and velocity at poin P — m_{OS} and m_{OV}, respectively—were computed. These values serve as the basis for evaluating the probability of each slamming condition. The critical reentry velocity V_{CR} was computed using the empirical expression derived by [12], based on Froude similarity [Equation (11)]:

$$V_{CR} = 0.093\sqrt{gL} \tag{11}$$

The probability that the vertical velocity v_3 at point P exceeds this critical threshold is given by Equation (12):

$$\Pr\{v_3 > V_{CR}\} = \exp\left(-\frac{V_{CR}^2}{2m_{OV}}\right) \tag{12}$$

Simultaneously, the probability that the absolute displacement at P exceeds the local draft T_P is defined by Equation (13):

$$\Pr\{s_3 > T_P\} = \exp\left(-\frac{T_P^2}{2m_{OS}}\right) \tag{13}$$

Assuming statistical independence between the two conditions, the overall probability of slamming per wave cycle is computed using Equation (14):

$$\Pr\{\text{Slam}\} = \exp\left(-\frac{T_P^2}{2m_{OS}} - \frac{V_{CR}^2}{2m_{OV}}\right) \tag{14}$$

To obtain long-term probability estimates, the results were weighted by the joint probability distribution of significant wave height and mean wave period, as shown in Figure 2. The weighted formulation is expressed in Equation (15):

$$\Pr(\text{Slam})_{\text{Total}} = \sum_{i=1}^{n}\Pr(\text{Slam})_i \Pr\left(H_{1/3}, T_Z\right)_i \tag{15}$$

The mean encounter period at point P, based on the spectral moments, is given by Equation (16):

$$T_{2S} = 2\pi\sqrt{\frac{m_{OS}}{m_{OV}}} \tag{16}$$

Thus, the expected number of slamming events per hour is computed according to Equation (17):

$$N_{\text{Slams/hr}} = \frac{3600}{T_{2S}}\Pr(\text{Slam})_{\text{Total}} \tag{17}$$

4. Results and Discussion

4.1. Hydrodynamic Coefficients

To assess the hydrodynamic effects of hull form variation, frequency-dependent coefficients were calculated for heave and pitch motions using linear strip theory. Among the four investigated parameters, the block coefficient (C_B) and the waterplane area coefficient (C_{WP}) produced the most expressive variations in excitation and radiation components.

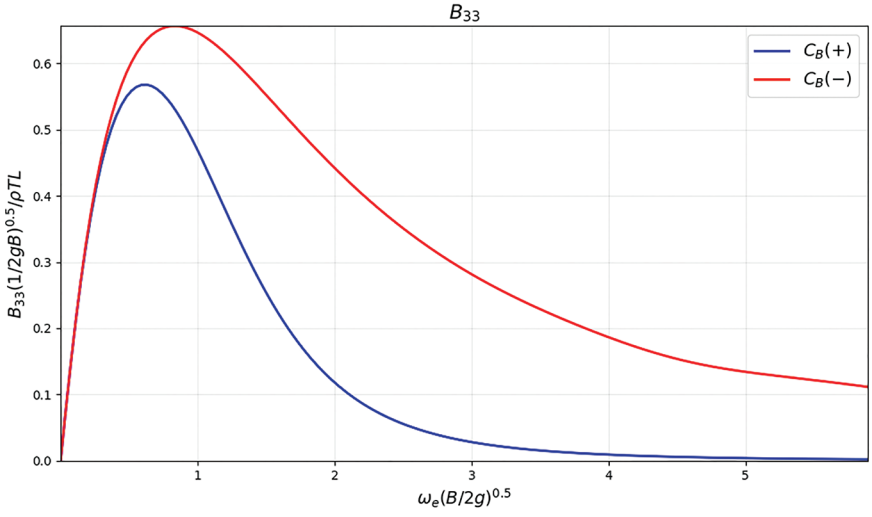


Figure 4. Damping coefficient B_{33} for C_B variants (adapted from [8]).

Therefore, only the most representative coefficients, specifically the heave damping coefficient B_{33} and the pitch restoring stiffness C_{55}, were selected for discussion. Other hydrodynamic terms, such as B_{55} or C_{33}, showed minimal variation across the hull variants and were omitted for brevity. Figure 4 presents the damping coefficient B_{33} for the C_B(+) and C_B(-) configurations. The finer hull form C_B(-) exhibits slightly higher damping values across most of the analyzed frequency range, particularly near the region of maximum response. This behavior aligns with expectations, as more slender geometries promote stronger wave radiation due to reduced sectional area and increased curvature near the bow and stern.

Figure 5 displays the hydrostatic restoring coefficient C_{55} for the C_{WP}(+) and C_{WP}(-s) models. Increasing the waterplane area coefficient significantly enhances the hydrostatic restoring moment in pitch, reinforcing the importance of waterplane geometry in seakeeping performance, especially regarding pitch stability. Other coefficients such as B_{55}, C_{33} and excitation terms F_3 and F_5 were also evaluated for C_{WP} variants but exhibited either low sensitivity or trends similar to those already presented. For brevity and focus, only the most relevant terms are included in this discussion.

4.2. Relative Motion and Velocity

Relative vertical displacements and velocities at the keel point P, located 10% of L_{PP} aft of the bow, were computed for all hull variants. As introduced in Section 4.2, the relative motion is defined as the difference between the vertical displacement of the hull and the local wave elevation at the same location [see Equation (5)]. This quantity is directly related to the occurrence of slamming events. In addition, the vertical relative velocity is essential for the probabilistic estimation of slamming, as it determines the kinetic severity of impact upon water reentry. Figures 6 through 9 present the relative displacement amplitude r_3 at point P for each pair of extreme hull variants, corresponding to variations in *LCB*, C_B, *LCF*, and C_{WP}. Each configuration shows distinct dynamic behavior, demonstrating how isolated geometric changes affect bow response. Figure 6 compares *LCB*(+) and *LCB*(-) variants.

Figure 7 presents C_B(+) and C_B(-). The fuller hull shape (C_B+) exhibits higher vertical motion amplitudes, especially near the peak response region. The lower damping and greater

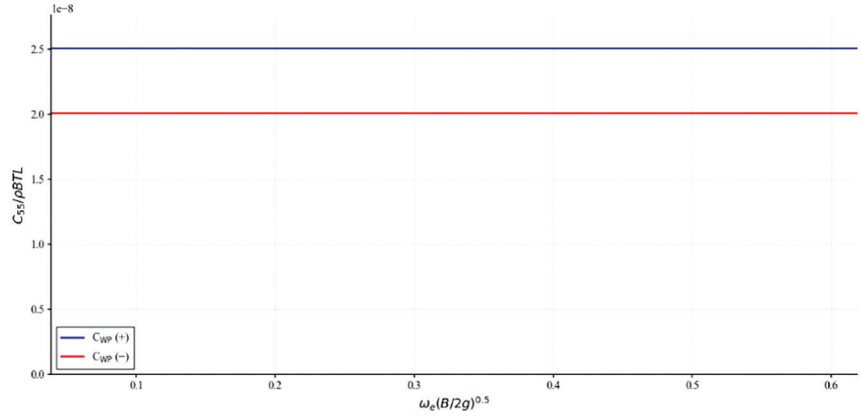


Figure 5. Restoring coefficient C_{55} for C_{WP} variants (adapted from [8]).

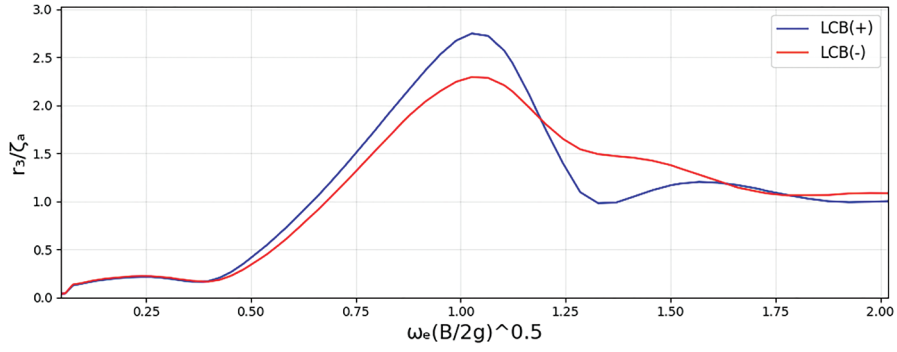


Figure 6. Relative vertical motion amplitude r_3 at point P for *LCB*(+) and *LCB*(-) configurations.

volume distribution in C_B(+) contribute to this amplification of bow dynamics.

Figure 8 shows results for *LCF*(+) and *LCF*(-). The *LCF*(-) variant, with its center of flotation positioned aft, demonstrates higher relative motion at point P, likely due to more pronounced pitch movement, which accentuates bow lift and drop.

Figure 9 highlights the impact of waterplane area. The C_{WP}(-) variant, representing a reduced waterplane, shows significantly increased motion amplitude. This configuration leads to lower hydrostatic stiffness and more abrupt responses to wave excitation.

Figure 10 summarizes the vertical relative velocity amplitude at point P for all geometric variants. As expected, the trends observed are closely aligned with those of the relative displacement: configurations that lead to higher vertical excursions [such as *LCB*(+), C_B(+), *LCF*(-), and C_{WP}(-)] also result in increased vertical velocities. These results reinforce the role of hull form in modulating the severity of water reentry and support the use of relative

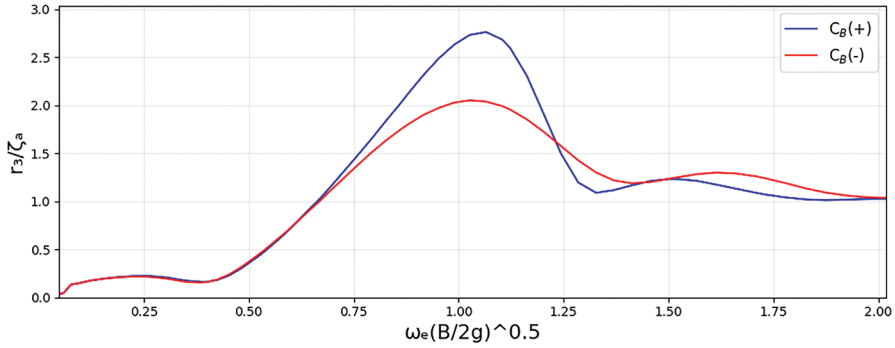


Figure 7. Relative vertical motion amplitude r_3 at point P for C_B(+) and C_B(-) configurations.

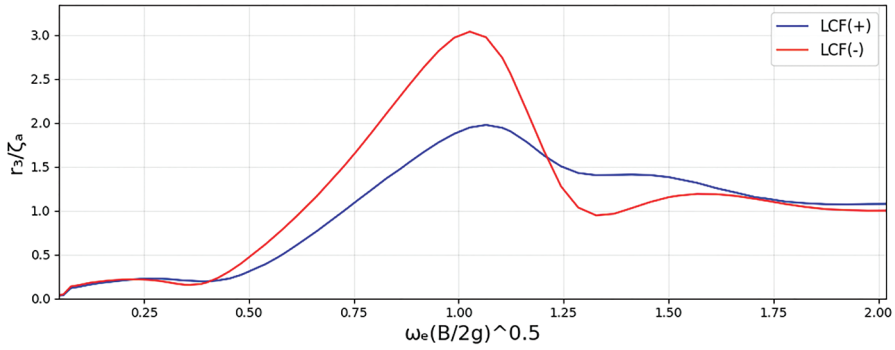


Figure 8. Relative vertical motion amplitude r_3 at point P for *LCF*(+) and *LCF*(-) configurations.

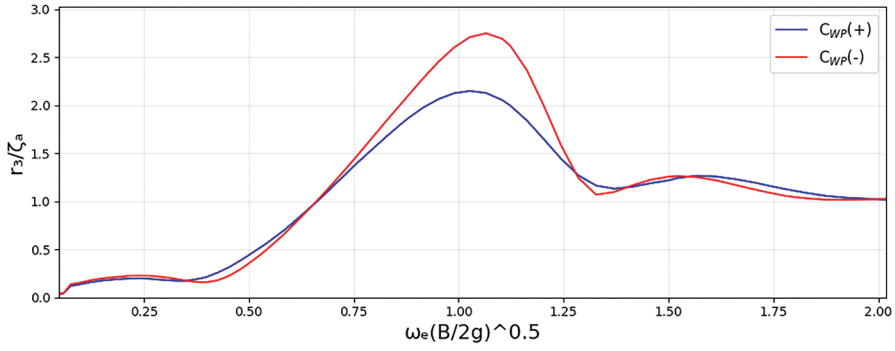


Figure 9. Relative vertical motion amplitude r_3 at point P for C_{WP}(+) and C_{WP}(-) configurations.

velocity as a key variable in slamming probability estimations.

4.3. Slamming Ocurrence

To assess how variations in hull form affect the ship's vulnerability to slamming, the predicted slamming probability (PR{slam}) was computed for each of the eight extreme configurations. These results were derived from the spectral moments associated with relative vertical velocity at point P and integrated with long-term wave statistics, as described in Section 4.3. Table 3 summarizes the predicted probability of slamming and the corresponding number of events per hour. Notably, most hull variants remained within the operational threshold defined by RINAMIL (2007), which recommends a maximum of 20 slamming events per hour for safe operation.

To better quantify the influence of each form parameter, a sensitivity index was defined as the change in PR{slam} divided by the corresponding geometric variation (in percentage points), normalized as ΔPR/ΔGeom×100. This index allows for a direct comparison of how responsive slamming behavior is to a given parameter variation. The results show that *LCF* exhibits the highest sensitivity (7.79), indicating that even moderate shifts in the longitudinal center of flotation can substantially affect slamming incidence. The C_{WP} and *LCB* also demonstrate moderate sensitivity, while C_B shows the lowest influence, despite its significant geometric variation. These findings are visually reinforced in Figure 11, which plots the geometric variation against the corresponding PR{slam}.

5. Limitations of the Adopted Methodology

This work is based on linear strip theory formulated within a frequency-domain seakeeping framework. This approach assumes linearized free-surface boundary conditions, small-amplitude wave excitation, and linear superposition of responses. Although widely adopted in preliminary ship design due to its robustness and computational efficiency, these assumptions limit the ability of the model to represent strongly non-linear hydrodynamic phenomena.

Slamming is a transient event involving rapid variations in wetted surface area, localized impact pressures, and non-linear fluid-structure interaction effects. Phenomena such as bow flare slamming, time-varying buoyancy, and possible air entrapment are not explicitly resolved within linear potential flow theory. Moreover, the frequency-domain formulation does not capture short-duration time-domain impact peaks that may occur in severe sea states.

In this study, slamming susceptibility was inferred from relative motion criteria combined with long-term probabilistic analysis, rather than through direct computation of impact pressures. The results should therefore be interpreted as indicators of comparative trends among hull configurations, rather than detailed predictions of local structural loads.

Non-linear time-domain solvers or high-fidelity CFD approaches may therefore produce different absolute magnitudes of motion amplitudes and impact-related metrics, particularly under steep or breaking wave conditions. Such non-linear effects could influence peak responses and local load estimates. However, for comparative parametric investigations within a consistent hull family, relative

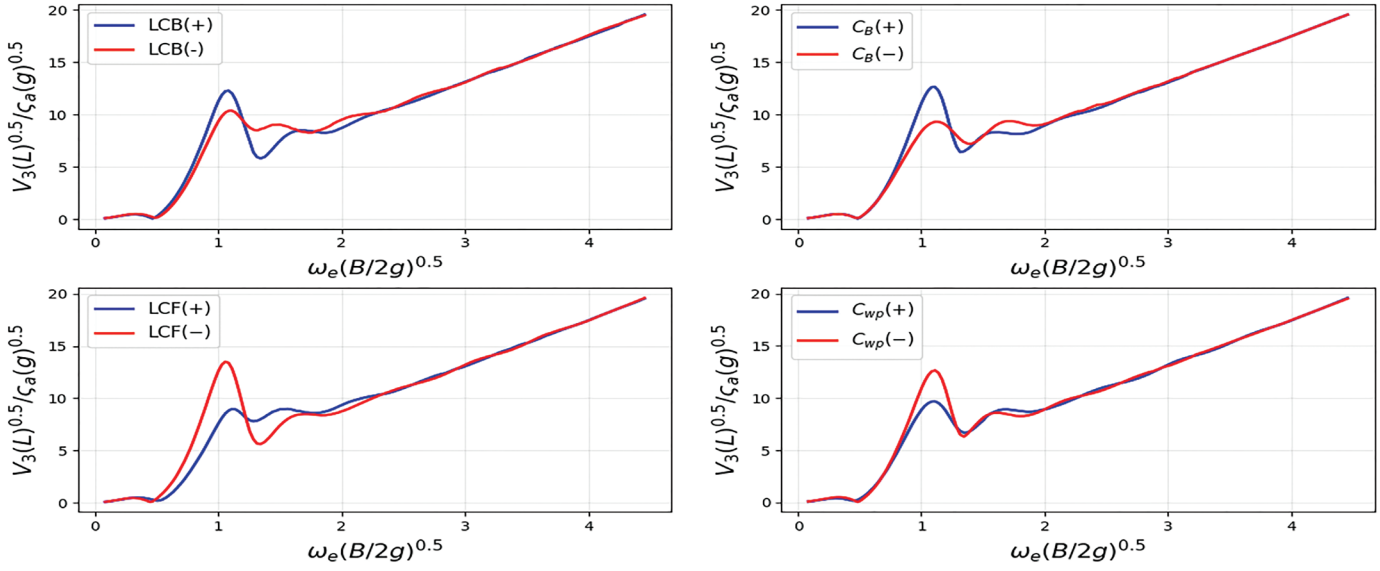


Figure 10. Relative vertical velocity amplitude at point P for all hull form variants.

sensitivity trends are expected to be less affected by these non-linear corrections.

The vessel was modeled as a rigid body, and hydroelastic effects were not considered. In addition, no dedicated experimental measurements or high-fidelity CFD simulations were performed for validation. While the adopted hydrodynamic framework is well established for preliminary seakeeping assessment, further validation through model testing or non-linear time-domain CFD analyses would improve the representation of impact phenomena.

The present analysis considered only heave and pitch motions, consistent with head-sea conditions. Surge, roll, and yaw were neglected under the assumption of symmetric wave encounter. However, in oblique or quartering seas, roll-pitch coupling and asymmetric bow immersion may influence slamming occurrence and severity. The inclusion of additional degrees of freedom in future time-domain analyses could provide a more comprehensive assessment of motion-impact interaction effects.

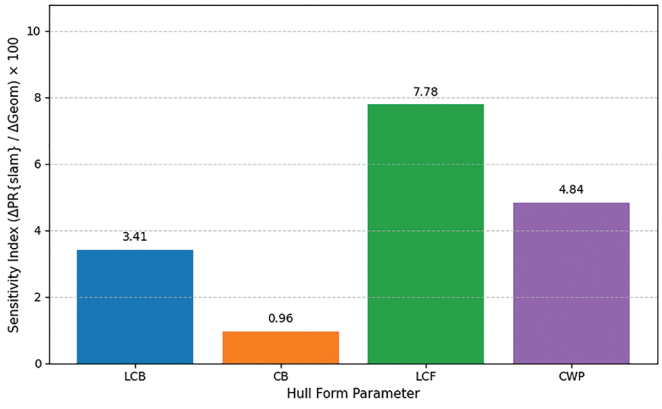


Figure 11. Sensitivity index (ΔPR{slam}/ΔGeom) for each hull form parameter.

The slamming assessment was restricted to a single longitudinal location (Point P at 10% L_{PP} from the forward perpendicular). Although this position is situated within the bow impact region typically adopted for preliminary slamming evaluations, slamming susceptibility may vary along the forward body depending on local flare geometry and entrance shape. A distributed longitudinal assessment considering multiple sections could reveal spatial sensitivity variations and further refine the interpretation of local impact risk.

Despite these limitations, the methodology remains suitable for comparative parametric studies aimed at identifying the relative sensitivity of hull form parameters to slamming susceptibility in early-stage design.

6. Conclusion

This study investigated the influence of key hull form parameters on the slamming susceptibility of a ship based on the hull geometry of the Friesland-class frigate, considering operation in a region near the southern tip of South America. This area is known for severe sea states, making it an ideal setting for evaluating slamming behavior under extreme wave conditions. By systematically varying *LCB*, C_B, *LCF*, and C_{WP}, eight extreme hull configurations were generated and analyzed. The assessment considered hydrodynamic coefficients, motion responses in waves, and a probabilistic evaluation of slamming based on long-term sea statistics.

Among the tested parameters, *LCF* and C_{WP}, which relate to the waterplane area, exhibited the strongest influence on slamming probability. An increase in these coefficients reduced the likelihood of bow immersion and thus slamming events. In contrast, volume-related parameters, particularly the block coefficient (C_B), had lower influence on the predicted slamming incidence. Notably, C_B exhibited the smallest variation in slamming probability, despite inducing the largest geometric modification among all parameters.

Table 3. Geometric variation, slamming probability, and sensitivity index for each hull form parameter.

Variant	PR{slam} (%)	Events/hour	ΔGeom (%)	ΔPR{slam} (%)	Sensitivity index (ΔPR/ΔGeom×100)
Baseline	1.03	19	-	-	-
LCB (+)	1.36	25	14.09	0.48	3.42
LCB (-)	0.88	17			
C_B (+)	1.33	25	64.80	0.62	0.96
C_B (-)	0.71	13			
LCF (+)	0.44	9	18.39	1.43	7.79
LCF (-)	1.87	34			
C_{WP} (+)	0.77	14	11.58	0.56	4.87
C_{WP} (-)	1.33	25			

This finding is particularly relevant for preliminary design. Since C_B greatly affects global ship geometry and displacement characteristics, its limited impact on slamming response suggests that it is the least suitable parameter to be used in optimizing hull form solely to mitigate slamming. From a design standpoint, the results support the use of targeted variations in *LCF* and C_{WP} as more effective and less intrusive strategies to control slamming. The introduction of a non-dimensional sensitivity index proved useful in quantifying how geometric changes translate into changes in slamming behavior, assisting early-stage design decisions.

As previously discussed, the adopted linear frequency-domain framework does not explicitly resolve non-linear impact phenomena. Nevertheless, for the purpose of comparative parametric assessment in the preliminary design stage, the methodology proved adequate in identifying relative slamming susceptibility trends among the investigated hull configurations. Further refinement through non-linear or high-fidelity approaches may enhance impact load prediction in future studies.

Footnotes

Financial Disclosure: The author declared that this study received no financial support.

NOMENCLATURE

$A(\omega)$	Added mass matrix
B	Beam at the waterline
$B(\omega)$	Radiation damping matrix
C_B	Block coefficient
C	Hydrostatic restoring matrix
CG	Center of Gravity
C_{WP}	Waterplane area coefficient
$F(\omega)$	Wave excitation force vector
$H_{1/3}$	Significant wave height
LCB	Longitudinal center of buoyancy
LCF	Longitudinal center of flotation
L_{PP}	Length between perpendiculars
S_η	Motion response spectrum
T	Draft
T_1	Mean wave period
T_{2S}	Mean encounter period
V_{CR}	Critical reentry velocity
m_0	Zeroth-order spectral moment
r	Relative displacement
s	Absolute displacement
v	Relative velocity
η	Motion response vector
ζ_a	Wave amplitude
ϕ	Velocity potential
ω	Encounter frequency

7. References

[1] G. K. Kapsenberg, “Finding the hull form for given seakeeping characteristics,” MARIN, Wageningen, the Netherlands, 2005.

[2] N. K. Bales, “Optimizing the seakeeping performance of destroyer type hulls,” in *Proceedings of the 13th ONR Symposium on Naval Hydrodynamics*, Tokyo, Japan, 1980.

[3] A. R. Lloyd, *Seakeeping: ship behaviour in rough weather*. Chichester, UK: Ellis Horwood Ltd., 1989.

[4] F. C. Belga, “Seakeeping optimization of a fast displacement catamaran on the basis of strip theory codes,” Master’s thesis, Instituto Superior Técnico, Lisbon, Portugal, 2017.

[5] M. L. Hakim, A. Firdaus, G. M. Ahadyanti, and T. Yulianto, “Comparative analysis of slamming phenomenon prediction between U and V hulls using strip theory method,” *Kapal: Jurnal Ilmu Pengetahuan dan Teknologi Kelautan,* vol. 19, no. 3, pp. 122-132, Oct 2022.

[6] X. Liao, Z. Chen, H. Gui, and M. Du, “CFD prediction of ship seakeeping and slamming behaviors of a trimaran in oblique regular waves,” *Journal of Marine Science and Engineering,* vol. 9, no. 10, p. 1151, Oct 2021.

[7] J. S. Gerritsma and W. E. Smith, “Full scale destroyer motion measurements,” *Journal of Ship Research,* vol. 11, no. 1, pp. 1-27, 1967.

[8] M. O. Predes, "Parametric analysis involving variations of form coefficients in slamming," Master's thesis, Federal University of Rio de Janeiro, Rio de Janeiro, Brazil, 2020. Available at: https://pantheon.ufrj.br/handle/11422/23176.

[9] M. O. Predes. "A simple combined method for parametric generation of ship hull variants," *Journal of Naval Architecture and Marine Technology*, vol. 227, pp. 52-63, 2025.

[10] N. T. Salvesen, E. O. Tuck, and O. M. Faltinsen, “Ship motions and sea loads,” *SNAME Transactions*, 1970.

[11] M. K. Ochi, “Prediction of occurrence and severity of ship slamming at sea”, in Proceedings of the 5th Symposium Naval Hydrodynamics, 1964.

[12] M. K. Ochi, and L. E. Motter, “A method to estimate slamming characteristics for ship design,” *Marine Technology,* vol. 8, 1971.

RESEARCH ARTICLE

DOI: 10.54926/jnamt.2026.2538

J Nav Architect Mar Technol 2026;228:43-54

Modal Decomposition on the Emergence of High Mean Lift Regimes in 2-DOF Cylinder Forced Motions

Erdem Aktosun

İzmir Katip Çelebi University Faculty of Naval Architecture and Maritime, Department of Shipbuilding and Ocean Engineering, İzmir, Türkiye

To cite this article: E. Aktosun. Modal decomposition on the emergence of high mean lift regimes in 2-DOF cylinder forced motions. *J Nav Architect Mar Technol*. 2026;228:43-54.

Received: 17.12.2025 - **Revision Requested:** 21.01.2026 - **Last Revision Received:** 12.02.2026 - **Accepted:** 04.04.2026 - **Publication Date:** 20.05.2026

Abstract

This study investigates the wake dynamics and mechanisms of mean-lift generation in the two degrees of freedom forced motion of a circular cylinder subjected to combined in-line and cross-flow oscillations. A comprehensive experimental database of 9555 force measurements and 819 Digital Particle Image Velocimetry cases was analyzed using Proper Orthogonal Decomposition. The results show that, under certain motion conditions, a significant mean-lift coefficient arises, which is comparable in magnitude to the oscillatory component. Modal decomposition reveals that while low-mean-lift cases are dominated by two modes that capture approximately 50% of the total flow energy in the first two subspaces, high-mean-lift regimes show increased modal energy dispersion, where the first two subspaces account for approximately 35% of the energy and require three dominant modes for accurate wake reconstruction. These results provide a new physical understanding of coupled forced motion interactions and a foundation for data-driven modeling of high mean-lift regimes in offshore systems.

Keywords: 2-DOF forced motion, POD, wake asymmetry, mean lift coefficient, fluid-structure interactions

1. Introduction

Slender cylindrical structures such as marine risers, subsea pipelines, and mooring lines are critical components of offshore oil, gas, and renewable energy systems. These structures are subjected to ocean currents that trigger complex fluid-structure interactions (FSIs). A primary concern is vortex-induced vibration (VIV), which arises from periodic vortex shedding in the wake of a bluff body. VIV can result in large oscillatory motions, significantly increasing fatigue damage and compromising structural integrity [1-3]. Over recent decades, researchers have focused on predicting VIV, specifically regarding cross-flow and in-line oscillatory responses.

These oscillatory behaviors have several implications. Operationally, they can restrict serviceability and, in severe cases, cause structural failure through accumulated fatigue damage. For offshore structures, VIV impacts are amplified by the combination of harsh environmental conditions and high structural slenderness. Therefore, accurate VIV prediction and modeling are critical for the safe design and reliable operation of deep-water risers, mooring systems, and related infrastructure.

VIV dynamics are nonlinear because the flow strongly interacts with the structural motion. This interaction becomes more complex when motion occurs in both the cross-flow and in-line directions. While earlier works mainly focused

Address for Correspondence: İzmir Katip Çelebi University Faculty of Naval Architecture and Maritime, Department of Shipbuilding and Ocean Engineering, İzmir, Türkiye

E-mail: erdem.aktosun@ikcu.edu.tr

ORCID ID: orcid.org/0000-0002-7391-4060

Copyright© 2026 The Author(s). Published by Galenos Publishing House on behalf of UCTEA Turkish Chamber of Naval Architects and Marine Engineers. Licensed under a Creative Commons Attribution-NonCommercial-NoDerivatives 4.0 (CC BY-NC-ND) International License

on one degree of freedom (1-DOF) motion [4], real offshore structures undergo multiple degrees of freedom vibrations. Therefore, 2-DOF systems have shown a more accurate approach to predict VIV [5]. Including in-line motion complicates the vortex shedding process, significantly changing wake patterns and hydrodynamic forces. Studies show that in-line motion shifts the vortex shedding phase and transforms wake structures, sometimes eliminating vortex modes observed in purely transverse oscillations.

An experimental study investigated VIV in elastically mounted cylinders within low-Reynolds-number uniform flows, identifying various wake modes [4]. These modes depend strongly on oscillation amplitude and wavelength. Later experiments by Morse and Williamson [6] expanded this understanding by exploring a wide parameter space of motion frequencies and amplitudes at higher Reynolds numbers. They observed a transitional vortex mode characterized by two vortex pairs per shedding cycle, where the second pair is weaker than the first. This work highlighted the necessity of mapping vortex modes and hydrodynamic forces across diverse motion conditions to fully capture VIV complexity.

When in-line motion is combined with cross-flow oscillations, additional wake modes emerge. Research by Morse and Williamson [7] showed that harmonic in-line motion significantly alters wake structures during transverse oscillation. Free vibration studies [8] confirmed these results and identified complex vortex patterns typically associated with large cross-flow amplitudes in low-mass ratio systems. The complexity increases when the cylinder follows the figure-eight trajectories inherent in 2-DOF free vibrations. Experiments by Aronsen [9] and subsequent computational studies by [10,11] revealed that clockwise and counter-clockwise trajectories produce different wake asymmetries. These results indicate that combined motions are not a simple superposition of independent effects but represent a fundamentally coupled nonlinear system.

Understanding these complex wake dynamics is important for fatigue life estimation and structural integrity assessments. However, modeling VIV in long flexible structures remains challenging due to nonlinear FSIs and varying Reynolds numbers. While direct numerical and large-eddy simulations provide fundamental insights, their application to full-scale structures is computationally demanding. Therefore, semi-empirical approaches, which couple simplified structural models with experimentally derived hydrodynamic coefficients, have emerged as a practical engineering alternative.

Research by Chaplin et al. [12] showed that semi-empirical models using experimental force data can predict cross-flow motions in long flexible structures more reliably than high-resolution simulations under certain conditions. However, [13-15] noted that hydrodynamic forces during combined cross-flow and in-line motion differ significantly from those during 1-DOF oscillations. These results emphasize the necessity of dedicated experimental datasets capturing the coupled nature of VIV. Constructing such databases is challenging due to the vast parameter space required, including variations in amplitude ratio, frequency ratio, phase difference, and trajectory pattern.

Recent studies have shown significant mean lift forces during certain forced combined motions [16]. These forces can be comparable in magnitude to oscillatory lift, suggesting a clear asymmetry in the wake structure. Such asymmetry has important implications for long, flexible structures, potentially leading to mean deflections or kiting perpendicular to the flow. These phenomena present a new challenge in understanding the physics governing asymmetric wake formation. Identifying the conditions that trigger these large mean lift forces and correlating them with specific wake modes remains a critical research question with considerable practical relevance.

To address the complexity of wake dynamics in combined motion systems, advanced data-driven methods have been employed to extract dominant flow features and characterize the time evolution of vortical structures. Among these, Proper Orthogonal Decomposition (POD) has emerged as a powerful technique for analyzing large experimental and computational datasets. POD decomposes flow fields into orthogonal modes ranked by energy content, providing a systematic way to identify the structures most critical to the overall dynamics. Unlike traditional phase-averaging techniques, which assume periodicity and require phase alignment, POD captures both coherent and intermittent features. This makes it particularly suitable for analyzing the nonlinear and potentially chaotic wake patterns in combined-motion VIV [17].

Previous studies [17-20] have utilized POD and related modal decomposition techniques to identify the dominant flow structures associated with different wake modes and to correlate these modes with the structural responses of a circular cylinder undergoing VIV. Similarly, [21] applied POD to analyze the nonlinear responses of flexible cylinders exhibiting hysteresis and mode transitions. These works highlight POD's potential not only as a diagnostic tool but also as a foundation for developing reduced-order models (ROMs) for predictive purposes.

In the context of large mean forces and asymmetric wakes, POD offers a promising approach for identifying the spatial modes responsible for asymmetry and linking them to

specific motion parameters. Decomposing the flow field to examine the contribution of individual modes to mean lift generation clarifies how combined cross-flow and in-line motions produce wake asymmetry. Such insights are essential for advancing semi-empirical models to include mean force effects and for improving the resolution of VIV prediction frameworks.

While previous studies [16,22,23] provided extensive force mappings, a fundamental research gap remains regarding the physical modal interactions that trigger sustained wake asymmetry**.** This study fills that gap by using POD to isolate the specific coherent structures responsible for high mean-lift generation, which were not detailed in the earlier studies. A mean lift coefficient map was created from the database [22] to explore the complex dynamics of combined in-line and cross-flow vibrations of a circular cylinder under forced motion. In this study, the primary objective is to isolate the coherent structures responsible for the transition between low and high mean-lift regimes. By applying POD to representative cases, we characterize the phase-dependent vortex shedding that triggers the kiting effect, a phenomenon in which sustained hydrodynamic lift causes significant mean structural deflection. This focused analysis provides the physical understandings necessary to bridge the gap between observed force responses and predictive modeling for 2-DOF VIV systems.

2. Materials and Methods

2.1. Flow Visualization Experiment

Experiments were conducted in the flow tank at the University of Rhode Island's Ocean Engineering Department [24]. The tank measures 1.05 m by 0.75 m by 2.80 m and can generate flow speeds up to 1.3 m/s. A test cylinder was mounted on a force sensor and secured to an aluminum frame spanning the tank width for stability, positioned 3.5 mm above the bottom to avoid tip vortices. Wake structures were recorded using a Phantom V10 high-speed camera at 250 Hz with 2400×540-pixel resolution and a lateral green laser sheet mounted on a motorized frame, shown in Figure 1. The carbon cylinder had a diameter of 3.85 cm, a submerged span of 57.25 cm, and a mass of 0.268 kg. Tests were performed at a Reynolds number of 7620 under prescribed sinusoidal cross-flow and in-line motions (Equation 1).

$$y = \frac{A_y}{D}\sin(\omega t) \;\&\; x = \frac{A_x}{D}\sin(2\omega t + \theta) \qquad (1)$$

Where y and x are normalized motions, $A_y^* = A_y/D$ and $A_x^* = A_x/D$ are the cross-flow and in-line amplitudes ω, is the motion frequency and, θ is the phase difference between cross-flow and in-line motions.

A Phantom V10 high-speed camera and a laser system were employed for Digital Particle Image Velocimetry (DPIV) measurements to capture the wake dynamics around the test cylinder. The initially collimated laser beam was converted into a thin sheet using optical elements, allowing planar illumination of multiple particles simultaneously. This laser sheet was carefully positioned within the fluid to illuminate the region of interest for flow visualization. Motion parameters were systematically varied during the experiments: in-line oscillation amplitude ranged from 0.1 to 0.3, cross-flow amplitude from 0.1 to 1.6, reduced velocity from 5 to 7, and phase angle from -180° to 180° in 30° increments. A total of 819 test cases were performed, forming a comprehensive experimental database. Variations in phase angle produced distinct orbital trajectories of the cylinder, with θ=0° corresponding to a counter-clockwise figure-eight path, consistent with previous studies [16,22,24].

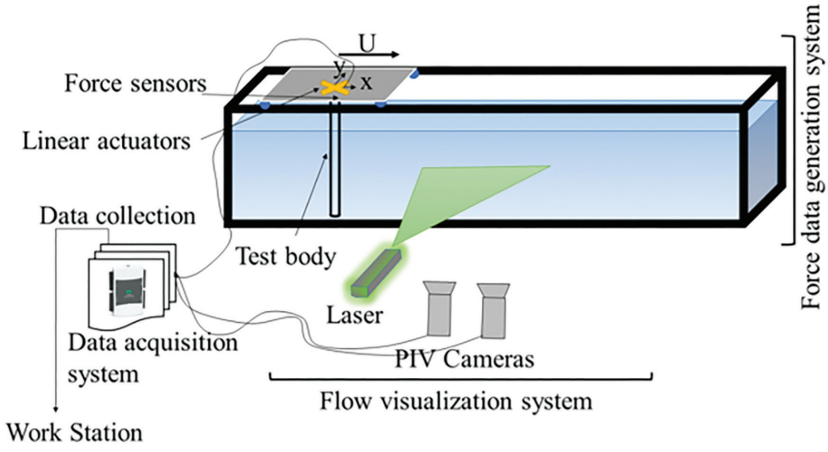


Figure 1. Schematic of the experimental setup at the flow tank, showing the integrated force data generation system (linear actuators and force sensors) and the flow visualization system (PIV cameras and laser sheet orientation)

PIV: Particle Image Velocimetry

2.2. Modal Decomposition Method

Vortex patterns behind an oscillating circular cylinder were investigated using flow visualization experiments and POD analysis, as explained in [23]. By varying motion parameters and applying the POD analysis based on the formulation in [23], the study identified and correlated wake structures with experimental data to improve the prediction of vortex behavior and enhance the understanding of FSIs. The modal decomposition approach, following [23], was used to analyze wake patterns associated with both low and high mean lift forces, as identified from a comprehensive force and wake database [16,22,24]. In this approach, let us consider that the function $\Gamma(X,t)$ denotes the vorticity field as a function of both spatial position X along the spanwise direction and time, t. The temporal evolution of this quantity can be described through a modal representation in which the flow field is expressed as a linear combination of orthogonal spatial modes. Mathematically, this can be formulated as (Equation 2):

$$\Gamma(X,t) \approx \sum_{k=1}^{N} a_k(t)\,\Phi_k(X) \qquad (2)$$

In this formulation, $\Phi_k(X)$ corresponds to the spatial structure (or shape function) of the k^{th} mode, while $a_k(t)$ represents its associated time-dependent coefficient or amplitude. The index enumerates the modes, and defines the number of modes retained in the modal expansion. This decomposition provides a compact representation of the system's dynamics by isolating dominant flow patterns from the full data field.

To obtain these modal structures from empirical or simulated flow data, Singular Value Decomposition (SVD) can be applied to the vorticity matrix $\Gamma(X,t)$. The decomposition takes the following canonical form: $\Gamma(X,t) = U\Sigma V^{T}$. Here, U is an orthogonal matrix of dimension MxM containing the spatial modes, commonly referred to as Proper Orthogonal Modes (POMs). The matrix $V(NxN)$ encodes the temporal evolution of the corresponding modes, while $\Sigma(MxN)$ is a diagonal matrix whose elements, the singular values σ_i, quantify the energy contribution of each mode to the overall dynamics.

Through this POD framework, the original high-dimensional dataset can be approximated using only a subset of modes that capture the most energetic flow features. The data can thus be reconstructed with reduced dimensionality by retaining the leading singular values, such that $r < N$. The resulting truncated representation preserves the dominant physical characteristics of the system while significantly reducing computational cost.

The accuracy and physical relevance of this ROM depend strongly on the singular value spectrum in Σ. Each singular value reflects the portion of total kinetic or vorticity energy contained within its associated mode. The fractional energy contribution of the k^{th} mode can therefore be defined as (Equation 3):

$$E_k = \frac{\sigma_k}{\sum_{i=1}^{N}\sigma_i} \qquad (3)$$

This energy ratio provides a quantitative measure of the significance of each mode in describing the system's overall motion. Typically, only a small number of dominant modes are required to capture the essential dynamics, while higher-order modes primarily represent small-scale or noise-like structures.

The POD was implemented using the snapshot method via SVD on a dataset of 793 DPIV realizations. To isolate fluctuating coherent structures, the vorticity field was first centered by subtracting the ensemble mean from each snapshot. The spatial domain consisted of a 142x111 grid, with a sampling frequency of 250 Hz. To ensure spectral accuracy, a Hamming window was applied to the modal coefficients to minimize spectral leakage during frequency estimation. Finally, the POD reconstruction served as a physics-based filter; by retaining only the dominant modes and discarding higher-order ones, high-frequency experimental noise was removed while preserving the physically significant vortex dynamics.

The selection of dominant POD modes is based on cumulative energy contribution. In low mean-lift regimes, the first two subspaces capture approximately 50% of the total fluctuation energy, representing periodic shedding. For high mean-lift cases, a third mode is included (approximately 35% for two subspaces) to accurately reconstruct the biased vortex formation. Modes beyond the third represent incoherent noise and were excluded to focus on the large-scale structures driving mean-lift forces.

3. Results and Discussion

This section presents the flow visualization and POD results for wake structures behind a circular cylinder undergoing combined motions under low and high mean lift force conditions. The objective is to identify dominant flow features and correlate motion parameters with wake asymmetry and vortex dynamics. By systematically varying amplitudes, reduced velocity, and phase, large mean lift forces were observed at specific parameters. POD allows the decomposition of complex vorticity fields into energy-ranked spatial modes, facilitating a clear observation of dominant coherent structures. The following sections discuss wake pattern evolution, the energetic contribution of leading modes, and their relationship to asymmetric flow features.

Analysis of the decomposed hydrodynamic forces reveals several notable characteristics of the coupled motion. A key

finding is the significant variability of the effective cross-flow added mass coefficient across the tested parameters, aligning with results for freely vibrating cylinders [16]. In contrast, the in-line added mass coefficient remains relatively stable at low motion amplitudes typical of free vibration. For most cases, this coefficient is negative and nearly constant. These results suggest that variations in the effective natural frequency of systems undergoing simultaneous oscillations are primarily driven by the cross-flow component rather than the in-line response [16,22].

Considering excitation forces in phase with cylinder velocity provides further insights into in-line motion. While excitation in 1-DOF transverse systems is characterized by the velocity-aligned force component, this simplification is insufficient for coupled systems. Because energy is exchanged dynamically between in-line and cross-flow components, the total energy transfer must be considered. Therefore, a total power coefficient was introduced based on the combined forces in phase with both motion directions [24,25]. Results show that in-line motion expands the region of positive energy transfer from the fluid to the structure, thereby enhancing oscillation amplitudes. This aligns with free-vibration studies where coupled motion amplifies the system's dynamic response.

3.1. High Mean-Lift regimes in 2-DOF Forced Motions

It is well established that VIV can increase the mean drag force experienced by a cylinder. However, an unexpected result from the present investigation is the appearance of a substantial mean lift coefficient under specific motion combinations. In some cases, the mean lift reaches values exceeding 1.0, comparable to the amplitude of the fluctuating lift coefficient observed during certain oscillations. Figure 2 presents contour maps of the mean lift coefficient for two selected in-line motion amplitudes of 0.2 and 0.5 when cross-flow amplitude is fixed at 0.35. These plots illustrate the influence of reduced velocity (radial coordinate) and the phase difference between motions (angular coordinate). The results demonstrate that large mean lift coefficients emerge only due to the cylinder's forced motion, indicating significant wake asymmetry. Although asymmetric wakes occur under purely cross-flow forcing [4], the magnitudes observed here suggest that such asymmetry could induce substantial mean lift on elongated or flexible structures. Detailed wake visualizations for high-mean-lift cases are presented below to further explore this phenomenon.

To investigate these dynamics, we compared the wake structures of two distinct cases: one with a low mean lift force and another with a high mean lift force. POD was then applied to analyze the modal decomposition of each wake. This analysis revealed that high mean lift cases show significantly more complex and disorganized wake topologies than low mean lift cases.

Figures 3 and 4 present the wake structures behind the cylinder for selected low and high mean lift conditions. In Figure 3 (low mean lift), the wake exhibits a highly coherent vortex shedding pattern, maintaining periodicity and structural integrity several diameters downstream. Correspondingly, the time histories of non-dimensional lift and drag forces show periodic oscillations with stable amplitudes and frequencies. The presence of a small, nonzero mean lift component suggests a weak but persistent wake asymmetry that remains stable throughout the observation period.

In contrast, Figure 4 shows a flow field with a more complex and messier vortex formation in the wake. The vorticity contours indicate a breakdown of symmetry with vortex cores appearing diffuse and occasionally merging as they move downstream. Such irregularities and complexities are accompanied by stronger fluctuations in both lift and drag force with potential evidence of amplitude modulation and phase shift. The variation in the mean lift level and sign between Figures 3 and 4 implies that the existing wake asymmetry may have reversed or altered due to differences in the initial conditions or the phase relationship between in-line and cross-flow motion. This interpretation aligns with observations from previous studies that report small variations in reduced velocity or phase can lead to distinct asymmetric wake states characterized by opposite signs of mean lift [26,27].

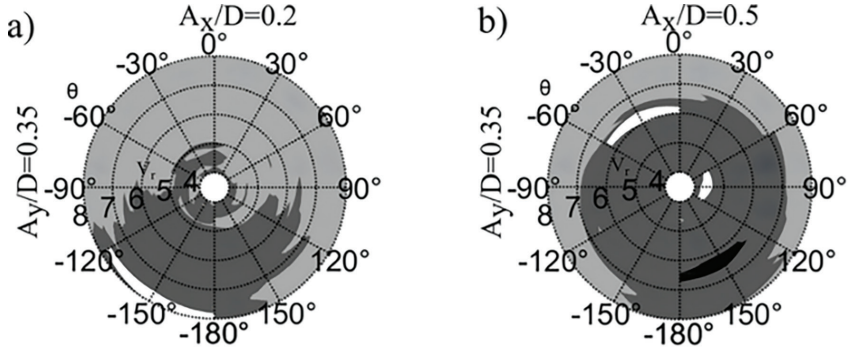


Figure 2. Contour maps of the mean lift coefficient as a function of reduced velocity and phase angle for two cases: (a) Small in-line amplitude (A_y/D=0.35, A_x/D =0.2) and (b) High in-line amplitude (A_y/D=0.35, A_x/D=0.5). The color scale highlights are high mean lift regimes at specific phases.

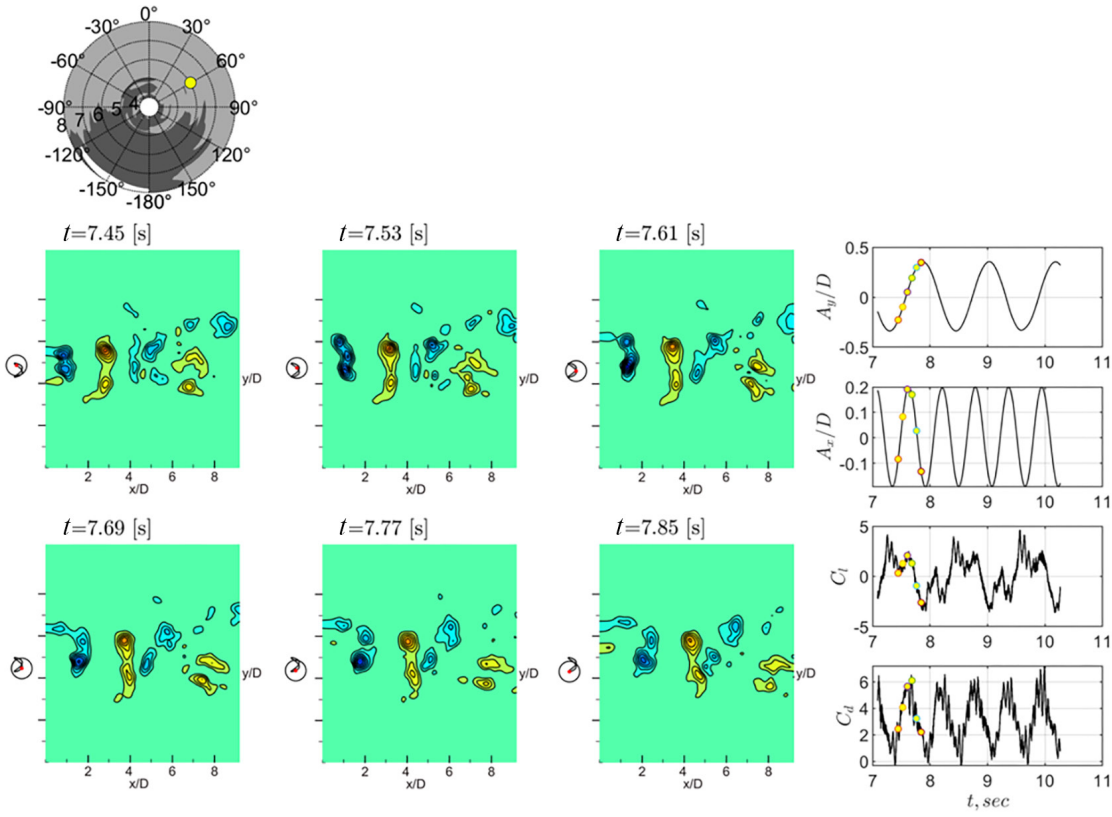


Figure 3. Flow visualization and force response for a low mean-lift case (A_y/D=0.35, A_x/D=0.2, V_r=6, and θ=60°). The panels show instantaneous vorticity across one cycle highlighting clear vortex shedding pattern.

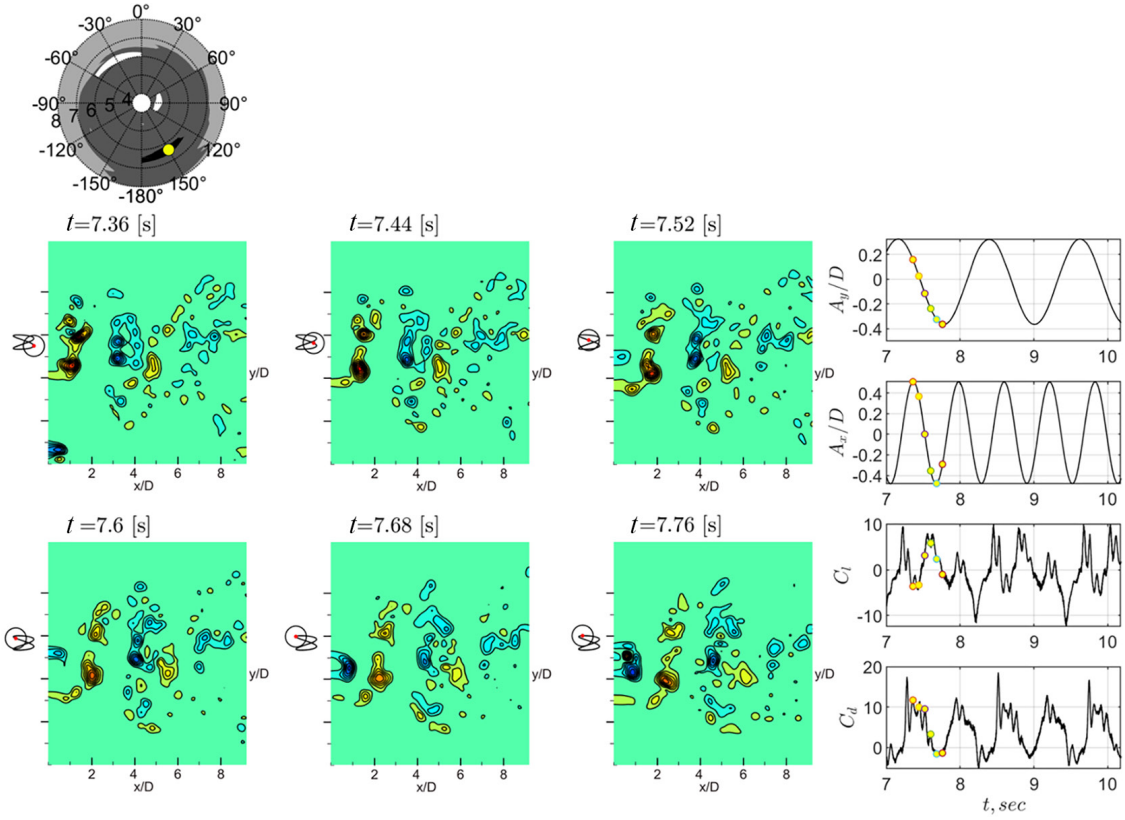


Figure 4. Flow visualization and force response for a high mean-lift case (A_y/D=0.35, A_x/D=0.5, V_r=6.4, and θ=150°). The broken symmetry in the vortex formation leads to a substantial mean lift component comparable to the oscillatory amplitude.

3.2. Modal Decomposition Results

Two representative cases were selected from the forced VIV database to evaluate POD's capability in capturing coherent structures at different mean lift levels. The low-mean lift is defined by $A_y/D = 0.35$, $A_x/D = 0.2$, $V_r = 6$, and $\theta = 60°$, while the high-mean lift is characterized by $A_y/D = 0.35$, $A_x/D = 0.5$, $V_r = 6.4$, and $\theta = 150°$. Analysis focused on the first two dominant subspaces, with particular emphasis on the primary mode. A third case with larger in-line motion and moderate variations in reduced velocity and phase was also examined; however, significant noise and nonlinear FSIs made the identification of a dominant mode uncertain. This suggests that further investigation is required to better resolve the complex coupling and improve modal decomposition accuracy.

Figure 5a presents the POD analysis for twelve modes under the low mean lift condition. The first two POMs exhibit well-defined, coherent spatial structures that capture approximately 50% of the total energy, indicating a dominant and repeatable wake pattern. Conversely, POM3 through POM6 display distinct characteristics, representing secondary flow features. Beyond these six modes, the spatial structures become progressively disorganized, suggesting that higher-order subspaces primarily represent small-scale fluctuations rather than coherent dynamics. Importantly, the POMs must be viewed alongside their temporal coefficients to fully reveal the underlying evolution of these structures.

Furthermore, Figure 5b reveals another energy grouping encompassing subspaces 3 through 6. Examination of their corresponding POMs, Proper Orthogonal Coefficients, and Proper Orthogonal Values indicates that these modes share comparable spatial and temporal behavior, implying that their combination forms a secondary coherent mode representing a distinct wake pattern. Modes beyond the sixth subspace exhibit no clear structure and are therefore interpreted as noise or residual turbulence in the wake.Although twelve subspace dimensions (six modes) are presented for completeness, the analysis indicates that only two distinct coherent wake patterns exist, with one clearly dominating the overall flow dynamics.

Figure 6 analyzes the high mean lift regime where the wake shows increased complexity. The energy distribution (Figure 6b) indicates that a third mode is necessary to represent the enhanced asymmetry, with the he first two subspaces capturing approximately 35% of the total energy. The first two POMs share similar temporal evolutions and frequency components (Figures 6c and 6d), signifying that their combination represents the primary vortex-shedding mode. This dominant frequency aligns with the wake dynamics observed in the vorticity contours (Figure 6a). Conversely, modes beyond the third mode show no discernible patterns and likely contribute to observed wake noise. Higher-order modes (subspaces>6) exhibit irregular spatial structures and minimal energy, representing small-scale turbulence or residual irregularities. Their fluctuating temporal behavior and broad frequency spectra confirm that these modes capture high-frequency, low-energy disturbances rather than coherent shedding.

Figure 7 compares raw DPIV vorticity fields (left) with POD reconstructions (right) for two distinct mean lift cases. Figure 7a represents the low mean lift condition ($A_y/D = 0.35$, $A_x/D = 0.2$, $V_r = 6$, and $\theta = 60°$), while Figure 7b captures the high mean lift condition ($A_y/D = 0.35$, $A_x/D = 0.5$, $V_r = 6.4$, and $\theta = 150°$). Instantaneous snapshots are shown at four non-dimensional times (t/T=0.2, 0.5, 0.8, 1.2), covering a full oscillation cycle. For the low mean lift case, a reconstruction using only the first two POD modes effectively captures the dominant vortices and their phase-dependent evolution, successfully filtering out fine-scale experimental noise. In contrast, the high mean lift case exhibits a more complex, asymmetric wake with intense vortex interactions. Here, a three-mode reconstruction is required to accurately reproduce the dominant vortex cores and their deformation while significantly reducing the random fluctuations visible in the raw DPIV data.

Quantitative comparisons reveal that the high mean-lift regime is defined by a distinct shift in modal energy and spectral power. While low-lift cases are dominated by symmetric shedding captured by the first two modes, the high-lift case requires a three-mode reconstruction, as the first two subspaces account for only approximately 35% of the cumulative energy required to resolve wake asymmetry. Specifically, the energy contribution of Mode 3 increases significantly in high-lift cases, representing the physical spatial bias or "kiting" of the wake. Furthermore, spectral analysis shows that the peak power magnitude of these primary modes is substantially higher in the high-lift regime. This confirms that increased mean lift results from more energetic, phase-locked coherent structures rather than a simple spatial displacement of the wake.

The transition to wake asymmetry is quantitatively evidenced by the emergence of a high mean lift coefficient that reaches values exceeding 1.0, effectively matching the magnitude of the oscillatory lift component. POD analysis further quantifies this behavior through modal energy distribution: while low-mean-lift cases are characterized by two dominant energetic modes that capture over 50% of the total flow energy, high-mean-lift regimes exhibit increased modal energy dispersion where the two subspaces account for approximately 35% of the total energy and require three dominant modes for accurate wake reconstruction.

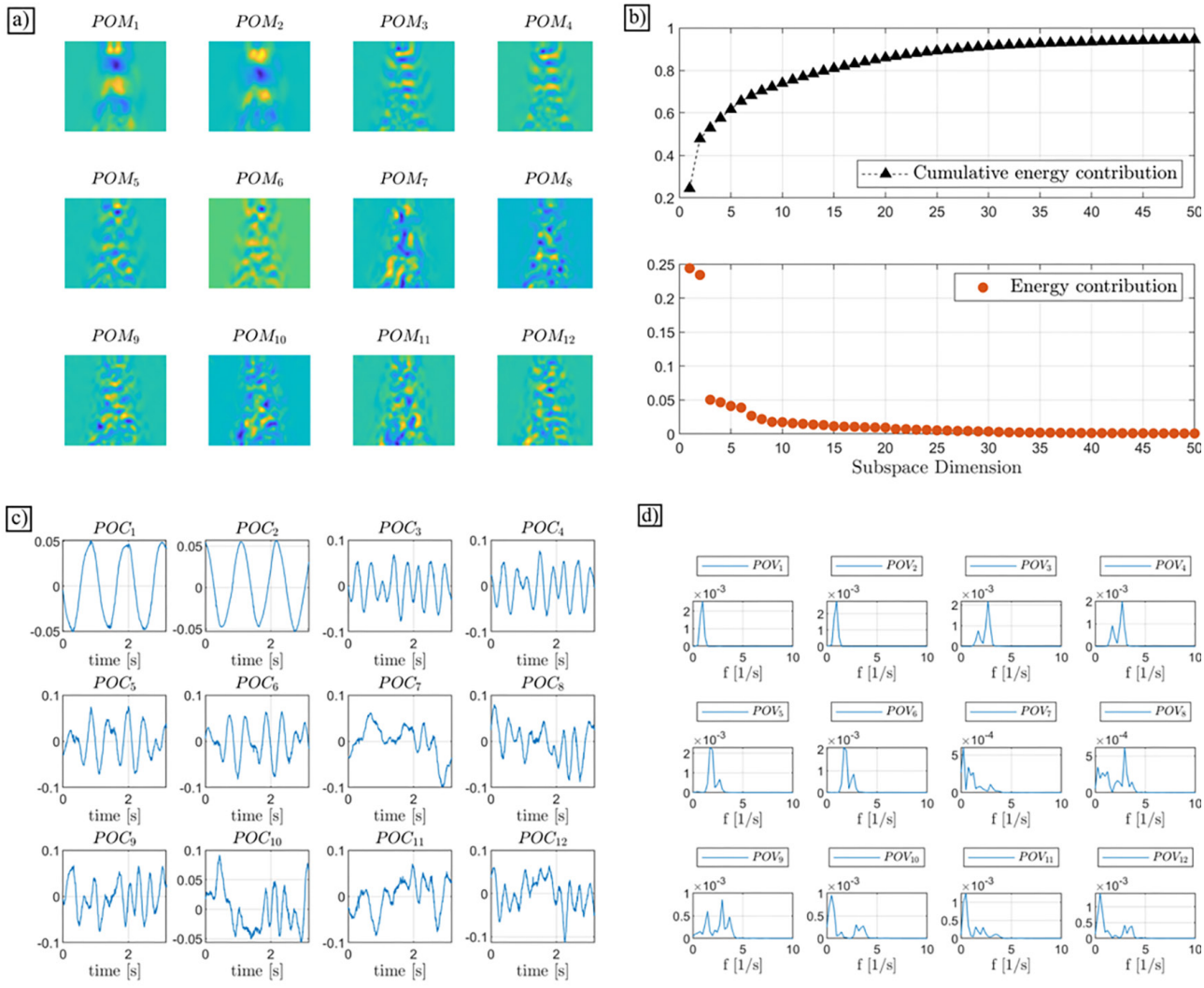


Figure 5. POD analysis for the low mean-lift case (A_y/D=0.35, A_x/D=0.2, V_r=6, θ=60°): (**a**) The first 12 spatial modes (POMs), (**b**) cumulative energy showing that the first two modes dominate, (**c**) temporal coefficients (POCs), and (**d**) frequency spectra (POVs) of the leading modes.

3.3. Discussion

This study shows that 2-DOF forced-motion VIV experiments provide a more comprehensive and physically representative description of FSI than traditional 1-DOF models. Building on the foundational force and wake database of [16,23], this study uniquely implements POD to systematically isolate the coherent structures responsible for mean-lift generation. Unlike traditional phase-averaging methods used in previous studies, our POD-based approach enables the identification of specific energetic modes that drive wake asymmetry even in the presence of experimental noise. While prior studies have established fundamental wake modes through 1-DOF studies [7,28] or sparser 2-DOF measurements [14,15], this study was based on a high-resolution 2-DOF experimental database. Specifically, we expanded the parameter space to include 9555 force measurements and 819 DPIV cases. This density of data allows for the first comprehensive mapping of the high-mean-lift regime, which remained largely unresolved in lower-resolution datasets.

Comparisons with previously reported free-vibration and forced-motion results show strong agreement in wake branches and hydrodynamic force trends [8,13,15,22]. In particular, the broad variation observed in the cross-flow added mass coefficient is consistent with free-vibration studies [13], confirming the reliability of the measurements. More significantly, the present results clearly identify a high mean lift regime, where the mean lift coefficient reaches values comparable to the oscillatory lift component for specific combinations of motion parameters. Flow visualization and POD analysis indicate that this regime is associated with persistent wake asymmetry, consistent with earlier observations in [16].

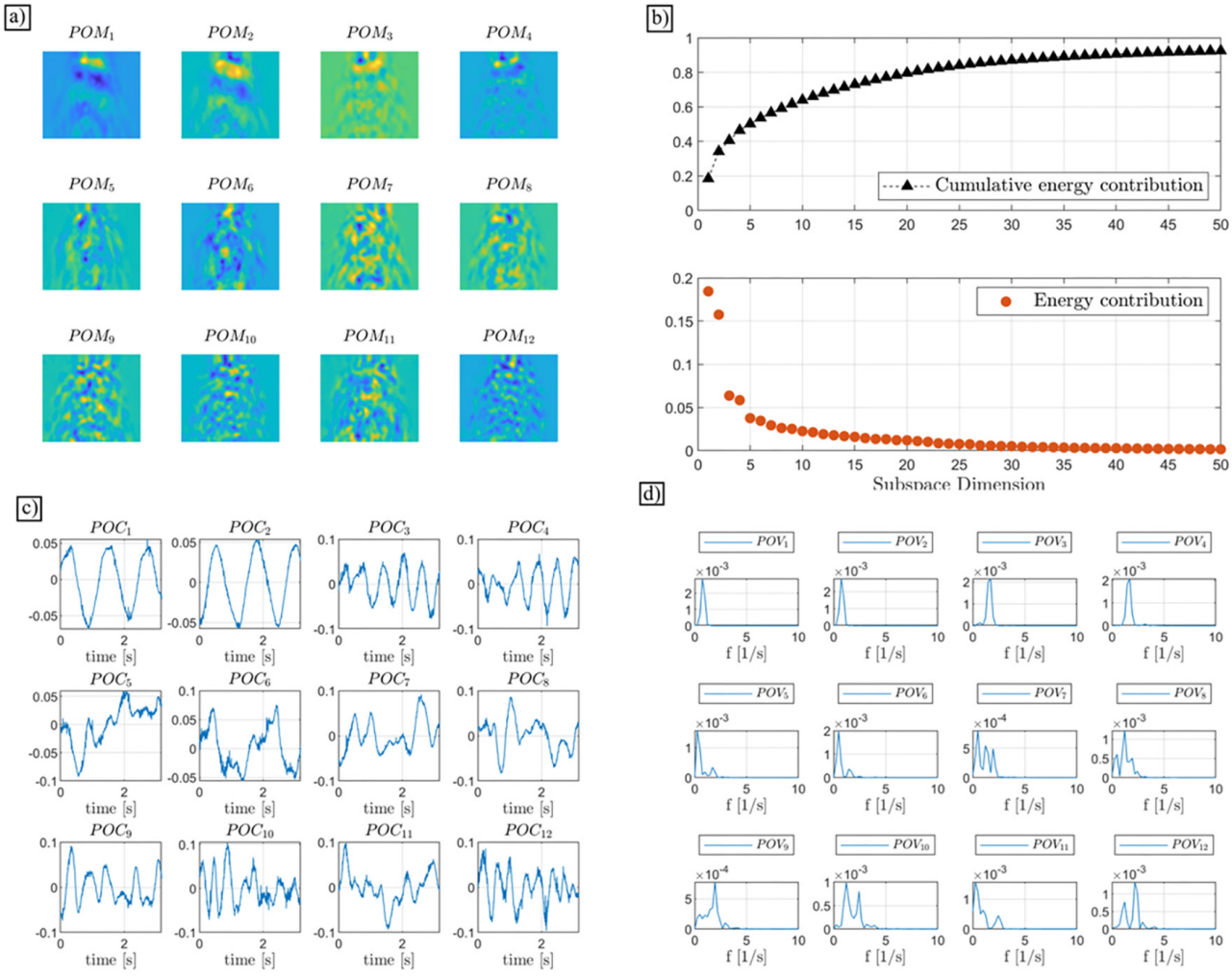


Figure 6. POD analysis for the high mean-lift case (A_y/D=0.35, A_x/D=0.5, V_r=6.4, θ=150°): Increased complexity in the spatial modes and higher energy dispersion across the spectrum compared to the low-lift regime.

Modal decomposition shows that low mean lift cases are dominated by two energetic POD modes, corresponding to relatively symmetric and periodic wake structures. In contrast, high mean lift cases require three dominant modes to accurately reconstruct the wake, reflecting increased asymmetry and nonlinear vortex interactions. Despite this complexity, POD effectively captures the dominant coherent structures while filtering noise, as demonstrated by the reconstructed wake fields.

The presence of sustained mean lift forces has important implications for offshore risers and slender marine structures, potentially leading to kiting-like behavior even for bare cylinders [16]. While the present experiments were conducted at a constant Reynolds number [8,29], Reynolds number effects remain an important limitation, as wake asymmetry and force characteristics may vary significantly [30-32]. This study utilized a constant Reynolds number to align with previous benchmarks. However, Reynolds number is a critical parameter that may influence the high mean-lift regions identified in this database. It remains an open question how varying Reynolds number affects the boundaries of these regions or the underlying vortex formation in the wake. Specifically, higher Reynolds numbers could modify the wake asymmetry that drives these forces. While our results provide a fundamental map of the mean-lift regime, testing at higher Reynolds number is necessary to determine if these 'kiting' forces persist or evolve in the conditions with varying Reynolds numbers typical of full-scale offshore applications.

The presence of a strong mean lift force implies a significant and persistent asymmetry in the wake. While such asymmetries have been observed for forced cross-flow motion [6], the lift magnitudes measured here are comparable to coefficients associated with true lifting

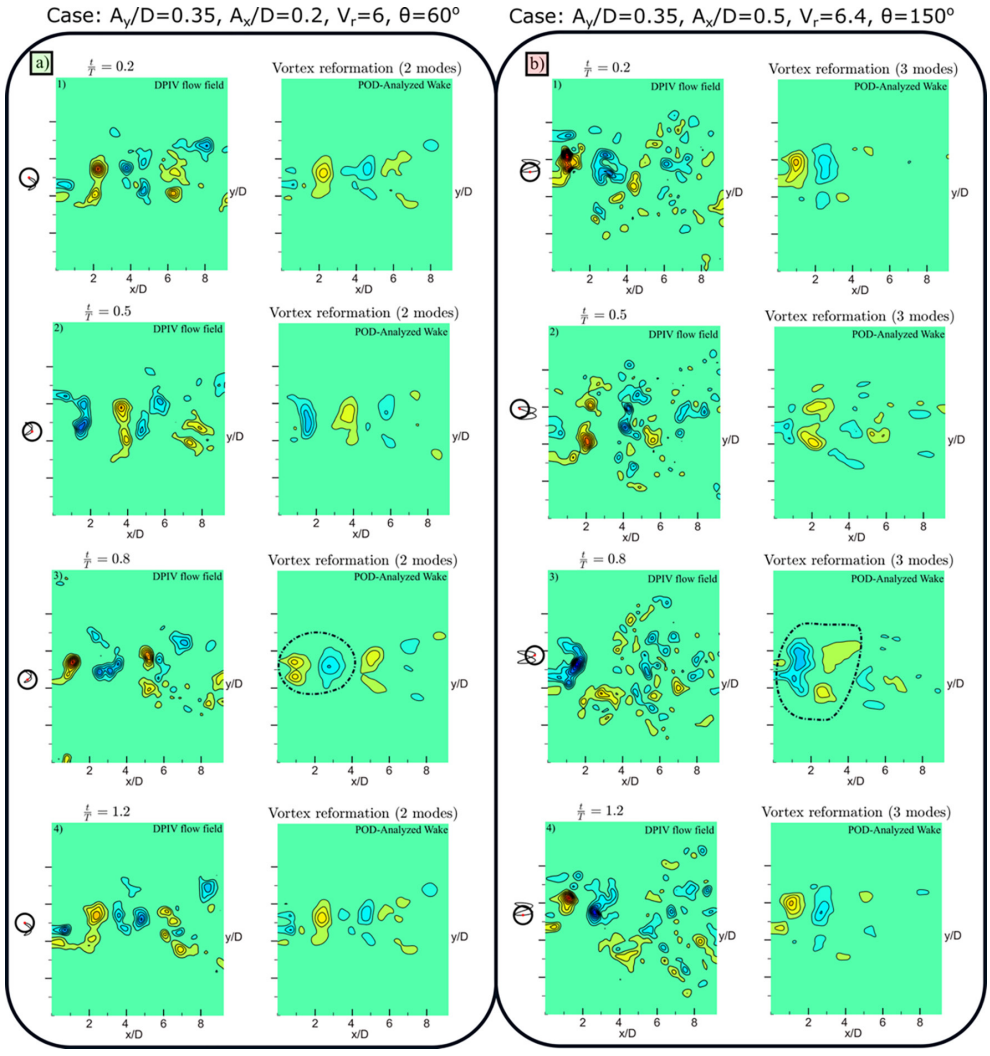


Figure 7. **a**) Comparative snapshots of raw DPIV vorticity and POD reconstructions at non-dimensional times. **a**) Reconstruction using 2 modes for low mean lift; (**b**) Reconstruction using 3 modes for high mean lift, illustrating how POD captures the essential asymmetric wake structures while filtering experimental noise.

surfaces. Importantly, this mechanism defines the mean lift region within our database. We observed that the mean lift does not switch signs when experiments are repeated [16], suggesting that the specific asymmetry is a stable feature of the forming wake structure. Furthermore, experiments with similar motion parameters exhibit consistent behaviors, where a significant mean lift of a specific sign is observed across multiple cases. On long, slender structures like marine risers, this hydrodynamic state can lead to "kiting" or mean deflections perpendicular to the flow. In the case of a riser undergoing VIV, these motion conditions would result in a side deflection dependent on the structural stiffness, making the characterization of this asymmetric regime critical for predicting the equilibrium of flexible structures.

Future numerical investigations [33], combined with data-driven approaches such as Artificial Neural Network-based force modeling [25,34] and complementary modal techniques including D Dynamic Mode Decomposition (DMD) [35] and Smooth Orthogonal Decomposition (SOD) [21,36] offer promising pathways to generalize these results and enhance predictive VIV frameworks.

4. Conclusion

This study presents a detailed modal decomposition analysis of wake structures generated by a circular cylinder undergoing 2-DOF forced motion in uniform flow. Using an extensive DPIV experimental database, POD effectively identifies the dominant coherent modes responsible for wake asymmetry and high mean lift generation. The analysis shows that cases with high mean lift show complex, asymmetric vortex interactions and increased modal energy dispersion, whereas low mean-lift conditions are

characterized by clear and symmetric wake patterns. The results confirm that the emergence of large mean lift forces is closely associated with complexity and nonlinear coupling between in-line and cross-flow motions. By reconstructing wake fields using a limited number of energetic modes, the study highlights POD's capability as a robust diagnostic tool for noise reduction and ROM of complex VIV flows. These results advance the physical understanding of asymmetric wake dynamics and provide a valuable experimental basis for improving predictive models in offshore engineering applications, including flexible risers, cables, and tethered systems operating in oscillatory flow environments.

Footnotes

Financial Disclosure: The author declared that this study received no financial support.

References

[1] C. H. K. Williamson, and R. Govardhan, "Vortex-induced vibrations," *Annual Review of Fluid Mechanics,* vol. 36, no. 1, pp. 413-455, Jan 2004.

[2] T. Sarpkaya, "Vortex-induced oscillations: a selective review," *Journal of Applied Mechanics,* vol. 46, no. 2, pp. 241-258, Jun 1979.

[3] M. S. Triantafyllou, R. Bourguet, J. Dahl, and Y. Modarres-Sadeghi, "Vortex-induced vibrations," in *Springer Handbook of Ocean Engineering*, Cham: Springer International Publishing, 2016, pp. 819-850.

[4] C. H. K. Williamson, and A. Roshko, "Vortex formation in the wake of an oscillating cylinder," *Journal of Fluids and Structures,* vol. 2, no. 4, pp. 355-381, Jul 1988.

[5] P. W. Bearman, "Understanding and predicting vortex-induced vibrations," *Journal of Fluid Mechanics,* vol. 634, pp. 1-4, Aug 2009.

[6] T. L. Morse, and C. H. K. Williamson, "Prediction of vortex-induced vibration response by employing controlled motion," *Journal of Fluid Mechanics,* vol. 634, pp. 5-39, Sep 2009.

[7] T. L. Morse and C. H. K. Williamson, "Fluid forcing, wake modes, and transitions for a cylinder undergoing controlled oscillations," *Journal of Fluids and Structures,* vol. 25, no. 4, pp. 697-712, May 2009.

[8] N. Jauvtis, and C. H. K. Williamson, "The effect of two degrees of freedom on vortex-induced vibration at low mass and damping," *Journal of Fluid Mechanics*, vol. 509, pp. 23-62, Jun 2004.

[9] K. H. Aronsen, "An experimental investigation of in-line and combined in-line and cross-flow vortex induced vibrations," Norwegian University of Science and Technologhy, 2007.

[10] S. Peppa, L. Kaiktsis, and G. S. Triantafyllou, "Numerical simulation of three-dimensional flow past a cylinder oscillating at the strouhal frequency," *Journal of Pressure Vessel Technology,* vol. 137, no. 1, 011302, Feb 2015.

[11] S. Peppa, L. Kaiktsis, and G. S. Triantafyllou, "Hydrodynamic forces and flow structures in flow past a cylinder forced to vibrate transversely and inline to a steady flow," *Journal of Offshore Mechanics and Arctic Engineering,* vol. 138, no. 1, 011803, Feb 2016.

[12] J. R. Chaplin *et al.*, "Blind predictions of laboratory measurements of vortex-induced vibrations of a tension riser," *Journal of Fluids and Structures,* vol. 21, no. 1, pp. 25-40, Nov 2005.

[13] J. M. Dahl, F. S. Hover, and M. S. Triantafyllou, "Two-degree-of-freedom vortex-induced vibrations using a force assisted apparatus," *Journal of Fluids and Structures,* vol. 22, no. 6-7, pp. 807-818, Aug 2006.

[14] J. M. Dahl, F. S. Hover, M. S. Triantafyllou, S. Dong, and G. E. Karniadakis, "Resonant Vibrations of Bluff Bodies Cause Multivortex Shedding and High Frequency Forces," *Physical Review Letters,* vol. 99, no. 14, 144503, Oct 2007.

[15] H. Zheng, J. M. Dahl, Y. Modarres-Sadeghi, and M. S. Triantafyllou, "Coupled inline-cross flow VIV hydrodynamic coefficients database," in *International Conference on Offshore Mechanics and Arctic Engineering Proceedings Series Volume 2: CFD and VIV*, Jun 2014.

[16] E. Aktosun, and J. M. Dahl, "Experimental force database from controlled in-line and cross flow cylinder motion," in *the 28th International Ocean and Polar Engineering Conference*, 2018. [Online]. Available: https://onepetro.org/ISOPEIOPEC/proceedings-abstract/ISOPE18/All-ISOPE18/ISOPE-I-18-547/20713

[17] G. Riches, R. Martinuzzi, and C. Morton, "Proper orthogonal decomposition analysis of a circular cylinder undergoing vortex-induced vibrations," *Physics of Fluids*, vol. 30, no. 10, 105103, Oct 2018.

[18] D. Deep, A. Sahasranaman, and S. Senthilkumar, "POD analysis of the wake behind a circular cylinder with splitter plate," *European Journal of Mechanics - B/Fluids*, vol. 93, pp. 1-12, May-Jun 2022.

[19] Z. Sun, D. Chen, M. Zhang, S. Zhang, and L. Zou, "The pressure mode decomposition analysis of circular cylinder under stationary and VIV conditions," *Ocean Engineering,* vol. 310, 118711, 2024.

[20] H. Jiang and S. Cao, "Balanced proper-orthogonal-decomposition-based feedback control of vortex-induced vibration," *Physical Review Fluids,* vol. 9, no. 7, 73901, Jul 2024.

[21] E. D. Gedikli, J. M. Dahl, and D. Chelidze, "Multivariate analysis of vortex-induced vibrations in a tensioned cylinder reveal nonlinear modal interactions," *Procedia Engineering*, vol. 199, pp. 546-551, 2017.

[22] E. Aktosun, E. D. Gedikli, and J. M. Dahl, "Observed wake branches from the 2-DOF forced motion of a circular cylinder in a free stream," *Journal of Fluids and Structures,* vol. 124, 104035, Jan 2024.

[23] E. Aktosun, and E. D. Gedikli, "Modal decomposition analysis of two-degree-of-freedom vortex-induced vibrations," *Paper presented at the The 34th International Ocean and Polar Engineering Conference,* Rhodes, Greece, Jun 2024.

[24] E. Aktosun, "Investigation of Vortex-Induced Vibration of a Cylinder by Employing Cross-Flow and In-Line Motion," University of Rhode Island, 2020.

[25] E. Aktosun, "Modeling fluid forces in 2-DOF forced motion experiments using neural network and analytical nonlinear approaches," *Ocean Engineering*, vol. 330, 121231, Jun 2025.

[26] A. Khalak, and C. H. . Williamson, "Motions, forces and mode transitions in vortex-induced vibrations at low mass-damping," *Journal of Fluids and Structures,* vol. 13, no. 7-8, pp. 813-851, Oct 1999.

[27] T. Sarpkaya, "A critical review of the intrinsic nature of vortex-induced vibrations," *Journal of Fluids and Structures,* vol. 19, no. 4, pp. 389-447, May 2004.

[28] R. Gopalkrishnan, "Vortex-induced forces on oscillating bluff cylinders," Massachusetts Institute of Technology, 1993.

[29] J. J. M. Dahl, "Vortex-induced vibration of a circular cylinder with combined in-line and cross-flow motion," Massachusetts Institute of Technology, 2008. [Online]. Available: https://dspace.mit.edu/handle/1721.1/44747

[30] M. Rajabi, B. Mingels, E. Aktosun, J. Dahl, and E. Gedikli, "New insights into complex vortex-induced vibrations through 3d modeling and wake response analysis," *Bulletin of the American Physical Society*, Nov 2023.

[31] B. Mingels, J. Dahl, M. Rajabi, E. Gedikli, and E. Aktosun, "Evaluating 2D and 3D VIV wake modes and forces through forced motion simulations," *Bulletin of the American Physical Society,* Nov 2023.

[32] M. Rajabi, E. Aktosun, B. Mingels, J. Dahl, and E. D. Gedikli, "2D numerical forced-motion simulations of vortex-induced vibration wakes: Toward understanding the onset of three-dimensional effects," in *4th International Naval Architecture and Maritime Symposium*, 2023.

[33] B. Mingels, E. Aktosun, and J. Dahl, "Verification of wake branch response regions observed in 2-DOF forced motion of a circular cylinder," in *APS Division of Fluid Dynamics Meeting Abstracts*, 2024, pp. X38--003.

[34] N. I. Xiros and E. Aktosun, "Stabilization of neural network models for VIV force data using decoupled, linear feedback," *Journal of Marine Science and Engineering,* vol. 10, no. 2, 272, Feb 2022.

[35] P. J. Schmid, "Dynamic mode decomposition and its variants," *Annual Review of Fluid Mechanics,* vol. 54, no. 1, pp. 225-254, Jan 2022.

[36] D. Chelidze, "Higher-order decompositions for modal identification and model order reduction," in *Nonlinear Structures & Systems, Volume 1: Proceedings of the 38th IMAC, A Conference and Exposition on Structural Dynamics 2020*, 2020, pp. 271-278.

RESEARCH ARTICLE

DOI: 10.54926/jnamt.2026.2652

J Nav Architect Mar Technol 2026;228:55-63

Numerical Investigation of Flow Characteristics Around Rudder with Sacrificial Anodes

Hasan İslam Çopuroğlu[1], Mehmet Zeki Şener[2], Emre Peşman[2], Yücel Özmen[3]

[1]Osaka Metropolitan University Graduate School of Engineering, Department of Marine System Engineering, Sakai (Osaka), Japan
[2]Karadeniz Technical University Sürmene Faculty of Marine Sciences, Department of Naval Architecture and Marine Engineering, Trabzon, Türkiye
[3]Karadeniz Technical University Faculty of Engineering, Department of Mechanical Engineering, Trabzon, Türkiye

To cite this article: H. İ. Çopuroğlu, M. Z. Şener, E. Peşman, and Y. Özmen. Numerical investigation of flow characteristics around rudder with sacrificial anodes. *J Nav Architect Mar Technol*. 2026;228:55-63.

Received: 07.07.2026 - **Revision Requested:** 22.07.2026 - **Last Revision Received:** 18.08.2026 - **Accepted:** 08.09.2026 - **Publication Date:** 30.09.2026

Abstract

Cathodic protection is a method for protecting steel structures immersed in water from electrochemical corrosion. In the maritime industry, this protection is achieved by installing zinc or magnesium galvanic anodes on the hull and underwater components of ships, such as rudders, propellers, and shafts. Although sacrificial anodes effectively prevent corrosion, their presence may alter the flow characteristics around protected components. In this study, the effects of anode shape on the hydrodynamic characteristics of a rudder with a National Advisory Committee for Aeronautics 0018 cross-section were numerically investigated. Three cases were considered: a bare rudder without an anode, a rudder fitted with a rectangular (flat bar) anode, and a rudder fitted with a semi-elliptical (disc) anode. The volumes of both anodes were kept identical for a fair comparison of their hydrodynamic effects. All cases were analyzed at a Reynolds number of 15000 and rudder angles of attack of 0°, 10°, 20°, and 30°. Three-dimensional, time-dependent numerical simulations were performed using computational fluid dynamics (CFD). The numerical methodology was validated against experimental data, and the Realizable k-ε turbulence model was selected because it showed better agreement. The numerical results were evaluated in terms of the flow lines around the rudders, pressure coefficient distributions, and lift and drag coefficients. The results indicate that the anode shape has a noticeable influence on the flow characteristics around the rudder. The rectangular anode generated larger reverse flow regions and stronger flow disturbances than the semi-elliptical anode, resulting in higher drag coefficients. In contrast, the semi-elliptical anode produced smoother pressure coefficient distributions and smaller reverse flow regions. Moreover, oscillations in both lift and drag forces became more significant at higher angles of attack, particularly at 20° and 30°, which may increase the possibility of vibration. Overall, the results suggest that semi-elliptical anodes provide more favorable hydrodynamic performance than rectangular anodes while maintaining the cathodic protection function.

Keywords: Cathodic protection, rudder hydrodynamics, CFD

1. Introduction

The surfaces of metals in contact with seawater corrode over time. This is an electrochemical corrosion process caused by the transfer of electrons. Cathodic protection is a method used to protect steel structures immersed in water from electrochemical corrosion. It can be employed for many steel structures. Today, this method is still used to prevent corrosion on the wetted surfaces of ship hulls and underwater components such as rudders, propellers, and shafts.

Address for Correspondence: Asst. Prof. Hasan İslam Çopuroğlu, Osaka Metropolitan University Graduate School of Engineering, Department of Marine System Engineering, Sakai (Osaka), Japan
E-mail: hasan.marine@omu.ac.jp
ORCID ID: orcid.org/0000-0001-5486-1277

Copyright© 2026 The Author(s). Published by Galenos Publishing House on behalf of UCTEA Turkish Chamber of Naval Architects and Marine Engineers. Licensed under a Creative Commons Attribution-NonCommercial-NoDerivatives 4.0 (CC BY-NC-ND) International License

Cathodic protection is a technology that was developed by Davy [1]. At present, this method is still utilized by placing zinc or magnesium galvanic anodes on the hull and components of ships. These anodes are bolted or welded directly to the hull or ship components. Zinc hull anodes of suitable design can provide useful current outputs for periods of eight to ten years in seawater [2]. In addition, various zinc alloys can offer unique performance in cathodic protection [3]. Furthermore, coatings can also be beneficial for protection. It has been reported that coatings provide the most effective protection when they are used in combination with an anode protection system [4].

Anodes can be classified based on their shape, size, material, mounting method, and method of securing to the surface to be protected. Anodes can have various shapes depending on their application. The selection of the shape of an anode depends on several factors, such as the shape of the surface to be protected, the availability of space, accessibility, and ease of installation. However, different anode shapes may cause different levels of resistance on the surface to be protected. Flat or block-shaped, cylindrical or semi-cylindrical, tear-drop, bracelet, and disc-shaped anodes are among the widely used anode shapes [5].

In the maritime sector, rudders are used to change the course of a ship and facilitate its manoeuvring by generating hydrodynamic forces depending on the ship's cruising speed. Parameters such as the geometric shape of the rudder section, the rudder angle, and the rudder clearance significantly affect the hydrodynamic force generated by the rudder. Therefore, it is beneficial to examine the flow around the rudder and evaluate the effects of these parameters. Nakano et al. [6] investigated the flow and noise characteristics around a National Advisory Committee for Aeronautics (NACA) 0018 airfoil at various angles of attack in an experimental study and determined that the angle of attack affects noise generation. Gim and Lee [7] experimentally observed the flow around a rudder with a NACA 0018 cross-section and a plate attached to its end and determined the effects of the attached plate on the flow. Lee et al. [8] examined the flow characteristics and pressure distributions around the rudder and stated that there is an interaction among the hull, rudder, and ship propeller. Fakorede et al. [9] studied the impact of ice accretion on the aerodynamic coefficients of a wind turbine airfoil.

However, since no anodes were used in any of these studies, the effects of the anodes on the flow around the rudder could not be observed. Rudders made of metal are among the components on which anodes are used to prevent corrosion. Since the flow around the rudder is important, the effects of anodes on the flow should be investigated.

1.1. Aim of the Study

In this study, the effects of various anode shapes on the flow around the rudder were examined. The examined rudder has a NACA 0018 cross-section. Two different anode shapes were placed on the rudder, and three cases were considered. The first case was a bare rudder without an anode. The second case was a rudder with a flat bar anode, and the third case was a rudder with a semi-elliptical (disc) anode. The turbulent water flows around these three rudders were numerically investigated using the commercial software package ANSYS FLUENT 16. The aim was to examine the effects of the anodes on the flow characteristics around the rudder for the three cases by performing three-dimensional, time-dependent numerical simulations. The results were evaluated in terms of the flow lines around the rudders, the pressure distributions on the rudder surfaces, and the lift and drag force coefficients of the rudders.

2. Numerical Study

2.1. Governing Equations

Continuity equation of three-dimensional time-dependent motion of an incompressible fluid in Cartesian coordinates can be shown as,

$$\frac{\partial u_i}{\partial x_i} = 0 \tag{1}$$

Momentum equation can be shown as,

$$\frac{\partial(\rho u_i)}{\partial t}+\frac{\partial}{\partial x_j}(\rho u_i u_j) = -\frac{\partial \rho}{\partial x_i}+\frac{\partial \rho}{\partial x_j} \left[\mu\left(\frac{\partial u_i}{\partial x_j}+\frac{\partial u_j}{\partial x_i}-\frac{2}{3}\delta_{ij}\frac{\partial u_j}{\partial x_i}\right)\right]+\frac{\partial}{\partial x_j}\left(-\rho\overline{u_i' u_j'}\right) \tag{2}$$

In this study, Smagorinsky, Realizable k-ε and Standard k-w turbulence models in FLUENT commercial package based on finite volume approach were used. The numerical results obtained from these two different turbulence models were compared with the experimental data in the literature and the sensitivity of the turbulence models were tested. Since the results obtained from Realizable k-ε turbulence model are more compatible with the experimental data, all the other solutions of the study were conducted with Realizable k-ε turbulence model. The modelled transport equations for k and ε is,

$$\frac{\partial(\rho k)}{\partial t}+\frac{\partial}{\partial x_j}(\rho k u_j) = \frac{\partial}{\partial x_j}\left[\left(\mu+\frac{\mu_t}{\sigma_k}\right)\frac{\partial k}{\partial x_j}\right]+G_k+G_b-\rho\varepsilon-Y_M+S_k \tag{3}$$

$$\frac{\partial(\rho\varepsilon)}{\partial t}+\frac{\partial}{\partial x_j}(\rho\varepsilon u_j)=\frac{\partial}{\partial x_j}\left[(\mu+\frac{\mu_t}{\sigma_\varepsilon})\frac{\partial\varepsilon}{\partial x_j}\right]+\rho C_1 S_\varepsilon-\rho C_2\frac{\varepsilon^2}{k+\sqrt{\nu\varepsilon}}+C_{1\varepsilon}\frac{\varepsilon}{k}C_{3\varepsilon}G_b+S_\varepsilon \quad (4)$$

In these equations, G_k produces turbulent kinetic energy production due to the average velocity gradient; G_b refers to turbulent kinetic energy production due to buoyancy. σ_k and σ_ε are the turbulent Prandtl numbers, S_k and S_ε are the source terms. The constants for the turbulence model are $C_{1\varepsilon}$=1.44, C_2=1.9, σ_k=1.0

2.2. Computational Domain and Boundary Conditions

The computational domain and boundary conditions are shown in Figure 1. Water was utilized as a fluid at a temperature of 15 °C. The rudder has a cross-sectional area of NACA 0018. It has a chord length of 0.1 m and a width of 0.3 m. The Reynolds number calculated according to the chord length is R_e=15000.

In this study, three cases were considered. The first case is a rudder without an anode. The second case is a rudder with a rectangular prism anode, and the third case is a rudder with a semi-elliptical anode. The volumes of the rectangular prism anode and the semi-elliptical anode are equal. The anodes are located at the transverse and longitudinal midsections of the rudder. The geometries of all cases are shown in Figure 2.

The mesh structure in the flow field was generated with increasing mesh density around the rudders, as shown in Figure 3. Calculations were conducted using different numbers of tetrahedral mesh elements to obtain mesh-independent solutions. Approximately 2.8 million mesh elements were used to achieve mesh-independent solutions. A time step of 0.001 s was used for the transient simulations, and the Courant number was maintained below 1. The SIMPLEC algorithm was employed for pressure-velocity coupling. The Least Squares Cell Based method was used for gradient calculation. The Second Order scheme was used for pressure, while the Second Order Upwind scheme was used for momentum, turbulent kinetic energy, specific dissipation rate, and energy. The first-layer height of the mesh elements around the rudder was determined according to the criterion of (y^+<2). The convergence criterion was defined as non-normalized residuals of less than 10^{-6} In addition, all cases were analyzed at four different rudder angles: 0°, 10°, 20°, and 30°.

2.3. Validation

Since validation is one of the most essential criteria in CFD analysis, a validation study was performed. Validation is necessary to ensure the reliability and accuracy of the numerical results. In this study, the validation was performed by comparing the CFD results with the experimental study conducted by Gim [10] (2013). Figure 4 shows the comparison between the numerical and experimental results. The Realizable k-ε, Standard k-ω, and Smagorinsky turbulence models were used for validation. It should be noted that the validation case has a twin-rudder configuration, whereas the present study investigates a single rudder with different anode geometries. Therefore, this validation does not directly validate the present single-rudder configuration or the hydrodynamic effects of the anodes, but provides support for the capability of the numerical methodology and turbulence model to predict the flow characteristics around a NACA 0018 rudder. It was observed that all turbulence models predicted the average velocity profiles behind the twin rudders close to the experimental data, but the Realizable *k-ε* model produced slightly better results than the Standard *k-ω* and Smagorinsky models. Therefore, the Realizable *k-ε* turbulence model was employed in all subsequent numerical simulations.

A grid independence study was conducted using different mesh densities. The grid independence assessment was performed for the 0° case, which was used to determine the mesh density for the subsequent simulations. The normalized velocity values (U/U_0) at the selected Y/C location were compared for the different mesh configurations, as shown in Figure 5. The results showed that the normalized velocity



Figure 1. Flow area and boundary conditions.

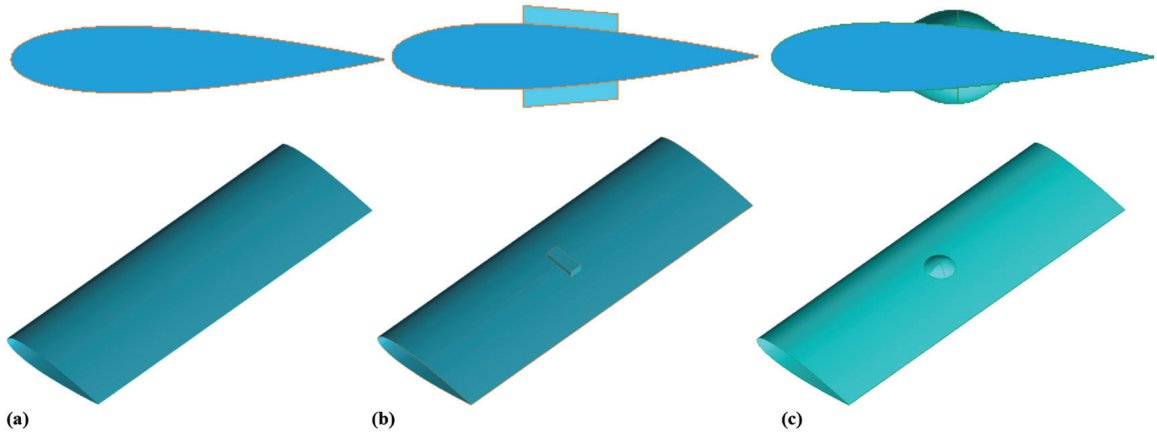


Figure 2. Rudder types: **(a)** without anode, **(b)** with rectangular anode **(c)** with semi elliptical anode.

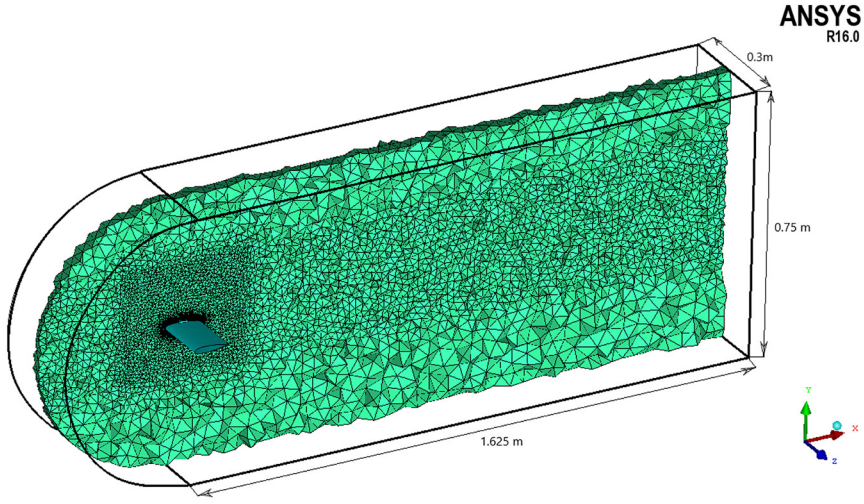


Figure 3. Numerical domain dimensions and three-dimensional mesh structure.

values became sufficiently insensitive to further mesh refinement. Therefore, the mesh consisting of approximately 2.8 million tetrahedral elements was selected for the subsequent numerical simulations.

3. Results

In this study, the effects of the rectangular and semi-elliptical anode shapes on the rudder were numerically investigated. Three-dimensional, time-dependent numerical simulations were performed for the anode and non-anode cases at different angles of attack. The results obtained from these analyses are presented as flow lines around the rudder surface, pressure coefficient distributions at the midsection of the rudder surfaces, and lift and drag coefficients of the rudders. Based on these findings, the effects of the anodes on the flow characteristics were determined for different angles of attack.

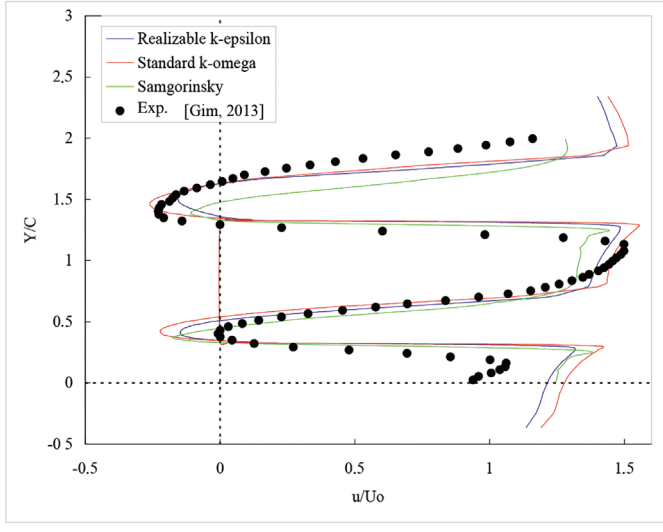


Figure 4. Average velocity profiles behind double rudders.

Figure 6 shows the flow lines around the rudder at different angles of attack. At angles of attack of 0°, 10°, and 20°, the size of the reverse flow regions formed at the midsection of the rudder increases due to the anode shape. At an angle of attack of 30°, the effect of the anode shape on the reverse flow regions becomes negligible. In addition, the cases without anodes have the smallest reverse flow regions, whereas the cases with rectangular anodes have larger reverse flow regions than the others because the sharp edges of the anodes promote flow separation. Therefore, it can be inferred that the cases with anodes exhibit more complex and larger reverse flow regions.

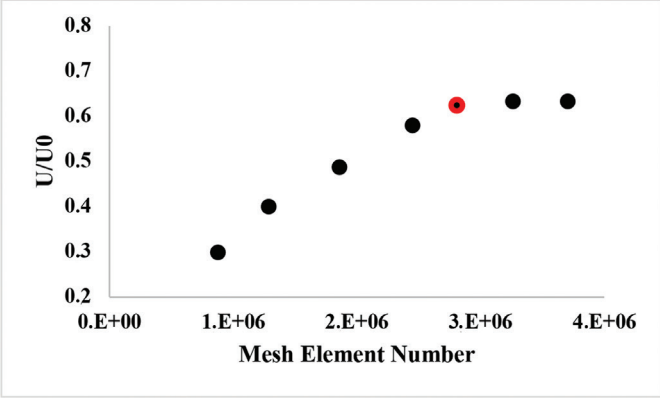


Figure 5. Grid independence study based on normalized velocity values.

When the changes in the lift and drag coefficients were examined at 0°, the lift coefficient was almost zero for all cases (Figure 7a). At an angle of attack of 10°, the highest lift coefficient was obtained for the rudder with the semi-elliptical anode (Figure 7b). At an angle of attack of 20°, it can be said that the rudder with the semi-elliptical anode and the rudder without an anode have higher lift forces than the rudder with the rectangular anode (Figure 7c). At an angle of attack of 30°, although the highest lift coefficient was obtained for the rudder with the rectangular anode, the rudder with the semi-elliptical anode and the rudder without

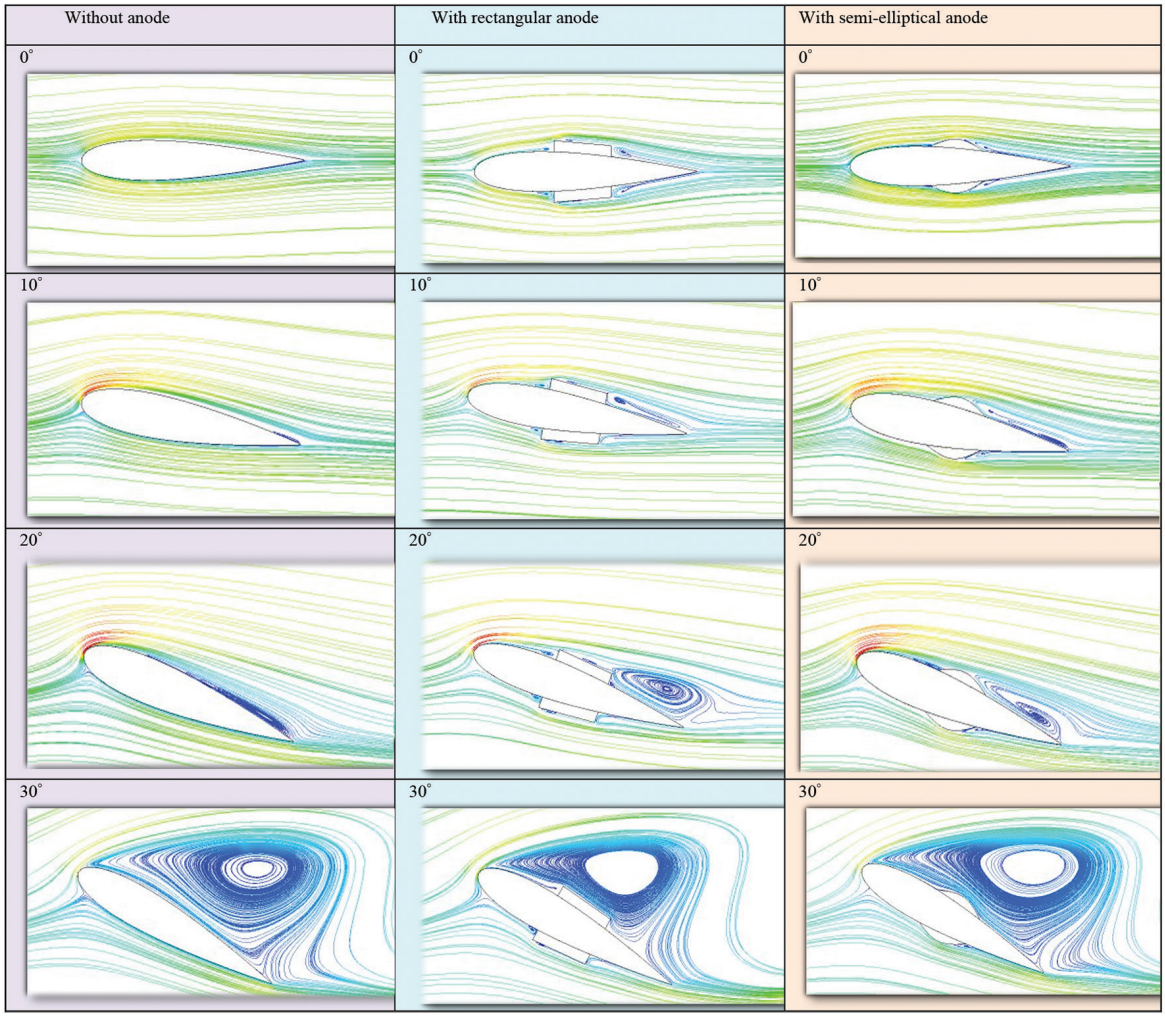


Figure 6. Velocity magnitude lines around the rudders.

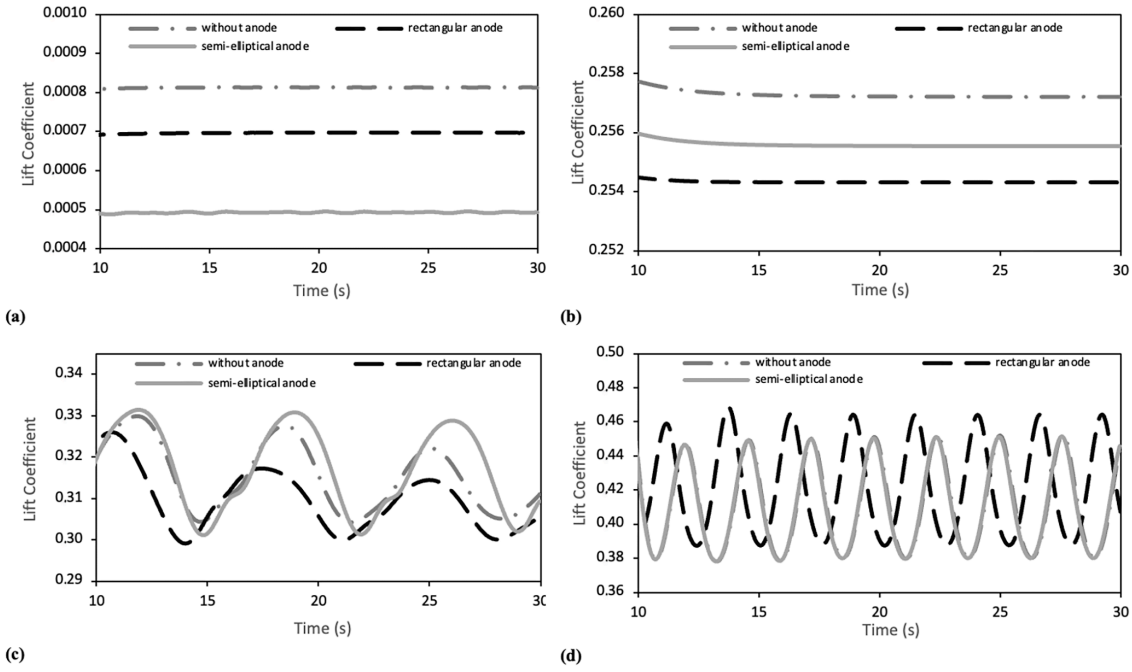


Figure 7. Lift coefficients of the various cases. **(a)** Rudder with different anode types at the angle of 0°, **(b)** rudder with different anode types at the angle of 10°, **(c)** rudder with different anode types at the angle of 20°, **(d)** rudder with different anode types at the angle of 30°.

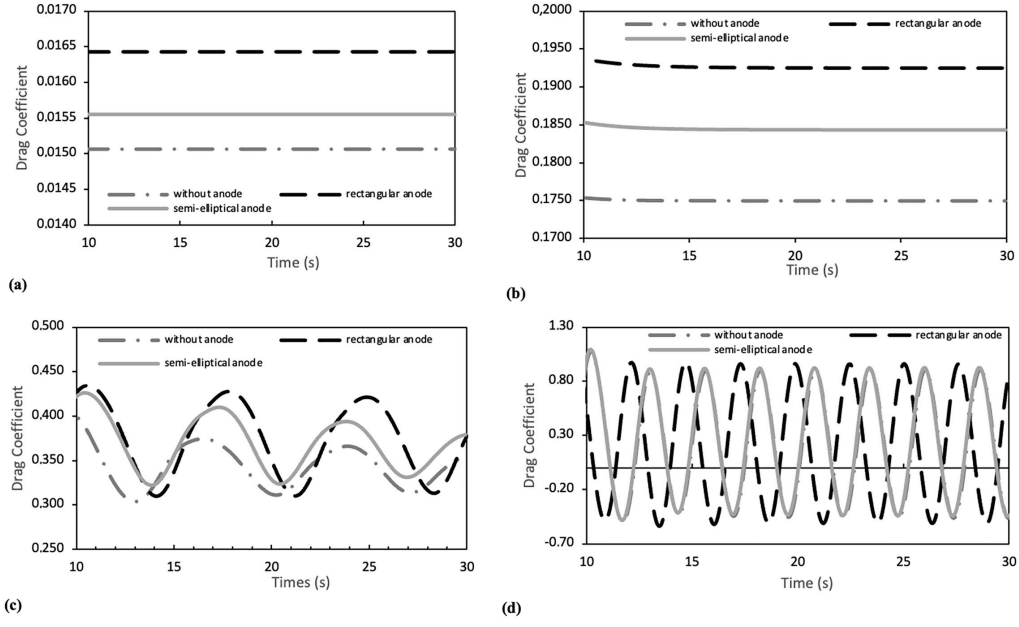


Figure 8. Drag coefficients of the various cases. **(a)** Rudder with different anode types at the angle of 0°, **(b)** rudder with different anode types at the angle of 10°, **(c)** rudder with different anode types at the angle of 20°, **(d)** rudder with different anode types at the angle of 30°.

an anode exhibited almost the same lift coefficient values (Figure 7d). On the other hand, the lift forces at angles of attack of 20° and 30° exhibited significant oscillations, which can cause vibration, an undesirable phenomenon. Furthermore, the cases at 30° exhibited a higher oscillation frequency.

The rudder with the rectangular anode exhibited the highest drag coefficient overall (Figure 8a). Since the drag force

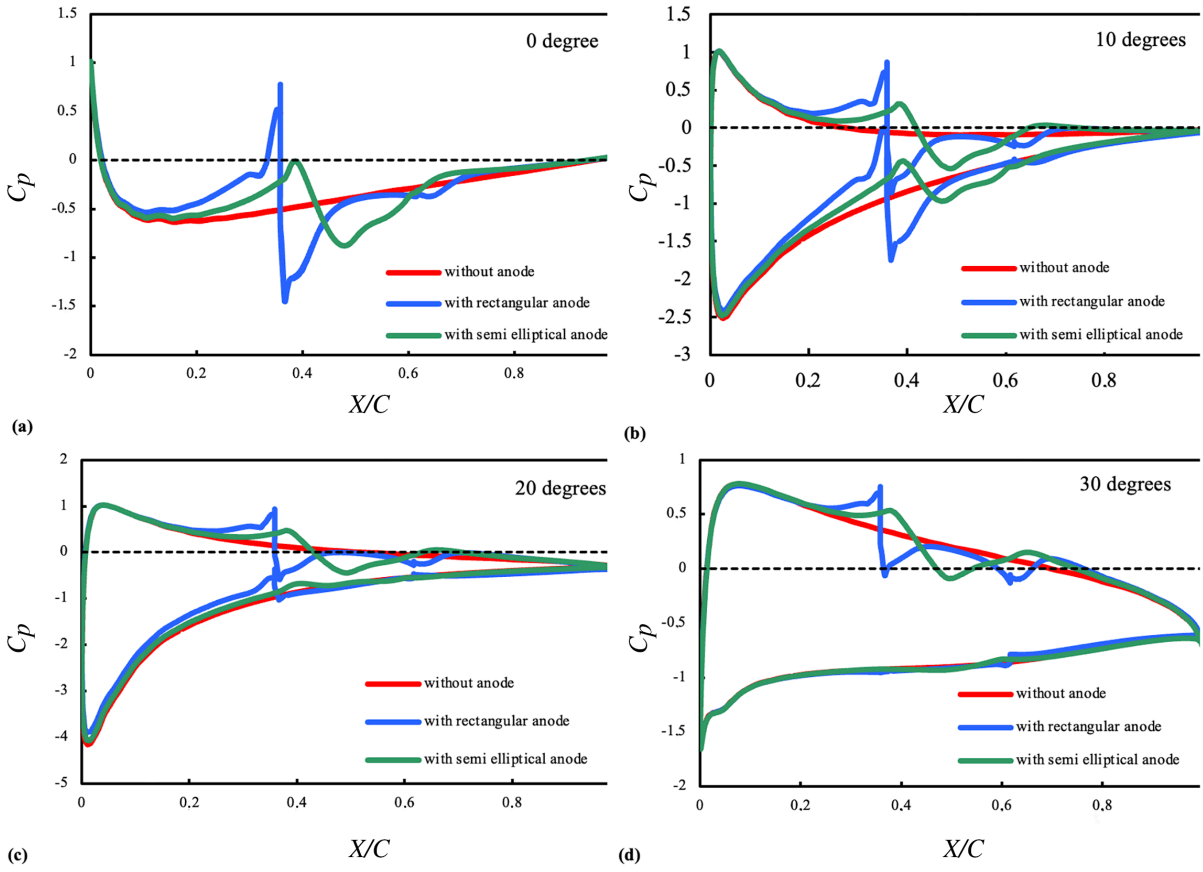


Figure 9. Pressure coefficients on the rudders' surface cases for **(a)** 0°, **(b)** 10°, **(c)** 20°, **(d)** 30°.

Table 1. Average values of the lift coefficients.

Cases	Rudder without anode	Rudder rectangular anode	Absolute difference	Percentage change	Rudder with semi-elliptical anode	Absolute difference	Percentage change
0°	0.00079	0.00067	-0.00012	-15.19%	0.00048	-0.00031	-39.24%
10°	0.25614	0.25334	-0.00280	-1.09%	0.25463	-0.00151	-0.59%
20°	0.33524	0.32284	-0.01240	-3.70%	0.33612	+0.00088	0.26%
30°	0.46737	0.47383	+0.00646	1.38%	0.46678	-0.00059	-0.13%

Table 2. Average values of the drag coefficients.

Cases	Rudder without anode	Rudder rectangular anode	Absolute difference	Percentage change	Rudder with semi-elliptical anode	Absolute difference	Percentage change
0°	0.01507	0.01643	+0.00136	9.02%	0.01555	+0.00048	2.85%
10°	0.17500	0.19261	+0.01761	10.06%	0.18447	+0.00947	5.41%
20°	0.34235	0.37298	+0.03063	8.95%	0.36906	+0.02671	7.80%
30°	0.24237	0.25425	+0.01188	4.90%	0.24860	+0.00623	2.57%

is a resistance force that increases the fuel consumption of ships, lower drag forces are beneficial for energy efficiency. In addition, similar to the lift forces, the cases at 20° and 30° exhibited oscillating drag forces, which can cause vibration of the rudder (Figure 8c, d).

These inferences can also be observed from the flow lines shown in Figure 6. The reverse flow regions are significantly larger in the cases at 20° and 30°. These flow patterns are caused by the oscillations of the drag and lift forces.

The average values of the lift and drag coefficients are presented in Tables 1 and 2. These values were obtained from the simulation results between the 10th and 30th seconds. At an angle of attack of 30°, a large and highly unsteady vortex structure develops around the rudder, with vortices separating from the tip region and being shed downstream. This vortex shedding results in strong fluctuations in the pressure distribution and consequently produces significant oscillations in the lift and drag forces. The negative instantaneous drag coefficient values observed in Figure 8d occur during these force oscillations and do not indicate a negative mean drag force. The mean drag coefficient remains positive for all three cases, as shown in Table 2. The percentage changes relative to the case without an anode are also presented. It is important to note that the drag forces increase significantly, whereas the lift forces decrease when anodes are installed. In particular, the drag force increases by up to 10% with the rectangular anode. This observation is also consistent with the findings of Fakorede et al. [9], who reported that ice accretion on wind turbine airfoils reduces the lift force and increases the drag force.

Plots of the pressure distribution are key to identifying flow separation and other adverse flow phenomena around the rudder. Therefore, these plots should be analyzed carefully, and the pressure fluctuations should be examined in detail. The pressure coefficients obtained from the midsection of the rudder are shown in Figure 9.

In the midsection of the rudder, it can be observed that a step effect occurs in the pressure coefficient distributions under the influence of the anode shape. For all cases, the pressure coefficients on most of the front surface have positive values since these surfaces are exposed to the water flow. A low-pressure region is formed on the rear surface of the rudders. Negative pressure coefficient values indicate the presence of low-pressure regions. For all cases, the differences between the (C_p) curves are caused by the anodes. It can be seen that the anodes lead to increases in both the minimum and maximum (C_p) peaks. It can also be seen that this effect is more pronounced in the case with the rectangular anode. When (X/C) is between 0.7 and 0.8, the (C_p) curves are similar for all cases, whereas the case with the semi-elliptical anode exhibits smoother curves than the case with the rectangular anode. This effect can also be observed in Figure 6. The case with the rectangular anode has larger reverse flow regions behind the anode.

4. Conclusion

This article focused on the flow patterns and forces around a NACA 0018 foil at a Reynolds number of 15000 to investigate the influence of rectangular and semi-elliptical anode shapes. It should be noted that the Reynolds number of 15000 used in the present study is considerably lower than that of full-scale ship rudder applications. Therefore, the present results should not be directly extrapolated to full-scale operating conditions. The main objective of this study was to compare the relative effects of rectangular and semi-elliptical anode geometries on the flow characteristics around the rudder under controlled conditions. Further studies at higher Reynolds numbers are required to evaluate the applicability of these findings to full-scale operating conditions. The flow around the foil at various angles of attack for a bare rudder, a rudder with a rectangular anode, and a rudder with a semi-elliptical anode was calculated using the CFD method. The observations and analyses are summarized as follows.

- The CFD method and the turbulence model used in this study showed good agreement with the experimental data in the validation study. Therefore, CFD can be used for similar problems.

- When the flow lines are examined, it can be seen that the use of anodes creates flow disturbances that affect the flow structures behind the rudder and the anodes.

- The shape of the anode is also important for the forces acting on the rudder. The lift and drag forces differ for each case, and regarding the drag force, which contributes to flow resistance, the rudder with the rectangular anode exhibits the highest drag force. Therefore, the use of sharp-edged anodes, such as rectangular anodes, is not recommended from the viewpoint of flow resistance.

- In terms of the lift force, all cases exhibit similar values. However, oscillations in the lift force can be observed after 20°. These oscillations may cause vibration, which is undesirable. In particular, the case with the rectangular anode exhibits higher peak and trough values. This indicates that the variation between the maximum and minimum lift forces is greater. Consequently, the rectangular anode may induce vibration more easily than the other anode configurations.

In general, it can be concluded that avoiding the use of sharp-edged anodes, such as rectangular anodes, may be beneficial in terms of reducing flow resistance and improving manoeuvrability. In future studies, different anode types will be investigated under various Reynolds numbers and angles of attack.

Footnotes

Authorship Contributions

Concept: H. İ. Çopuroğlu, M. Z. Şener, E. Peşman, and Y. Özmen, Design: H. İ. Çopuroğlu, M. Z. Şener, E. Peşman, and Y. Özmen, Data Collection or Processing: H. İ. Çopuroğlu, M. Z. Şener, E. Peşman, and Y. Özmen, Analysis or Interpretation: H. İ. Çopuroğlu, M. Z. Şener, E. Peşman,

and Y. Özmen, Literature Review: H. İ. Çopuroğlu, M. Z. Şener, E. Peşman, and Y. Özmen, Writing: H. İ. Çopuroğlu, M. Z. Şener, E. Peşman, and Y. Özmen.

Conflict of Interest: No conflict of interest was declared by the authors.

Financial Disclosure: The authors declared that this study received no financial support.

NOMENCLATURE

Symbol	Description
u_i	Mean velocity component in the *i*-direction
u_j	Mean velocity component in the *j*-direction
k	Turbulent kinetic energy
ε	Turbulent dissipation rate
G_k	Turbulent kinetic energy production due to the average velocity gradient
G_b	Turbulent kinetic energy production due to buoyancy
σ_k	Turbulent Prandtl number for k
σ_ε	Turbulent Prandtl number for ε
S_k	Source term for k
S_ε	Source term for ε
C_2	Model constant
C_L	Lift coefficient
C_D	Drag coefficient
C_p	Pressure coefficient
Re	Reynolds number
U_0	Freestream velocity
X/C	Normalized longitudinal position
Y/C	Normalized transverse position
y^+	Dimensionless wall distance
U_∞	Freestream velocity
Y_M	Contribution of the fluctuating dilatation in compressible turbulence

References

[1] Sir H. Davy, "Recollections of the development of my mind and character," *Philosophical Transactions of the Royal Society,* vol. 114, pp. 151-242, 1824.

[2] J. A. H. Carson, "Zinc as a self-regulating galvanic anode for ship hulls," Corrosion, vol. 16, no. 10, pp. 491t-496t, 1960.

[3] J. A. H. Carson, W. L. M. Phillips, and J. R. Wellington, "A laboratory evaluation of zinc anodes in sea water," Corrosion, vol. 16, no. 4, pp. 171t-177t, 1960.

[4] T. Tezdogan, and Y. K. Demirel, "An overview of marine corrosion protection with a focus on cathodic protection and coatings," *Brodogradnja : An International Journal of Naval Architecture and Ocean Engineering for Research and Development,* vol. 65, no. 2, pp. 49-59, Jun 2014.

[5] TheNavalArch, "*Ship corrosion: cathodic protection and sacrificial anodes*," Accessed: Jul 7, 2025. [Online]. Available: https://thenavalarch.com/ship-corrosion-cathodic-protection-sacrificial-anodes/

[6] T. Nakano, N. Fujisawa, Y. Oguma, Y. Takagi, and S. Lee, "Experimental study on flow and noise characteristics of NACA 0018 airfoil," *Journal of Wind Engineering and Industrial Aerodynamics,* vol. 95, pp. 511-531, 2007.

[7] O. S. Gim, and G. W. Lee, "Flow characteristics and tip vortex formation around a NACA 0018 foil with an endplate," *Ocean Engineering*, vol. 60, pp. 28-38, 2013.

[8] Y. G. Lee, J. W. Yu, B. H. Kang, and K. R. Pak, "A numerical study on the flow around a rudder behind low-speed full ship," *Journal of Ship and Ocean Technology*, vol. 12, no. 2, pp. 41-52, 2008.

[9] O. Fakorede, H. Ibrahim, A. Ilinca, and J. Perron, "Experimental investigation of power requirements for wind turbines electrothermal anti-icing systems," in *Wind Turbines - Design, Control and Applications*, IntechOpen, 2016.

[10] O. S. Gim, "Assessment of flow characteristics around twin rudders with various gaps using PIV analysis in uniform flow," *Ocean Engineering,* vol. 66, pp. 1-11, 2013.

RESEARCH ARTICLE

DOI: 10.54926/jnamt.2026.2653

J Nav Architect Mar Technol 2026;228:64-91

Assessing Functional Variability and Risk in Tugboat Design Using an Integrated FRAM-Fuzzy FMEA Framework

Adem Viran

General Directorate of Coastal Safety, Naval Architecture and Ocean Engineer, İstanbul, Türkiye

To cite this article: A. Viran. Assessing functional variability and risk in tugboat design using an integrated FRAM-fuzzy FMEA framework. *J Nav Architect Mar Technol.* 2026;228:64-91.

Received: 13.07.2026 - **Revision Requested:** 18.08.2026 - **Last Revision Received:** 18.09.2026 - **Accepted:** 23.09.2026 - **Publication Date:** 15.10.2026

Abstract

Tugboats are essential auxiliary vessels that play a vital role in port and offshore operations. The life cycle of tugboat involve complex couplings among hydrodynamic performance, propulsion systems, stability requirements, operational demands, production activities, regulatory compliance, and organizational coordination. Such socio-technical systems, variabilities may propagate significant technical and operational consequences. In this study, the functional resonance analysis method was applied to identify functional couplings, performance variability, and potential variability propagation throughout the tugboat design and construction lifecycle. The identified variability sources were subsequently transformed into failure modes and assessed using fuzzy failure mode and effects analysis. Expert judgments obtained from tugboat designers, shipyard managers, captains, and operators were represented through fuzzy numbers to address uncertainty in risk evaluation. fuzzy risk priority numbers were calculated based on occurrence, severity, and detection criteria. The results revealed that hull propulsion-incompatibility, propulsion system alignment deficiencies, accumulated functional resonance at ship delivery, verification shortcomings, classification compliance deficiencies, engineering team limitations, and coordination failures constitute the most critical risk areas. The findings demonstrate that risks emerge not only from isolated technical failures but also from interacting functional variabilities. The proposed framework supports proactive risk identification, prioritization, and more reliable tugboat design and construction processes.

Keywords: FRAM, fuzzy FMEA, tugboat design, functional variability, risk

1. Introduction

Ship design is a long and controlled process in which numerous technical and operational parameters are considered. Depending on different ship types, the main parameters are determined during the concept design stage, and ships are constructed through preliminary and detailed design processes [1]. In this process, identifying design-related problems before the construction stage is critical in order to prevent cost increases and schedule deviations. In this context, tugboats are special purpose marine vessels that perform various port operations, strait and canal transits, as well as rescue and assistance activities, and require high performance [2]. Compared to other ship types, tugboats stand out with their more robust hull structures, powerful main engines, and propulsion systems with advanced maneuverability capabilities; therefore, they must be designed to satisfy structural strength, appropriate service speed, sufficient bollard pull capacity, dynamic stability, and operational safety criteria [3]. Reflecting their growing operational importance, the global tugboat market was valued at approximately USD 700.2 million in 2025 and is projected to reach USD 1,114.2 million by 2034, representing an increase of approximately 60% over the 2025-2034 period [4].

Address for Correspondence: Adem Viran, Ph.D., General Directorate of Coastal Safety, Naval Architecture and Ocean Engineer, İstanbul, Türkiye
E-mail: viran@itu.edu.tr
ORCID ID: orcid.org/0000-0002-2702-3953

Copyright© 2026 The Author(s). Published by Galenos Publishing House on behalf of UCTEA Turkish Chamber of Naval Architects and Marine Engineers.
Licensed under a Creative Commons Attribution-NonCommercial-NoDerivatives 4.0 (CC BY-NC-ND) International License

Tugboat design and construction are realized as the result of a process involving complex and layered activities [5]. Therefore, the manner in which activities are generally performed throughout this process [Work-As-Done (WAD)] was defined using the Functional Resonance Analysis Method (FRAM) method, which is a Resilience Engineering (RE) approach [6]. Furthermore, in some studies, FRAM has been positioned within the Safety-II risk perspective [7]. Recently, in maritime safety studies, particularly with the RE approach, the ability of systems to adapt to changing conditions has become increasingly prominent. Rather than completely eliminating errors, this approach focuses on the system's abilities to anticipate, monitor, respond, and learn [8]. Although its importance has increased significantly in recent years, the systematic integration of the resilience approach into the tugboat design process remains limited. Existing studies in the literature mostly address accidents and root causes or operational safety separately [9], while holistic approaches evaluating technical design parameters together with system behavior have not been sufficiently developed. FRAM has a wide range of applications in the analysis of complex socio-technical systems and is used in many sectors such as aviation, healthcare, industrial operations, maritime transportation, railways, construction, oil and natural gas, information technologies, and nuclear systems [10]. In this approach, unlike traditional methods, risk analysis is addressed through the interactions and performance variability of functions in the daily operation of the system rather than through accidents and root causes [11]. The concept of functional resonance, which forms the basis of FRAM, states that variabilities among system components may combine and lead to unexpected outcomes [12]. Maritime applications of the FRAM have expanded significantly in recent years, particularly in the analysis of complex socio-technical systems involving operational variability, human interaction, and safety management. Existing studies can generally be categorized into four major thematic areas: maritime accident analysis, vessel traffic and operational management, emergency and hazardous cargo operations, and ship design and engineering applications. One major application area of FRAM is maritime accident analysis and systemic risk evaluation. Praetorius et al. [13] analyzed systemic failures through the Herald of Free Enterprise disaster, while Kee [14] compared different systemic accident-analysis techniques based on the Sewol ferry accident. Similarly, Wang et al. [15] evaluated the Eastern Star accident by comparing FRAM with other accident-analysis approaches. Studies conducted by Rammos [16] and Salihoglu and Beşikçi [17] and Ümitli et al. [18] further demonstrated the effectiveness of FRAM in identifying root causes and functional couplings in maritime accidents. Another important research area involves vessel traffic management and operational resilience. Praetorius [19] and Praetorius et al. [20] investigated Vessel Traffic Service operations using FRAM to understand variability propagation in daily maritime operations. In addition, Kulkarni et al. [21] examined waterway traffic management and maritime resilience within the Baltic Sea region. Adhita et al. [22] analyzed ship operations from a Safety-II perspective, emphasizing adaptive operational performance under variable conditions.

FRAM has also been widely applied in emergency-response processes, hazardous cargo transportation, and autonomous maritime systems. Aguilera et al. [23] evaluated oil-spill emergency-response operations, while Qiao et al. [24] investigated emergency management for hazardous cargo leakage scenarios by integrating FRAM with Bayesian approaches. Ma et al. [25] focused on hazardous chemical transportation systems, whereas Nasur et al. [26] analyzed emergency unmooring procedures for autonomous and manned ships. Furthermore, Liu et al. [27] examined resilience in Arctic ship operations, while Zhao et al. [28] evaluated post-pandemic maritime transportation resilience. Human-machine interaction and autonomous ship safety were also investigated by Zhang et al. [29]. In addition to operational applications, several studies demonstrated the applicability of FRAM in ship engineering and design-related processes. Abaei et al. [30] developed a human-error prediction approach for ship operation in harsh environments, while Smith et al. [31] modeled operational risks associated with the Exxon Valdez accident. Smith et al. [32] further demonstrated the applicability of FRAM within ship-design processes.

Fuzzy Failure Mode and Effects Analysis (Fuzzy FMEA) complements FRAM by enabling variability-induced failure modes to be prioritized under conditions of uncertainty. Compared with classical FMEA, fuzzy-based approaches provide more realistic evaluations in systems involving ambiguity and expert uncertainty [33]. In maritime applications, Fuzzy FMEA has been employed in various operational and engineering problems. Zaman et al. analyzed ship-collision risks in the Malacca Strait using AIS-based data [34], while Akyüz et al. [35] applied Fuzzy FMEA to ship inspection processes. Akyüz and Çelik [36] investigated tanker accident scenarios using interval type-2 fuzzy FMEA. Sharma et al. [37] compared conventional and fuzzy-based FMEA approaches for reliability and maintenance assessment. Fuzzy FMEA has been utilized in oil spill analysis [38], ship-originated air pollution risk assessment [39], bunkering operations [40], and petrochemical transportation systems [41]. Design-oriented applications were also reported in shipyard occupational accidents [42], offshore engineering

systems [43], yacht-system design processes [44] and ship hydraulic steering systems [45]. These studies indicate that Fuzzy FMEA is not only applicable to operational safety assessment, but also highly suitable for early-stage ship design and engineering evaluations. Tugboat construction is shaped by couplings among design decisions, production processes, shipyard capabilities, equipment installation, classification requirements, and human factors, resulting in multi-layered cause-and-effect relationships [46]. These couplings may cause functional variabilities to combine and produce unexpected performance outcomes. Therefore, tugboat design should be addressed not only through performance indicators but also through a system behavior and variability-based approach [47].

In complex and multilayered systems such as shipbuilding, where technical criteria and engineering practices are predominant, how decisions are shaped within organizational and operational processes and what risks they involve remain issues requiring clarification. Previous tugboat studies have generally focused on individual topics, such as tugboat design [5,48], towing performance [3], escort capability, maneuverability, and harbor or offshore operations [2]. However, these studies do not provide an integrated framework for evaluating the lengthy and multistage design and construction process together with operational feedback. Addressing this gap by considering the process as a whole rather than examining its stages separately constitutes the main motivation of this study. Accordingly, FRAM was selected to model tugboat design and construction decisions as coupled functions and to examine how performance variability propagates through their couplings [32]. Fuzzy FMEA risk analysis was preferred to quantify the performance variabilities of decisions related to design, construction, and operational functions. The novelty of the proposed approach lies in integrating FRAM-based functional coupling and variability propagation analysis with Fuzzy FMEA-based risk prioritization and operational feedback within a single system-level framework.

The main objectives and contributions of this study can be summarized as follows:

(i) An integrated FRAM-Fuzzy FMEA framework is proposed to represent the tugboat design and construction process, including operational feedback, as a network of coupled technical, production, regulatory, and organizational functions.

(ii) A systematic approach is developed to transform FRAM-derived functional variabilities and propagation pathways into failure modes and to quantify and prioritize their risks through fuzzy aggregation of expert severity, occurrence, and detection assessments.

(iii) The framework model is demonstrated through an actual 70-ton bollard-pull Azimuth Stern Drive (ASD) tug case involving 16 main functions, seven support functions, and 40 functional variabilities. The high-priority failure modes corresponded with major warranty-period deficiencies, supporting the practical applicability of the framework and enabling the development of targeted risk-control measures.

2. Methodology

This study combines FRAM and fuzzy FMEA to analyse functional variability and risk in tugboat design and construction. The framework was applied to an ASD tugboat project with the input of five experts from tugboat design, construction, and operation. The method consists of two phases, as shown in Figure 1. In Phase 1, 16 main and seven support functions were modelled as Work-As-Imagined (WAI). Project and operational records were then examined as WAD to identify 40 functional variabilities and their propagation paths. In Phase 2, these variabilities were converted into failure modes and evaluated using Fuzzy FMEA. The calculated fuzzy risk priority numbers (*FRPNs*) values were ranked and compared with warranty records.

2.1. System Boundary and Process Definition

The system boundary was defined to include the activities that directly influenced the design, construction, testing, and delivery of the case tugboat. It includes concept, preliminary and detail design, performance and stability analyses, physical construction, outfitting, class approval, and acceptance tests. Operational experience and warranty records were incorporated as feedback sources for identifying WAD rather than being modelled as a separate operational stage. Only activities within this boundary were considered when defining

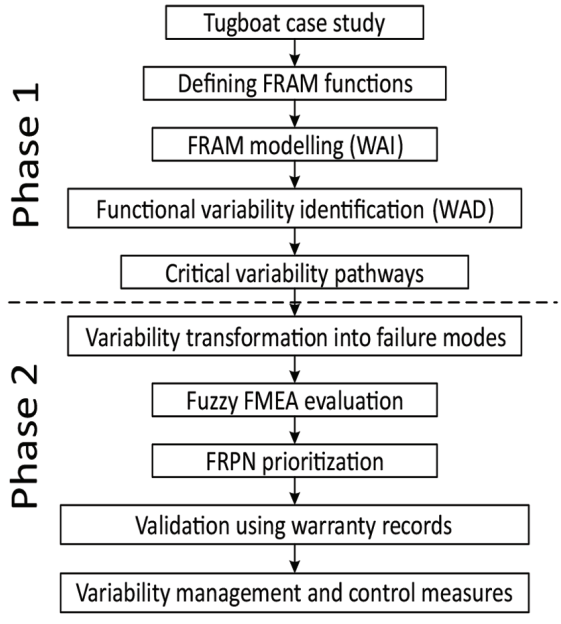


Figure 1. Analysis flowchart.

the FRAM functions and selecting the functional variabilities. The main stages are presented in Table 1.

Based on the system boundary and process stages defined above, the 40 functional variabilities were identified and selected through the following six-step procedure:

- Establishment of WAI: Technical specifications, approved design documents, classification requirements, contract documents, and testing and acceptance criteria were used.
- Identification of WAD: Field observations, construction and acceptance records, non-conformity reports, failure and warranty records, and expert interviews were examined.
- Identification of candidate variabilities: Differences between WAI and WAD were assigned to the relevant FRAM functions and couplings.
- Application of selection criteria: Variabilities were retained if they were within the system boundary, associated with a specific FRAM function, supported by project records or expert assessments, and capable of affecting downstream functions.
- Elimination and consolidation: Duplicate or overlapping items were merged, while items outside the system boundary or without a direct functional relationship were excluded.
- Expert review: The five experts reviewed the list in terms of relevance, clarity, and correspondence with the identified functions, resulting in a final list of 40 functional variabilities.

Table 1. Tugboat shipbuilding process stages.

Main phase	Sub-process/activity	Description
Design process	Concept design	Establishment of operational requirements and general design
	Preliminary design	Main dimensions and initial performance analysis
	Detail design	Engineering calculations and production drawings
Stability	Initial and final stability	Weight distribution control/trim and heel control
Hydrodynamic and performance analysis	Resistance analysis	Determination of hull resistance characteristics
	Powering analysis	Calculation of required engine power
	Propulsion system design	Determination of propulsion configuration
	Stability analysis	Evaluation of vessel stability criteria
Physical construction	Hull structure	Shell thicknesses, strength calculations, and construction
	Coating/paint system	Determination of corrosion protection systems
	Insulation	Fire, vibration, thermal, and acoustic insulation
Outfitting	Piping systems	Design of fuel, cooling, fire, etc. lines
	Electrical systems	Power distribution, lighting, and control systems
	Heating-ventilation and air conditioning (HVAC) systems	Heating, ventilation, and air conditioning
	Main engine/propulsion system	Integration of main engine, shaft, and propulsion equipment
	Auxiliary systems	Generators and auxiliary equipment
	Deck machinery	Cranes, windlasses, towing winches, etc. equipment
	Fire fighting systems	Fi-Fi systems
	Deck outfitting	Outfitting works
	Safety equipment	Life-saving and safety equipment
Navigation and communication	Navigation systems	Radar, ECDIS, AIS, etc. systems
	Communication systems	GMDSS and other communication systems
Testing and verification processes	Class approval	Compliance of design and production with class rules
	Factory acceptance test (FAT)	Testing of equipment at manufacturer facilities
	Harbour acceptance test (HAT)	System tests in harbour conditions
	Sea acceptance test (SAT)	Performance and system tests under sea conditions

2.2. FRAM Method

FRAM is an innovative approach developed by Erik Hollnagel and particularly used in the analysis of complex socio-technical systems. While traditional safety and risk analysis methods mostly focus on investigating the root causes of accidents, the FRAM approach aims to understand how a system actually works. This approach evaluates system performance not only through failures, but also through the continuously repeated "successful" functioning in daily operations [49].

Classical approaches assume that work processes are carried out in accordance with procedures, rules, and standards, and they consider deviations as exceptional situations. However, in real working environments, operations do not always proceed as planned, and continuous adaptations are made through the interaction of humans, organizations, and technology. Therefore, the starting point of system analysis is not how the work should theoretically be performed (WAI), but rather how it is actually performed in practice (WAD). The main reason why operations are mostly carried out successfully in daily activities is the ability of system components to adapt to variable conditions. This adaptation process occurs through small-scale adjustments and flexible decision-making mechanisms. The FRAM approach considers adaptive behaviors as an integral part of system performance and aims to analyze how performance variability emerges rather than focusing solely on errors. In this context, FRAM is not a classical risk or accident analysis method, but rather a qualitative modeling approach that explains system behavior [6].

2.2.1. FRAM functions

The FRAM method is based on modeling the functions within a system and the couplings among these functions in order to understand how the system operates. In the analysis process, the functions existing within the system are first identified, and the connections among these functions are revealed. Subsequently, the typical performance variabilities of these functions are evaluated, and the functional resonance that may occur within the system are analyzed. According to the FRAM approach, a function is a set of activities performed to achieve a specific objective. These functions may be simple or complex and play a fundamental role in the formation of system outputs. The correct identification of functions is critically important for the accuracy of the analysis.

Each function is defined in the FRAM methodology through six basic aspects: Input, Output, Precondition, Resource, Control, and Time. Input: Information, instruction, or warning that initiates the function and is used to produce an output. Output: The result of the function, which may become an input for another function. Precondition: Conditions that must be satisfied before the function begins. Resource: Information, equipment, and workforce required during the execution of the function. Control: Rules, procedures, and supervision mechanisms that ensure the function produces the intended result. Time: The time factor that constrains or directs the execution of the function [6]. The aspects of the FRAM function cell are shown below in Figure 2.

2.2.2. Performance and variability

In the FRAM model, functions are in continuous couplings with each other. These constitute the main source of variability in system performance. The couplings established among functions through input-output relationships, control mechanisms, and resource utilization play an important role in understanding system behavior. The relationships among functions are not always dependent on a linear time sequence. In some cases, functions may occur in parallel or indirectly affect each other. Therefore, system analysis should include not only sequential processes but also simultaneous couplings.

In the FRAM approach, performance variability is accepted as a natural characteristic of the system. Human, organizational, and technological components generate variability at different levels. While the human factor generally exhibits high frequency variability, technological systems display a more stable structure. Criteria called Common Performance Conditions are used for the evaluation of performance. These criteria include factors such as resource adequacy, communication quality, working environment, time pressure, and organizational support. Processes such as tugboat design, which involve human-technology-organization structures, contain high levels of variability. Therefore, variability levels may be classified using linguistic expressions in performance evaluations. This approach enables the dependencies among system functions to be understood more clearly [50].

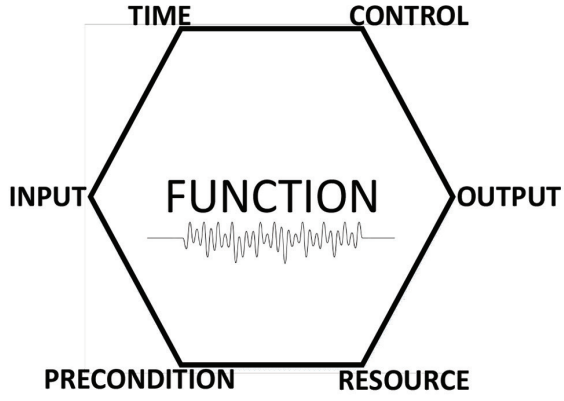


Figure 2. FRAM Function cell and its aspects.

2.2.3. Variability management and control measures

In the FRAM methodology, the analysis of variability is a critical stage for understanding system performance. Small variabilities occurring during daily operations may not individually cause system failure. However, when these variabilities couple with other functions, a functional resonance may emerge and lead to serious consequences. FRAM provides an important framework for managing variability in system performance. In this context, systems are required to develop resilience and adaptation capability. The ability of systems to respond rapidly and effectively to changing conditions is a determining factor in controlling risks [51]. During the variability management process, continuous monitoring, feedback, and learning mechanisms should be established. In this way, system performance can be continuously evaluated and opportunities for improvement can be identified [52].

One of the most important contributions of the FRAM method is that it enables complex systems to be analyzed in a holistic manner. Evaluating system performance not only through failures but also through normal operations is one of the strong aspects of the method [6]. However, the fact that the method is a qualitative analysis approach brings certain limitations. Since the analysis results largely depend on expert opinions, subjective evaluations may occur. In addition, the difficulty of data collection processes and the long duration of analysis are among the disadvantages of the method [24]. In order to overcome these limitations, the FRAM method is integrated with multi-criteria decision-making techniques, fuzzy logic, and quantitative risk analysis methods. In this way, qualitative analysis results can be transformed into numerical values, enabling more concrete risk evaluations [53]. The output variability belonging to functions may be formulated as follows. Depending on the scale of the model, clearly determining these requires highly complex and lengthy calculations [54-56].

$$\Delta v_{O,F1} = \sum_{F1}\left(\left(\Delta v_{I,1} * w_{I,1}\right) + \left(\Delta v_{R,1} * w_{R,1}\right) + \left(\Delta v_{C,1} * w_{C,1}\right) + \left(\Delta v_{PC,1} * w_{PC,1}\right)\right) \quad (1)$$

In the example of the interacting F1 and F2 functions, the variability relationship can be expressed mathematically as follows:

$$\Delta v_{O,F_2} = \left[\left(\left(\Delta v_{i,2} * w_{i,2}\right) + \left(\Delta v_{r,2} * w_{r,2}\right) + \left(\Delta v_{c,2} * w_{c,2}\right) + \left(\Delta v_{pc,2} * w_{pc,2}\right)\right) + \Delta v_{O,F_1}\right] \quad (2)$$

2.3. FMEA Method

The risks that may arise from functional variabilities were evaluated by integrating the fuzzy FMEA method, and *FRPN* were calculated for each failure mode. Accordingly, the performance variabilities identified through the FRAM analysis were transformed into semi-quantitative risk scores, and critical risk areas within the design process were identified. FMEA is a risk analysis method that systematically evaluates potential failure modes that may occur in products, processes, or systems and the effects of these failures [57].

In multidisciplinary engineering processes such as tugboat design, it is used as an important tool especially in the analysis of systems, design, construction, quality, reliability, and their couplings [58]. The tugboat design process has a complex structure requiring the combined evaluation of hull structure, hydrodynamic performance, main engine and propulsion system integration, stability, structural integrity, bollard pull performance, and operational requirements. Therefore, the early identification of errors that may arise during the design stage is critically important. FMEA provides an effective approach for identifying potential failure modes in this process, analyzing the effects of these failures on design and operation, and prioritizing risks. The method was first developed in military applications in the 1940s and was later systematized by NASA and became widely used in engineering applications [59].

For each failure mode, RPN values were calculated through severity, occurrence probability, and detectability scales, and the risks were therefore classified according to their priority levels. This approach enabled the identification of necessary improvement and control mechanisms within the design process [60]. FMEA was considered a proactive method that provided the opportunity to predict potential future problems by utilizing past design experiences and to reduce these risks during the early stages of design [61]. In this respect, the method was found to be compatible with the FRAM approach, as it enabled the semi-quantitative evaluation of the performance variabilities identified through FRAM and supported the establishment of a holistic risk assessment framework.

2.3.1. FMEA analysis procedure

The three fundamental evaluation criteria most commonly used in FMEA applications are Occurrence (O), Severity (S), and Detection (D) parameters. Failure modes identified within the tugboat design process are evaluated and scored according to these three factors based on expert opinions. According to the United States Department of Defense (1949), a failure mode is defined as the inability of a function within the tugboat design system to provide the expected performance, operate insufficiently or irregularly, or produce

undesired results [62]. Effect refers to the consequences of these failures on system performance, operational safety, and the end user. The Severity (S) parameter is determined according to the worst potential consequence of the relevant failure mode and is particularly evaluated in terms of safety of life, equipment damage, and operational losses.

2.3.2. Fuzzy FMEA

Fuzzy logic enables direct operation with linguistic expressions used in FMEA and models the uncertainty in expert evaluations more realistically. This approach allows uncertain or qualitative information to be effectively used in risk prioritization. In this context, a fuzzy logic-based structure was established by considering the O, S, and D parameters through linguistic variables in the evaluation of failure risk. In FMEA, the prioritization of failure modes is often considered as a multi criteria decision-making process, and in the literature, the integration of fuzzy logic with methods such as TOPSIS, VIKOR, AHP, and DEMATEL is widely used [58,61]. The classical FMEA approach includes certain limitations such as the assumption that risk factors have equal weights, different O, S, D combinations being able to produce the same RPN value, and evaluations being limited to precise numerical expressions. Therefore, it is necessary to perform a more flexible and representative evaluation using fuzzy linguistic variables and membership functions. In this study, potential failure modes, effects, and causes related to the functions determined by FRAM were analyzed using fuzzy FMEA. Evaluations were performed by experts according to the O, S, and D scales specified in Tables 2, 3, 4. These assessments were processed through fuzzification, and *FRPN* were subsequently calculated through the defuzzification procedure. Based on the obtained *FRPN* values, risk prioritization was performed, and corrective control measures for critical functions were identified [63,64].

Table 2. Fuzzy ratings for occurrence of a failure [57,65].

Probability	Probability of occurance	Failure probability	Fuzzy number
Almost None: Has not occurred before	Remote (R)	≤1/1.500.000	(1,1,2)
Remote Probability: Occurred very very rarely	Low (L)	1/150.000	(2,3,4)
Very Low: Relatively infrequent failures		1/15.000	
Low: Failures occasionally occurring		1/2000	(4,5,6)
Minor: Occurring in small numbers	Moderate (M)	1/400	
Medium: Occurring at medium frequency		1/80	
Slightly High: Occurring in slightly high numbers	High (H)	1/20	(6,7,8)
High: Occurring in high numbers		1/8	
Very High: Occurring in very high numbers	Very High (VH)	1/3	(8,9,10)
Almost Certain: Failure is almost certain		>1/2	

Table 3. Fuzzy ratings for severity of a failure [57,65].

Severity of effect	Effect	Fuzzy number
No effect	None (N)	(1,1,2)
Failure causing confusion in tugboat design	Very minor (VM)	(1,2,3)
Failure slowing down tugboat design	Minor (MIN)	(2,3,4)
Failure causing short-term disruption in tugboat design	Very low (VL)	(3,4,5)
Failure causing short-term disruption in tugboat design, production, and organization	Low (L)	(4,5,6)
Failure causing moderate losses in tugboat design, production, and decision-making processes	Moderate (MOD)	(5,6,7)
Failure having an effect causing complete system damage, incomplete production, and delay	High (H)	(6,7,8)
Failure having a destructive effect causing complete damage to tugboat design, production losses, etc.	Very high (VH)	(7,8,9)
Potential failure causing severe damage in tugboat design, production stoppage, and multiple fatalities	Hazardous with warning (HAZ)	(8,9,10)
Potential failure having an effect that may lead to catastrophe on the tugboat, organization, and environment	Hazardous without warning (CAT)	(9,10,10)

Table 4. Fuzzy ratings for detection of a failure [57,65].

Likelihood detection	Detection	Fuzzy number
Detectability of the cause of the potential failure and the subsequent failure is almost certain	Almost certain (AC)	(1,1,2)
Detectability of the cause of the potential failure and the subsequent failure is very high	Very high (VH)	(1,2,3)
Detectability of the cause of the potential failure and the subsequent failure is high	High (H)	(2,3,4)
Detectability of the cause of the potential failure and the subsequent failure is moderately high	Moderately high (MH)	(3,4,5)
Detectability of the cause of the potential failure and the subsequent failure is moderate	Moderate (M)	(4,5,6)
Detectability of the cause of the potential failure and the subsequent failure is low	Low (L)	(5,6,7)
Detectability of the cause of the potential failure and the subsequent failure is very low	Very low (VL)	(6,7,8)
Detectability of the cause of the potential failure and the subsequent failure is remote	Remote (R)	(7,8,9)
Detectability of the cause of the potential failure and the subsequent failure is unlikely	Very remote (VR)	(8,9,10)
Detectability of the cause of the potential failure and the subsequent failure is impossible	Impossible (IMP)	(9,10,10)

2.3.2.1. Fuzzy representation of expert evaluations

In fuzzy sets, different membership functions such as triangular, trapezoidal, and bell shaped curves are used in order to determine the membership degrees of elements. Among these functions, triangular and trapezoidal fuzzy numbers are particularly prominent as the most commonly preferred approaches in applications. Membership functions play an important role in modeling situations involving uncertainty and enable the representation of complexities encountered in fuzzy logic systems. Determining membership degrees through linguistic expressions allows the boundaries of system parameters to be defined [65,66]. A fuzzy set is generally expressed as:

$$A = \{(x, \mu_A(x)) : x \in X, \mu_A(x) \in [0,1]\} \quad (3)$$

Here, X represents the universal set, A represents the fuzzy set, μA denotes the membership function of the fuzzy set, and μA(x) represents the membership degree of the element x belonging to the related set. The membership degree varies between 0 and 1, where the value 0 indicates that the element does not belong to the set, while the value 1 represents full membership. Intermediate values indicate partial membership. The triangular membership function used in this study is defined by three parameters, namely the lower limit a, the peak point m, and the upper limit b, and satisfies the condition $l \le m \le b$. The triangular membership function is shown in Figure 3.

Triangular membership functions are also effectively used in the quantification of linguistic variables. The triangular membership function used in this study is defined by three parameters, namely the lower limit a, the peak point m, and the upper limit b, and satisfies the condition $a \le m \le b$. The fuzzy membership structure used in this study wΩs established based on the approaches proposed by Liu et al. [57] and Wang et al. [65]. The mathematical representation of the membership function is given below:

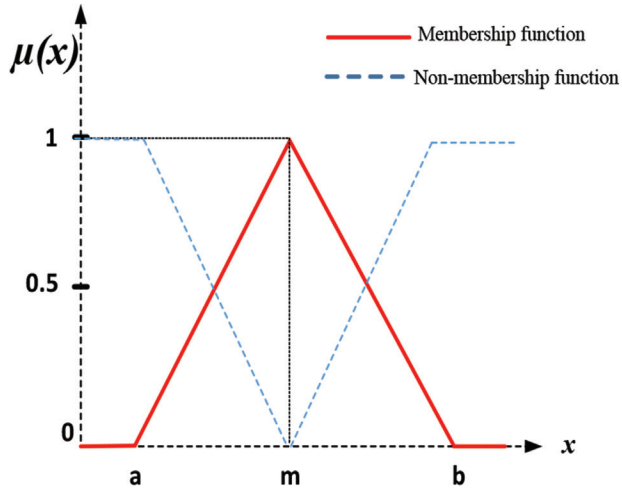


Figure 3. Triangular membership function.

$$\mu_{A(X)} = \begin{cases} 0, & x \le a \\ \frac{x-a}{m-a}, & a < x \le m \\ \frac{b-x}{b-m}, & m < x \le b \\ 0, & x > b \end{cases} \quad (4)$$

2.3.2.2. Aggregation of expert opinions

In the study, risks associated with tugboat design and construction were evaluated using a Fuzzy FMEA approach integrated with FRAM-based variability analysis. Linguistic expert evaluations were transformed into triangular fuzzy numbers according to the scales given in Tables 2, 3, and 4. For each failure mode, the fuzzy evaluations provided by the experts were aggregated using the arithmetic mean

method. The aggregated occurrence probability value is expressed as:

$$\widetilde{O} = \frac{1}{n}\left(\sum_{i=1}^{n} a_i , \sum_{i=1}^{n} m_i , \sum_{i=1}^{n} b_i \right) \quad (5)$$

2.3.2.3. Calculation of the FRPN

The *FRPN* is a measure that numerically expresses the risk level of each potential failure mode. As shown in equation 6, the *FRPN* value is calculated by multiplying the occurrence probability (O), severity (S), and detection (D) values.

$$\widetilde{FRPN} = \widetilde{O} \otimes \widetilde{S} \otimes \widetilde{D} \quad (6)$$

The multiplication of triangular fuzzy numbers was performed on a component basis and is expressed as:

$$\widetilde{FRPN} = \left(a_O a_S a_D, m_O m_S m_D, b_O b_S b_D\right) \quad (7)$$

Through this approach, the risk levels related to failure modes were represented not only by a single precise value but also by a fuzzy interval including uncertainty.

2.3.2.4. Defuzzification

In order to rank the fuzzy *FRPN* values and perform comparative risk evaluation, a defuzzification process was applied. In this study, the centroid method was preferred as the defuzzification method. The defuzzified *FRPN* value is calculated as:

$$FRPN_{crisp} = \frac{\sum_{i=1}^{n} x_i \, \mu\left(x_i\right)}{\sum_{i=1}^{n} \mu\left(x_i\right)} \quad (8)$$

As a result of this process, fuzzy risk values were transformed into a single numerical value, and it became possible to determine the risk priorities of failure modes. Thus, the failure modes creating critical risks were quantitatively ranked and prioritized.

2.4. Case Study and Expert Selection

In this study, a FRAM-based framework was developed through a real tugboat building project. Initially, the functional couplings of tugboat design and building processes under ideal operational conditions were established. Then, the interactions among variable functions were analyzed through a real tugboat building case. The investigated tugboat case was built based on a local design approach rather than a ready-made design package, in a shipyard possessing limited infrastructural resources and located far from major logistics supply chains. Furthermore, the shipbuilding company maintained a highly limited control and engineering team throughout the project lifecycle. The construction process exceeded the original project schedule and the tugboat was delivered with delay. The most dominant source of operational problems was identified as excessive shaft angles between the main engine output and ASD input shafts, resulting in bearing-related problems and vibration. In order to reduce the angular difference along the propulsion line, two cardan shafts were integrated into the shaft system. Following the provisional acceptance of the tugboat, more than 400 user-reported deficiency notifications were recorded during the warranty period. Among these records, accommodation sweating caused by the Heating, Ventilation and Air Conditioning (HVAC) system, high vibration, alarm monitoring system deficiencies, improper material usage, and equipment failures were the most prominent issues. In addition, numerous deficiency reports were submitted regarding insufficient chain-locker dimensions, accommodation cabin arrangements, and deck equipment integration problems. The principal particulars and technical information of the tugboat used in this study are presented in Table 5.

Subsequently, the Fuzzy FMEA analysis stage was carried out based on the identified functional variabilities. Potential variabilities arising from functional couplings were defined as failure modes, and the associated risks were evaluated through a semi-quantitative risk assessment approach.

FRAM analysis requires field observations and expert evaluations [67]. Similarly, expert evaluations ensure that the Fuzzy FMEA analysis produces accurate results [68]. In this context, general information regarding the experts consulted in the study is presented in Table 6. In order for the study to produce reliable and realistic results, the experts

Table 5. Tugboat main particulars.

Parameter	Ship particular
Vessel type	Open sea tugboat
Length overall (LOA)	32 m
Moulded Beam	11.83 m
Moulded Depth	5.55 m
Bollard pull (BP)	70 t
Propulsion type	Azimuth Stern Driver (ASD)
Service speed	13 kn
Gross tonnage	546
Net tonnage	164
Hull material	Steel
Main engine power	2 x 2100 kW
Classification notation	1A5 Y ESCORT TUG + M AUT-8h Fi-Fi1
Keel laying date	01 January 2018
Delivery date	30 May 2019

Table 6. General qualifications of the experts.

Expert code	Position	Experience (years)	Professional qualifications
E1	Tugboat design department director	20	Ph.D. Naval Architecture and Marine Engineering
E2	Tugboat designer	10	B.Sc. Naval Architecture and Marine Engineering
E3	Tugboat shipyard manager	15	M.Sc. Naval Architecture and Marine Engineering
E4	Tugboat captain	12	B.Sc. Maritime Transportation and Management Engineering, Master Mariner
E5	Tugboat operator/fleet owner	25	B.Sc. Maritime Transportation and Management Engineering, Master Mariner

were selected from individuals with design, construction, and operational experience. The main reason for this is that certain deficiencies that cannot be foreseen during the design stage may only emerge during the construction and operational processes. Similarly, experiences conveyed solely by designers and construction teams remain incomplete without the contribution of operator users who know how the tugboat behaves under actual operating conditions and what performance limitations it encounters. Therefore, the expert group was formed with the aim of bringing together knowledge and experience covering the entire lifecycle of the tugboat.

2.5. Sensitivity and Uncertainty Analysis

Fuzzy numbers address the vagueness of linguistic evaluations but do not directly quantify expert disagreement or the sensitivity of the results to model assumptions. Therefore, three supplementary analyses were conducted to evaluate the robustness of the *FRPN* results. First, agreement among the five experts was assessed separately for occurrence, severity, and detection using tie-corrected Kendall's *W* formula as given in Equation 9. Kendall's coefficient of concordance (*W*) is a non-parametric measure used to evaluate for rank correlation. The coefficient ranges from 0 to 1, where values close to 0 indicate weak agreement and values close to 1 indicate strong agreement [69].

$$W = \frac{12\sum_{i=1}^{n}\left(R_i - R^{-}\right)}{m^2(n^3 - n) - m\sum_{j=1}^{m} T_j} \tag{9}$$

Second, a leave-one-expert-out (LOEO) analysis was performed by excluding each expert and recalculating the *FRPN* values and rankings. Finally, parameter sensitivity was tested using occurrence, severity, and detection dominant weighting scenarios of (0.50,0.25,0.25), (0.25,0.50,0.25), and (0.25,0.25,0.50) by the equation 10. Spearman's rank correlation and maximum rank shifts were used to compare the results with the baseline ranking.

$$FRPN_w = \frac{O_a^{3w_O} O_a^{3w_S} O_a^{3w_D} + O_m^{3w_O} O_m^{3w_S} O_m^{3w_D} + O_b^{3w_O} O_b^{3w_S} O_b^{3w_D}}{3} \tag{10}$$

3. Analysis

3.1. FRAM Analysis

3.1.1. Defining tugboat design functions as WAI

The tugboat design and construction process was modeled by considering the process from the definition of operational requirements to the delivery of the vessel. The related functions were developed by assuming that the construction process progressed in accordance with the planned project schedule (WAI). The system consisted of 16 main and 7 sub-functions as given in Table 7 covering preliminary design, performance analyses, propulsion system selection, stability verification, class compliance controls, production organization, and verification/revision processes. The first function initiating the system is Sub1, which defines the customer/shipowner demand, while the final function terminating the system is Sub7, which represents the delivery of the vessel. The functions between F1 and F8 are preparation functions, the functions between F9 and F13 are detail process functions, the functions between F14 and F16 are control functions, and the functions between Sub1 and Sub7 are support functions.

Tugboat design was modeled by accepting the existence of standard functions required to be performed. This assumption includes the basic functions and aspects that should exist within the broadest framework. While projects having similar design characteristics are received as standardized design packages, some intermediate forms are redesigned by being subjected to re-analysis processes. Tugboat design and construction have a complex process realized through HuMan (M), Technology (T), and Organization (O) couplings [44]. If all functions involved in all construction processes were defined in detail, the modeling framework would become excessively broad, which would cause deviations in the analysis results. By defining boundaries for the FRAM model through the functions, the analysis was prevented from becoming excessively complex and more consistent results were achieved.

The primary requirements are the intended service, main engine power, propulsion system, and bollard pull

Table 7. FRAM function description and complex group.

No	Type	Function	M-T-O
F1	Preliminary	To define operational requirement	M-O
F2	Preliminary	To define preliminary design parameters	M-T
F3	Preliminary	To perform performance analyses	M-T
F4	Preliminary	To determine main engine power	M-T
F5	Preliminary	To decide propulsion system	M-T-O
F6	Preliminary	To determine weight distribution	M-T
F7	Preliminary	To check initial stability	M-T
F8	Preliminary	To estimate bollard pull target	M-T
F9	Development	To arrange deck equipment	M-T-O
F10	Development	To determine accommodation and bridge layout	M-T-O
F11	Development	To design engine room arrangement	M-T-O
F12	Development	To define firefighting and safety systems	M-T-O
F13	Development	To start physical construction	M-T-O
F14	Control	To check building class-maritime rules	M-T-O
F15	Control	To organize shipbuilding	M-O
F16	Control	To verify and revise project	M-O
Sub1	Support	To give the main profile	M-O
Sub2	Support	To meet design constraints	M-T-O
Sub3	Support	To utilize available data sources	M-T
Sub4	Support	To define equipment list	M-T-O
Sub5	Support	To provide project team	M-O
Sub6	Support	To ensure shipyard infrastructure	T-O
Sub7	Support	To deliver the vessel	M-T-O

capacity. During the concept design stage, customer/shipowner requirements must be established within a consistent framework. Design according to the service purpose is essential. When this is not clearly determined, the operational framework expands and negatively affects equipment selection and the construction process. Strong main engine and propulsion performance are the principal capabilities of a tugboat. Harbor or offshore tugboats require specific characteristics regarding draft heights and propulsion systems according to their service area. In ports and terminals, lower-draft propulsion systems are preferred. In escort and towing services, voith-type propulsion systems are highly efficient in terms of maneuverability. In tugboats, reinforced skeg structures, bulwark lines, and bow and stern form constructions facilitate harsh operational working conditions. The installation process of the propulsion system region to the hull requires highly sensitive engineering solutions. Bridge control consoles are equipped to control and monitor both bow and stern operations [1,5,70].

The engine room arrangement should be designed in a way that facilitates equipment maintenance operations. Tugboats are generally propelled and driven by two main engines and two propulsion systems. According to electrical load calculations, a minimum of two diesel generators are installed. In addition, auxiliary equipment such as main engine and diesel generator coolers, compressors, hydraulic power units, sewage treatment systems, oily water separators, oil and fuel separators, air conditioning units, hydrophore units, pumps, filters, batteries, rectifiers and inverters, transformers, exhaust silencers, and main and distribution switchboards are included in engine room equipment arrangements. For external firefighting, water and foam-type liquids are sprayed from fire monitors through high-suction pumps located in the engine room. Accommodation arrangements should be equipped according to the minimum safe manning certificate based on the service class of the tugboat. Master and chief engineer cabins are designed as separate cabins [1,5,70].

Although there are certain variations in the rules depending on tonnage and classification society, tugboat construction should be subjected to control and inspection through classification societies. Structural, outfitting, and piping

drawings, physical construction, and the quality standards of equipment and materials are subject to class approval. It is essential that physical construction progresses in coordination with the class approval process. Progress is achieved as a result of periodic class surveys. At this stage, drawing and field remarks
issued by the class should be followed and subjected to a re-approval process. Similarly, the employment of design and project teams together with the adequacy of shipyard infrastructure are sub-functions having extensive interaction originating from human and organizational factors [45,71].
Each function was modeled using the six basic aspects of FRAM, namely input, output, precondition, resource, control, and time, as shown in the example in Table 8. Thus, dependencies among functions and the propagation of output variabilities throughout the system were analyzed.

The couplings among the identified functions were modeled using the FRAM Model Visualiser software and are presented in Figure 4. In the model, each function was defined by considering the aspects of input, output, precondition, resource, control, and time.
Figure 5 FRAM functional coupling graph shows that the connection intensity among system functions is not distributed homogeneously throughout the model. The FRAM functions have a total of 108 couplings. The function with the highest number of couplings is F13 (to start shipbuilding). The function with the lowest number of couplings is the Sub1 (to give main profile). In particular, F13, F3, and F9 were identified as the functions having the highest number of couplings. The functions F10, F11, F12, and F15, which exhibit moderate coupling intensity, are mainly associated with detail design, compartment

Table 8. F2-F3 function aspects.

F2-to define preliminary design parameters	
Input	Concept design determined
	Contract-technical specification prepared
Output	Main dimensions (*L, B, T, D*) determined
	Hull form and displacement preliminary assumption determined
	Total ship resistance determined
	Propulsion and maneuvering characteristics determined
	Bollard pull preliminary assumption determined
	General arrangement plan draft prepared
Precondition	Basic performance and mission requirements determined
Resource	Design software, similar vessel database, hydrodynamic knowledge
Control	Design criteria, class limitations, draft and port constraints
Time	-
F3-to perform performance analysis	
Input	Main dimensions (*L, B, T, D*) determined
	Hull form and displacement preliminary assumption determined
	Total ship resistance determined
	Propulsion and maneuvering characteristics determined
	Bollard pull preliminary assumption determined
	General arrangement plan draft prepared
Output	Preliminary design finalized
	Model test results
	Start detail design
Precondition	Basic performance and mission requirements determined
	Design criteria, class limitations, draft and port constraints
Resource	Design software, similar vessel database, hydrodynamic knowledge
Control	-
Time	-

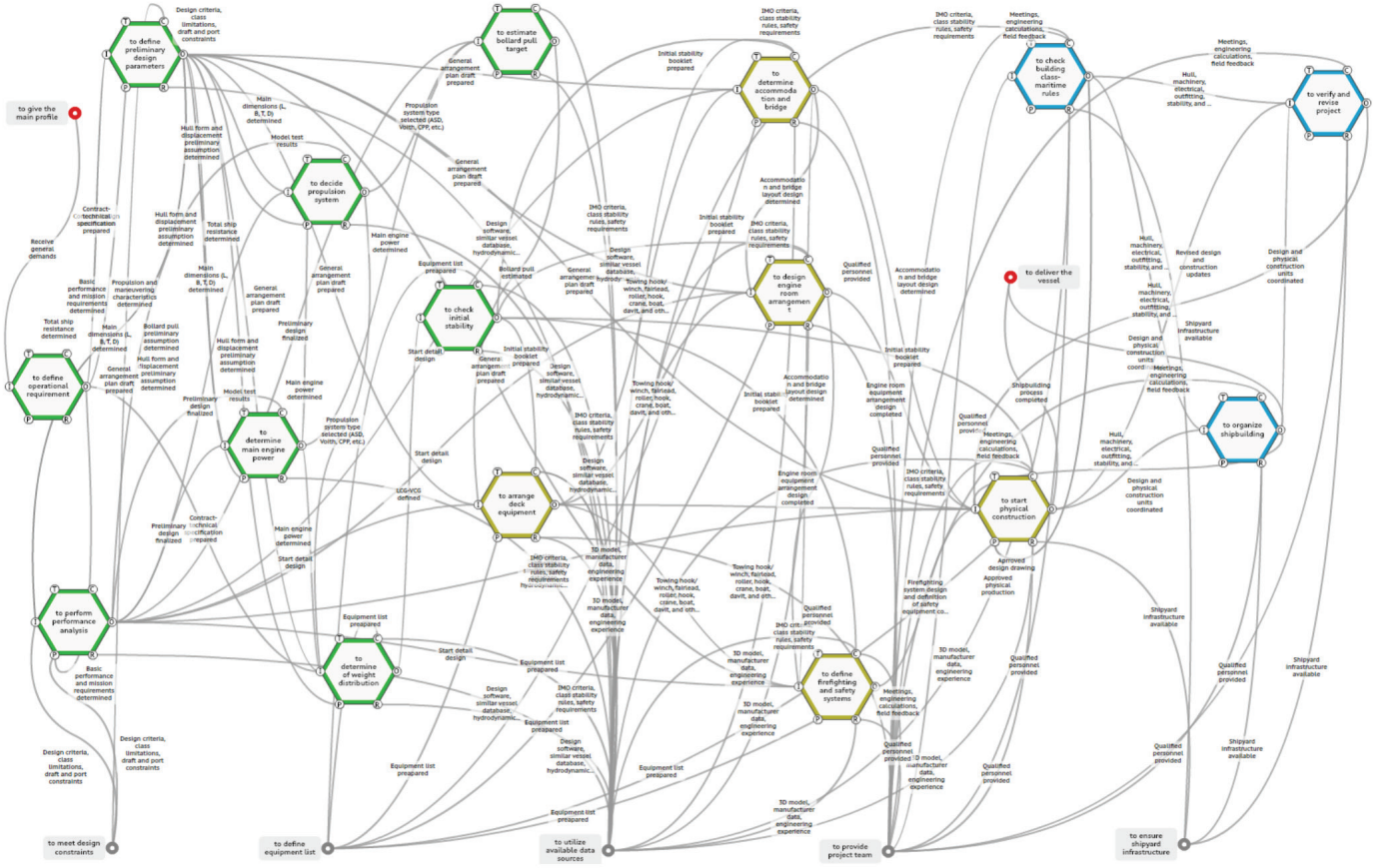


Figure 4. FRAM analysis visualization with functional couplings.

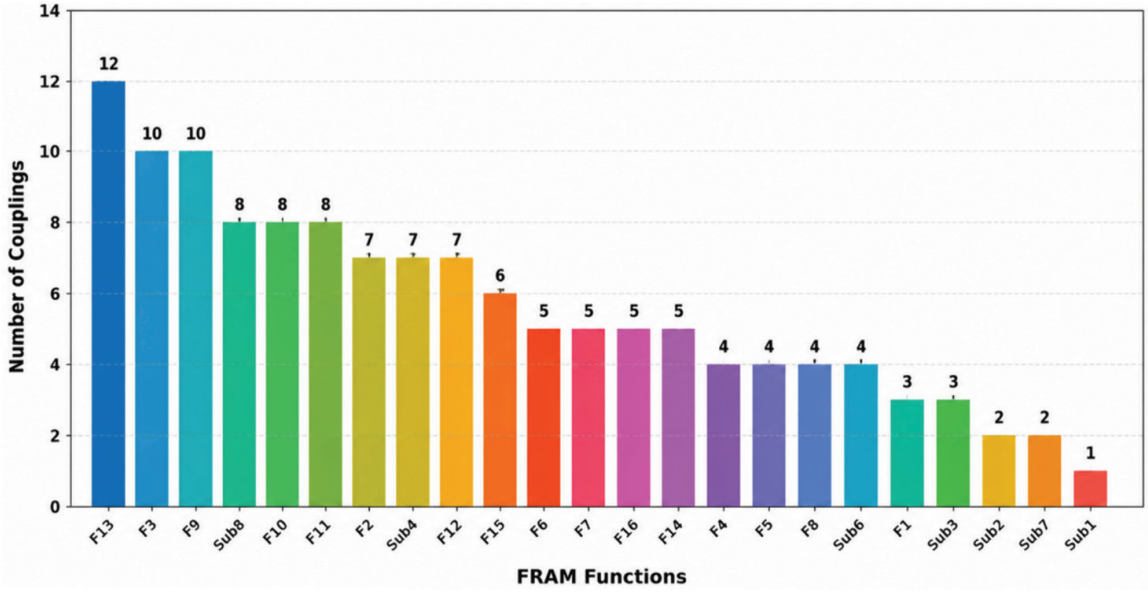


Figure 5. FRAM functional coupling intensity.

arrangements, and verification processes. Support functions with lower coupling levels were evaluated as auxiliary structures ensuring system continuity in terms of personnel, data flow, and infrastructure support, even though they do not directly generate critical resonance.

3.1.2. Aggregation of functions variability as WAD

In the tugboat case, the first major problem identified was the high shaft angle between the main engine output and ASD input caused by main engine arrangement related limitations. As shown in Figure 6, additional bearings and universal/cardan shafts were required due to the angular shaft arrangement between the main engine and the ASD unit. The approximately 19° angular difference was accommodated through the use of two cardan shafts and two additional bearings. Although the arrangement was considered acceptable by both the design team and the main engine-ASD manufacturers, the approximately 19° shaft angle is considerably higher than the 5.5° angle generally permitted in conventional straight-shaft installations. This increased angular difference may contribute to alignment deficiencies, bearing wear, and vibration-related problems. Due to these angular differences, bearing clearances decreased as a result of overheating problems occurring in the shaft bearings. Although the bearings are designed to withstand temperatures up to 225° C, overheating problems were observed during operation. Before the improvement works, vibration measurements on the ASD unit reached 77.6 mm/s in the horizontal direction, 162.9 mm/s in the transverse direction, and 203.4 mm/s in the vertical direction. Furthermore, due to vibration complaints originating from the shaft bearings, the vessel was taken out of service and corrective actions were attempted through re-bearing operations. Following shaft-bearing replacement during the warranty period, vibration levels were reduced to acceptable ISO limits. The critical resonance pathway of the related problem in terms of FRAM functions is presented in Figure 7.

The functional resonance aggregation pathway of the propulsion-system problems was identified as F1-F2-F4-F5-F11-F13. The variabilities occurring within the main performance requirements, acceptance criteria, and calculation processes affected the outputs of the propulsion-system selection function as inputs. F5 directly affected F11, while F11 subsequently affected the F13. In addition, insufficient controls within the F16 created negative variability on the shaft arrangement in the engine room. Furthermore, insufficient qualified personnel, limited shipyard capabilities, misinterpretation of previous design data, and design constraints constituted sources of variability affecting the outputs of the related propulsion-system functions.

The accommodation spaces of the vessel are climatized by a seawater-fed chiller system located in the engine room. Fan-coil units belonging to the system are installed within the cabins. In the project, sweating caused by the HVAC system resulted in leakage into the wheelhouse and personnel cabins. Accommodation panel coverings and insulation materials became wet, and some sections became unusable. As a corrective action, additional drains were opened on the gutter bars and the insulation of the fan-coil pipes was revised. This situation negatively affected personnel living conditions on board. It was observed that the related problem negatively affected the system by generating variability.

The outputs of the F1-F2, concept design, preliminary design, and general arrangement plan, served as inputs for F10 and transferred variability into this function. The output of the F10 (to determination of the accommodation and

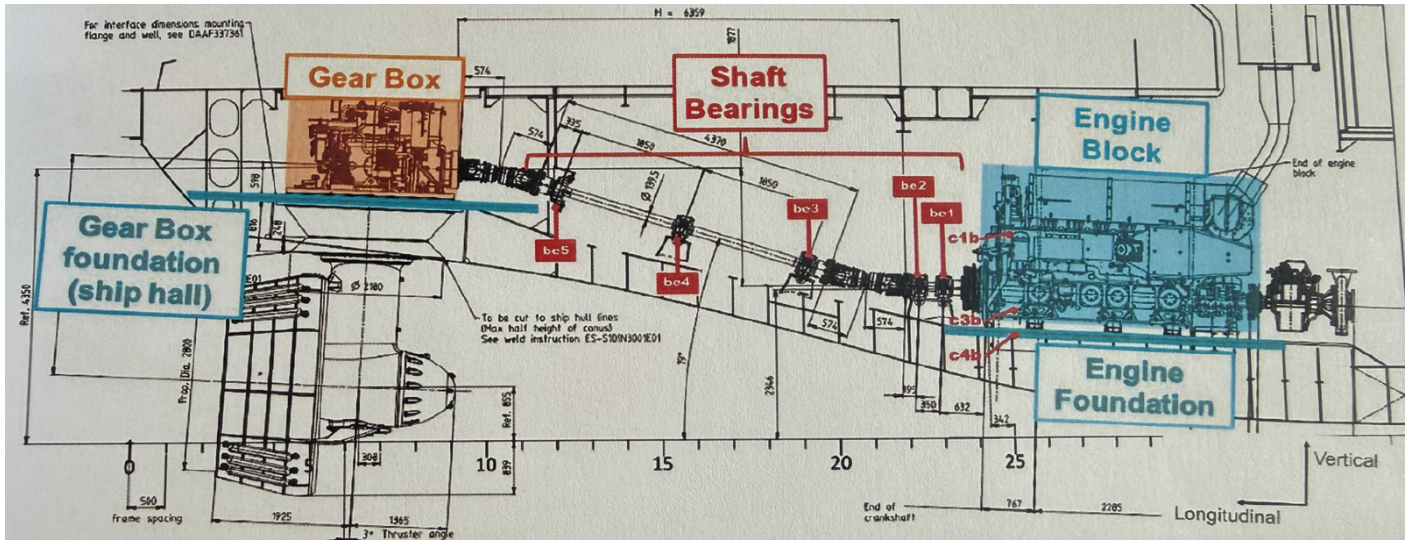


Figure 6. Main engine-ASD angular shaft alignment configuration.

bridge layout), affected the Sub7-vessel delivery function as an input of F13. Furthermore, insufficient personnel (Sub5), shipyard infrastructure deficiencies (Sub6), and equipment selection deficiencies and faults (Sub4) originating from the other support functions contributed to the growth of variability. The F1-F2-F10-F13-Sub7 sequence represents the critical variability pathway of the related problem as given in Figure 8.

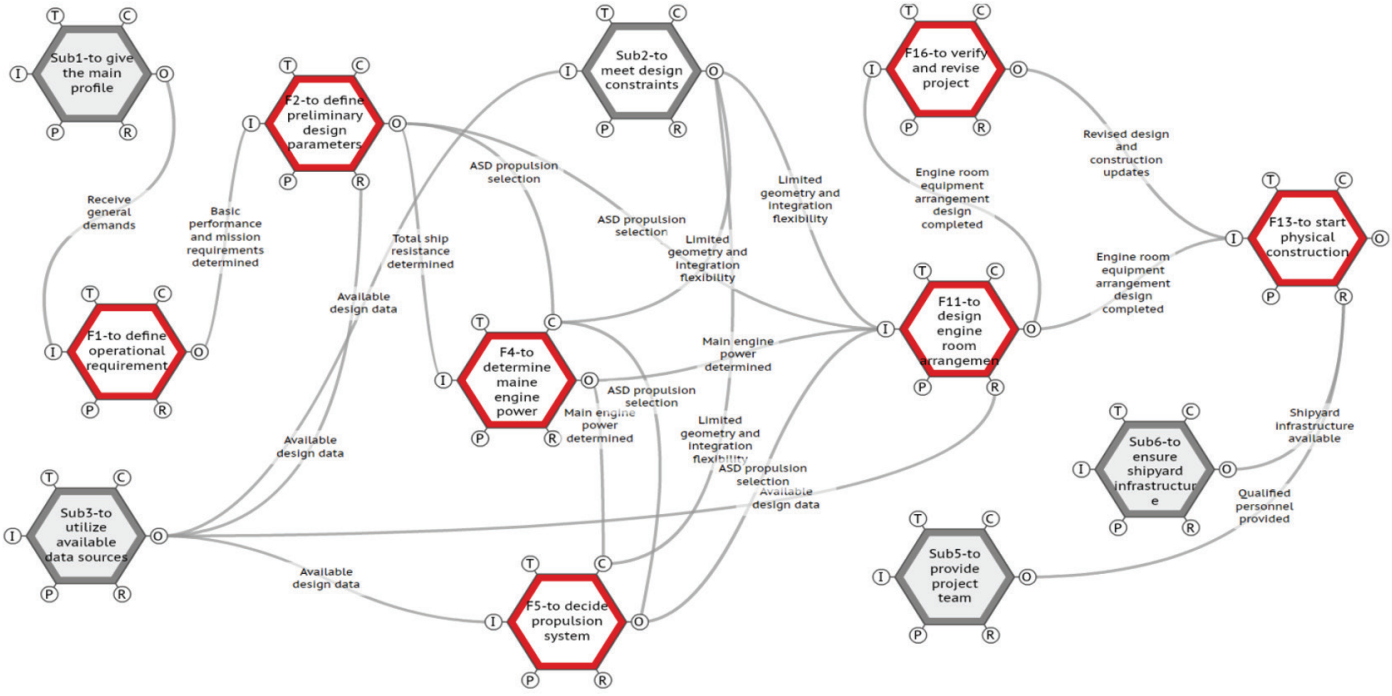


Figure 7. Functional resonance pathway associated with the main engine-ASD angular shaft alignment problem.

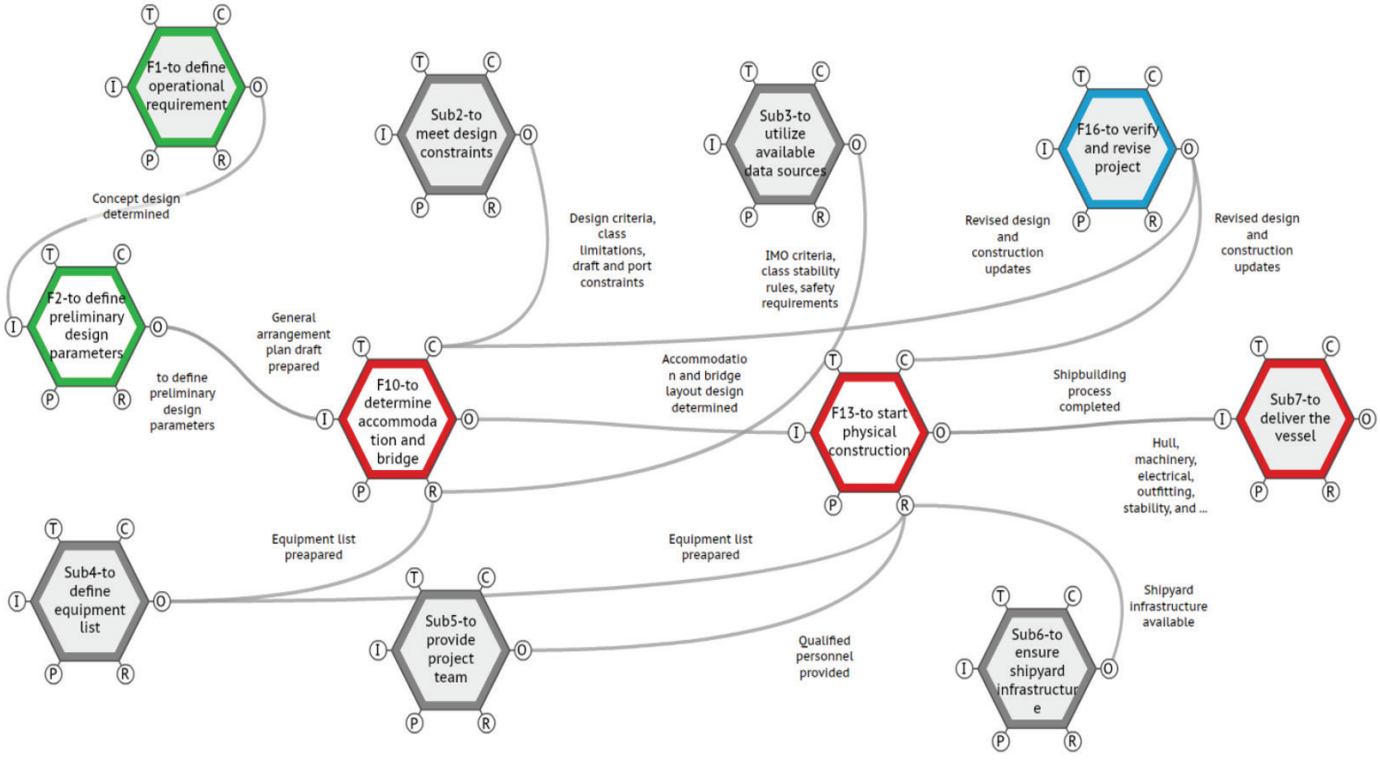


Figure 8. Functional resonance pathway associated with the HVAC problem.

Equipment and material selection deficiency problems originated from accumulated variability among equipment definition, compliance with classification rules, physical construction, and project verification functions. Equipment installation errors emerged as a result of accumulated variability among equipment selection, utilization of design data, physical construction, and verification functions. The insufficient chain-locker capacity problem originated from accumulated variability among deck equipment arrangement, equipment definition, physical construction, and Project verification functions. Alarm monitoring system failures emerged not as isolated equipment malfunctions, but rather as a result of accumulated variability among equipment selection, system integration, verification, and physical construction functions. Accommodation layout problems originated from aggregated variability among accommodation arrangement, design constraints, physical construction, and verification functions. Deck equipment integration deficiencies emerged as a result of accumulated variability among bollard-pull requirements, deckequipment arrangement, equipment selection, physical construction, and verification functions. High vibration complaints emerged as a result of accumulated variability among propulsion system selection, machinery arrangement, project verification, production quality, shipyard infrastructure, and project team capability functions.

With scope of the FRAM analysis, the effects of variability on the entire system were taken into consideration. Although the ultimate objective was the smooth delivery of the vessel and the minimization of failures during the warranty period, it was observed that this objective could not be achieved in the investigated case.

Similarly, the variability aggregation pathway for other problems as:

- Equipment and material selection deficiency:
  F1→F2→Sub4→F14→F13→F16→Sub7.
- Equipment installation errors:
  F1→F2→Sub4→Sub3 →F13→F16→Sub7.
- Insufficient chain-locker capacity:
  F1→F2→F9→Sub4→F13→F16→Sub7.
- Alarm monitoring system failures:
  F1→F2→Sub4→F12→F13→F16→Sub7.
- Accommodation-layout problems:
  F1→F2→F10→Sub2→F13→F16→Sub7.
- Deficiencies in deck-equipment arrangement:
  F1→F2→F8→F9→Sub4→F13→F16→Sub7.
- High vibration complaints:
  F1→F2→F4→F5→F11→F16→F13→Sub6/Sub5→Sub7.

3.2. Tansformation of Functional Variability into Fuzzy FMEA Failure Modes

The FRAM analysis revealed that the problems observed in the investigated tugboat case originated from triggered functional variabilities. Therefore, the outputs obtained from the FRAM variability aggregation pathways were transformed into failure modes and evaluated using the Fuzzy FMEA methodology as presented in Table 9. FRAM was first applied to identify variability propagation pathways within the tugboat design and construction processes. The identified variability-induced failure modes were then assessed using fuzzy FMEA to determine their criticality and risk priority levels.

3.3. Fuzzy FMEA Analysis

Following the FRAM-based functional variability analysis, fuzzy FMEA was conducted in order to semi-quantitatively evaluate the risks associated with the identified functional variabilities and potential failure modes. The integration of FRAM and fuzzy FMEA enabled both the identification of variability propagation mechanisms and the prioritization of the associated risks under uncertainty conditions. Within the scope of the analysis, potential failure modes derived from the FRAM model were systematically evaluated by considering design, production, operational, and organizational aspects of tugboat design and construction processes. Unlike conventional FMEA approaches relying mainly on historical failure records, the proposed method also considers functional couplings and variability propagation under uncertainty conditions.

The analysis process consisted of several methodological stages, including the identification of failure modes (Table 9), expert evaluations, transformation of linguistic assessments into fuzzy numbers (Table 10), aggregation of expert opinions, calculation of the *FRPN*, and defuzzification of the obtained results (Table 11). The experts assessed each failure mode in terms of occurrence probability, severity of consequences, and detectability using predefined linguistic scales. Due to the inherent uncertainty and subjectivity of expert judgments, triangular fuzzy numbers were utilized to model the evaluation process. The obtained fuzzy risk values were subsequently defuzzified to determine crisp *FRPN* values, enabling the prioritization of critical failure modes. Accordingly, the proposed framework enabled the identification and prioritization of critical technical and organizational vulnerabilities within tugboat design and construction processes.

The risk-level ranges were defined based on the theoretical *FRPN* scale of 0-1000 and expert judgment, with higher ranges representing risks requiring greater priority and more immediate corrective action. According to Table 12, risk thresholds were classified as follows: very high ≥500; high ≥350; moderately high ≥200; moderate ≥100; low <100. The calculated *FRPN* values and corresponding risk rankings of the identified failure modes are presented in Table 13.

Table 9. Potential function output variability.

No	Functional variability	Failure mode	Effect
F1V1	Inconsistencies in operational preferences	Incompatible operational design basis	Design-operation mismatch
F1V2	Failure of the vessel to fully meet its intended construction purpose	Operational requirement deficiency	Operational performance loss
F2V3	Preliminary design stage was not carried out properly	Preliminary design mismatch	Propulsion-system integration constraints
F2V4	Errors and deficiencies in analyses and engineering calculations	Incorrect engineering calculations	Design-verification problems
F4V5	Main engine-propulsion system integration was not sufficiently controlled	Limited propulsion integration flexibility	Increased shaft-angle susceptibility
F5V6	Propulsion system is not compatible with the hull	Hull-propulsion system incompatibility	Main engine-ASD alignment difficulty
F5V7	Installation errors exist in the propulsion system	Propulsion-system alignment deficiency	Vibration propagation
F5V8	Reduction in propulsion efficiency due to additional shaft arrangement	Cardan shaft dependency	Propulsion efficiency loss
F8V9	Operational deficiencies caused by deck arrangement	Bollard-pull integration pressure	Operational usability constraints
F9V10	Excessive limitations in anchoring and mooring operations	Insufficient chain-locker capacity	Towing-operation limitation
F9V11	Improper towing hook/winch/chain-locker arrangement	Deck-equipment integration inconsistency	Inefficiency in deck operations
F10V12	Errors in accommodation-space arrangement	Accommodation-layout incompatibility	Crew comfort loss
F10V13	Insufficient and improper ventilation circuit installation	HVAC outfitting deficiency	HVAC condensation and leakage
F11V14	Accessibility difficulties due to equipment arrangement	Engine-room arrangement mismatch	Maintenance and accessibility difficulties
F11V15	Errors and deficiencies in piping/circuit installations	Difficulty in accessing piping/circuits	Extended repair time and system unavailability
F12V16	Constraints exist in engine-room equipment arrangement	Safety-system integration constraint	Operational safety weakness
F12V17	Excessive number of alarms in the alarm monitoring system	Alarm-system integration instability	Monitoring and control deficiencies
F13V18	Incomplete and improper installations exist	Construction-stage implementation deviation	Repetitive operational failures
F13V19	Excessive number of rework activities	Inadequate production coordination	Loss of construction efficiency
F13V20	Poor workmanship quality	Low production quality	Construction-quality problems
F13V21	Construction process did not progress according to the planned schedule	Construction-process delay	Extension of vessel delivery period
F14V22	Insufficient inspection and supervision by the classification society	Classification inspection deficiency	Incomplete nonconformity detection
F14V23	Incorrect implementation of classification rules	Improper classification practices	Operational incompatibility
F14V24	Construction progressed without considering classification rules	Classification compliance deficiency	Certification and safety problems
F15V25	Lack of coordination between departments	Organizational communication deficiency	Construction coordination problems
F15V26	Shipyard organizational units are not of sufficient quality	Organizational management deficiency	Production quality loss

Table 9. Continued.

No	Functional variability	Failure mode	Effect
F16V27	Insufficient follow-up of revision works	Project-verification insufficiency	Incomplete corrective actions
F16V28	Incomplete and improper inspections exist	System-validation insufficiency	Repetitive operational nonconformities
Sub1V29	Errors in the selection of the vessel's main characteristic dimensions	Main characteristic design incompatibility	Hull-system integration problems
Sub2V30	Design constraints were incorrectly interpreted	Design-constraint interpretation error	Integration and arrangement problems
Sub3V31	Previous project data were incorrectly applied to the new project	Design-data interpretation inconsistency	Local design adaptation error
Sub4V32	Improper equipment and material selections exist	Improper equipment/material selection	System incompatibility
Sub4V33	Delays occurred in the delivery of equipment to the shipyard	Critical equipment procurement delay	Construction-process delay
Sub5V34	Engineering team is insufficient	Engineering-team capability limitation	Insufficient engineering supervision
Sub5V35	Quality-control activities are insufficient	Quality-control deficiency	Operational quality problems
Sub6V36	Shipyard infrastructure is insufficient	Shipyard infrastructure limitation	Reduced construction quality
Sub6V37	Vessel construction in a location remote from material logistics and qualified workforce resources	Shipyard logistics and workforce accessibility limitation	Delays in construction activities and reduced production quality
Sub7V38	Vessel was delivered with existing failures	Operational transfer instability	High warranty-period deficiency reports
Sub7V39	Excessive failure reports during warranty period	Aggregated functional resonance	Operational reliability loss
Sub7V40	Delay in vessel delivery date	Delivery-process delay	Operational planning loss

3.4. Sensitivity and Uncertainty Analysis

The robustness of the results was examined in terms of expert agreement, individual expert influence, and changes in the O-S-D weights. The results are summarized in Table 14.

4. Results and Discussion

According to the Fuzzy FMEA results, the highest-ranked functional variability was identified as F5V6 with an *FRPN* value of 622.667 related to the failure mode "hull-propulsion system incompatibility." The second-ranked variability was identified as Sub7V39 with an *FRPN* value of 525.765 related to the failure mode "aggregated functional resonance." F16V28 ranked third with an *FRPN* value of 483.984 related to the failure mode "system-validation insufficiency." F4V5 was identified as the fourth-ranked variability with an *FRPN* value of 473.675 related to the failure mode "limited propulsion integration flexibility." F5V7 ranked fifth with an *FRPN* value of 447.952 related to the failure mode "propulsion-system alignment deficiency." In addition, F14V24 ranked sixth with an *FRPN* value of 441.760 related to the failure mode "classification compliance deficiency," Sub5V34 was identified as the seventh-ranked variability with an *FRPN* value of 438.843 related to the failure mode "engineering-team capability limitation," Sub7V38 ranked eighth with an *FRPN* value of 424.083 related to the failure mode "operational transfer instability," Sub5V35 ranked ninth with an *FRPN* value of 417.904 related to the failure mode "quality-control deficiency". Finally, F11V15 was identified as the tenth-ranked variability with an *FRPN* value of 396.965 related to the failure mode "difficulty in accessing piping/circuits."

Figure 9 presents the distribution of the average *FRPN* values of the main and sub-functions identified within the scope of the investigated tugboat case. The results indicate that the highest functional risk contribution is related to the propulsion-system selection function (F5). This is followed respectively by the main engine power determination (F4), preliminary design parameter definition (F2), and project verification and revision (F16) functions. In addition, organizational and support functions such as project-team capability (Sub5), shipyard infrastructure (Sub6), and vessel delivery process (Sub7) are also observed to have significant functional risk contributions.

Table 10. Experts' linguistic evaluations.

Code	O_E1	S_E1	D_E1	O_E2	S_E2	D_E2	O_E3	S_E3	D_E3	O_E4	S_E4	D_E4	O_E5	S_E5	D_E5
F1V1	M	MOD	M	M	H	MH	H	H	M	M	MOD	L	M	H	M
F1V2	M	H	M	H	H	L	H	VH	L	H	H	L	H	VH	M
F2V3	H	H	L	H	VH	L	H	VH	VL	H	H	L	H	VH	M
F2V4	M	H	L	H	VH	VL	H	VH	VL	M	H	L	H	VH	M
F4V5	H	VH	VL	H	HAZ	R	VH	HAZ	R	H	VH	VL	H	HAZ	L
F5V6	H	HAZ	R	VH	HAZ	R	VH	CAT	VR	H	HAZ	R	VH	CAT	VL
F5V7	H	VH	L	H	HAZ	VL	VH	HAZ	R	H	VH	L	H	HAZ	VL
F5V8	H	H	M	H	VH	L	H	VH	L	M	H	M	H	VH	L
F8V9	M	MOD	M	H	H	M	M	H	L	H	H	M	H	H	L
F9V10	M	H	M	H	H	L	H	VH	L	H	H	M	H	VH	L
F9V11	M	MOD	M	H	H	M	H	H	L	M	H	M	H	H	L
F10V12	H	MOD	M	H	H	L	H	H	L	M	H	M	H	H	L
F10V13	H	H	M	VH	H	L	VH	VH	L	H	H	M	VH	VH	L
F11V14	M	MOD	M	H	H	M	H	H	L	M	H	M	H	H	L
F11V15	H	H	L	H	VH	VL	VH	VH	R	H	H	L	H	VH	VL
F12V16	M	H	M	H	H	L	H	VH	L	M	H	M	H	VH	L
F12V17	H	MOD	M	VH	H	L	VH	H	L	H	H	M	VH	H	L
F13V18	H	H	M	VH	VH	L	VH	VH	L	H	H	M	VH	VH	L
F13V19	H	MOD	M	H	H	L	VH	H	L	H	MOD	M	H	H	L
F13V20	H	H	L	VH	H	L	VH	VH	VL	H	H	L	H	VH	M
F13V21	H	MOD	H	H	H	M	VH	H	M	H	H	H	H	H	M
F14V22	M	H	VL	H	VH	R	H	VH	R	M	H	VL	H	VH	L
F14V23	M	H	VL	H	VH	R	H	VH	R	M	H	VL	H	VH	L
F14V24	M	VH	R	H	HAZ	R	H	HAZ	VR	M	VH	R	H	HAZ	VL
F15V25	H	MOD	M	H	H	L	VH	H	L	H	H	M	H	H	L
F15V26	H	H	M	VH	H	L	VH	VH	VL	H	H	M	VH	VH	L
F16V27	H	H	L	H	VH	VL	VH	VH	R	H	H	L	H	VH	VL
F16V28	H	VH	L	VH	VH	VL	VH	HAZ	R	H	VH	L	VH	HAZ	VL
Sub1V29	M	H	L	H	H	VL	H	VH	VL	M	H	L	H	VH	M
Sub2V30	H	H	L	H	VH	VL	VH	VH	R	H	H	L	H	VH	VL
Sub3V31	H	H	L	H	VH	VL	H	VH	R	M	H	L	H	VH	VL
Sub4V32	H	H	M	H	H	L	VH	VH	L	H	H	M	H	VH	L
Sub4V33	H	MOD	H	H	H	M	VH	H	M	H	MOD	H	H	H	M
Sub5V34	H	H	L	VH	VH	VL	VH	VH	R	H	H	L	VH	VH	VL
Sub5V35	H	H	L	VH	VH	VL	VH	VH	R	H	H	L	H	VH	VL
Sub6V36	H	H	M	VH	VH	L	VH	VH	VL	H	H	M	VH	VH	L
Sub6V37	H	MOD	M	VH	H	L	VH	H	L	H	H	M	VH	H	L
Sub7V38	H	VH	M	VH	HAZ	L	VH	HAZ	VL	H	VH	M	VH	HAZ	L
Sub7V39	VH	VH	L	VH	HAZ	VL	VH	CAT	R	H	VH	L	VH	HAZ	VL
Sub7V40	H	MOD	H	H	H	M	VH	H	M	H	H	H	H	H	M

Table 11. Defuzzification.

Code	O_a	S_m	D_b	O_a	S_m	D_b	O_a	S_m	D_b	*FRPN_a*	*FRPN_m*	*FRPN_b*
F1V1	4.40	5.60	4.00	5.40	6.60	5.00	6.40	7.60	6.00	98.560	178.200	291.840
F1V2	5.60	6.40	4.60	6.60	7.40	5.60	7.60	8.40	6.60	164.864	273.504	421.344
F2V3	6.00	6.60	5.00	7.00	7.60	6.00	8.00	8.60	7.00	198.000	319.200	481.600
F2V4	5.20	6.60	5.20	6.20	7.60	6.20	7.20	8.60	7.20	178.464	292.144	445.824
F4V5	6.40	7.60	6.20	7.40	8.60	7.20	8.40	9.60	8.20	301.568	458.208	661.248
F5V6	7.20	8.40	7.00	8.20	9.40	8.00	9.20	10.00	9.00	423.360	616.640	828.000
F5V7	6.40	7.60	5.80	7.40	8.60	6.80	8.40	9.60	7.80	282.112	432.752	628.992
F5V8	5.60	6.60	4.60	6.60	7.60	5.60	7.60	8.60	6.60	170.016	280.896	431.376
F8V9	5.20	5.80	4.40	6.20	6.80	5.40	7.20	7.80	6.40	132.704	227.664	359.424
F9V10	5.60	6.40	4.60	6.60	7.40	5.60	7.60	8.40	6.60	164.864	273.504	421.344
F9V11	5.20	5.80	4.40	6.20	6.80	5.40	7.20	7.80	6.40	132.704	227.664	359.424
F10V12	5.60	5.80	4.60	6.60	6.80	5.60	7.60	7.80	6.60	149.408	251.328	391.248
F10V13	7.20	6.40	4.60	8.20	7.40	5.60	9.20	8.40	6.60	211.968	339.808	510.048
F11V14	5.20	5.80	4.40	6.20	6.80	5.40	7.20	7.80	6.40	132.704	227.664	359.424
F11V15	6.40	6.60	5.80	7.40	7.60	6.80	8.40	8.60	7.80	244.992	382.432	563.472
F12V16	5.20	6.40	4.60	6.20	7.40	5.60	7.20	8.40	6.60	153.088	256.928	399.168
F12V17	7.20	5.80	4.60	8.20	6.80	5.60	9.20	7.80	6.60	192.096	312.256	473.616
F13V18	7.20	6.60	4.60	8.20	7.60	5.60	9.20	8.60	6.60	218.592	348.992	522.192
F13V19	6.40	5.60	4.60	7.40	6.60	5.60	8.40	7.60	6.60	164.864	273.504	421.344
F13V20	6.80	6.40	5.00	7.80	7.40	6.00	8.80	8.40	7.00	217.600	346.320	517.440
F13V21	6.40	5.80	3.20	7.40	6.80	4.20	8.40	7.80	5.20	118.784	211.344	340.704
F14V22	5.20	6.60	6.20	6.20	7.60	7.20	7.20	8.60	8.20	212.784	339.264	507.744
F14V23	5.20	6.60	6.20	6.20	7.60	7.20	7.20	8.60	8.20	212.784	339.264	507.744
F14V24	5.20	7.60	7.00	6.20	8.60	8.00	7.20	9.60	9.00	276.640	426.560	622.080
F15V25	6.40	5.80	4.60	7.40	6.80	5.60	8.40	7.80	6.60	170.752	281.792	432.432
F15V26	7.20	6.40	4.80	8.20	7.40	5.80	9.20	8.40	6.80	221.184	351.944	525.504
F16V27	6.40	6.60	5.80	7.40	7.60	6.80	8.40	8.60	7.80	244.992	382.432	563.472
F16V28	7.20	7.40	5.80	8.20	8.40	6.80	9.20	9.40	7.80	309.024	468.384	674.544
Sub1V29	5.20	6.40	5.20	6.20	7.40	6.20	7.20	8.40	7.20	173.056	284.456	435.456
Sub2V30	6.40	6.60	5.80	7.40	7.60	6.80	8.40	8.60	7.80	244.992	382.432	563.472
Sub3V31	5.60	6.60	5.80	6.60	7.60	6.80	7.60	8.60	7.80	214.368	341.088	509.808
Sub4V32	6.40	6.40	4.60	7.40	7.40	5.60	8.40	8.40	6.60	188.416	306.656	465.696
Sub4V33	6.40	5.60	3.20	7.40	6.60	4.20	8.40	7.60	5.20	114.688	205.128	331.968
Sub5V34	7.20	6.60	5.80	8.20	7.60	6.80	9.20	8.60	7.80	275.616	423.776	617.136
Sub5V35	6.80	6.60	5.80	7.80	7.60	6.80	8.80	8.60	7.80	260.304	403.104	590.304
Sub6V36	7.20	6.60	4.80	8.20	7.60	5.80	9.20	8.60	6.80	228.096	361.456	538.016
Sub6V37	7.20	5.80	4.60	8.20	6.80	5.60	9.20	7.80	6.60	192.096	312.256	473.616
Sub7V38	7.20	7.60	4.80	8.20	8.60	5.80	9.20	9.60	6.80	262.656	409.016	600.576
Sub7V39	7.60	7.80	5.80	8.60	8.80	6.80	9.60	9.60	7.80	343.824	514.624	718.848
Sub7V40	6.40	5.80	3.20	7.40	6.80	4.20	8.40	7.80	5.20	118.784	211.344	340.704

Table 12. Failures' risk level color scale.

Crisp *FRPN* range	Risk level	Scale
FRPN≥500	Very high	
350≤*FRPN*<500	High	
200≤*FRPN*<350	Moderately high	
100≤*FRPN*<200	Moderate	
FRPN<100	Low	

As presented in Table 15, the comparison between warranty-period deficiency records and the FRAM-Fuzzy FMEA results indicates that the highest-ranked variability-induced failure modes correspond well with the major operational problems observed during the vessel's warranty period. In particular, propulsion-system integration deficiencies, verification shortcomings, HVAC-related failures, alarm-monitoring system instabilities, and accommodation-layout problems were identified both in the operational records and in the *FRPN* prioritization results. These findings provide practical validation of the proposed FRAM-Fuzzy FMEA framework under real shipbuilding and operational conditions.

According to the results, failure modes related to the propulsion system were found to have the highest perceived risk levels (F5V6, F4V5, and F5V7). High maneuverability is one of the fundamental performance requirements that must be achieved in tugboats for operational success [72]. Particularly during active escort operations, a tugboat is expected to perform under high dynamic loads without compromising either its own safety or the safety of the assisted vessel. The compatibility between main engine power, propulsion system characteristics, and hull form plays a decisive role in achieving this performance. Incompatibilities among these elements may lead to deficiencies in bollard pull capacity, maneuverability, and overall operational performance. Furthermore, reductions in propulsion efficiency may adversely affect service quality, while vibration-related problems may negatively influence both crew working conditions and equipment reliability. Therefore, the experts evaluated hull-propulsion system incompatibility as a critical failure modes that may affect multiple functions in the later stages of the design process and lead to significant operational consequences, and consequently ranked it as the variability with the highest perceived risk.

The objective of ship design is to construct vessels that comply with safe navigation standards. Negative variabilities occurring from the beginning of the design process to the final stage affect the vessel delivery process. During delivery, failures and deficiencies that do not affect the vessel's floatability or navigation safety are generally rectified through warranty processes. However, failures and deficiencies related to propulsion performance, insufficient bollard pull, structural systems, stability, piping arrangements, and similar systems may lead to delivery delays and major revisions [73]. Therefore, it is essential that failures and deficiencies are identified and eliminated throughout the entire process before reaching the delivery stage. For this reason, major failures and deficiencies at the delivery stage (Sub7V39) were evaluated by the experts as a high-risk failure mode.

Although classification rules are clearly defined, deficiencies may still occur during their implementation in the design and physical construction stages. Such deficiencies must be eliminated through appropriate revisions. At this point, cost and schedule pressures may lead to certain requirements being overlooked or interpreted incompletely. Furthermore, the failure of plan approval and quality control departments to detect these deficiencies may result in revision processes being bypassed. This situation increases functional variability negatively during tugboat delivery. Therefore, the failure mode (F14V24, F16V28), associated with the function of verification of design and construction and revision of deficiencies, was evaluated by the experts as having a high perceived risk level.

Failure modes generated by variabilities originating from organizational functions were generally perceived by the experts as an important source of risk (Sub5V34, Sub5V35). These findings indicate that human and organizational factors play a significant role in the design and construction process [74]. Even when technical design procedures are well defined, insufficient expertise, communication deficiencies, or inadequate quality assurance practices may increase functional variability throughout the design process and consequently affect the vessel delivery process.

For sensitivity and uncertainty the Kendall's W results indicated significant agreement among the experts for occurrence (W=0.689), severity (W=0.872), and detection (W=0.805), with p<0.001 in all cases. In the LOEO analysis, Spearman's correlation coefficients ranged from 0.991 to 0.998, while the maximum rank shift ranged from two to four positions. Under the alternative weighting scenarios, the correlations ranged from 0.961 to 0.992. The largest rank

Table 13. Failures' *FRPN* values and risk rankings.

Code	Crisp *FRPN*	Rank	Risk level
F1V1	189.533	40	Moderate
F1V2	286.571	29	Moderately High
F2V3	332.933	21	Moderately High
F2V4	305.477	25	Moderately High
F4V5	473.675	4	High
F5V6	622.667	1	Very High
F5V7	447.952	5	High
F5V8	294.096	28	Moderately High
F8V9	239.931	34	Moderately High
F9V10	286.571	29	Moderately High
F9V11	239.931	34	Moderately High
F10V12	263.995	33	Moderately High
F10V13	353.941	18	High
F11V14	239.931	34	Moderately High
F11V15	396.965	10	High
F12V16	269.728	32	Moderately High
F12V17	325.989	22	Moderately High
F13V18	363.259	15	High
F13V19	286.571	29	Moderately High
F13V20	360.453	16	High
F13V21	223.611	37	Moderately High
F14V22	353.264	19	High
F14V23	353.264	19	High
F14V24	441.760	6	High
F15V25	294.992	27	Moderately High
F15V26	366.211	14	High
F16V27	396.965	10	High
F16V28	483.984	3	High
Sub1V29	297.656	26	Moderately High
Sub2V30	396.965	10	High
Sub3V31	355.088	17	High
Sub4V32	320.256	24	Moderately High
Sub4V33	217.261	39	Moderately High
Sub5V34	438.843	7	High
Sub5V35	417.904	9	High
Sub6V36	375.856	13	High
Sub6V37	325.989	22	Moderately High
Sub7V38	424.083	8	High
Sub7V39	525.765	2	Very High
Sub7V40	223.611	37	Moderately High

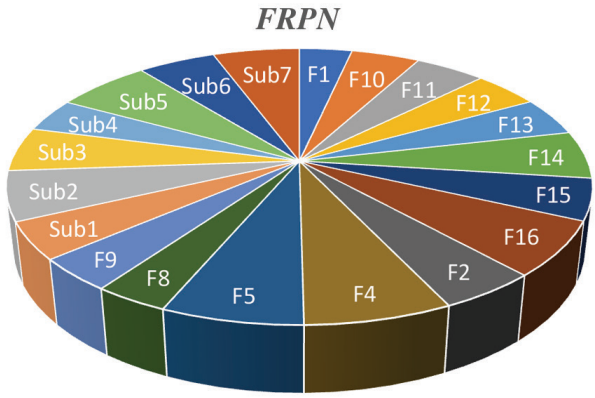


Figure 9. Distribution of average *FRPN* values according to functional variabilities.

Table 14. Failures' *FRPN* values and risk rankings.

Analysis	Criterion/scenario	Spearman's ρ	Maximum rank shift
Expert agreement	Occurrence	W=0.689	-
Expert agreement	Severity	W=0.872	-
Expert agreement	Detection	W=0.805	-
LOEO analysis	Exclusion of E1-E5	ρ=0.991-0.998	2-4
Weight sensitivity	O-dominant (0.50, 0.25, 0.25)	ρ=0.961	11
Weight sensitivity	S-dominant (0.25, 0.50, 0.25)	ρ=0.992	4
Weight sensitivity	D-dominant (0.25, 0.25, 0.50)	ρ=0.977	7

Table 15. Comparison of warranty-period deficiencies and FRAM-Fuzzy FMEA results.

Operational deficiency observed during warranty	Variability	Failure mode	*FRPN* rank
Propulsion system vibration and bearing overheating	F5V6	Hull-propulsion system incompatibility	1
Multiple deficiencies accumulated at delivery	Sub7V39	Aggregated functional resonance	2
Repetitive operational non-conformities	F16V28	System-validation insufficiency	3
Main engine-ASD integration problems	F4V5	Limited propulsion integration flexibility	4
Propulsion alignment and vibration problems	F5V7	Propulsion-system alignment deficiency	5
Classification and compliance deficiencies	F14V24	Classification compliance deficiency	6
Engineering supervision limitations	Sub5V34	Engineering-team capability limitation	7
Vessel delivered with existing failures	Sub7V38	Operational transfer instability	8
Insufficient quality-control activities	Sub5V35	Quality-control deficiency	9
Errors and deficiencies in piping/circuit installations	F11V15	Difficulty in accessing piping/circuits	10
HVAC condensation and leakage	F10V13	HVAC outfitting deficiency	18
Alarm monitoring system deficiencies	F12V17	Alarm-system integration instability	22
Improper equipment/material selection	Sub4V32	Improper equipment/material selection	24
Chain-locker capacity deficiency	F9V10	Insufficient chain-locker capacity	29
Accommodation-layout deficiencies	F10V12	Accommodation-layout incompatibility	33

shift occurred in the occurrence-dominant scenario. Overall, the results indicate that the *FRPN* ranking is stable, although it is relatively more sensitive to changes in occurrence weighting.

The results indicate that risk mitigation efforts should primarily focus on propulsion system selection and hull integration, construction control and verification activities, and the organizational capability of the shipyard. It can be observed that risk perception is mainly shaped in areas where failure modes originating from human, technological, and organizational factors intersect. In the case study, the FRAM method identified the areas where variability accumulated in a negative manner. These areas essentially represent the reference points where risk-reducing control measures should be implemented. During the design process, the integration of the propulsion system and hull should be verified through calculations, model studies, and previous projects. Calculations should be reviewed again in accordance with any changes in principal dimensions. The integration process of new orders with ongoing construction projects should be managed through detailed control checklists. Based on the findings of the study, the recommended risk mitigation and control measures for reducing the identified critical risks are presented in the following Figure 10. Risk control measures generally consist of monitoring, planning, anticipating, and supporting activities [75].

Since the tugboat design and construction process was systematically and functionally defined using the FRAM method, the development of practical control checklists may contribute to the management of variability and the early identification of risks. In addition, storing project information and progress details in cloud-based systems may enable rapid reviews and monitoring whenever required. In this regard, the development of a cloud-based platform covering the entire construction process could facilitate the work of project managers by improving control, coordination, and decision-making activities throughout the project lifecycle.

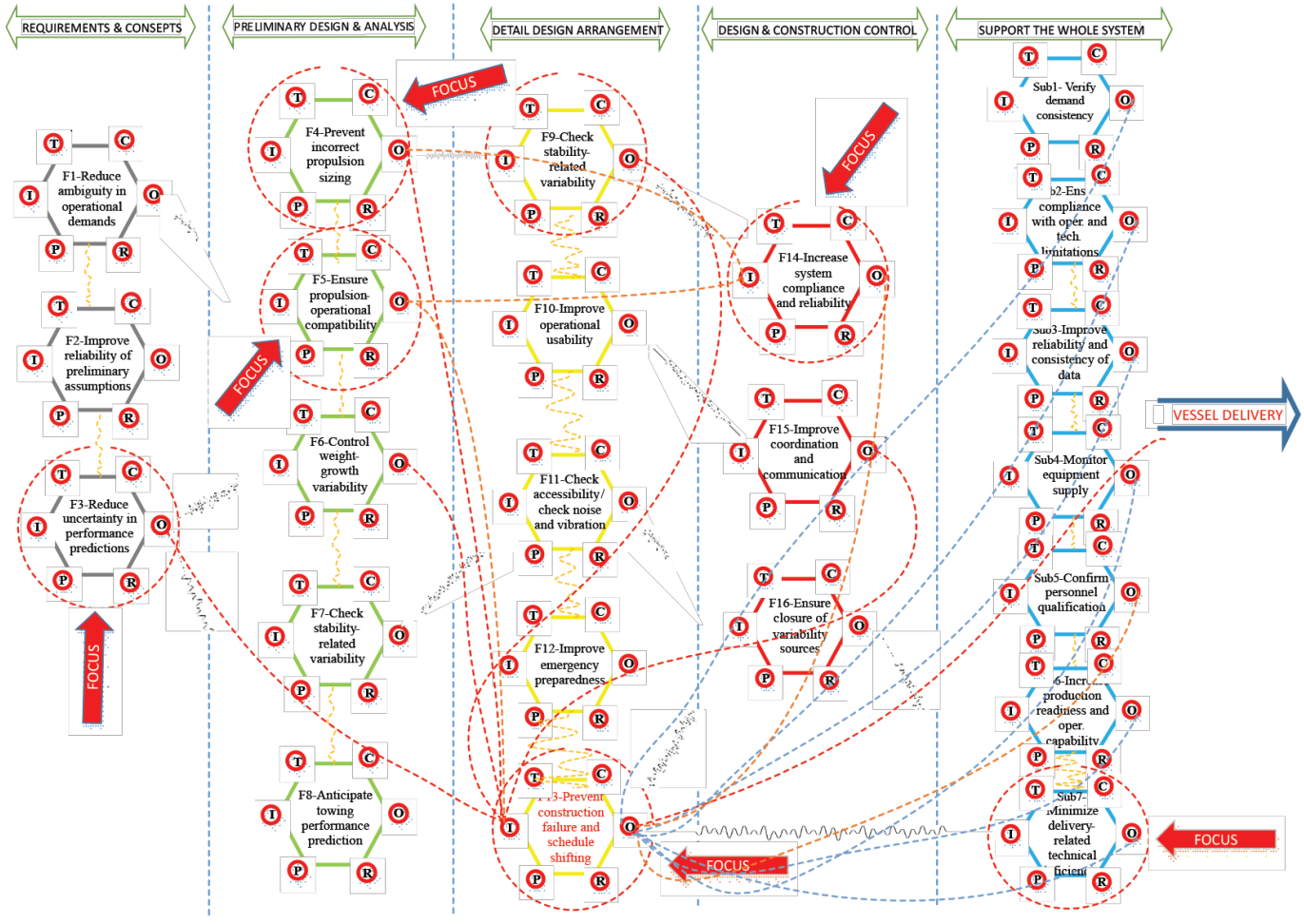


Figure 10. Risk mitigation and control measures.

5. Conclusion

This study presents an integrated FRAM-Fuzzy FMEA framework to evaluate functional variability and risk propagation within tugboat design and shipbuilding processes from a resilience-oriented systems perspective. Unlike conventional linear risk-assessment approaches, the methodology considers tugboat design and shipbuilding as a complex socio-technical system in which technical calculations, operational requirements, production activities, classification-society compliance processes, and organizational interactions continuously influence each other. Through the FRAM analysis, the functional relationships among design phases, main engine and propulsionsystem selection, stability verification, general and deck equipment arrangement, physical construction, shipbuilding organization with all sub-activities, revision-management processes and ship delivery were systematically modeled. The findings demonstrated that variability generated during early design stages may propagate throughout subsequent engineering, production, and verification activities, thereby creating system-wide variability effects. In particular, operational requirement definition, hull-main engine-propulsion compatibility, revision-management processes, engineering team, quality performance, classification and communication of shipyard departments, and ship delivery were identified as critical functions with high variability potential.

The results showed that propulsion system incompatibilities, aggregation of negative variability on ship delivery and project validation insufficiency, and coordination failures between design and production units constitute the most critical risk areas within tugboat projects. The findings further demonstrated that organizational and communication-related deficiencies may become as critical as technical engineering failures in complex maritime systems. Accordingly, the study revealed that risk formation within tugboat projects emerges not only from isolated technical failures, but also from the interaction, aggregation, and propagation of functional variabilities across interconnected system functions.

The integration of FRAM and Fuzzy FMEA enabled the transformation of qualitative functional variability into semi-quantitative risk prioritization. In this respect, the framework provides a proactive, resilience-oriented, and system-based safety assessment approach for tugboat design and shipbuilding processes. From a practical perspective, the framework may support shipyards, designers, shipowners, and classification stakeholders in identifying critical variability sources during early-stage design, verification, and production-planning activities. The framework enables the early identification of critical variability pathways associated with propulsion-system integration, accommodation and HVAC arrangements, classification compliance, organizational coordination, and project-verification activities. By prioritizing variability-induced failure modes according to their *FRPN* values, engineering resources, inspection efforts, and quality-control activities can be allocated more effectively. Consequently, potential design deficiencies, integration problems, and coordination weaknesses may be detected before they evolve into costly rework activities, warranty-period deficiencies, operational failures, or project delays. Furthermore, the study demonstrated that strengthening monitoring capability, technical verification procedures, revision management, and interdisciplinary coordination may significantly reduce variability propagation and improve overall system reliability. Accordingly, the proposed framework may contribute to improving construction quality, reducing warranty-period deficiencies, enhancing operational safety, and supporting the timely delivery of vessels with increased reliability.

Although the construction functions were defined to represent the general tugboat design and construction process, the empirical analysis was based on a single 70-ton bollard-pull ASD tug and five experts. Therefore, the *FRPN* values and risk rankings may be influenced by project-specific conditions and the composition of the expert panel, limiting the generalizability of the findings. Future studies should apply the framework to different tugboat types and shipyards using larger and more diverse expert panels.

Future studies may further improve the framework through the integration of real-time operational and maneuvering data obtained from harbor tug operations, including escort towing conditions, indirect towing forces, dynamic loading effects, and bollard-pull performance variations. In addition, the effects of hybrid and electric propulsion systems, alternative fuel applications, autonomous tugboat concepts, and advanced propulsion arrangements on functional variability and system resilience may be investigated in future research. The proposed methodology may also be expanded through full-scale operational data collection, digital-twin-supported tugboat simulations, and lifecycle-based maintenance analyses. Furthermore, integrating predictive maintenance systems, operational performance monitoring, and human-factor assessments involving tug masters, pilots, and shipyard personnel may further improve the realism and applicability of variability and risk assessments in future tugboat projects.

Footnotes

Financial Disclosure: The author declares that this study did not receive any financial support.

References

[1] A. Papanikolaou, *Ship design: Methodologies of preliminary design*. Springer Cham. 2014.

[2] J.-S. Park, T.-N. Nguyen, C.-T. Dinh, T. Huynh, and Y.-B. Kim, "Modeling and control of tugboat-assisted operation for marine vessels," *Journal of Marine Science and Engineering*, vol. 13, no. 4, pp. 804, Apr 2025.

[3] B. Gürgen, and M Ada, "Risk assessment to improve reliability in towing system of tugboats using fuzzy based FMEA," *Brodogradnja*, vol. 76, pp. 1-24, Aug 2025.

[4] "*Tugboat Market Size (Report ID: FBI108157)*", Fortune Business Insights, Accessed: April 6, 2026, https://www.fortunebusinessinsights.com/tugboats-market-108157.

[5] B. Das, and N. Tejpal, "Major factors affecting tugboat ship design and construction," *Journal of Ship Production*, vol. 24, no. 4, pp. 214-220, Nov 2008.

[6] E. Hollnagel. *FRAM-the functional resonance analysis method*, CRC Press: London. 2017.

[7] M. Sujan, et al. "Operationalising FRAM in healthcare: a critical reflection on practice," *Safety Science*, vol. 158, 105994, Feb 2023.

[8] C. Chen, et al. "Resilience assessment and management: a review on contributions on process safety and environmental protection," *Process Safety and Environmental Protection*, vol. 170, pp. 1039-1051, Feb 2023.

[9] J. Friederich, and S. Lazarova-Molnar, "Reliability assessment of manufacturing systems: a comprehensive overview, challenges and opportunities," *Journal of Manufacturing Systems*, vol. 72, pp. 38-58, 2024.

[10] R. Patriarca, "Framing the FRAM: a literature review on the functional resonance analysis method," *Safety Science*, vol. 129, pp. 1-23, 2020.

[11] E. Hollnagel, *Barriers and accident prevention* (1st ed.), Routledge: London. 2004.

[12] J. C. Le Coze, "The 'new view' of human error: origins, ambiguities, successes and critiques," *Safety Science*, vol. 154, 105853, Oct 2022.

[13] G. Praetorius, M. Lundh, and M. Lützhöft, "Learning from the past for pro-activity: a re-analysis of the accident of the MV herald of free enterprise," In: *Proceedings of the 4th Resilience Engineering Symposium*, pp. 217-226, 2011.

[14] D. Kee, "Comparison of systemic accident investigation techniques based on the Sewol Ferry capsizing," *Journal of Ergonomics Society of Korea*, vol. 36, no. 5, pp. 485-498, Oct 2017.

[15] Y. Wang, E. Zio, X. Wei, D. Zhang, and B. Wu, "A resilience perspective on water transport systems: the case of Eastern Star," *International Journal of Disaster Risk Reduction*, 33, 343-354, Feb 2019.

[16] A. K. Rammos, "*Application of the functional resonance analysis method (FRAM) on fires onboard ship*," Bachelor's Thesis, National Technical University of Athens. 2019.

[17] E. Salihoglu, and E. B. Beşikçi, "The use of functional resonance analysis method (FRAM) in a maritime accident: a case study of prestige," *Ocean Engineering*, vol. 219, 108223, 2021.

[18] S. H. Ümitli, B. O. Ceylan, and A. Ercetin, "Functional resonance analysis (FRAM) of a chemical tanker fire: a systematic approach to enhancing maritime accident analysis," *Ocean Engineering*, vol. 355, no. 1, p. 125077, May 2026.

[19] G. Praetorius, "*Vessel traffic service (VTS): a maritime information service or traffic control system? Understanding everyday performance and resilience in a socio-technical system under change*," Ph.D. Dissertation, Chalmers University of Technology. 2014.

[20] G. Praetorius, E. Hollnagel, and J. Dahlman, "Modelling vessel traffic service to understand resilience in everyday operations," *Reliability Engineering and System Safety*, vol. 141, pp. 10-21, Sep 2015.

[21] K. Kulkarni, F. Goerlandt, J. Li, V. O. Banda, and P. Kujala, "Preventing shipping accidents: past, present, and future of waterway risk management with Baltic Sea focus," *Safety Science*, vol. 129, p. 104798, Sep 2020.

[22] I. G. M. S. Adhita, M. Fuchi, T. Konishi, and S. Fujimoto, "Ship navigation from a safety-ii perspective: a case study of training-ship operation in coastal area," *Reliability Engineering and System Safety,* vol. 234, p. 109140, Jun 2023.

[23] M. V. C. Aguilera, et al. "Modelling performance variabilities in oil spill response to improve system resilience," *Journal of Loss Prevention in the Process Industries*, vol. 41, pp. 18-30, May 2016.

[24] W. Qiao, X. Ma, Y. Liu, and W. Deng, "Resilience evaluation of maritime liquid cargo emergency response by integrating FRAM and a BN: a case study of a propylene leakage emergency scenario," *Ocean Engineering*, vol. 247, p. 110584, Mar 2022.

[25] L. Ma, X. Ma, Y. Liu, W. Deng, and H. Lan, "Risk assessment of coupling links in hazardous chemicals maritime transportation system," *Journal of Loss Prevention in the Process Industries*, vol. 82, p. 105011, Apr 2023.

[26] J. Nasur, K. Bogusławski, P. Wolska, M. Gil, and K. Wróbel, "Toward modeling emergency unmooring of manned and autonomous ships: a combined FRAM+HFACS-MA approach," *Safety Science*, vol. 181, p. 106676, Jan 2025.

[27] Y. Liu, X. Ma, W. Qiao, and B. Han, "A systematic methodology for resilience evaluation of ship operation in Arctic waters combining FRAM and extended Bayesian network," *SSRN Electronic Journal*, Mar 2024. [Preprint]

[28] Y. Zhao, X. Ma, W. Qiao, and J. Zhang, "Resilient maritime transportation system from the perspective of FRAM: conceptualization and assessment," *Reliability Engineering and System Safety*, vol. 262, p. 111155, Oct 2025.

[29] Z. Zhang, et al. "Safety analysis of human-machine interaction of autonomous ships using system theory and complex networks," *Ocean Engineering*, vol. 351(Part 1), p. 124266, 2026.

[30] M. M. Abaei, R. Abbassi, V. Garaniya, E. Arzaghi, and A. Bahoo Toroody, "A dynamic human reliability model for marine and offshore operations in harsh environments," *Ocean Engineering*, vol. 173, pp. 90-97, Feb 2019.

[31] D. Smith, B. Veitch, F. Khan, and R. Taylor, "Using the FRAM to understand Arctic ship navigation: assessing work processes during the exxon valdez grounding," *International Journal on Marine Navigation and Safety of Sea Transportation*, vol. 12, no. 3, 2018a.

[32] D. Smith, B. Veitch, F. Khan, and R. Taylor, "Using FRAM to evaluate ship designs and regulations," *Marine Design XIII, Taylor and Francis Group, London, UK*, pp. 677-684, 2018b.

[33] B. O. Ceylan, Ç. Karatuğ, E. Akyüz, Y. Arslanoğlu, and G. Boustras, "A system theory (STAMP) based quantitative accident analysis model for complex engineering systems," *Safety Science*, vol. 166, p. 106232, Oct 2023.

[34] M. B. Zaman, et al. "Fuzzy FMEA model for risk evaluation of ship collisions in the Malacca Strait based on AIS data," *Journal of Simulation*, vol. 8, pp. 91-104, 2014.

[35] E. Akyüz, İ. Akgün, and M. Çelik, "A fuzzy failure mode and effects approach to analyse concentrated ınspection campaigns on board ships," *Maritime Policy and Management*, vol. 43, pp. 887-908, Apr 2016.

[36] E. Akyüz, and E. Çelik, "A quantitative risk analysis by using interval type-2 fuzzy FMEA approach: the case of oil spill," *Maritime Policy and Management*, vol. 45, no. 8, pp. 979-994, 2018.

[37] R. K. Sharma, D. Kumar, and P. Kumar, "Fuzzy modeling of system behavior for risk and reliability analysis," *International Journal of Systems Science*, vol. 39, pp. 563-581, Apr 2008.

[38] P. Liu, Y. Wu, Y. Li, and X. Wu, "An improved FMEA method based on the expert trust network for maritime transportation risk management," *Expert Systems with Applications*, vol. 238 (Part A), p. 121705, Mar 2024.

[39] B. O. Ceylan, D. A. Akyar, and M. S. Çelik, "A novel FMEA approach for risk assessment of air pollution from ships," *Marine Policy,* vol. 150, p. 105536, 2023.

[40] B. Doğanay, B. Çavuşoğlu, and Ç. B. Güler, "A study on minimizing potential accidents in ship bunkering operation through use of failure mode and effect analysis," *Journal of Marine and Engineering Technology*, vol. 3, no. 1, pp. 1-13, 2023.

[41] L. Guo, J. Gao, J. Yang, and J. Kang, "Criticality evaluation of petrochemical equipment based on fuzzy comprehensive evaluation and a BP neural network," *Journal of Loss Prevention in the Process Industries*, vol. 22, pp. 469-476, Jul 2009.

[42] M. Özkok, "Risk assessment in ship hull structure production using FMEA," *Journal of Marine Science and Technology*, vol. 22, no. 2, 2014.

[43] Z. Yang, and J. Wang, "Use of fuzzy risk assessment in FMEA of offshore engineering systems," *Ocean Engineering*, vol. 95, pp. 195-204, Feb 2015.

[44] Ş. Helvacıoğlu, and E. Özen, "Fuzzy based failure modes and effect analysis for yacht system design," *Ocean Engineering*, vol. 79, pp. 131-141, Mar 2014.

[45] V. Karanović, B. O. Ceylan, and M. Jocanović, "Reliable ships: a fuzzy FMEA based risk analysis on four-ram type hydraulic steering system," *Ocean Engineering*, 314(Part 2), p. 119758, Dec 2024.

[46] A. Papanikolaou, "*Ship design, construction and operation*," The Maritime Engineering Reference Book, A. F. Molland, ed., Butterworth-Heinemann, pp. 636-727, 2008.

[47] A. Borzyszkowski, "*Predicting port tugboat operations for arriving and departing vessels using machine learning*," Master's Thesis. Feb 2022.

[48] O. Royet del Gallego, and D. Orozco Howard, "Conceptual design of a 20 TBP port tugboat for the 'Bahía Málaga' ARC naval base," *Ship Science and Technology,* vol. 12, no. 24, pp. 39-48, 2019.

[49] D. D. Woods, "Four concepts for resilience and the implications for the future of resilience engineering," *Reliability Engineering and System Safety*, vol. 141, pp. 5-9, 2015.

[50] E. Hollnagel, *Cognitive reliability and error analysis method (CREAM)*, Elsevier Science, 1998.

[51] L. V. Rosa, A. N. Haddad, and P. V. R. de Carvalho, "Assessing risk in sustainable construction using the functional resonance analysis method (FRAM)," *Cognition, Technology and Work*, vol. 17, pp. 559-573, Apr 2015.

[52] P. Rutkowska, and M. Krzyżanowski, "FRAM modelling of the transfer of control over aircraft," *Scientific Journal of Silesian University of Technology. Series Transport*, vol. 101, pp. 159-166, 2018.

[53] R. G. Mock, L. Lopez de Obeso, C. Zipper, and M. Schönenberger, "Resilience assessment of internet of things: a case study on smart buildings," *ESREL 2016 Conference Proceedings*, Glasgow, UK, pp. 2260-2267, 2017.

[54] R. Patriarca, G. Di Gravio, F. Costantino, and M. Tronci, "The functional resonance analysis method for a systemic risk based environmental auditing in a sinter plant: a semi-quantitative approach," *Environmental Impact Assessment Review*, vol. 63, pp. 72-86, Mar 2017.

[55] H. Slim, and S. A. Nadeau, "Proposal for a predictive performance assessment model in complex sociotechnical systems combining fuzzy logic and the functional resonance analysis method (FRAM)," *American Journal of Industrial and Business Management*, vol. 9, pp. 1345-1375, Jun 2019.

[56] H. Slim, and S. Nadeau, "A mixed rough sets/fuzzy logic approach for modelling systemic performance variability with FRAM," *Sustainability*, vol. 12, p. 1918, Mar 2020.

[57] H. C. Liu, L. Liu, and N. Liu, "Risk evaluation approaches in failure mode and effects analysis: a literature review," *Expert Systems with Applications*, vol. 40, pp. 828-838, Feb 2013.

[58] J. Huang, J. X. You, H. C. Liu, and M. S. Song, "Failure mode and effect analysis improvement: a systematic literature review and future research agenda," *Reliability Engineering & System Safety*, vol. 199, p. 106885, Jul 2020.

[59] J. B. Bowles, and C. E. Peláez, "Fuzzy logic prioritization of failures in a system failure mode, effects and criticality analysis," *Reliability Engineering & System Safety*, vol. 50, pp. 203-213, 1995.

[60] N. R. Sankar, and B. S. Prabhu, "Modified approach for prioritization of failures in a system failure mode and effects analysis," *International Journal of Quality & Reliability Management*, vol. 18, pp. 324-336, Apr 2001.

[61] C. S. Carlson, "*Effective FMEAs: Achieving Safe, Reliable and Economical Products and Processes Using Failure Mode and Effect Analysis*," 1st ed., Hoboken, NJ: John Wiley & Sons; Apr 2012.

[62] United States Department of Defense, 1949, MIL-P-1629-Procedures for Performing a Failure Mode Effect and Critical Analysis, Department of Defense, U.S. https://src.alionscience.com/pdf/MIL-STD-1629RevA.pdf (accessed Mar. 9, 2026).

[63] N. Chanamool, and T. Naenna, "Fuzzy FMEA application to improve decision-making process in an emergency department," *Applied Soft Computing*, vol. 43, pp. 441-453, Jun 2016.

[64] Z. X. Zhang, L. Yang, Y. N. Cao, and Y. W. Xu, "An improved FMEA method based on ANP with probabilistic linguistic term sets," *Int J Fuzzy Syst*, vol. 24, pp. 2905-2930, May 2022.

[65] Y.-M. Wang, K.-S. Chin, G. K. K. Poon, and J.-B. Yang, "Risk evaluation in failure mode and effects analysis using fuzzy weighted geometric mean," *Expert Systems with Applications*, vol. 36, no. 2, Part 1, pp. 1195-1207, Mar 2009.

[66] L. A. Zadeh, "Fuzzy sets," *Information and Control*, vol. 8, pp. 338-353, Jun 1965.

[67] A. McGill, R. McCloskey, D. Smith, V. Salehi, and B. Veitch, "Building a functional resonance analysis method model: practical guidance on qualitative data collection and analysis," *International Journal of Qualitative Methods*, vol. 22, Nov 2023.

[68] B. Jakkula, M. G. Raj, and C. S. N. Murthy, "Fuzzy-FMEA risk evaluation approach for LHD machine-a case study," *Journal of Sustainable Mining*, vol. 18, pp. 257-268, Nov 2019.

[69] M. G. Kendall, and J. D. Gibbons, *"Rank Correlation Methods,"* Oxford University Press, New York. 1990.

[70] H. Hensen, *"Tug Use in Port: A Practical Guide,"* 4th ed., STC Publishing; 2003.

[71] International Association of Classification Societies, 2022, classification societies: what, why and how?, International Association of Classification Societies. https://iacs.org.uk/wp-content/uploads/2022/06/Classification-what-why-how.pdf.

[72] J.-H. Choi, J.-Y. Jang, and J. Woo, "A review of autonomous tugboat operations for efficient and safe ship berthing," *Journal of Marine Science and Engineering*, vol. 11, p. 1155, May 2023.

[73] G. Vizentin, G. Vukelic, L. Murawski, N. Recho, and J. Orovic, "Marine propulsion system failures-a review," *Journal of Marine Science and Engineering*, vol. 8, p. 662, Aug 2020.

[74] J. E. M. França, and E. Hollnagel, "*Human factors approach to assess risks and reliability in offshore operations with FRAM (functional resonance analysis method),*" Conference: Offshore Technology Conference Brasil, Oct 2023.

[75] T. A. Saurin, J. Rooke, and L. Koskela, "A complex systems theory perspective of lean production," *International Journal of Production Research*, vol. 51, pp. 5824-5838, Oct 2013.

RESEARCH ARTICLE

DOI: 10.54926/jnamt.2026.2649

J Nav Architect Mar Technol 2026;228:92-116

A Geographically Anchored MMG-Based Ship Maneuvering Simulator for Comparative Control Testing

Ahmad Irham Jambak[1], Mostafa Abdelkhalek[2], Ismail Bayezit[2], Omer Kemal Kinaci[3]

[1]İstanbul Technical University Faculty of Mechanical Engineering, Department of Mechatronics Engineering, İstanbul, Türkiye
[2]İstanbul Technical University Faculty of Aeronautics and Astronautics, Department of Aeronautical Engineering, İstanbul, Türkiye
[3]İstanbul Technical University Faculty of Naval Architecture and Ocean Engineering, Department of Naval Architecture and Ocean Engineering, İstanbul, Türkiye

To cite this article: A. I. Jambak, M. Abdelkhalek, I. Bayezit, and O. K. Kinaci. A geographically anchored MMG-based ship maneuvering simulator for comparative control testing. *J Nav Architect Mar Technol*. 2026;228:92-116.

Received: 06.06.2026 - **Revision Requested:** 10.08.2026 - **Last Revision Received:** 19.08.2026 - **Accepted:** 12.09.2026 - **Publication Date:** 20.10.2026

Abstract

Reliable evaluation of ship-maneuvering controllers requires more than a dynamically plausible vessel trajectory. For example the maneuvering model, geographically defined scenario, controller interface, and performance evidence must be connected through a reproducible workflow. This study develops a geographically referenced simulator that integrates a Maneuvering Modeling Group (MMG) representation of the full-scale and L7 KVLCC2 model with waypoint guidance, heading and speed control, synchronized data logging, and post-run assessment for an archived route segment in the İstanbul Strait. A dual-loop proportional-integral-derivative (PID) controller, a fuzzy-logic controller, and a neural-network controller are implemented through a common heading-control interface. The recorded signals are evaluated using peak overshoot, median settling time, heading root-mean-square error, rudder-saturation ratio, and maximum speed-loss ratio, with user-defined PASS/WARN/FAIL thresholds. Model-scale and full-scale cases demonstrate the end-to-end route, control, MMG state-propagation, visualization, and diagnostic chain and expose controller-dependent differences in transient response and actuator use. The main contribution is therefore a traceable experimental environment for implementing and examining alternative ship-control strategies within geographically meaningful scenarios.

Keywords: Ship maneuvering simulator, MMG model, comparative control testing, waypoint guidance, fuzzy control, neural network control

1. Introduction

Reliable ship maneuvering is central to safe and efficient operation in ports, narrow channels, and congested waterways, where small heading errors or delayed actuator responses can compromise route keeping and increase rudder activity and speed loss. The problem is consequential for a transport system that carries more than 80% of international trade by volume [1]. The broader economic role of maritime transport is also extensively discussed in maritime economics literature [2]. Additionally, shipping also accounted for 2.89% of global anthropogenic CO_2 emissions in 2018 [3]. Although a simulator alone cannot establish an environmental benefit, this scale motivates methods that support safer and more efficient controller development. From a control perspective, the difficulty arises from nonlinear, strongly coupled surge-sway-yaw dynamics, actuator constraints, and environmental loads. Controller development must therefore be supported by evidence that is physically meaningful, repeatable, and directly related to operational performance.

Physical model experiments and sea trials are still essential for validating maneuvering predictions. However, their high cost, safety requirements, and limited repeatability make

Address for Correspondence: Assoc. Prof. Dr. Ismail Bayezit, İstanbul Technical University Faculty of Aeronautics and Astronautics, Department of Aeronautical Engineering, İstanbul, Türkiye
E-mail: bayezit@itu.edu.tr
ORCID ID: orcid.org/0000-0001-9345-5108

Copyright© 2026 The Author(s). Published by Galenos Publishing House on behalf of UCTEA Turkish Chamber of Naval Architects and Marine Engineers.
Licensed under a Creative Commons Attribution-NonCommercial-NoDerivatives 4.0 (CC BY-NC-ND) International License

them impractical at every stage of controller development. Numerical simulation offers a useful intermediate step, allowing control laws to be implemented, tested under challenging conditions, and compared before moving to physical trials [4]. Nevertheless, the strength of simulation-based evidence depends on the accuracy of the maneuvering equations, hydrodynamic coefficients, numerical solver, actuator model, and selected scenarios. Simulation should therefore be viewed as a tool for guiding and reducing the need for physical experiments rather than replacing experimental validation [5].

Among physics-based modeling approaches, the Maneuvering Modeling Group (MMG) framework is particularly suitable for controller-oriented simulation because it separates the contributions of the hull, propeller, and rudder while retaining variables with clear engineering meaning [6,7]. However, model fidelity alone is not enough to ensure a reproducible controller evaluation. A geographically defined route must be converted consistently into the local coordinate frame used by the guidance and control algorithms. Competing controllers must also be tested using equivalent references, constraints, and operating conditions, while reference commands, vessel states, and actuator responses must remain properly synchronized. Without this consistency throughout the simulation process, a trajectory that appears successful offers limited evidence of either prediction accuracy or controller performance.

Previous studies have advanced several elements of this workflow, including MMG-based maneuvering prediction, path-following control, autonomous-navigation test environments, and mission-level simulation [8-12]. However, methodological weakness remains at the interfaces between these elements. When vessel dynamics, geographic visualization, controller implementation, and post-processing are handled in separate tools, it becomes difficult to trace model assumptions and signal definitions across the full workflow. As a result, observed differences in performance may arise from inconsistent scenarios, reference signals, or evaluation metrics rather than from the controllers themselves. An integrated simulator becomes scientifically valuable only when it maintains a clear and traceable connection between route definition, dynamic response, and quantitative evaluation.

Against this background, this study develops and evaluates an MMG simulation environment designed to support repeatable controller implementation and post-simulation assessment. The platform combines the full-scale and L7 KVLCC2 vessel models with waypoint-based guidance and a geographic representation of an archived route through the İstanbul Strait. It also maintains a consistent exchange of heading references, vessel states, and actuator commands throughout the simulation workflow. Manual control, dual-loop proportional-integral-derivative (PID) heading and speed control, fuzzy-logic (FL) heading control, and neural-network (NN) heading control are implemented as representative case studies.

This study examines whether route definition, maneuvering dynamics, controller implementation, and performance evaluation can be combined within a single traceable workflow without obscuring the assumptions that shape the results. To investigate this issue, the simulator records synchronized reference commands, vessel states, and actuator responses throughout each run. Completed simulations are then assessed using measures of transient response, tracking error, rudder activity, and speed loss. The same signal and data-processing structure is applied to all controller modes, allowing their performance to be compared within a consistent experimental framework.

This work does not propose a new MMG force formulation or controller-synthesis method. Instead, its contribution is the organization of the simulation chain into a coherent and traceable experimental workflow. This distinction is important because the scientific value of the platform is determined not by the number of software functions it includes, but by the extent to which route, model, controller, and diagnostic information remain connected and interpretable throughout each simulation run.

Within this scope, the study makes three related contributions:

(i) A unified architecture that ensures consistent data exchange among geographic route definition, waypoint guidance, controller calculations, and MMG state propagation.

(ii) An interchangeable controller interface that provides a common structure for reference signals, vessel states, actuator commands, and logged data across PID, FL, and NN implementations.

(iii) A traceable assessment layer that connects geographic route execution with heading transients, root-mean-square tracking error, rudder saturation, speed loss, and user-defined diagnostic thresholds.

Full-scale and L7 KVLCC2 model cases are presented to demonstrate the complete workflow and show how different controller configurations lead to different recorded responses. These cases are not intended as a controlled benchmark and therefore cannot be used to establish hydrodynamic prediction accuracy or controller superiority. The study is consequently positioned as a contribution to simulator workflow development. Stronger performance claims would require benchmark maneuver validation, standardized controller-tuning procedures, environmental-disturbance scenarios, and repeated quantitative experiments. The remainder of the paper reviews related studies, describes the simulator architecture and MMG formulation, presents the control and

assessment modules, examines the demonstration cases, and discusses the main limitations and future validation needs.

2. Related Work and Research Gap

2.1. Ship Maneuvering Simulators for Control Testing

Ship maneuvering simulators have become an important tool for the development and validation of maritime control systems. Compared with physical sea trials, simulation-based testing provides a repeatable and low-risk environment in which different control strategies can be evaluated before implementation on real vessels. This is especially important for autonomous and semi-autonomous ship applications, where controller behavior must be examined under various operating conditions, including waypoint tracking, restricted-water navigation, and maneuvering in the presence of other vessels.

Recent studies increasingly treat maritime simulators as engineering platforms for autonomy development rather than solely as training tools [8,9]. A preliminary MMG-based ship simulator integrating autonomous PID control, manual operation, geographic visualization, and real-time vessel-state monitoring was presented in [13]. Dai et al. [10] developed an immersive virtual reality-based testing method and performance indicator system for autonomous navigation. Hinostroza and Lekkas [11] combined temporal mission planning with a guidance, navigation, and control framework in a realistic marine environment. Together, these studies highlight the importance of linking scenario definition, vessel dynamics, autonomy functions, and performance evaluation within a consistent simulation framework.

The review by Xu and Guedes Soares [12] organizes maritime autonomous surface-ship path-following research around guidance, control, vessel dynamics, stability, and environmental disturbances. For simulator-based assessment, these elements imply that reference generation, tracking error, control action, and maneuvering-model assumptions should be recorded together with the vessel trajectory. Robust-control studies have additionally considered the effect of hydrodynamic-parameter uncertainty on nonlinear surface-vessel control [14].

2.2. Data-Driven Modeling and Maneuver Prediction

In addition to model-based simulation, data-driven techniques have been investigated for ship maneuvering prediction and modeling. Long Short-Term Memory networks have been applied to identify and predict ship maneuvering motion by learning nonlinear time-dependent behavior from maneuvering data [15]. Sensor-data-based identification has also been combined with modular autopilot instrumentation and PID heading control [16]. Artificial Neural Networks have also been widely reviewed and applied in maritime applications, including modeling, prediction, and decision-making tasks [17]. These methods are useful because ship maneuvering dynamics are nonlinear and can be difficult to describe accurately under all operating conditions using only analytical models.

Other studies focus on maneuvering prediction, navigation decision-making, or route generation rather than on simulator validation itself [18]. Their relevance to the present study is therefore indirect. Although they help identify the information that a simulation platform should provide, they do not verify the accuracy of the MMG implementation or ensure that controller comparisons are conducted under equivalent conditions.

MMG-based simulation is particularly useful when controller assessment requires physically interpretable surge, sway, yaw, rudder, and propeller variables. Mitsuyuki et al. [19] demonstrated uncertainty-aware identification of MMG hydrodynamic maneuvering coefficients from observed motion and control data. Liu et al. [20] combined an MMG model with event-triggered predictive path-following control and evaluated tracking performance together with steering activity. These studies motivate an assessment structure that links model assumptions, controller computation, and actuator-level measurements.

Taken together, recent studies address model identification, guidance and control, autonomous-navigation testing, and mission planning at different levels of the simulation chain. The present study focuses on their implementation interface by combining geographic route execution, MMG state propagation, interchangeable heading-control modules, synchronized logging of vessel and actuator variables, and post-run diagnostic calculation in one simulator. The contribution is the integrated and traceable assessment process rather than a new MMG formulation or control law.

2.3. Route Optimization and Maritime Decision Support

Another relevant research direction is maritime route optimization and decision support. Route optimization studies aim to improve navigation safety and efficiency while considering geographical constraints, traffic density, and port-area characteristics. For example, ship path optimization methods that account for geographical traffic characteristics have been proposed to improve maritime port safety [21]. More recently, model-based predictive path planning has incorporated MMG vessel dynamics directly into constrained-environment path generation [22]. Such studies are relevant to maneuvering simulator development because route planning and path-following performance are strongly connected to the vessel's control capability. Model-based navigation and control have also been investigated for tankship operation in narrow waterways [23].

Nevertheless, many route optimization and decision-support studies focus mainly on path generation or safety

evaluation. In contrast, a control-testing simulator must also evaluate whether a particular vessel model and controller can physically follow the generated path with acceptable heading error, overshoot, settling behavior, actuator usage, and speed response. This distinction is important because a geometrically feasible path may still be difficult for a real ship to follow due to hydrodynamic limitations and actuator constraints. Feasibility can also depend on the propulsion mechanism. For autonomous sailing vehicles, geometrically safe avoidance headings may become unsailable when they enter the wind no-go zone [24].

2.4. Industrial Simulator and Navigation Platforms

Industrial developers have also made significant progress in maritime simulators, navigation-support systems, and autonomous-vessel technologies. Kongsberg has developed advanced maritime simulation platforms, including systems used for training and the evaluation of autonomous ship operations [25]. Furuno has introduced navigation-support technologies such as augmented-reality navigation and autonomous marine solutions, where radar, AIS, camera information, and visualization tools are integrated to improve situational awareness [26-28]. JRC has focused on simulator systems that support maritime pilot training and environmental-condition representation [29].

Other industrial platforms emphasize training, traffic simulation, and operational decision support. Wärtsilä provides navigation simulation systems with functions for user-performance evaluation during training scenarios [30]. Transas has contributed to maritime traffic simulation and full-mission bridge simulators, supporting traffic management and risk-analysis applications [31]. Siemens has investigated autonomous navigation and intelligent co-pilot concepts for supporting operational decisions [32]. Rolls-Royce has also worked on autonomous ship concepts and simulation-supported development for future remote-controlled and autonomous vessels [33].

Commercial platforms demonstrate the practical importance of maritime simulation, training, and navigation support. However, publicly available product material generally does not disclose model equations, controller source code, parameter files, or reproducible benchmark data. Table 1 therefore compares documented functional emphasis rather than making claims about unreported cost, performance, or internal architecture.

Table 1. Comparison of selected industrial maritime simulator and navigation-support platforms.

Platform	Main focus	Relevant capability	Limitation from control-testing perspective	Relevance to the present study
Kongsberg [25]	Maritime simulation and decision support	Supports complex maneuvering scenarios and autonomous ship operation evaluation	Public information does not expose model equations, controller source code, or reproducible benchmark data.	Shows the importance of high-fidelity simulation for maneuvering and control-system evaluation
Furuno [26-28]	Navigation visualization and situational awareness	Integrates navigation information, camera-based visualization, radar, AIS, and 3D situational display	Public information emphasizes navigation assistance; controller-level extensibility is not documented.	Motivates the integration of map-based visualization and real-time navigation feedback in the simulator
JRC [29]	Simulator-based maritime training and environmental representation	Provides realistic training environments and supports the representation of environmental conditions	Public information emphasizes training; controller-level extensibility	Highlights the need to include realistic operating conditions while maintaining control-test flexibility
Wärtsilä [30]	Navigation training and user-performance assessment	Evaluates user decisions and supports targeted training improvement	Public information emphasizes training and assessment; research access and algorithm modification are not documented.	Motivates the use of post-run analysis and performance assessment after simulation
Transas [31]	Maritime traffic simulation and full-mission bridge simulation	Supports traffic management, risk analysis, and complex maritime scenario generation	Public information emphasizes operational training and traffic simulation; controller source-code access is not documented.	Shows the value of traffic-aware and scenario-based simulation for future simulator extension
Siemens [32]	Autonomous navigation and intelligent co-pilot systems	Supports route generation and operational decision-making under different conditions	Public information emphasizes operational decision support; research-oriented controller modification is not documented.	Indicates the relevance of decision-support functions in autonomous ship control testing
Rolls-Royce [33]	Autonomous ship concepts and simulation-supported development	Focuses on environmental awareness, remote operation, and autonomous-vessel development	Public information describes proprietary autonomous-vessel concepts; reproducible controller-level access is not documented.	Provides industrial motivation for developing transparent and user-configurable, simulators

On this basis, the study examines whether a geographically referenced MMG simulator can provide a coherent path from controller implementation to post-run maneuver assessment. The platform is assessed in terms of:

(i) Integration of guidance, control, vessel dynamics, visualization, and logging.

(ii) Execution of interchangeable heading-control implementations.

(iii) Calculation of maneuver-quality indicators from a saved route run.

Controller plots are used to demonstrate platform operation, whereas quantitative interpretation is restricted to cases for which compatible raw logs are available.

3. Simulator Framework

3.1. Overall Architecture

The simulator is structured as an interactive control-development environment composed of five tightly connected layers: waypoint guidance, heading and speed control, MMG-based maneuvering dynamics, geographic conversion and visualization, and post-run data analytics. Figure 1 summarizes this organization.

The guidance layer interprets user-defined waypoints and transforms them into sequential maneuvering objectives. The control layer generates rudder and propulsion commands either autonomously or through manual intervention. The plant layer propagates vessel motion using the MMG model. The visualization layer converts Cartesian states back to geographic coordinates for map-based display. Finally, simulation logs are stored for offline analysis, replay, and automatic quality assessment. More detailed descriptions of each layer are presented in Table 2.

3.2. MMG-Based Maneuvering Model

The ship model employed in this study adheres to the standardized MMG (Maneuvering Mathematical Group)

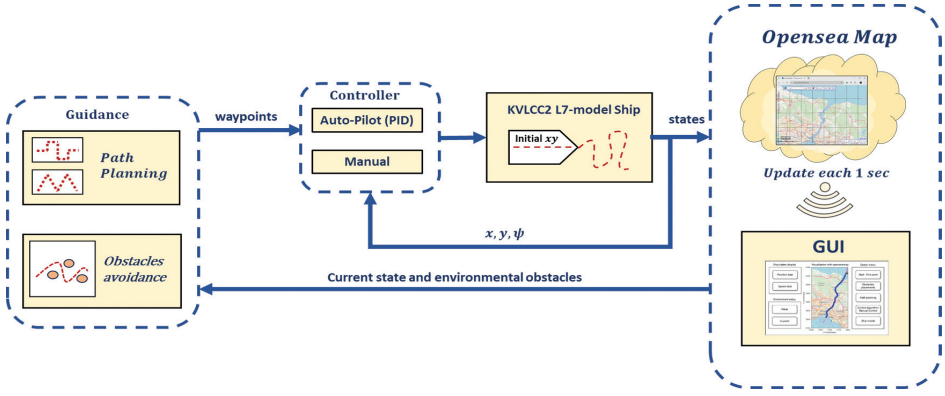


Figure 1. Overall ship-simulator software model.

PID: Proportional-integral-derivative, GUI: Graphical User Interface

Table 2. Functional layers of the simulator architecture.

Layer	Main role	Typical inputs	Main outputs
Input and initialization layer	Defines route, initial conditions, vessel parameters, actuator limits, disturbance settings, and simulation settings.	Waypoint CSV file, ship parameters, initial state, controller parameters, simulation time-step/update settings.	Validated initial configuration and local Cartesian waypoint set.
Guidance and reference layer	Selects the active waypoint and computes the reference heading or route-following command.	Current vessel position, waypoint list, waypoint-switching rule.	Reference heading, active waypoint index, path-tracking information.
Control layer	Converts heading and speed errors into rudder and propeller commands using the selected controller mode.	Reference heading, measured heading, reference speed, measured speed, controller parameters.	Rudder command, propeller-speed command, selected control mode.
Ship-dynamics layer	Propagates the vessel states using the maneuvering model and actuator commands.	Rudder angle, propeller speed, hydrodynamic coefficients, vessel state.	Surge speed, sway motion, yaw rate, position, heading.
Visualization and analysis layer	Displays the run, stores simulation data, plots selected variables, and evaluates maneuver performance after the run.	State histories, control histories, map data, performance thresholds.	Map trajectory, time histories, exported data, post-run assessment report.

ship modeling framework [6,7]. Ship maneuvering in still water involves three primary motions: surge, sway, and yaw. These can be described by the following equations of motion:

$$(m + m_x)\dot{u} - (m + m_y) v_m r - x_G m r^2 = X \tag{1a}$$

$$(m + m_y)\dot{v}_m + (m + m_x) ur + x_G m\dot{r} = Y \tag{1b}$$

$$\left(I_{zG} + x_G^2 m + J_z\right)\dot{r} + x_G m(\dot{v}_m + ur) = N_m \tag{1c}$$

where u, v, and r are the surge velocity, sway velocity, and yaw rate, respectively. For practical purposes, the coupling terms involving added mass in v_m and r are neglected. The total hydrodynamic forces can be decomposed as follows:

$$X = X_H + X_R + X_P \tag{2a}$$

$$Y = Y_H + Y_R \tag{2b}$$

$$N_m = N_H + N_R \tag{2c}$$

Here, the subscripts H, R, and P refer to contributions from the hull, rudder, and propeller, respectively. The hydrodynamic forces on the hull, X_H, Y_H, and N_H, can be modeled as:

$$X_H = 0.5\rho L_{pp} d U^2 X'_H(v'_m, r') \tag{3a}$$

$$Y_H = 0.5\rho L_{pp} d U^2 Y'_H(v'_m, r') \tag{3b}$$

$$N_H = 0.5\rho L_{pp}^2 d\ U^2 N'_H(v'_m, r') \tag{3c}$$

where v'_m and r' are the non-dimensional lateral velocity and yaw rate, defined as $\frac{v_m}{U}$ and $r\frac{L_{pp}}{U}$. These coefficients are expanded into polynomial forms:

$$X'_H(v'_m, r') = -R'_0 + X_{vv} v'^2_m + X_{vr} v'_m r' + X_{rr} r'^2 + X_{vvvv} v'^4_m \tag{4a}$$

$$Y'_H(v'_m, r') = Y_v v'_m + Y_R r' + Y_{vvv} v'^3_m + Y_{vvr} v'^2_m r' + Y_{vrr} v'_m r'^2 + Y_{rrr} r'^3 \tag{4b}$$

$$N'_H(v'_m, r') = N_v v'_m + N_R r' + N_{vvv} v'^3_m + N_{vvr} v'^2_m r' + N_{vrr} v'_m r'^2 + N_{rrr} r'^3 \tag{4c}$$

The surge force generated by the propeller is expressed as:

$$X_P = (1 - t_P) T \tag{5}$$

where the propeller thrust T is given by:

$$T = \rho n_P^2 D_P^4 K_T(J_P) \tag{6}$$

with the thrust coefficient $K_T(J_P)$ modeled as a second-order polynomial:

$$K_T(J_P) = k_2 J_P^2 + k_1 J_P + k_0 \tag{7}$$

and the advance ratio defined as:

$$J_P = \frac{u(1 - w_P)}{n_P D_P} \tag{8}$$

The wake fraction w_P depends on the flow conditions and is approximated by:

$$\frac{1 - w_P}{1 - w_{P0}} = 1 + \left(1 - \cos^2\beta_p\right)\left(1 - |\beta_p|\right) \tag{9}$$

where $\beta_P = \beta - x'_P r'$ is the inflow angle at the propeller. The forces and moment due to steering are given by:

$$X_R = -(1 - t_R) F_N \sin\delta \tag{10a}$$

$$Y_R = -(1 + a_H) F_N \cos\delta \tag{10b}$$

$$N_R = -(x_R + a_H x_H) F_N \cos\delta \tag{10c}$$

where the rudder normal force F_N is defined as:

$$F_N = 0.5\rho A_R U_R^2 f_a \sin\alpha_R \tag{11}$$

The rudder inflow velocity U_R and inflow angle α_R are given by:

$$U_R = \sqrt{u_R^2 + v_R^2} \tag{12}$$

$$\alpha_R = \delta - \arctan\frac{v_R}{u_R} \approx \delta - \frac{v_R}{u_R} \tag{13}$$

The lateral velocity at the rudder, v_R, is influenced by flow straightening and is modeled as:

$$v_R = U \gamma_R \beta_R \tag{14}$$

where $\beta_R = \beta - l_R r'$ and γ_R accounts for the flow alignment effect.

The physical and hydrodynamic parameters used for the full-scale and L7 KVLCC2 models were obtained from [6,7]. The present implementation was not independently validated against experimental or published turning-circle and zig-zag benchmark results. Therefore, the simulations reported here are not intended to establish maneuvering-prediction accuracy.

3.3. Waypoint Guidance and Reference Generation

Although the user interacts with waypoints in latitude and longitude, control calculations are performed in a local Cartesian frame for numerical simplicity. Let (x_i^{wp}, y_i^{wp}) denote the current target waypoint and (x, y) the ship position. The commanded heading is then obtained from

$$\psi_{ref} = atan2\left(\frac{x_{\mathrm{ref},i}}{y_{\mathrm{ref},i}}\right) \tag{15}$$

$$\psi_{error} = \psi_{\mathrm{ref}} - \psi_{\mathrm{cur}} \tag{16}$$

where ψ is the current vessel heading. Figure 2 shows the resulting closed-loop information flow.

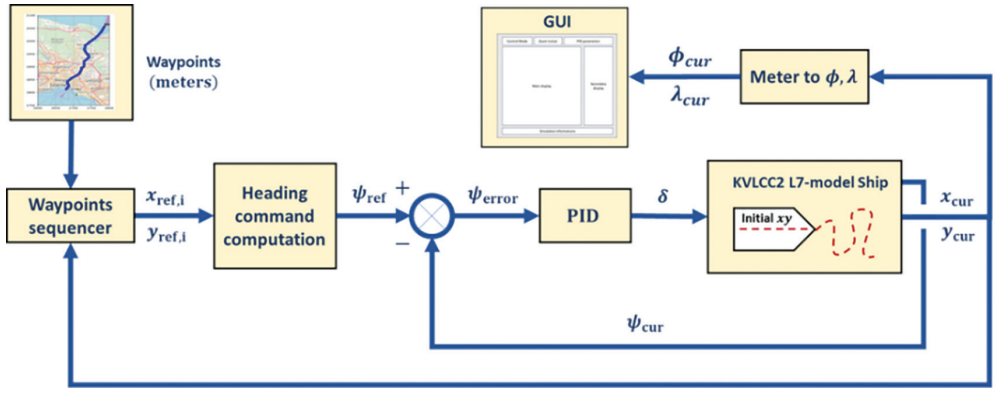


Figure 2. Closed-loop waypoint-following structure linking geographic waypoints, heading-command generation, control action, MMG state propagation, and GUI display.

MMG: Maneuvering Modeling Group

4. Simulator Product Layout and Interaction Design

4.1. Product-Oriented Design Philosophy

The simulator exposes the maneuvering workflow through an operator-facing interface rather than running the equations as an isolated numerical backend. Parameter initialization, controller selection, real-time visualization, signal logging, and post-run analysis are therefore treated as connected stages of a controller-development process.

The implemented software uses a tabbed desktop interface for configuration, execution, inspection, and evaluation. Table 3 summarizes the capability groups and their role in the workflow.

4.2. Tab-Based Workspace Architecture

The interface is divided into four functional tabs. Table 4 summarizes the responsibilities of each tab. The tabbed structure separates scenario initialization, run-time operation, data inspection, and post-run assessment. The implementation is described as following a Model-View-Controller organization with asynchronous controller execution and coordinate-conversion services.

4.2.1. Initialization Tab

According to the project reports, the initialization tab was designed around four core responsibilities:

- waypoint CSV import and automatic geographic calculations,
- ship-model and parameter loading,
- dynamic validation of parameters,
- multi-column organization of configuration fields.

The waypoint-import path is especially important because the simulator operates visually in geographic space but computes control actions in a local Cartesian frame. Once

Table 3. Integrated capability groups of the simulator product.

Capability group	Main implemented elements	Product value
Runtime simulation	Istanbul Strait route visualization, live telemetry, autonomous/manual operation, and real-time state updates	Makes maneuvering behavior spatially and dynamically interpretable while the simulation is running.
Controller workspace	PID-based heading and speed control loops, FL configuration, and neural-network control integration	Enables the simulator to function as a controller-development environment rather than only as a fixed playback tool.
Parameter management	Ship-model selection, editable MMG and physical parameters, disturbance settings, and initial-condition fields	Supports reusable scenario preparation under different vessel models and operating assumptions.
Data analysis	Log replay, axis selection, overlay plots, save/export actions, and embedded workspace panels	Preserves engineering evidence within the same application after the simulation run is complete.
Diagnostic review	Metric extraction, PASS/WARN/FAIL logic, radar-chart summaries, comparison actions, and recommendation text	Converts raw simulation traces into structured assessments of maneuvering quality.

Table 4. Functional organization of the simulator workspace.

Tab	Main objective	Principal widgets and controls	Typical outputs
Initialization	Configures the scenario and plant model before execution.	Waypoint CSV import, ship-model selection, editable physical parameters, parameter-validation fields, and multi-column setup panels.	Loaded route, validated ship parameters, and local Cartesian reference data.
Simulation	Executes autonomous or manual navigation in real time.	Controller mode selector, zoom controls, map canvas, secondary display, live plots, pause/restart/stop logic, and controller-parameter panel.	Ship motion on the Istanbul Strait map, instantaneous telemetry, and live heading, rudder, and speed traces.
Data analysis	Inspects completed runs without rerunning the plant model.	Dataset loader, workspace list, axis selectors, plot mode selector, plot/hold/clear/save actions, and table export.	Time-series plots, variable-versus-variable plots, overlay comparisons, and exported figures and tables.
Post run analyzer	Converts simulation logs into engineering judgments.	Metric threshold editor, comparison source selector, radar chart, report window, save-report action, and run-analysis trigger.	PASS/WARN/FAIL assessment, segment-level diagnostics, and controller-tuning recommendations.

a CSV route containing latitude and longitude values is loaded, the software transforms the route relative to the selected starting point, thereby preparing the waypoints for the guidance and control layers. The reports emphasize that this transformation is automatic, which reduces operator workload and helps maintain consistency between the visual map and the control-side geometry.

The ship-model panel plays an equally important role. It allows the user to inject or edit dimensions, mass properties, and maneuvering coefficients directly from the Graphical User Interface (GUI). In a product paper this is worth emphasizing because it moves the simulator away from being a hard-coded demonstrator and toward being a reusable vessel-testing platform.

Figure 3 summarizes the initialization workspace, including route loading, initial-state specification, disturbance configuration, controller setup, and vessel-parameter editing. Table 5 lists the corresponding functional groups.

4.2.2. Simulation Tab

The simulation tab is the visual core of the simulator. Figure 4 summarizes the principal regions of the runtime window schematically.

The top band contains run-time controls, the center-left region displays the geographic trajectory, the right column presents context and instrumentation views, and the lower status strip reports numerical telemetry. Tables 6 and 7 summarize these regions and variables.

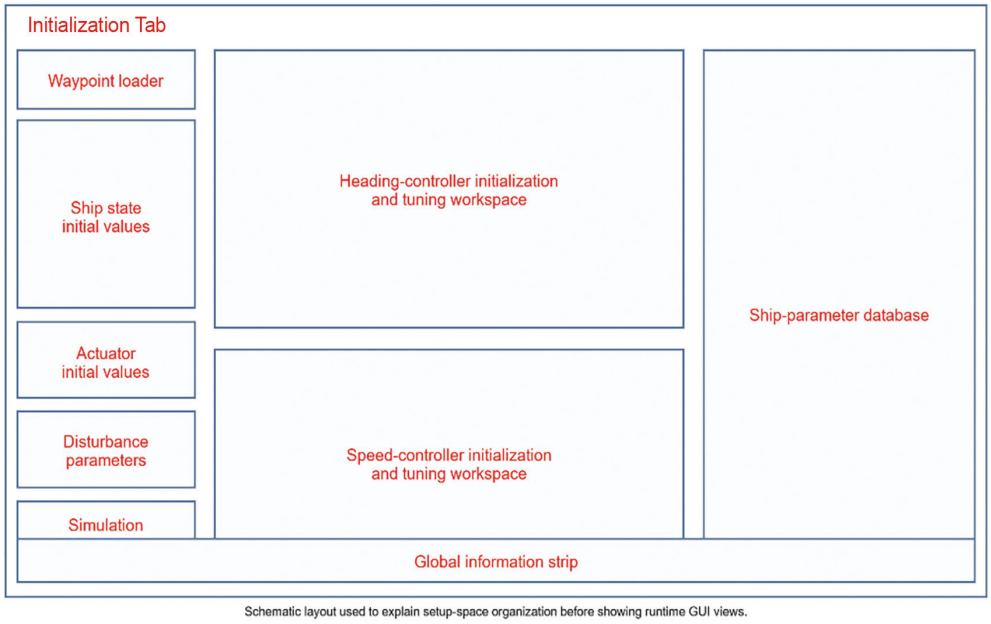


Figure 3. Schematic layout of the initialization tab showing route loading, initial-state panels, controller-initialization workspaces, the ship-parameter database, and the global information strip.

Table 5. Functional clustering inside the initialization tab in the implemented GUI.

Cluster	Main contents	Product purpose
Waypoint loader	CSV path display, file-open action, and total waypoint count.	Connects the navigation scenario to the rest of the setup process and makes the route provenance explicit.
State and disturbance panels	Initial latitude, longitude, heading, surge, sway, and yaw states, actuator initial values, wave parameters, and simulation-step settings.	Defines the operating point from which all later controller behavior should be interpreted.
Heading-controller workspace	PID tuning fields, test setup, response plotting area, and controller-tab hierarchy.	Allows the operator to tune and inspect heading-control behavior before or during scenario definition.
Speed-controller workspace	Speed PID tuning fields, manual test setup, and response plotting area.	Separates propulsion regulation from heading regulation while keeping both visible in the same engineering screen.
Ship-parameter database	Ship-model selector and editable hydrodynamic, geometric, and actuator parameters.	Turns the simulator into a reusable vessel-testing platform rather than a fixed one-ship demonstrator.
Information strip	Global status and information line.	Communicates the active application state without requiring additional dialogs.

GUI: Graphical User Interface, PID: Proportional-integral-derivative

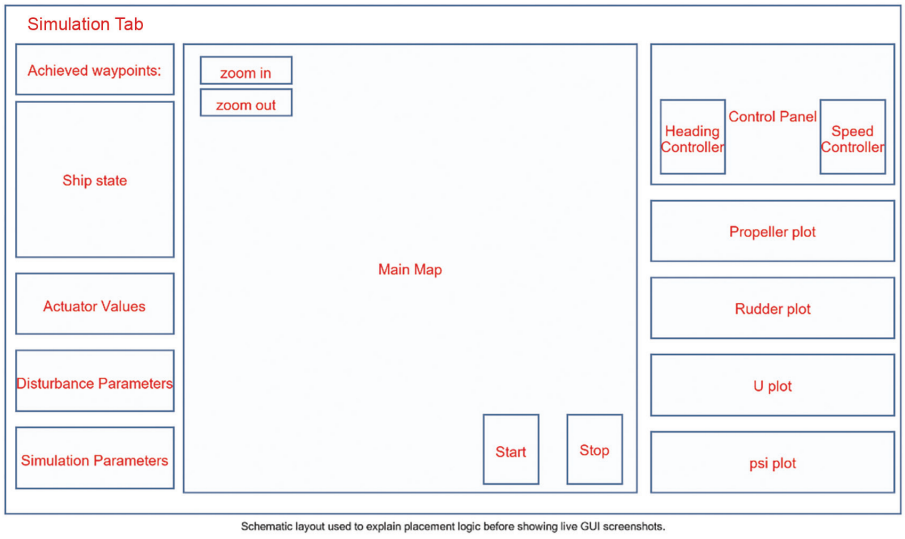


Figure 4. Schematic layout of the simulation tab showing the placement of the main map, left-side state panels, right-side control and plot regions, and run-control buttons.

Table 6. Runtime layout of the simulation tab.

Region	Placement	Contents	User benefit
Control mode selector	Top-left	Active control-mode indicator and autonomous/manual switching logic.	Makes control authority explicit and prevents mode ambiguity during testing.
Zoom controls	Top-center-left	Zoom-in and zoom-out buttons for the main map.	Allows rapid context changes during dense waypoint inspection.
Controller parameter strip	Top-center-right	Gain-entry boxes and apply action for the active controller.	Supports on-the-fly tuning during experimental runs.
Main map display	Center-left, dominant area	OpenSeaMap background, ship marker, route, waypoint geometry, and trajectory history.	Provides the primary situational-awareness view and makes maneuvering behavior spatially interpretable.
Secondary display column	Right side	Overview map and time-history plots of heading, rudder angle, and ship speed.	Provides compact local and global context without leaving the live simulation run.
Status bar	Bottom, full width	Simulation time, propeller speed, rudder angle, ship speed, latitude, longitude, heading, and waypoint count.	Consolidates machine-state information for quick reading and logging.

Table 7. Primary real-time variables exposed through the simulation-tab status strip.

Field	Unit or type	Engineering interpretation
Simulation time	s	Establishes event chronology and allows the operator to relate turning behavior to control action and waypoint switching.
Propeller speed (n_p)	rps	Indicates commanded propulsion effort and supports interpretation of surge-speed transients.
Rudder angle (δ)	deg	Shows immediate steering demand and is important for identifying controller saturation or oscillatory steering.
Ship speed (U)	m/s	Summarizes forward-motion efficiency and reveals maneuver-induced speed loss.
Latitude and longitude	deg	Keep the live trajectory anchored to the geographic context of the Istanbul Strait map.
Heading (ψ)	deg	Gives the vessel's instantaneous orientation for comparison with the reference-heading evolution.
Waypoint count/active route state	integer/state label	Informs the operator which part of the mission is currently being executed and whether waypoint advancement is behaving correctly.

During a run, the map displays the route, waypoints, vessel marker, and trajectory, while adjacent plots and telemetry panels expose selected state and actuator variables. Pause, restart, and stop functions support interactive testing.

4.2.3. Data Analysis Tab

The data-analysis tab loads completed simulation datasets and supports signal selection, overlay plots, table inspection, figure export, and numerical-data export (Table 8).

Keeping these operations within the simulator allows reference, state, and actuator histories to be inspected without rerunning the model. The workflow places dataset management on the left, signal selection at the top, numerical inspection in the center, and plots in the lower workspace. Figure 5 summarizes the data-analysis workspace and separates run management, plotting controls, numerical data, and the plot canvas.

4.2.4. Post-run Analyzer Tab

The post-run analyzer organizes completed-run assessment. The arrangement allows the user to inspect the detected context and thresholds before comparing the radar chart with the textual metric summary and recommendations. Figure 6 summarizes the post-run analyzer and separates context detection, action controls, threshold editing, radar-chart visualization, and the textual report.

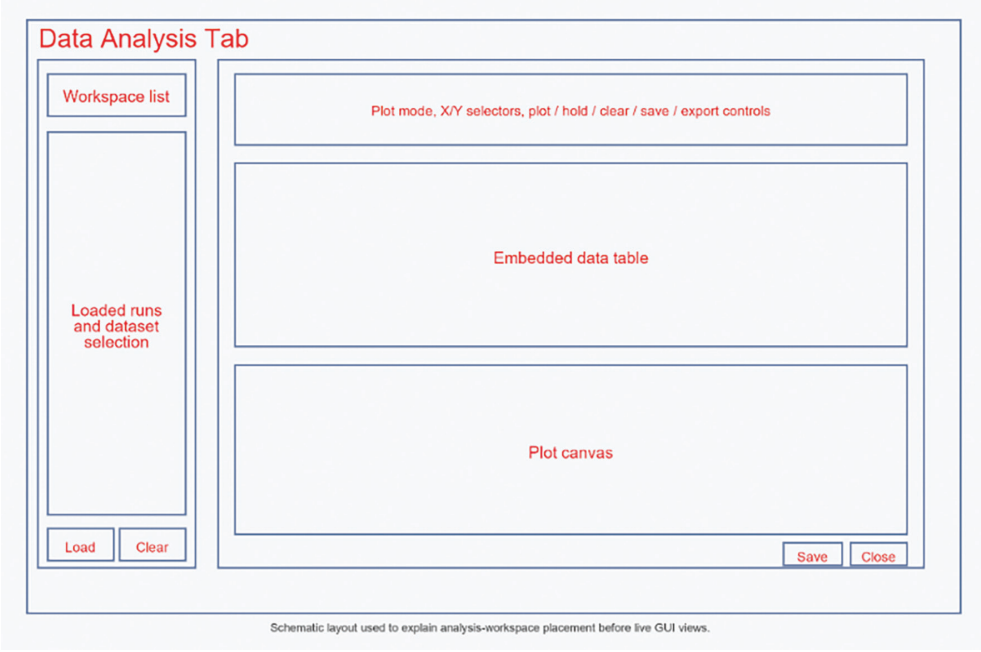


Figure 5. Schematic layout of the data-analysis tab showing the workspace list, plot-control strip, embedded data table, plot canvas, and export-oriented utility buttons.

GUI: Graphical User Interface

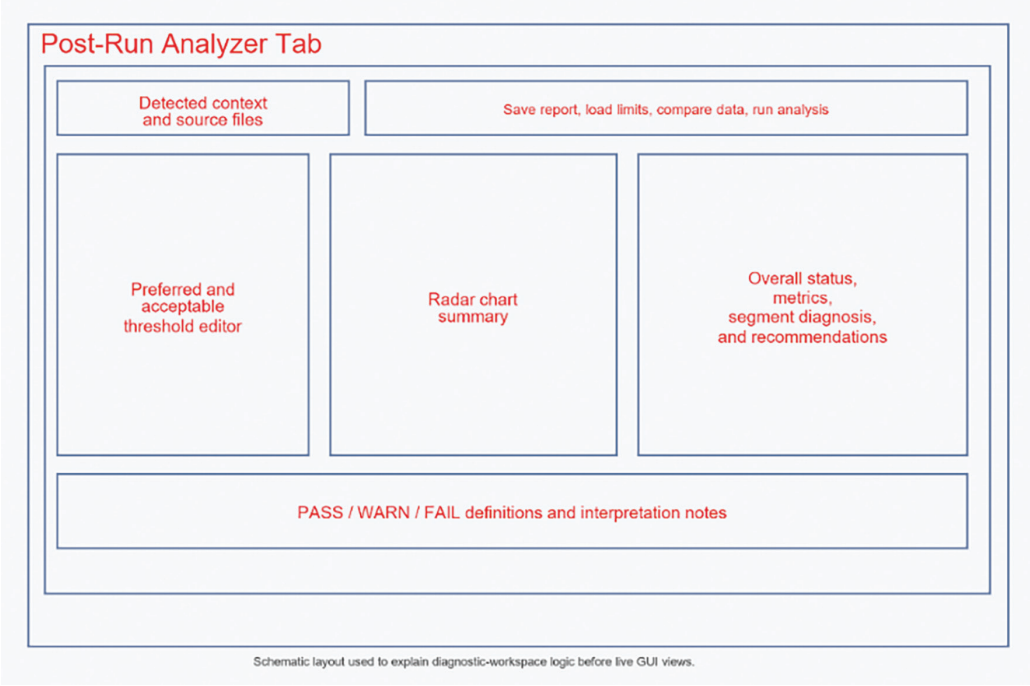


Figure 6. Schematic layout of the post-run analyzer tab showing context detection, analysis actions, threshold editing, the radar-chart panel, the textual diagnostic report, and the PASS/WARN/FAIL interpretation strip.

Table 8. Interaction logic of the data-analysis tab.

Interface element	Placement	Function in the workflow
Workspace list	Left column	Stores one or more completed runs so that the user can switch among experiments without relaunching the simulation.
Load/clear workspace actions	Upper-left and lower-left	Adds new datasets to the session and resets the analysis workspace when a fresh comparison cycle is needed.
Plot-mode selector	Upper control band	Switches between time-history plotting and variable-versus-variable interpretation.
X/Y axis selectors	Upper control band	Exposes simulation variables directly to the plotting engine and supports fast custom comparisons.
Plot, hold, clear, and save actions	Upper control band	Creates overlays, resets the current figure, and preserves publication-ready or report-ready plots.
Save table data action	Upper control band	Exports numerical logs for use in external spreadsheets or additional statistical analysis.
Embedded data table	Central pane	Provides exact sample-level values for debugging, sanity checks, and parameter tracing.
Plot canvas	Lower pane	Produces the visual engineering evidence used to compare runs and interpret controller behavior.

5. Control and Intelligence Modules

5.1. Controller Exposure Through the GUI

The controller modules are presented primarily as replaceable implementations that exercise the simulator workflow. Formal controller synthesis, gain optimization, robustness analysis, and statistically controlled benchmarking are outside the scope of the current evidence. Table 9 summarizes the control-related inputs exposed through the interface.

5.2. Dual-Loop PID Control

Control-oriented ship models have also been used with cascade-control architectures for vessel motion control [34]. PID control is retained as the main reference controller because of its interpretability and tuning transparency. The heading-control command is

$$\delta_{\mathrm{cmd}}(t) = K_{P,\psi} e_{\psi}(t) + K_{I,\psi} \int_0^t e_{\psi}(\tau) d\tau + K_{D,\psi} \dot{e}_{\psi}(t) \qquad (17)$$

Table 9. Controller-specific interaction capabilities of the simulator GUI.

Controller model	Exposed user inputs	Main engineering purpose	Reported interface emphasis
PID heading control	Editable (K_P), (K_I), and (K_D) values for the heading loop.	Tunes responsiveness, overshoot, and settling behavior during path following.	Baseline autonomous control and reference benchmark.
PID speed control	Editable (K_P), (K_I), and (K_D) values for the propulsion loop.	Regulates forward speed independently from heading stabilization.	Dual-loop precision maneuvering and speed maintenance.
Fuzzy logic control	Membership-function type, parameter ranges, and fuzzy-rule configuration.	Shapes nonlinear heading response and improves adaptability across operating conditions.	User-configurable linguistic control with smoother corrective behavior after tuning.
Neural network control	Training-data selection, network topology, training execution, and persistence support.	Develops data-driven heading-control policies and compares them against classical designs.	Background training integration and adaptive control experimentation.
Manual mode	Direct rudder commands through the keyboard.	Inspects plant behavior without autopilot authority and supports operator familiarization.	Interactive testing and training support.

subject to actuator saturation, typically within +/-30 deg. Where the speed error is defined as the difference between the reference speed and the measured surge speed. This dual-loop structure allows heading and forward-speed regulation to be studied independently and jointly. The heading and speed loops operate independently, although their responses remain coupled through the MMG vessel dynamics. The parameter configurations used to demonstrate the controller workspace for the PID controller are summarized in Table 10.

The gains reported in Table 10 were selected through limited exploratory simulation to produce bounded and visibly distinguishable responses within the configured actuator limits. For the full-scale heading example, a proportional gain of K_p=4 was first retained after it produced a usable closed-loop response. Small integral and derivative terms were then varied to demonstrate how changes in the entered parameters are reflected in the simulated response and subsequent analysis. The corresponding L7 and speed-control configurations were prepared for the same software-demonstration purpose. Therefore, these values should not be interpreted as optimal, generally applicable, or recommended controller gains. Configuration A and B were selected to produce different response characteristics for demonstration of the tuning and analysis functions.

5.3. FL Heading Control

A fuzzy-logic (FL) heading controller is included as a rule-based nonlinear alternative. The implementation maps heading-error information to a bounded rudder command using configurable membership functions, inference rules, and centroid defuzzification. A representative triangular membership function is

$$\mu_{\text{tri}}(x;a,b,c) = \begin{cases} 0 & x \le a \\ \dfrac{x-a}{b-a} & a < x \le b \\ \dfrac{c-x}{c-b} & b < x < c \\ 0 & x \ge c \end{cases} \tag{18}$$

while the crisp rudder command is obtained by centroid defuzzification,

$$\delta_{\text{FL}} = \frac{\sum_i \mu_i(x)\, x_i}{\sum_i \mu_i(x)} \tag{19}$$

The interface uses a heading-error range of ±40 deg and a rudder-command range of ±30 deg. Five linguistic sets are defined for both the heading-error input and rudder-angle output. The input sets are left large, left small, center, right small, and right large, while the corresponding output sets are hard left, soft left, neutral, soft right, and hard right.

Table 10. Illustrative PID parameter configurations used to demonstrate the controller workspace.

Model and loop	Config.	K_P	K_I, K_D	Model and loop	Config.	K_P	K_I, K_D
Full-scale heading	A	4	0.002, 15	L7 heading	A	20	0.01, 0.001
Full-scale heading	B	4	0.001, 0.001	L7 heading	B	20	0.01, 0.01
Full-scale speed	A	20	0.01, 0.001	L7 speed	A	35	0.3, 0.001
Full-scale speed	B	20	0.01, 0.01	L7 speed	B	20	0.1, 0.001

The implemented rule base maps these sets directly as summarized in Table 11. The GUI also allows the membership-function type and control ranges to be configured. These settings are provided to demonstrate the fuzzy-controller implementation within the simulator rather than an optimized fuzzy-control design.

The fuzzy controller therefore contains five rules, five input linguistic sets, and five output linguistic sets. The heading-error and rudder universes of discourse are [-40,40] deg and [-30,30] deg, respectively. Centroid defuzzification is used, and a 50-point precomputed input-output map with linear interpolation is employed for faster execution during simulation.

5.4. NN Heading Control

The neural-network (NN) controller is introduced as a data-driven alternative for mapping maneuvering error to control action. Training data were generated by repeatedly simulating the ship under constant rudder commands. Each sample covered a 10 s interval, and a dataset of 1000 samples was reported. The training input is the heading discrepancy

$$\Delta\psi = \psi_d - \psi_{\text{init}} \tag{20}$$

where ψ_d is the desired final heading and ψ_{init} is a randomly selected initial heading. The network output is the rudder demand. The model was trained with a mean-squared-error objective,

$$L(\theta) = \frac{1}{N}\sum_{i=1}^{N}\left(\delta_i - \hat{\delta}_i\right)^2 \tag{21}$$

using the Adam optimizer. The generic Adam update can be written as

$$\theta_{k+1} = \theta_k - \alpha\frac{\widehat{m}_k}{\sqrt{\widehat{v}_k} + \varepsilon} \tag{22}$$

where $\widehat{m}_k$ and $\widehat{v}_k$ are the bias-corrected first and second moment estimates. The specific NN configurations used for the reported L7 and full-scale demonstrations are summarized in Table 12. Each network uses ReLU activation in the hidden layers and a single linear output neuron representing rudder demand. Adam optimization and a mean-squared-error objective are used for all configurations. Training data consist of 1000 simulated samples with a 10 s maneuver interval per sample, and no explicit validation split is used in the implemented training call.

5.5. Automatic Post-Run Evaluation Logic

The simulator includes an automatic post-run analyzer intended to classify the quality of a completed maneuver. Instead of acting online, this module consumes simulation logs after execution and produces a structured diagnostic outcome. Figure 7 summarizes the logic.

The metrics are defined in a segment-aware manner so that major heading changes can be evaluated separately before being aggregated. Table 13 summarizes the diagnostic measures used by the analyzer and the engineering meaning attached to each on.

6. Simulator Interface and Experimental Results

6.1. Implemented GUI Views

Figures 8-11 show the implemented interface across the four main tabs: initialization, simulation, data analysis, and post-run analysis. Together they demonstrate that the simulator operates as a continuous engineering workflow rather than a single visualization screen. Route preparation, live maneuvering, result inspection, and performance diagnosis are all handled inside the same environment, which makes repeated controller tuning and comparison considerably easier.

Table 11. FL controller structure used in the simulator.

Heading-error set	Rudder-output set	Rule
Left large	Hard left	If heading error is left large, command hard left rudder
Left small	Soft left	If heading error is left small, command soft left rudder
Center	Neutral	If heading error is near zero, command neutral rudder
Right small	Soft right	If heading error is right small, command soft right rudder
Right large	Hard right	If heading error is right large, command hard right rudder

Table 12. Neural-network configurations used in the reported demonstrations.

Model	Config.	Time step (s)	Update rate	Hidden layers	Neurons/layer	Epochs	Batch size
Full-scale	A	0.25	20	2	32	200	64
Full-scale	B	1.00	20	10	50	700	150
L7	A	1.00	5	1	10	50	32
L7	B	1.00	5	1	50	700	150

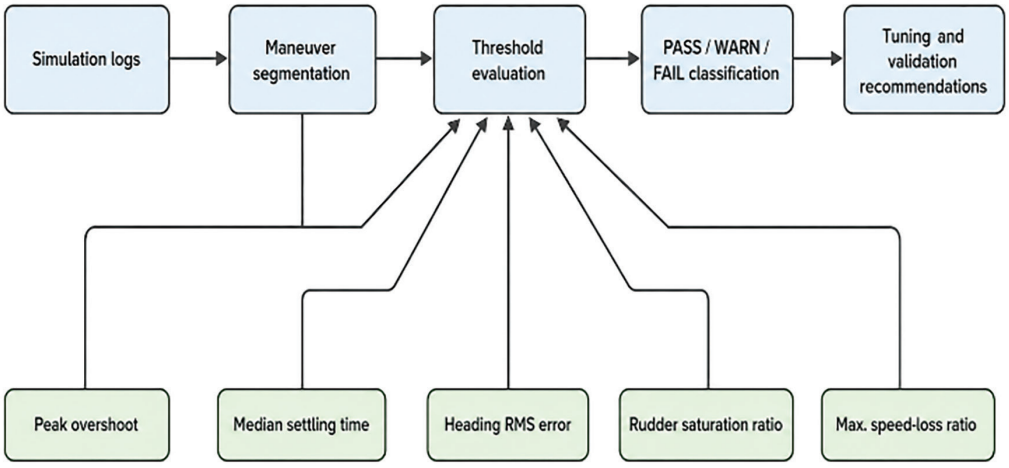


Figure 7. Post-run analyzer concept. Configurable thresholds convert raw simulation traces into engineering-level feedback.

Table 13. Diagnostic metrics used by the automatic post-run analyzer.

Metric	Definition and engineering meaning
Peak overshoot	$M_p = \max_j M_{p,j}$, where each $M_{p,j}$ measures how far the heading exceeds the segment target relative to the initial error magnitude. Large values indicate aggressive and weakly damped turning behavior.
Median settling time	$T_s = media\, n_j(Ts,j)$ where Ts,j is the first time at which $\lvert e_\psi \rvert$ remains inside a tolerance band for a sustained interval. Large values indicate slow recovery after reference changes.
Heading RMS error	$e_{\text{RMS}} = \sqrt{\frac{1}{N}\sum_{k=1}^{N} e_\psi^2(k)}$. This metric captures the average tracking accuracy over the full simulation run.
Rudder saturation ratio	$R_\delta = 1/N \sum_{k=1}^{N} = 1\lvert\delta(k)\rvert \geq \eta\lvert\delta_m ax\rvert$, where η is a configurable near-saturation fraction. High values indicate excessive actuator demand.
Maximum speed-loss ratio	$R_u = \max_j \frac{u_{0,j} - u_{min,j}}{u_{0,j} + \varepsilon}$ where $u_{0,j}$ is the baseline segment speed and $u_{min,j}$ the minimum speed reached during the maneuver. High values indicate that heading corrections are degrading forward-motion efficiency.

6.2. Controller-Comparison Results

Figures 12-19 demonstrate that changes in the controller configurations entered through the simulator are reflected in the recorded heading, rudder, and speed responses for both the L7 and full-scale models. Differences in transient behavior and actuator demand are visible among the demonstrated configurations. These cases are intended to demonstrate the controller-testing and analysis workflow rather than to establish the relative performance or superiority of the implemented control methods.

6.3. Full-Scale Simulation on a Selected İstanbul Strait Route Segment

Figures 20-25 demonstrate the complete software workflow using an archived full-scale vessel simulation conducted on a geographically referenced route segment of the İstanbul Strait. The simulated route covers only a limited section of the Strait near a navigationally constrained area and does not represent a complete İstanbul Strait transit. In this subsection, the term full-scale refers to the vessel dimensions and model parameters rather than the geographic extent of the simulated route. The purpose of this case is to demonstrate the integration of geographic visualization, closed-loop control, signal recording, data inspection, and post-run assessment within the developed software. It is not intended to establish an optimal controller design.

Figure 20 shows the Simulation tab during execution of the selected route. The central map displays the geographically referenced waypoints, the prescribed route, the current vessel position, and the trajectory generated during the maneuver. The surrounding interface panels provide the instantaneous vessel states, actuator values, simulation parameters, and active controller settings. The time-history panels on the right provide live visualization of selected motion and control variables. This arrangement allows the user to observe the spatial vessel motion and the corresponding dynamic response within the same software environment.

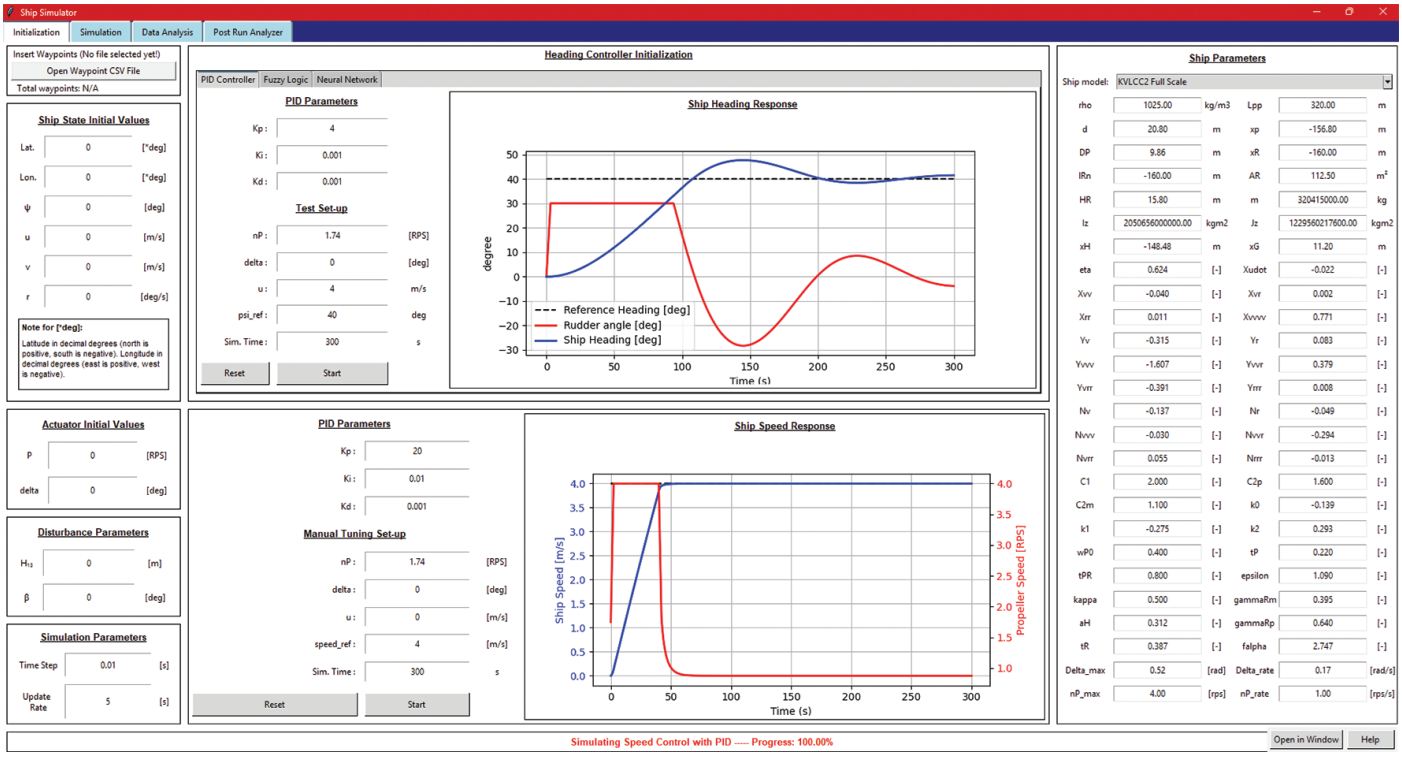


Figure 8. Initialization tab.

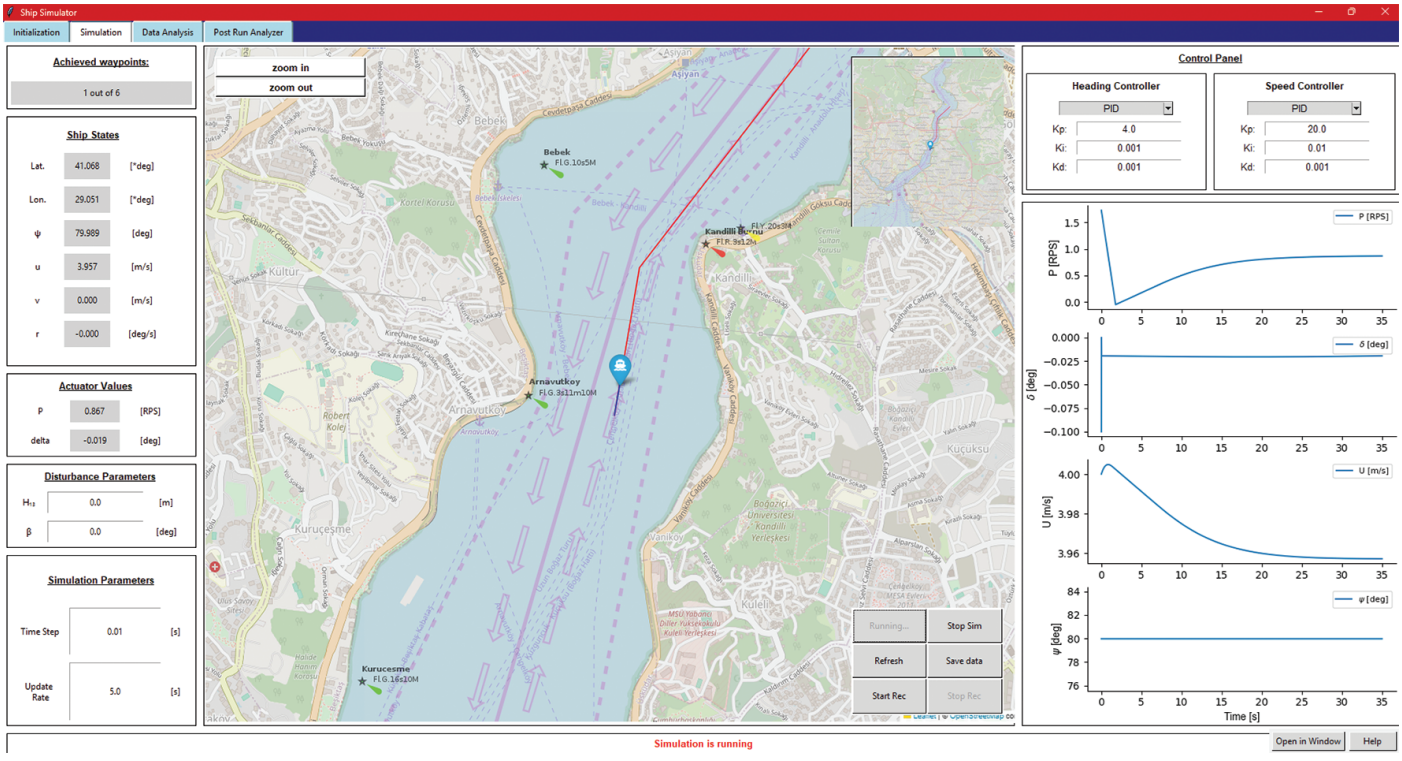


Figure 9. Simulation tab.

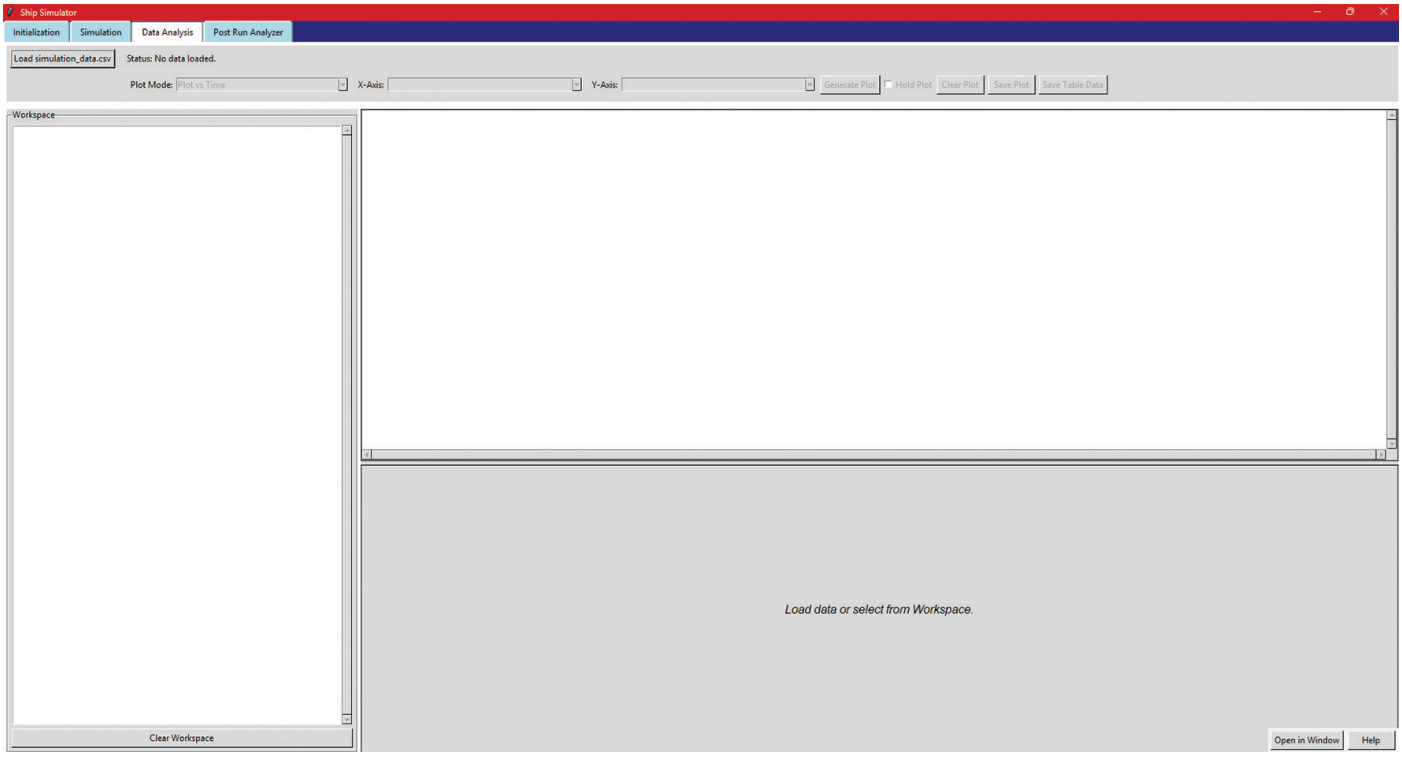


Figure 10. Data analysis tab.

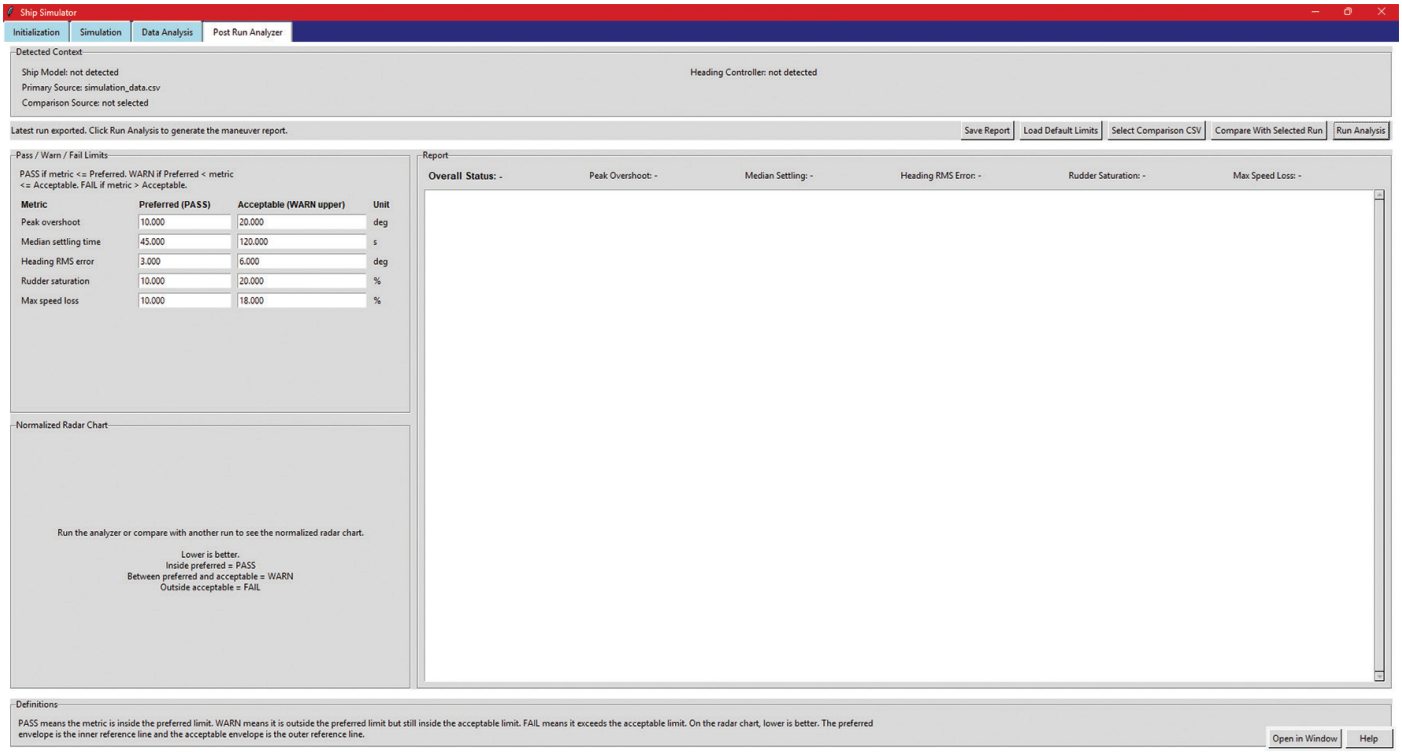


Figure 11. Post-run analyzer tab.

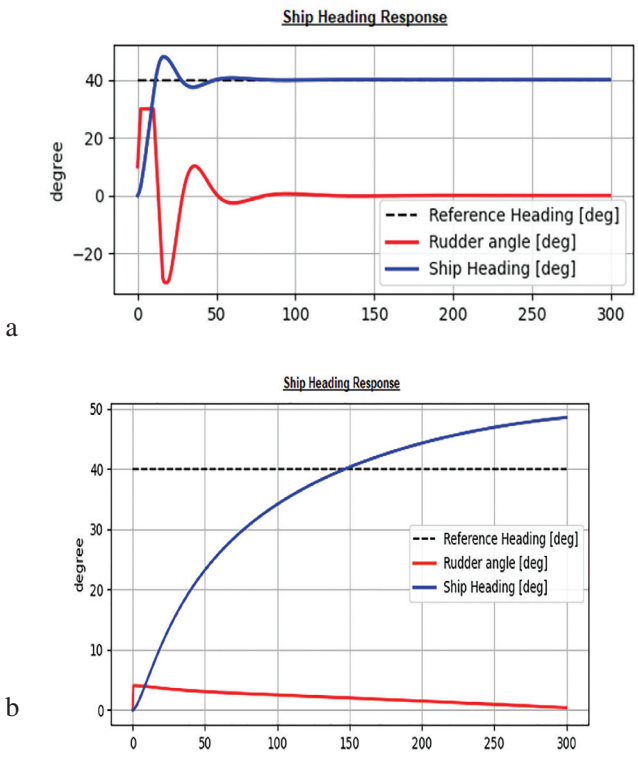


Figure 12. Configuration a) (left) vs. b) (right) for L7-model heading PID tests.

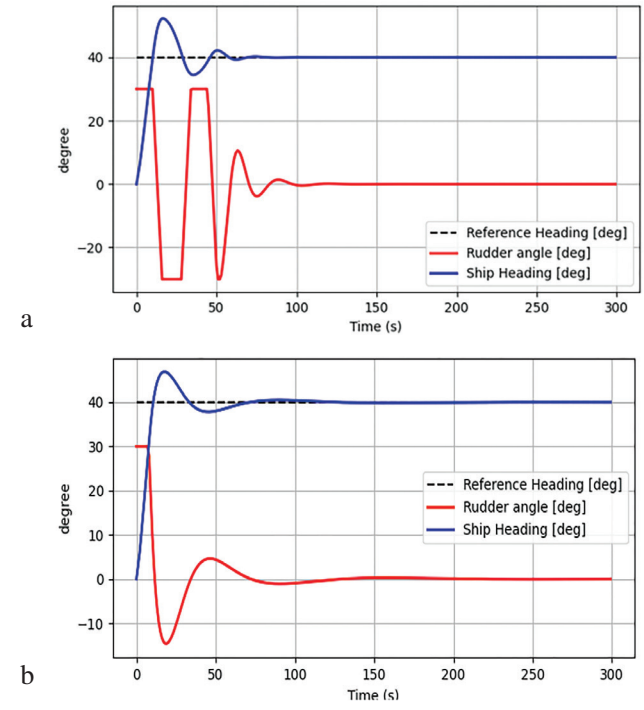


Figure 13. Configuration a) (left) vs. b) (right) for L7-model heading FL tests.

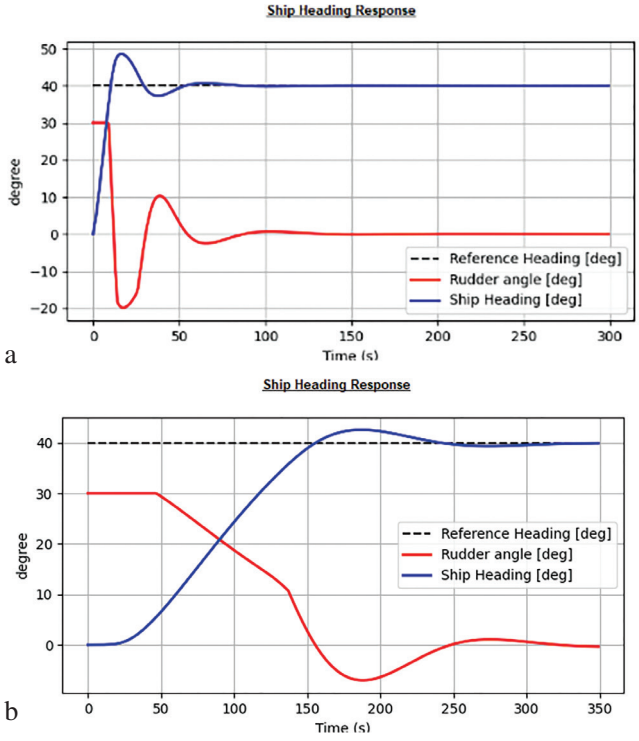


Figure 14. Configuration a) (left) vs. b) (right) for L7-model heading NN tests.

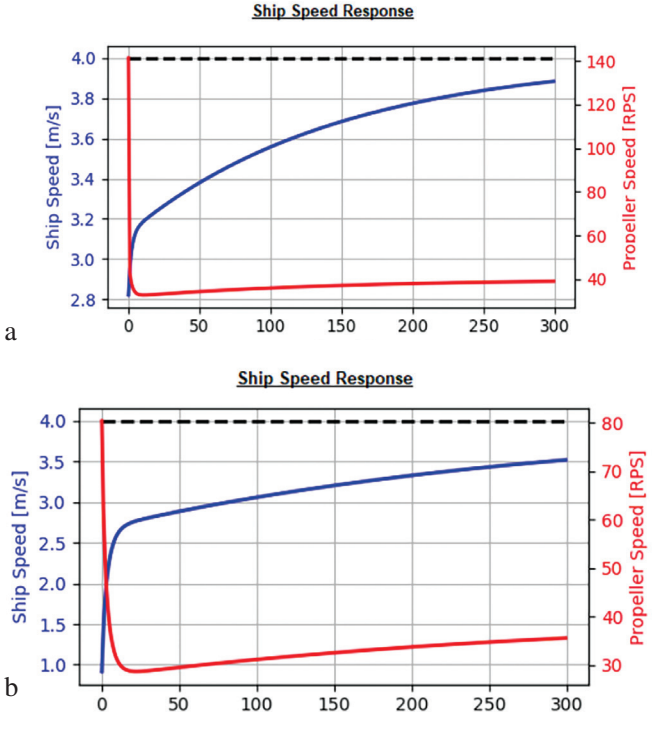


Figure 15. Configuration a) (left) vs. b) (right) for L7-model PID speed tests.

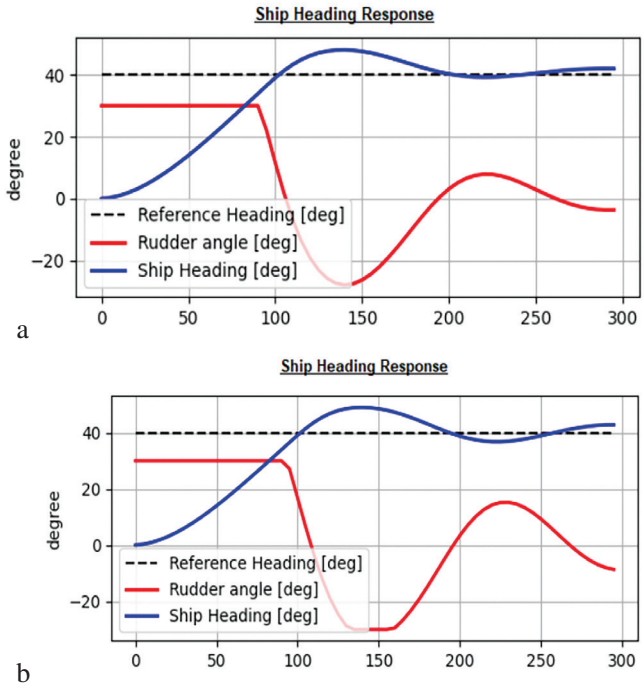


Figure 16. Configuration a) (left) vs. b) (right) for full-scale heading PID tests.

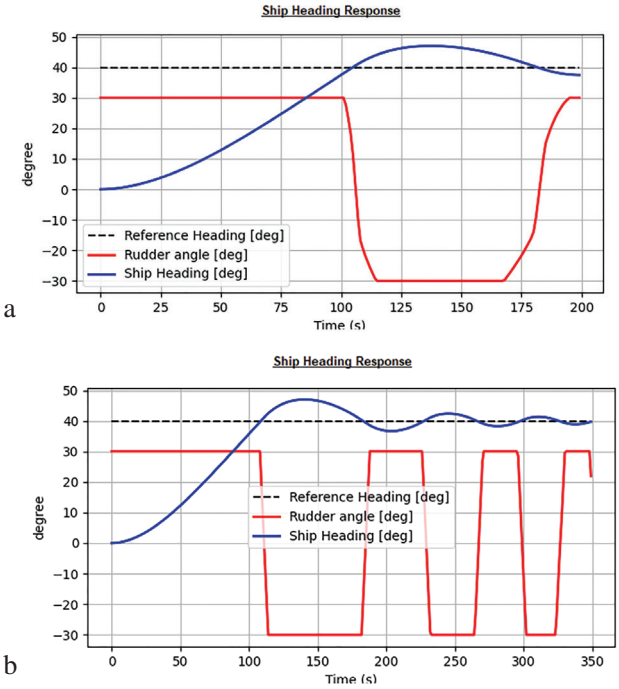


Figure 18. Configuration a) (left) vs. b) (right) for full-scale heading NN tests.

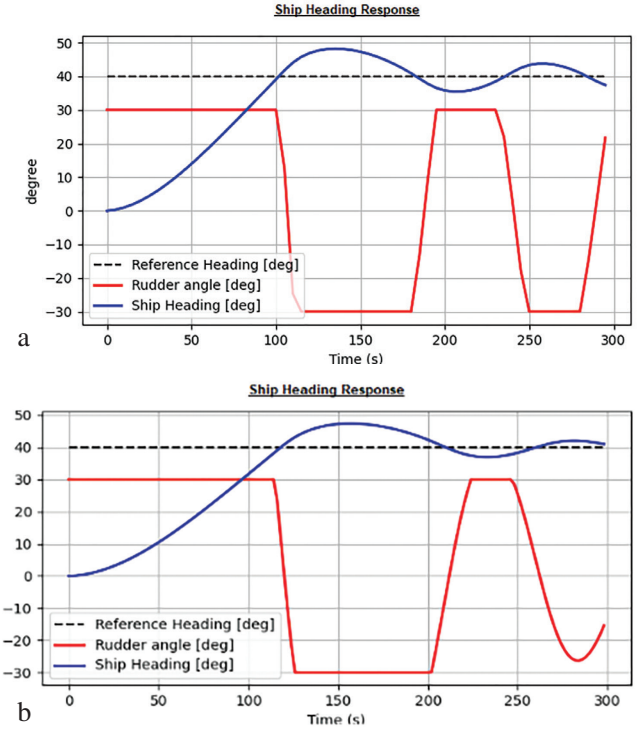


Figure 17. Configuration a) (left) vs. b) (right) for full-scale heading FL tests.

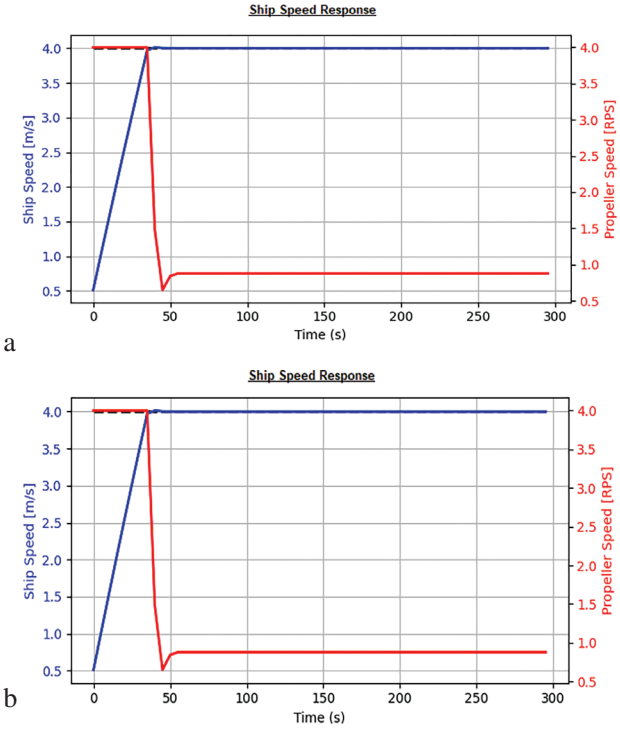


Figure 19. Configuration a) (left) vs. b) (right) for full-scale PID speed tests.

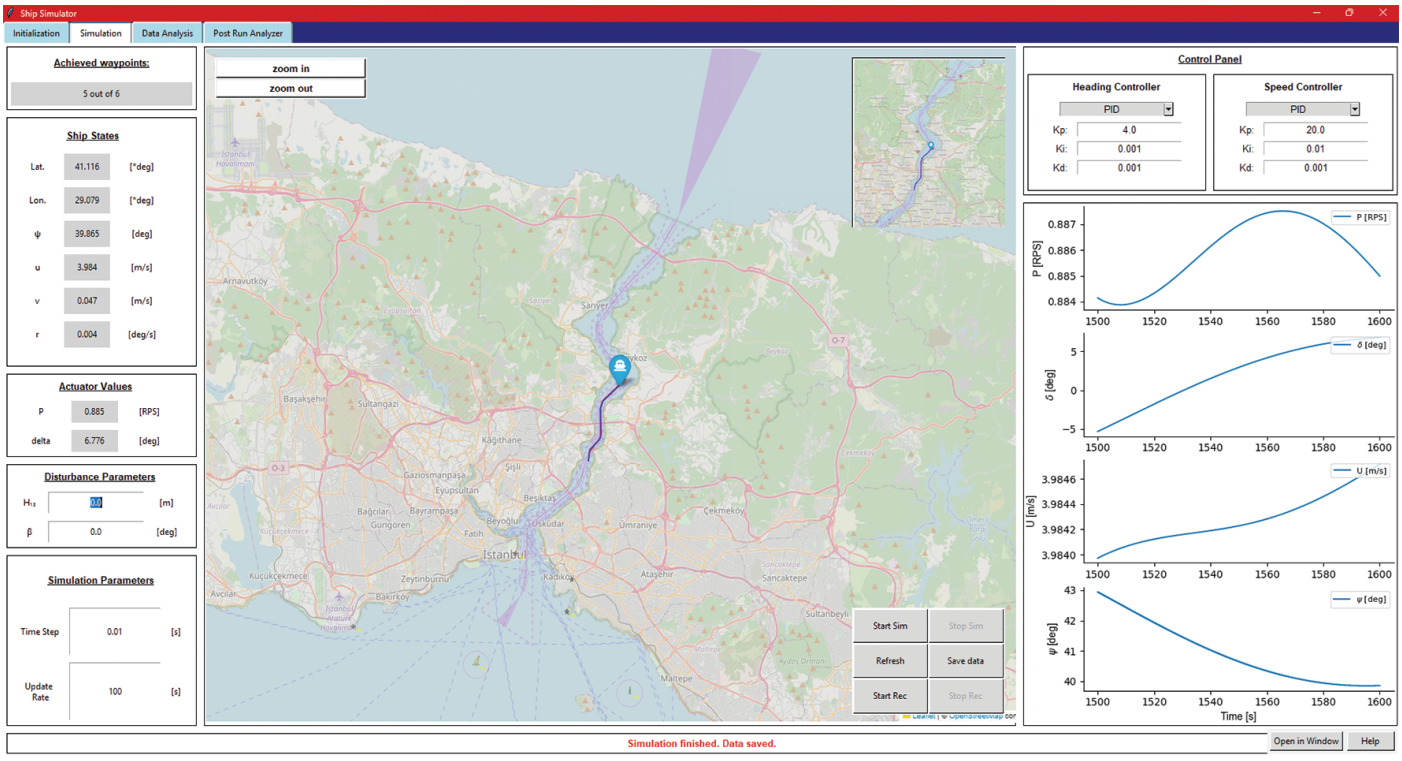


Figure 20. Simulated trajectory along the selected İstanbul Strait route segment in simulation tab.

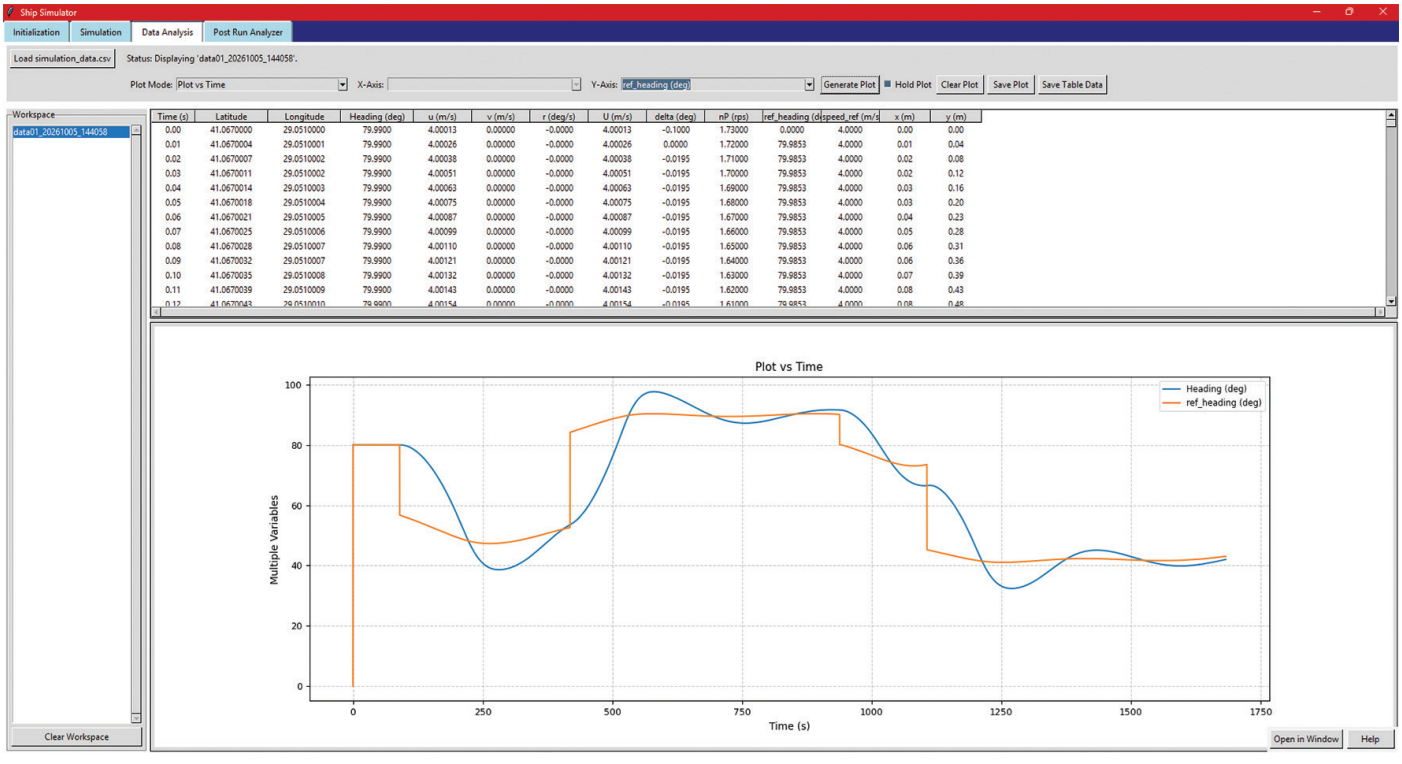


Figure 21. Heading vs. reference in data analysis tab.

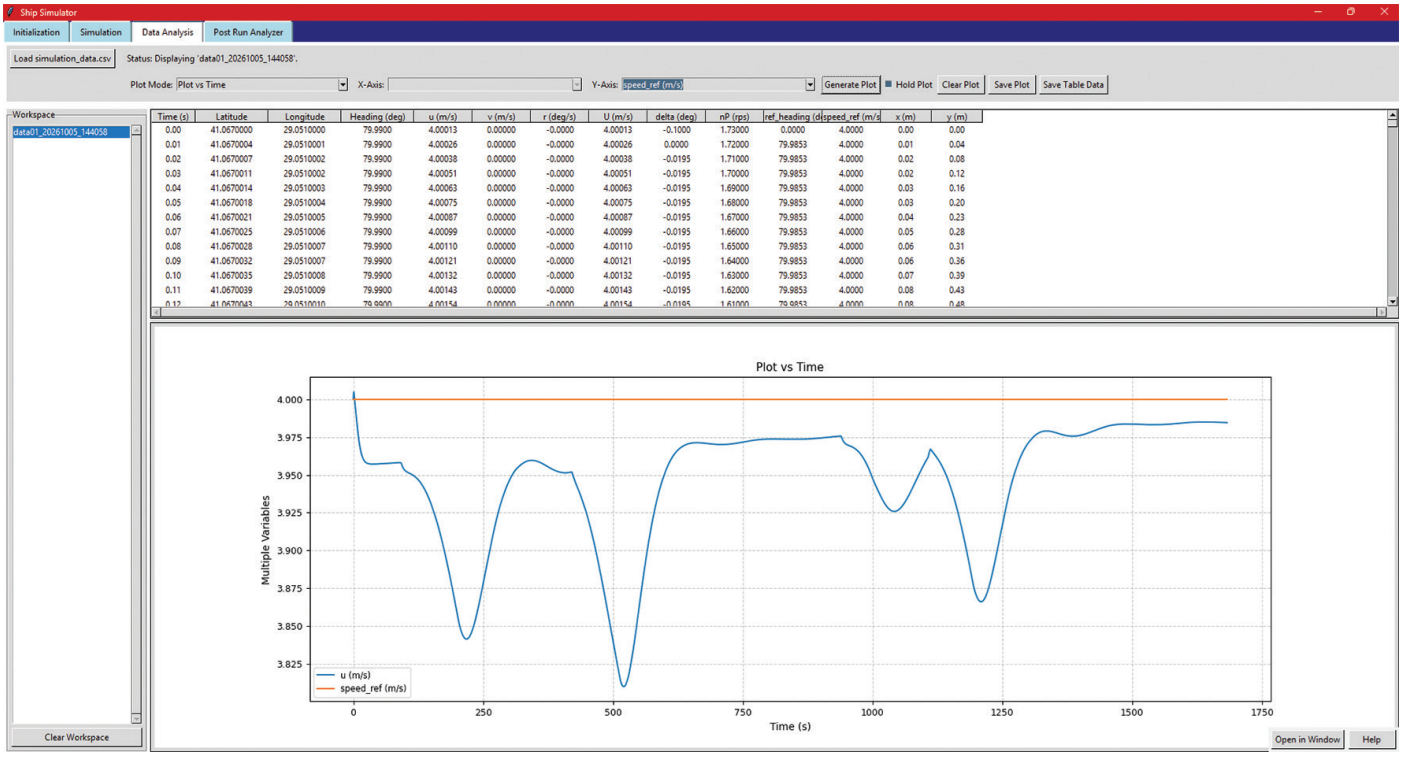


Figure 22. Speed vs. reference in data analysis tab.

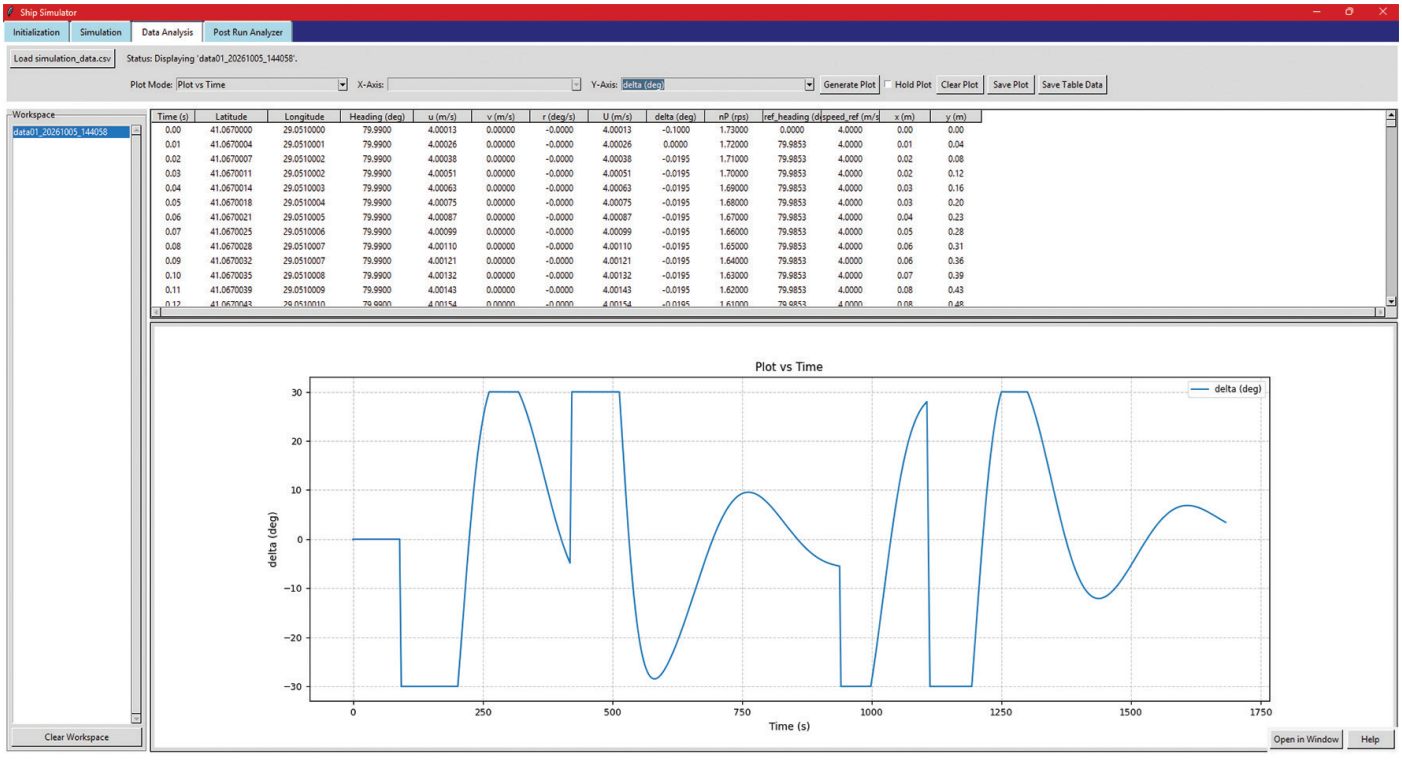


Figure 23. Rudder angle plot in data analysis tab.

Figure 21 presents the recorded vessel heading together with the reference heading generated by the waypoint-guidance module. The reference changes as the active waypoint is updated, producing several distinct turning segments along the route. The vessel follows the general sequence of commanded headings, although overshoot and oscillatory recovery are visible after some reference changes. These results are not presented as evidence of optimized heading control. Instead, they demonstrate that the Data Analysis tab can load an archived simulation, display recorded variables, overlay related signals, and reveal transient characteristics that are not immediately apparent from the geographic trajectory alone.

Figure 22 compares the vessel speed with the commanded reference speed. The measured speed remains relatively close to the reference, with temporary reductions occurring during the more demanding turning sections. The limited speed reduction should not be interpreted as an inconsistency with the heading oscillations shown in Figure 21. Heading and speed are regulated by separate closed-loop controllers. The heading controller generates the rudder command, whereas the speed controller modifies the propeller rotational speed according to the difference between the measured and commanded surge speeds. Their effects remain coupled through the MMG vessel dynamics, but the propulsion controller actively compensates for maneuver-induced changes in resistance and surge speed.

The rudder-angle history in Figure 23 provides the actuator-level information associated with the heading response. Large positive and negative rudder commands occur after several changes in the reference heading, and the rudder reaches its imposed limits during some portions of the maneuver. These periods correspond to the stronger heading corrections visible in Figure 21. The figure therefore demonstrates why route completion alone is insufficient for assessing controller behavior. A vessel may continue along the intended geographic route while requiring substantial steering activity or exhibiting weakly damped heading recovery.

Figure 24 shows that the propulsion input is not held constant during the maneuver. The propeller rotational speed changes throughout the simulation as the speed controller responds to deviations from the reference speed. Increases in propeller command occur around several turning events, indicating active compensation for transient speed loss and additional hydrodynamic resistance. This response explains why the vessel speed in Figure 22 remains comparatively close to its reference despite the pronounced rudder activity and heading oscillations. Figures 21-24 together provide a more complete interpretation of the maneuver by relating heading tracking, speed regulation, steering demand, and propulsion activity.

Figure 25 presents the same simulation in the Post-Run Analyzer tab. The module processes the recorded signals and reports overall and segment-level indicators, including peak overshoot, median settling time, heading RMS error, rudder-saturation ratio, and maximum speed-loss ratio. The calculated values are compared with user-defined preferred and acceptable limits and are displayed through both a normalized radar chart and a textual diagnostic report. Under the limits configured for this demonstration, the run is classified as FAIL because selected heading-tracking and actuator-use measures exceed the acceptable ranges, even though the speed-loss measure remains comparatively small.

This result illustrates the intended function of the post-run module. The simulator does not treat geometric route execution as sufficient evidence of acceptable maneuver quality. Instead, it preserves the complete state and actuator histories and converts them into structured engineering information that can support controller adjustment, comparison between archived runs, and subsequent software-based testing.

6.4. Limitations and Software Availability

The present study has several limitations. The implemented MMG model has not yet been independently evaluated against experimental maneuvering benchmarks, and the PID, FL, and NN configurations were not obtained through a common formal tuning or optimization procedure. Consequently, the demonstrated cases should not be interpreted as validation of hydrodynamic prediction accuracy or as a controlled comparison of controller superiority. The current experiments also do not systematically address environmental disturbances, parameter uncertainty, or robustness across different operating conditions. In addition, the geographically referenced full-scale case is limited to the selected İstanbul Strait route segment described in Section 6.3. These limitations define the scope of the present software demonstration and motivate future benchmark validation, disturbance-rich testing, and controlled controller comparisons. The current research implementation is not publicly distributed as an open-source software package.

7. Conclusion

This paper presented a ship simulator for control testing that combines MMG-based vessel dynamics, waypoint guidance, autonomous and manual control modes, İstanbul Strait-centered visualization, controller comparison, post-processing, and automatic maneuver-quality evaluation. The resulting platform goes beyond a simple route-following demonstrator and functions as a reusable environment for iterative maritime control development.

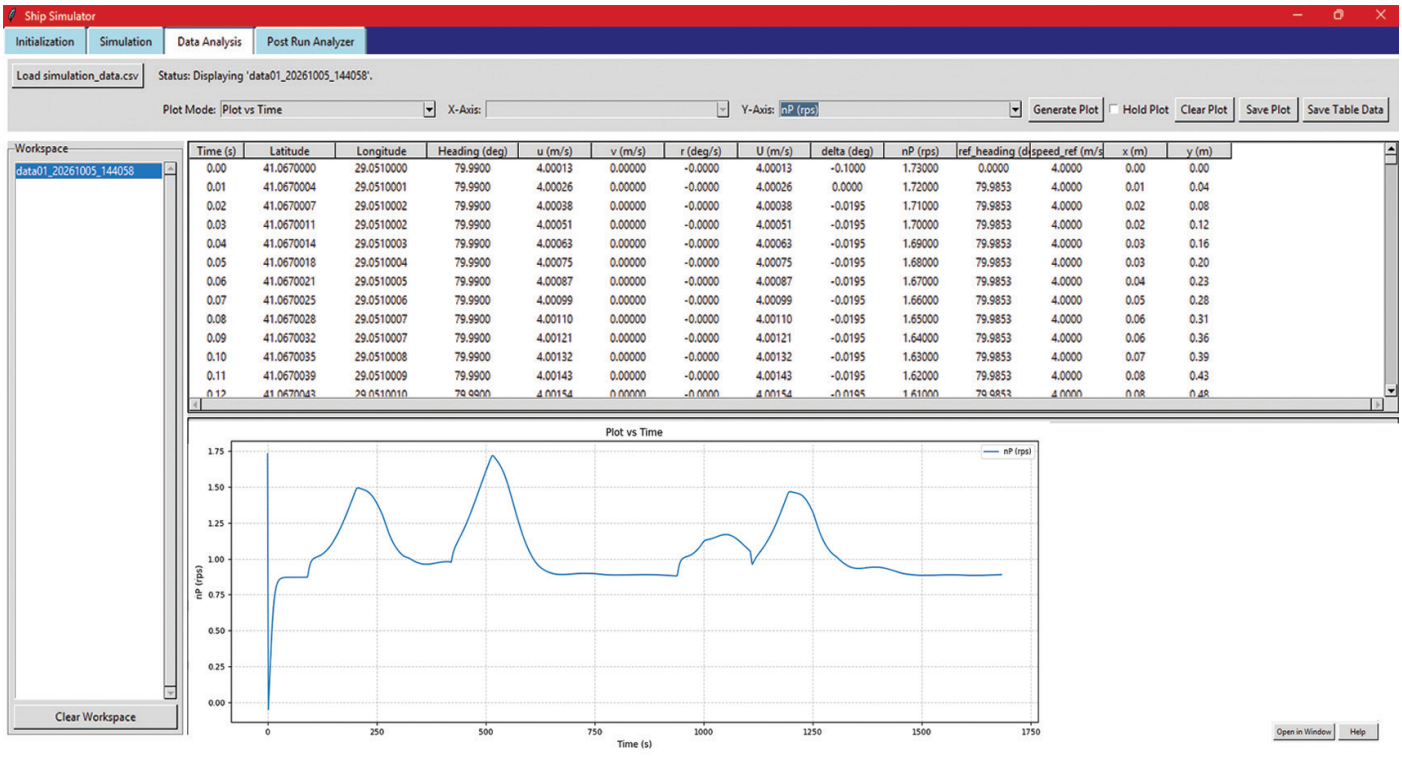


Figure 24. Propeller speed plot in data analysis tab.

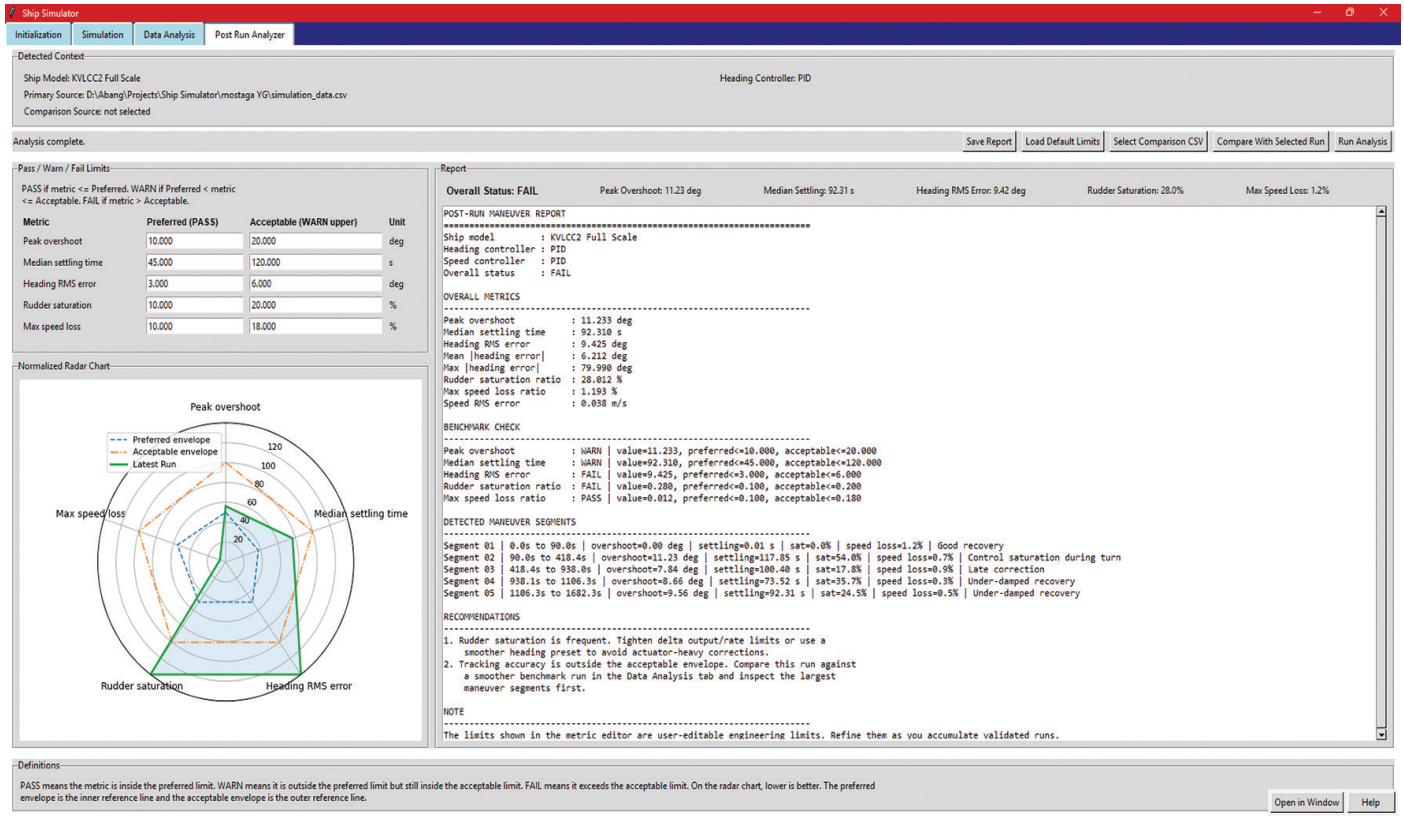


Figure 25. Controller performance result in post-run analyzer tab.

The reported cases demonstrate that the simulator can connect geographically defined routes, MMG-based vessel dynamics, interchangeable controller implementations, synchronized signal recording, and post-run assessment within a common workflow. The PID, FL, and NN examples further show that changes in controller configuration can be examined through the same visualization and analysis structure, although the present demonstrations are not intended to establish controller superiority. The data-analysis and post-run evaluation modules provide quantitative information on tracking response, actuator activity, and speed loss that complements the geographic trajectory. Future work should focus on benchmark validation of the maneuvering model, disturbance-rich scenarios, systematically tuned controller comparisons, and hardware-oriented validation.

Acknowledgements

This study was carried out within the collaboration of the Model-Based Design & Control Systems Laboratory and the Marine Robotics Laboratory at Istanbul Technical University. The work is financially supported by the TÜBİTAK Technology and Innovation Funding Programs Directorate under Program 1507, Project No.: 7240107.

Footnotes

Authorship Contributions

Concept: A. I. Jambak, M. Abdelkhalek, I. Bayezit, and O. K. Kinaci, Design: A. I. Jambak, M. Abdelkhalek, I. Bayezit, and O. K. Kinaci, Data Collection or Processing: A. I. Jambak, M. Abdelkhalek, and I. Bayezit, Analysis or Interpretation: A. I. Jambak, M. Abdelkhalek, and O. K. Kinaci, Literature Review: A. I. Jambak, I. Bayezit, and O. K. Kinaci, Writing: A. I. Jambak, M. Abdelkhalek, I. Bayezit, and O. K. Kinaci.

Conflict of Interest: No conflict of interest was declared by the authors.

Financial Disclosure: The work is financially supported by the TÜBİTAK Technology and Innovation Funding Programs Directorate under Program 1507, Project No.: 7240107.

NOMENCLATURE

Symbol	Description	Unit
m	Ship mass	kg
m_x	Added mass in surge	kg
m_y	Added mass in sway	kg
I_{zG}	Yaw moment of inertia about the center of gravity	kg·m²
J_z	Added yaw moment of inertia	kg·m²
x_G	Longitudinal position of the center of gravity	m
u	Surge velocity	m/s
v	Sway velocity	m/s
r	Yaw rate	rad/s
U	Resultant vessel speed	m/s
ψ	Vessel heading	deg
X	Total surge force	N
Y	Total sway force	N
N	Total yaw moment	N·m
X_H	Hull-induced surge force	N
Y_H	Hull-induced sway force	N
N_H	Hull-induced yaw moment	N·m
X_P	Propeller-induced surge force	N
X_R	Rudder-induced surge force	N
Y_R	Rudder-induced sway force	N
N_R	Rudder-induced yaw moment	N·m
ρ	Water density	kg/m³
L_{pp}	Length between perpendiculars	m
d	Ship draft	m
v'	Non-dimensional sway velocity	–
r'	Non-dimensional yaw rate	–
T	Propeller thrust	N
t_P	Propeller thrust-deduction factor	–
n_P	Propeller rotational speed	rps
D_P	Propeller diameter	m
K_T	Propeller thrust coefficient	–
J_P	Propeller advance ratio	–
w_P	Propeller wake fraction	–
β	Vessel drift angle	rad
δ	Rudder angle	deg
F_N	Rudder normal force	N
t_R	Rudder force-deduction factor	–
a_H	Hull-rudder interaction coefficient	–
x_R	Longitudinal rudder position	m
x_H	Longitudinal position of hull-rudder interaction force	m
A_R	Rudder area	m²
U_R	Resultant rudder inflow velocity	m/s
u_R	Longitudinal rudder inflow velocity	m/s
v_R	Lateral rudder inflow velocity	m/s
α_R	Rudder inflow angle	rad
γ_R	Rudder flow-straightening coefficient	–

x_{ref}	Reference waypoint x-coordinate	m
y_{ref}	Reference waypoint y-coordinate	m
ψ_{ref}	Reference heading	deg
e_{ψ}	Heading tracking error	deg
u_{ref}	Reference surge speed	m/s
e_{u}	Surge-speed tracking error	m/s
δ_{cmd}	Commanded rudder angle	deg
$n_{P,cmd}$	Commanded propeller rotational speed	rps
K_P	Proportional controller gain	–
K_I	Integral controller gain	–
K_D	Derivative controller gain	–
M_p	Peak overshoot	–
T_s	Settling time	s
e_{RMS}	Root-mean-square heading error	deg
R_{δ}	Rudder-saturation ratio	–
δ_{max}	Maximum allowable rudder angle	deg
R_u	Maximum speed-loss ratio	–
u_0	Baseline surge speed	m/s
u_{min}	Minimum surge speed during a maneuver	m/s

8. References

[1] H. Canton, United Nations Conference on Trade and Development (UNCTAD). In The Europa Directory of International Organizations. Springer. 2021.

[2] M. Stopford, "Maritime economics" (3rd ed.), 2008.

[3] T. H. Joung, S. G. Kang, J. K. Lee, and J. Ahn, "The IMO initial strategy for reducing greenhouse gas(GHG) emissions, and its follow-up actions towards 2050." *Journal of International Maritime Safety, Environmental Affairs, and Shipping,* vol. 4, no. 1, pp. 1-7, 2020.

[4] R. Sawada, et al. "Perspective on the marine simulator for autonomous vessel development." arXiv e-prints, 2407.19673. 2024.

[5] M. Abdelkhalek, et al. "E-VCU software toolbox for ARM cortex-R4 processor based electric vehicle control. *XXIX International Conference on Information, Communication and Automation Technologies (ICAT),* pp. 1-6, 2023.

[6] H. Yasukawa, and R. Sakuno, "Application of the MMG method for the prediction of steady sailing condition and course stability of a ship under external disturbances." *Journal of Marine Science and Technology,* vol. 25, pp. 196-220, Mar 2020.

[7] H. Yasukawa, and Y. Yoshimura, "Introduction of MMG standard method for ship maneuvering predictions." *Journal of Marine Science and Technology,* vol. 20, pp. 37-52, 2015.

[8] K. Yuen, G. Xu, and J. Lam, "Special issue on 'artificial intelligence & big data in shipping'." *Maritime Policy & Management,* vol. 47, pp. 575-576, 2020.

[9] M. Maniar, V. Deogaonkar, and A. Somayajula, "Development of a high fidelity multi-agent maritime simulator." *Conference: ASME 2024 43rd International Conference on Ocean, Offshore and Arctic Engineering,* Aug 2024.

[10] Y. Dai, Y. He, X. Zhao, and K. Xu, "Testing method of autonomous navigation systems for ships based on virtual-reality integration scenarios." *Ocean Engineering,* vol. 309, 118597, 2024.

[11] M. A. Hinostroza, and A. M. Lekkas, "Temporal mission planning for autonomous ships: design and integration with guidance, navigation and control." *Ocean Engineering,* vol. 297, 117104, Apr 2024.

[12] H. Xu, and C. Guedes Soares, "Review of path-following control systems for maritime autonomous surface ships." *Journal of Marine Science and Application,* vol. 22, pp. 153-171, Jul 2023.

[13] A. I. Jambak, M. M. H. Abdelkhalek, I. Bayezit, and O. K. Kinaci, "Development of ship simulator for control testing." 4th International Congress on Ship and Marine Technology (GMO-SHIPMAR 2024), pp. 467-476, 2024.

[14] A. I. Jambak, and I. Bayezit, "Robust optimal control of a nonlinear surface vessel model with parametric uncertainties." *Brodogradnja: An International Journal of Naval Architecture and Ocean Engineering for Research and Development,* vol. 74, no. 3, pp. 131-143, 2023.

[15] Y. Jiang, X. Hou, X. Wang, Z. Wang, Z. Yang, and Z. Zou, "Identification modeling and prediction of ship maneuvering motion based on LSTM deep neural network." *Journal of Marine Science and Technology,* vol. 27, pp. 125-137, May 2021.

[16] I. Bayezit, A. I. Jambak, O. K. Kinaci, and B. Fidan, "Sensor data based system identification and modular autopilot control instrumentation of marine craft." *Ocean Engineering,* vol. 317, 119793, Feb 2025.

[17] N. Assani, P. Matic, N. Kastelan, and I. Cavka, "A review of artificial neural networks applications in maritime industry." *IEEE Access,* vol. 11, pp. 139823-139848, Jan 2023.

[18] S. Chang, C. Xiong, and D. Xia, "*Algorithm and simulation of ship maneuver scheme in marine environment*." In: 2020 15th International Conference on Computer Science & Education (ICCSE), pp. 471-476, 2020.

[19] T. Mitsuyuki, "MMG 3DOF model identification with uncertainty of observation and hydrodynamic maneuvering coefficients using MCMC method." *Journal of Marine Science and Technology,* vol. 29, pp. 668-682, 2024.

[20] C. Liu, T. Li, W. Wu, H. Zheng, J. Li, and X. Chu, "Event-triggered predictive path following control of autonomous ships with an MMG model." *Ocean Engineering,* vol. 314, 119582, 2024.

[21] H. Yu, et al. "Ship path optimization that accounts for geographical traffic characteristics to increase maritime port safety." In: *IEEE Transactions on Intelligent Transportation Systems,* vol. 23, pp. 5765-5776, Jun 2022.

[22] A. I. Jambak, and I. Bayezit, "Rapid model-based predictive path planning algorithm for autonomous ship in constrained maritime environment." *Ocean Engineering,* vol. 362, 125724, Jul 2026.

[23] A. B. Ozcan, "*Model based navigation and control of a tankship in narrow waterways*." 4th International Naval Architecture and Maritime Symposium (INT-NAM), pp. 11-13, 2023.

[24] A. I. Jambak, I. Bayezit, and M. Reyhanoglu, "Obstacle avoidance for autonomous sailing sea drones with no-go-zone recovery." *Drones,* vol. 10, no. 8, 578, 2026.

[25] Kongsberg Digital, "Kongsberg Digital," Accessed: Nov 16, 2024. [Online]. Available: https://www.kongsberg.com

[26] Furuno Corporation, "Furuno Envision," Accessed: Nov 16, 2024. [Online]. Available: https://www.furuno.com/special/en/envision/

[27] Furuno Corporation, "Autonomous," Accessed: Nov 16, 2024. [Online]. Available: https://www.furuno.com/en/marine-dx/autonomous/

[28] Furuno Corporation, "Furuno," Accessed: Nov 16, 2024. [Online]. Available: https://www.furuno.com

[29] JRC, "JRC Industry Reports," Accessed: Nov 16, 2024. [Online]. Available: https://www.jrc.co.jp

[30] Wärtsilä Corporation, "Wärtsilä," Accessed: Nov 16, 2024. [Online]. Available: https://www.wartsila.com

[31] Transas Marine, "Transas Marine," Accessed: Nov 16, 2024. [Online]. Available: https://www.transas.com

[32] Siemens AG, "Siemens," Accessed: Nov 16, 2024. [Online]. Available: https://new.siemens.com

[33] Rolls-Royce Marine, "Rolls-Royce," Accessed: Nov 16, 2024. [Online]. Available: https://www.rolls-royce.com

[34] A.I. Jambak, I. Bayezit, O. K. Kinaci, and B. Fidan, "*Control-oriented modeling and cascade control of container ships.*" In: 2023 XXIX International Conference on Information, Communication and Automation Technologies (ICAT), pp. 1-6, 2023.